# Carbon-Dioxide-Enhanced Oil Production from the Citronelle Oil Field in the Rodessa Formation, South Alabama

Final Scientific/Technical Report

Reporting Period: January 1, 2007 to January 31, 2014

Peter M. Walsh, Konstantinos Theodorou, and Corey Shum
University of Alabama at Birmingham, Birmingham, AL

Ermson Z. Nyakatawa, Xiongwen Chen, Kathleen A. Roberts,
Latasha J.-T. Lyte, Loutrina T. Staley, and Rogers Atugonza
Alabama A&M University, Normal, AL

Tommy Chatfield, Gary N. Dittmar, Thomas Boelens, Caroline Donlon, Pete Guerra,
Jack Harper, Rick Jolly, Keith Murphy, Stephen Pennell, Mark Rainer,
Dylan Sheppard, Steve Walker, and William C. Williams
Denbury Resources, Inc., Plano, TX

Tommy Miller, Tommy Henderson, Michael Sullivan, Franklin Everett, Bartley Lambeth,
Paul Stanley, Alec Bailey, Danny Beasley, and Steven Brewer
Denbury Onshore, LLC, Citronelle, AL

David C. Kopaska-Merkel and Denise J. Hills
Geological Survey of Alabama, Tuscaloosa, AL

Peter E. Clark and Jack C. Pashin
Oklahoma State University, Stillwater, OK

Richard A. Esposito
Southern Company, Birmingham, AL

Eric S. Carlson and César A. Turmero
University of Alabama, Tuscaloosa, AL

Shen-En Chen, Yangguang Liu, Peng Wang, and Benjamin Smith
University of North Carolina at Charlotte, Charlotte, NC

Report Issued: June 2014

DOE Award Number DE-FC26-06NT43029

Chandra Nautiyal, Project Manager

Submitted by:

University of Alabama at Birmingham
Department of Mechanical Engineering, BEC 257
1720 2nd Avenue South
Birmingham, AL 35294-4461

# Disclaimer

---

# Abstract

The team of Alabama A&M University, Denbury Resources, Geological Survey of Alabama, Southern Company, University of Alabama, University of Alabama at Birmingham, and University of North Carolina at Charlotte were partners in a Cooperative Agreement with the NETL Strategic Center for Natural Gas and Oil, to evaluate the potential for carbon-dioxide-enhanced oil recovery ($CO_2$-EOR) to increase oil yield and extend the productive life of the Citronelle Oil Field in Mobile County, Alabama. To accomplish this objective, the analysis of the field and its response to $CO_2$ flooding had the following components: (1) Stratigraphy, sedimentology, and petrology, (2) Reservoir fluid properties and miscibility behavior, (3) Reservoir simulation and visualization, (4) $CO_2$ injection and oil production monitoring, (5) Environmental monitoring, (6) Seismic monitoring, and (7) Technology transfer.

The objectives of the project were to provide a detailed analysis of Citronelle geology, reservoir simulations, diagnostic and monitoring techniques, and water-alternating-gas (WAG) injection experience to assist the operator in designing and implementing a commercial $CO_2$ flood at Citronelle that would realize the expected EOR potential of the field and could also provide a secure sequestration site for $CO_2$ produced from electric power generation.

Carbon dioxide was injected through an infill well in an inverted five-spot well pattern into two sands at depths near 11,000 ft. A total of 8036 tons were injected, from December 2009 to September 2010, at an average rate of 31 tons/day, including the down time for maintenance. The only significant interruption in the injection was caused by a tubing leak repaired during January 2010. The following outcomes and events associated with the injection should be considered in any plan for a commercial $CO_2$ flood in the Citronelle Field:

Early breakthrough of injected $CO_2$ was observed at wells to the west-southwest and east-northeast from the injector, in the approximate direction of maximum horizontal compressive stress in the Southeast.

A pressure-transient test provided strong evidence for a 600 to 1000-ft-long hydraulic fracture intersecting the injector, consistent with the early breakthrough of $CO_2$ at the producer in the southwest corner of the test well pattern. In the plan for a $CO_2$ flood, a maximum injection pressure should be established by testing and calculation, to minimize the probability that pressure in the injection zone may initiate unwanted fractures or propagate existing fractures.

On completing the $CO_2$ injection and returning to water injection, power oil pumps experienced excessive erosion-corrosion by particles and scale mobilized by the combination of $CO_2$ and water. If WAG recovery were implemented, power oil pumps that are not resistant to erosion-corrosion should be replaced to avoid the loss of production during down time resulting from premature failure of the pumps.

Injectivity to water suffered a marked reduction following the $CO_2$ injection, from an average of 160 bbl/day before the $CO_2$ injection to 67 bbl/day after. The reduction occurred primarily in the finer-grained of the two target sands and is thought to have been caused by the same particles responsible for wear of the power oil pumps. The particles could not be flushed out by flowing back the injector.

During repair of a tubing leak in the injector the internal plastic coating in the tubing was found to be flaking off. A test is needed to assess the integrity of internal plastic coating in new tubing.

Treatments of the injector with surfactant, hydrocarbon solvent, and asphaltene dispersant had little permanent effect on injectivity to water, indicating that neither capillary blocking nor hydrocarbon precipitation was a significant contributor to the low injectivity to water following the $CO_2$ injection.

The difficulties experienced on switching from $CO_2$ to water injection suggest that continuous $CO_2$ injection would be preferable to WAG.

Conclusions from the study of oil and gas from Citronelle Field, geology of the Donovan Sands, reservoir simulation, seismic surveys, and environmental monitoring also provide valuable guidance for reservoir management during commercial $CO_2$-EOR and $CO_2$ storage:

The minimum miscibility pressure of $CO_2$ with Citronelle oil was found to be 2340 ± 160 psig, assuring a miscible flood at depths of ~11,000 ft.

The carbon-13 to carbon-12 isotope ratio in $CO_2$ was shown to be a robust method for distinguishing injected $CO_2$ from $CO_2$ native to the reservoir, without addition of tracer.

The sedimentologic and petrologic analysis was synthesized into a sequence stratigraphic model that provides a predictive framework for reservoir distribution and quality. Citronelle Field is structurally simple, but the interplay of depositional and diagenetic processes during the evolution of the field resulted in reservoir sandstone bodies in which heterogeneity occurs at disparate scales, an important consideration for prioritizing $CO_2$ injection targets and understanding flow pathways. The extreme facies heterogeneity is expected to present one of the greatest challenges to design of a commercial $CO_2$-EOR project for Citronelle Field.

A Core Workshop was developed by staff members at Geological Survey of Alabama, for education of interested groups at all levels of expertise, about the geology and resource potential of the Citronelle Field. Hundreds of thin sections from the Citronelle Field were added to the Survey's thin section archive.

Reservoir simulations showed that cumulative oil production increases with increasing amount of $CO_2$ injected, regardless of the assumed permeability distribution. However, there is an optimum $CO_2$ slug size, from the point of view of the profitability of a $CO_2$-EOR project. The optimum size of $CO_2$ slug increases with increasing oil price. The discount factor has little impact on the optimum size of $CO_2$ slug at high oil prices, but does have some impact at low oil prices.

A powerful open-source framework was developed for simulation of large-scale, fine-grid, porous media systems.

The refraction microtremor seismic technique, utilizing only existing ambient excitation sources, provided useful information on the stress state of the reservoir and formations above it. The method was able to distinguish stress changes in the oil-bearing layer from stress changes in the strata above.

Environmental and ecological monitoring throughout the project demonstrated that the impact of $CO_2$ handling and injection was minimal to non-existent.

The capacity of Citronelle Dome for $CO_2$ storage was estimated to be 530 to 2100 million short tons, sufficient to store the $CO_2$ produced from coal-fired generation at nearby Alabama Power Plant Barry (12 million tons/year) for at least 40 years.

Uncertainty introduced into the baseline oil production, during troubleshooting of $CO_2$ injection, undermined the ability to make a reliable estimate of the incremental gain or loss in oil production associated with the $CO_2$ injection.

# Acknowledgments

The material presented in this report is based upon work supported by the U.S. Department of Energy, National Energy Technology Laboratory, under Award Number DE-FC26-06NT43029, entitled, "Carbon-Dioxide-Enhanced Oil Production from the Citronelle Oil Field in the Rodessa Formation, South Alabama."

Additional support for the project was provided as cost share by Denbury Resources, Inc., Southern Company Services, Inc., Geological Survey of Alabama, University of Alabama, University of Alabama at Birmingham, and University of North Carolina at Charlotte.

The authors thank Chandra Nautiyal, in the NETL Strategic Center for Natural Gas and Oil, for his helpful and effective collaboration as NETL Project Manager.

The authors also thank Tracy Evans, at the time President and Chief Operating Officer of Denbury Resources, for his encouragement and support for the original proposal for the project when it was submitted to NETL in 2006, and for facilitating the collaboration of the groups at Denbury Resources in Plano and Denbury Onshore in Citronelle with members of the team at AAMU, GSA, UA, UAB, and UNCC.

# Table of Contents

# Table of Contents (continued)

# Table of Contents (continued)

# Table of Contents (continued)

# List of Tables

# List of Tables (continued)

# List of Figures

# List of Figures (continued)

# List of Figures (continued)

# List of Figures (continued)

# List of Figures (continued)

# List of Figures (continued)

# List of Figures (continued)

# List of Figures (continued)

# List of Figures (continued)

# Executive Summary

## Objective

The team of Alabama A&M University, Denbury Resources, Geological Survey of Alabama, Southern Company, University of Alabama, University of Alabama at Birmingham, and University of North Carolina at Charlotte were partners in a Cooperative Agreement with the NETL Strategic Center for Natural Gas and Oil, to evaluate the potential for carbon-dioxide-enhanced oil recovery to increase oil yield and extend the productive life of the Citronelle Oil Field in Mobile County, Alabama. To accomplish this objective, the analysis of the field and its response to $CO_2$ flooding had the following components: (1) Stratigraphy, sedimentology, and petrology, (2) Reservoir fluid properties and miscibility behavior, (3) Reservoir simulation and visualization, (4) $CO_2$ injection and oil production monitoring, (5) Environmental monitoring, (6) Seismic monitoring, and (7) Technology transfer.

The Citronelle Field, discovered in 1955, is operated by Denbury Onshore, LLC, a subsidiary of Denbury Resources, Inc., of Plano, TX. Original oil in place (OOIP) is estimated to have been 378.6 million bbl (Fowler et al., 1998), of which 173 million bbl, or 46%, have been produced to date. Secondary recovery by water flooding has been underway since 1961. Present production is approximately 540,000 bbl/year, or 6.6% of the peak of 8.2 million bbl produced in 1963. The field is approaching the ultimate recovery possible using conventional secondary recovery techniques.

According to the criteria enumerated by Kovscek (2002), the Citronelle Field is a good candidate for both $CO_2$-enhanced oil recovery ($CO_2$-EOR) and $CO_2$ sequestration. From the reservoir engineering prospective, the site is mature and water-flooded, with existing infrastructure, including deep wells, and from the geological prospective, the field consists of fluvial-deltaic sandstone reservoirs in a simple structural dome and, because of the presence of a regionally extensive anhydrite seal, four-way structural closure, and lack of faulting, is naturally stable with respect to $CO_2$ storage. However, the geology of Citronelle Field is quite different from that of the carbonate strata of the Permian Basin in Texas and New Mexico and the Williston Basin in North Dakota and Montana, well-known sites of commercially successful $CO_2$-EOR projects. The present project was designed to evaluate the potential of $CO_2$-EOR for tertiary recovery from highly heterogeneous sandstone reservoirs of the type found at Citronelle, and the capacity of the oil reservoirs and adjacent saline formations at Citronelle for sequestration of carbon dioxide.

## Impact

The Citronelle Field is Alabama's largest oil producer, and a significant contributor to the economy of the State and employment in the region. Estimates of the EOR potential at Citronelle range from 26 to 64 million bbl. Assuming a conservative 10% of OOIP to be economically recoverable (38 million bbl) using $CO_2$-EOR and a production rate increased to 1.1 million bbl/year (twice present production), the life of the field would be extended by 35 years.

The capacity of Citronelle Dome for $CO_2$ storage is estimated to be 530 to 2100 million short tons (Esposito et al., 2008), sufficient to store the $CO_2$ produced from coal-fired generation at nearby Alabama Power Plant Barry (12 million tons/year) for at least 40 years. Plant Barry is the

host site for a major demonstration of carbon capture and sequestration technology, including pipeline transport and geologic storage of $CO_2$ in a saline formation in Citronelle Dome (Esposito et al., 2011; Koperna et al., 2012). Plant Barry is anticipated, by Southern Company, Alabama Power Company, and Denbury Resources, to be a source of $CO_2$ for EOR in the Citronelle Field, if the present project indicates that $CO_2$-EOR will be profitable and provides the desired guidance for management of the reservoir under $CO_2$ flooding.

**Accomplishments**

***Phase I.*** An inverted five-spot well pattern and two target sands were chosen for testing. A detailed study of the geology of the sands established their permeability and connectivity. Reservoir simulations showed that 7500 tons of $CO_2$ were sufficient to demonstrate $CO_2$-EOR and produce significant incremental oil. Background conditions of $CO_2$ in air, $CO_2$ flux from soil, and the species distribution and growth rate of vegetation were established, for comparison with conditions during and after $CO_2$ injection. A rolling ball viscometer was designed, assembled, and calibrated, for measurement of $CO_2$-oil miscibility behavior.

Highlights of the work done in preparation for the injection of $CO_2$ were: (1) the stratigraphy, sedimentology, and petrology of the Donovan Sand in the vicinity of the test site were analyzed and documented at an unprecedented level of detail; (2) realistic and informative reservoir simulations were performed; (3) the minimum miscibility pressure and absence of precipitation from oil in the presence of $CO_2$ were established; (4) a geomechanical stability analysis showed that only small deformations from overburden pressure and no rupture of the target formation were likely; (5) the baseline environmental and ecological conditions surrounding the site were documented; (6) seismic surveys to the depth of the target formation were recorded during the baseline water flood; (7) a favorable economic analysis was conducted that identified the optimum $CO_2$ slug size for water-alternating-gas oil recovery under specified $CO_2$ cost and oil price constraints; and (8) the wells in the inverted five-spot were prepared for testing and the equipment and infrastructure for $CO_2$ storage, pumping, and injection were put in place.

***Phase II.*** After initially encountering difficulty in pumping liquid $CO_2$, the $CO_2$ injection, of 8036 tons, began in December 2009 and was completed on September 25, 2010. Water injection resumed 4½ hours later. Three problems having significant bearing on the design of a commercial $CO_2$ flood at Citronelle occurred during or shortly after the $CO_2$ injection: (1) excessive produced gas, primarily $CO_2$, appeared in May 2010, after 4 months of continuous $CO_2$ injection, at Well B-19-11 in the southwest corner of the inverted five-spot, (2) on returning to water injection following the $CO_2$ injection, the water injection rate, which had been an average of 160 bbl water/day before injection of $CO_2$, decreased to 67 bbl water/day, and (3) on returning to water injection, following the injection of $CO_2$, excessive wear of the down-hole power oil pumps occurred, due to erosion-corrosion by particulate matter mobilized by the $CO_2$ and water.

Oil production at Tank Battery B-19-8, which receives oil from producers B-19-7, B-19-8, and B-19-9 in the test pattern, had experienced an average decline of 20 bbl/day/year during the period from March to December 2009, when there was no injection of water or $CO_2$, due to the problems pumping liquid $CO_2$. Beginning in January 2010, coinciding with the start of continuous $CO_2$ injection, the decline in production was reversed, and, from January to September 2010, during injection of the 8036 tons of $CO_2$, oil production increased at the average rate of 18 bbl/day/year. Then, after switching from $CO_2$ back to water injection, and in response to the low water injection rate and erosion of the power oil pumps, oil production at Tank Battery B-19-8 decreased from its peak of 59 bbl/day in September 2010 to only 21 bbl/day in March 2011. Change of materials and

increase in the length of stroke in the power oil pumps restored the frequency of pump pulls to normal and oil production at Tank Battery B-19-8 recovered some of its loss, averaging 38 bbl/day from June 2011 to April 2014, though lower than the oil production before injection of $CO_2$.

The response to $CO_2$ injection at Tank Battery B-19-11, where oil from the fourth producer in the inverted five-spot is collected, was quite different from that observed at Tank Battery B-19-8. In contrast to the immediate increase in oil production observed at Tank Battery B-19-8 at the onset of $CO_2$ injection, production at Tank Battery B-19-11 continued for four months on the declining trajectory that it had been following for the previous 10 months. Then, coinciding with breakthrough of $CO_2$ at Well B-19-11 in May 2010, production at the battery abruptly decreased, by approximately the typical production from Well B-19-11 (8 to 9 bbl/day), then continued its steady decline over the next two years to production in the range from 21 to 30 bbl oil/day. Produced gas at Well B-19-11 was so excessive that the well was killed on September 2, 2010, three weeks before the end of the $CO_2$ injection, and remained shut in until May 5, 2011. Because Well B-19-11 was shut in during the transition from $CO_2$ back to water injection, the power-oil pumps in wells on Tank Battery B-19-11 were not subject to the erosion-corrosion experienced in the wells on Tank Battery B-19-8.

Documentation of the presence or absence of environmental consequences of $CO_2$ flooding had a high priority. Measurements of soil gas composition versus depth, $CO_2$ flux from soil, soil temperature, soil moisture, and soil elements (carbon, nitrogen, and phosphorus), were made before, during, and following $CO_2$ injection, at three locations surrounding the injector, each of three producers, and a plugged and abandoned well within the test pattern. No correlation of the $CO_2$ fluxes from soil with the location or timing of the $CO_2$ injection was detected. Measurements of $CO_2$ in ambient air were recorded at least once each quarter from September 2007 to June 2012, at 104 points on a grid covering the City of Citronelle and the oil field. The $CO_2$ measurements were consistent with the seasonal variations and long-term trends of the local NASA satellite-based Atmospheric Infrared Sounder data and worldwide average atmospheric $CO_2$ levels. The growth of trees and shrubs and their species distribution were monitored in test plots near the injector, producers, and tank batteries. Of the eight vegetation test plots established at the wells and tank batteries, an increase in the rate of growth of vegetation was observed only in the plot near the injector, Well B-19-10 #2, though this observation is at odds with the measurements of $CO_2$ in ambient air and measurements of $CO_2$ fluxes from soil near the well.

Advancement of diagnostic techniques for monitoring interaction between the $CO_2$ injection and geologic formation was another priority. Shear-wave velocities were measured using the Refraction Microtremor (ReMi) technique to depths of 12,500 feet using wireless geophones placed along two paths spanning 30,100 and 25,600 feet, to the south and southwest, respectively, from the injection well. Shear-wave velocities recorded before and during $CO_2$ injection suggested a 10% increase in stress associated with $CO_2$ injection, in layers above the injection zone. The record of normalized well-head pressure at the injector was consistent with the normalized equivalent stresses from the seismic sensor array at the depth of the target sands during $CO_2$ injection.

***Phase III.*** The key questions to be answered during Phase III were: (1) What property of the formation (e.g. fracture or high permeability zone) is responsible for the early $CO_2$ breakthrough and excessive gas production at Well B-19-11, to the southwest of the injector? (2) What are the causes of the marked loss in injectivity experienced on switching from $CO_2$ injection back to water, and can it be reversed? (3) Are significant environmental and ecological effects present after a longer period of time? (4) Did the reservoir simulations capture important features of the performance of the pilot test and can their accuracy and predictive power be improved by large-

scale, fine-grid simulations? and (5) Is continuous $CO_2$ injection or water-alternating-gas (WAG) the better strategy for commercial EOR at Citronelle?

A 15-day-long pressure-transient test on the injection well, consisting of two cycles of shut-in and water injection, was conducted from November 28 to December 12, 2011. The data, analyzed by Eric Carlson, strongly suggest that there is a hydraulic fracture intersecting the injector having a total length of 600 to 1000 ft, in a zone having a permeability of only approximately 0.4 mdarcy. The pressure-transient test does not provide any information about the direction of the fracture, but the most likely direction is that of maximum horizontal compressive stress in the Southeastern U.S., typically N70E to N80E. Two of the wells at which early breakthrough of $CO_2$ was detected lie on the line at N69E relative to the injector.

An injection profile test was conducted in January 2012 to determine if either of the target sands was primarily responsible for the loss in injectivity to water, following the $CO_2$ injection. The test established that 35% of the water flow was to Sand 14-1 and 65% was to Sand 16-2, so neither injection zone was completely blocked, but comparison with the results of an injection profile run before $CO_2$ injection showed that loss of flow into the finer-grained Sand 14-1 was primarily responsible for the low injectivity to water.

Injected water was treated with surfactant to reduce capillary pressure, if that were blocking the water flow. The surfactant treatment was conducted during the three months from July 25 to November 7, 2012. Though the surfactant was associated with a transient increase in injectivity, both during and following the treatment, after about six months the water injection rate returned to the low level typical of the period immediately following $CO_2$ injection. The conclusion from the surfactant treatment was that capillary blocking was not the principal effect responsible for the loss in injectivity experienced on returning to water injection following the $CO_2$ slug.

Following the surfactant treatment, during repair of a tubing leak, flakes of the internal plastic coating of the tubing and particles of iron oxide scale were discovered in the injector. Plugging of the finer-grained Sand 14-1 by fine particles of scale is considered the most likely cause of the injection well's low injectivity to water following the $CO_2$ injection. Problems with internal plastic coating were experienced by Denbury Resources throughout its oilfield operations at around the same time.

Treatment of the injector with hydrocarbon solvent and asphaltene dispersant had only a transient effect on its injectivity to water. Paraffins and asphaltenes left behind when supercritical $CO_2$ mobilized lighter components are not thought to have made a significant contribution to the loss in injectivity to water following the $CO_2$ injection.

A flow-back of the injector was conducted in an attempt to flush out particles, but the flow-back had no lasting effect. If particles were, in fact, responsible for the loss in injectivity, they were not easily dislodged.

Each of the attempts to restore injectivity to water: treatment with surfactant, treatment with hydrocarbon solvent and asphaltene dispersant, and flow-back, resulted in transient improvement in the water injection rate, but none of them had a permanent effect on injectivity. The recent average injection rate, in March and April 2014, was $72 \pm 26$ bbl water/day, not significantly higher than the average rate of $67 \pm 21$ bbl/day observed from the end of the $CO_2$ injection on September 28, 2010 (not including in the average the high water injection rates recorded on the first two full days of water injection, September 26 and 27), to the beginning of surfactant treatment on July 25, 2012.

Uncertainty introduced into the baseline oil production at both tank batteries, during the troubleshooting of liquid $CO_2$ injection, undermined the ability to make a reliable estimate of the incremental gain or loss in oil production associated with the $CO_2$ injection.

The difficulties experienced on switching from $CO_2$ to water injection suggest that continuous $CO_2$ injection would be preferable to WAG recovery.

Shen-En Chen and his coworkers at the University of North Carolina at Charlotte demonstrated the ability of the passive refraction microtremor seismic monitoring technique, utilizing only existing ambient excitation sources, to detect changes in the subsurface static stress distribution during $CO_2$ injection. They also showed that a lumped mass model was useful for the interpretation of the measurements, to detect changes in subsurface wave propagation associated with $CO_2$ injection.

Environmental and ecological monitoring throughout the project demonstrated that the impact of $CO_2$ handling and injection on the $CO_2$ in ambient air, $CO_2$ flux from soil, and growth of vegetation was minimal. Measurements of $CO_2$ in ambient air by Xiongwen Chen and Kathleen Roberts at Alabama A&M University were consistent with measurements by the NASA Atmospheric Infrared Sounder over a large region including Citronelle (NASA, 2012). Roberts (2013) did report an increase of 2.3 ppmv $CO_2$ in the averages over all sets of data taken before and after breakthrough of $CO_2$ at Well B-19-11 in May 2010, after correcting for the worldwide increase in atmospheric $CO_2$ during the period, but the scatter of the $CO_2$ measurements used to construct the averages is almost an order of magnitude larger. An increase in the rate of growth of vegetation was observed during the study period in the test plot established near the injector, but Roberts and Chen (2012) concluded that it was not significant and most likely could be explained by other factors. Ermson Nyakatawa and his coworkers at Alabama A&M University continued their monitoring of the condition of soils and $CO_2$ fluxes from soil at three locations surrounding the injector, each of three producers, and the plugged and abandoned well within the test pattern. They concluded that there were no indications that post-$CO_2$-injection $CO_2$ fluxes followed a different pattern compared to pre-injection $CO_2$ fluxes and that changes in the observed $CO_2$ fluxes were due to the natural variability associated with soil gas fluxes, attributable to natural processes such as soil biochemical activity and physical properties such as temperature and moisture content.

Jack Pashin, of Oklahoma State University, and David Kopaska-Merkel and Denise Hills at the Geological Survey of Alabama considered the geological implications for field management of their thorough analysis of the stratigraphy, sedimentology, and petrology of the Donovan Sandstone in Citronelle Field. Although Citronelle Field is structurally simple, analysis of depositional architecture reveals extreme facies heterogeneity. With so many productive sandstone units to consider, one of the greatest challenges in designing waterflood and $CO_2$-EOR programs for the field is expected to be management of that heterogeneity. Stratigraphic cross sections indicate that reservoir sandstone bodies tend to occur in clusters, thus initial planning should perhaps focus on assessment of those clusters in specific focus areas.

Experience from the $CO_2$ flood area employed in the present study indicates that, although several productive sandstone units may be present in a given area, most production comes from only a few of those units. Consequently, identifying the most productive sandstone units and assessing heterogeneity and oil-in-place appears to be an important element of long-term planning. Another factor for consideration when designing injection programs is stratigraphic isolation and hydraulic confinement of the target sandstone bodies. Keeping injectate in zone may be a significant problem where numerous sandstone bodies are stacked and amalgamated into multi-

storey successions, and this may limit the predictability of reservoir sweep, as well as predictability of the location and timing of $CO_2$ breakthrough.

Interwell heterogeneity is another key consideration in Citronelle Field. Although some sandstone units have great lateral continuity, each well may have a substantially different geophysical log signature, reflecting major variation of reservoir properties among wells. Original well spacing in the field was 40 acres, and downspacing when injection wells were drilled for the Tertiary Oil Recovery (TEOR) Project (Gilchrist, 1981, 1982) indicates that the original well pattern undersampled reservoir heterogeneity. Correlations based on the original well pattern have limited value for predicting the thickness and continuity of productive sandstone units in infill wells.

The most important sources of heterogeneity appear to be primary facies heterogeneity and diagenetic processes associated with pedogenesis. Primary facies heterogeneity is expressed as isolated channel fills in discontinuous sandstone units and nesting of multiple channel fills within the more widespread sandstone units. Fining upward and plugging of upper-tier channels with mud is a source of significant relief at the tops of the sandstone bodies that may exceed relief at the bases of the sandstone units. Because of this, high potential exists for oil and injected $CO_2$ to be stranded in the sandstone between mud-plugged channels.

Two conditions must be met for pay development in the Donovan sandstone. The first is porosity enhancement by dissolution of feldspar during pedogenesis. The second is flushing of the dissolution products out of the sandstone. Where those products have accumulated, moreover, the sandstone is plugged with clay matrix and has the petrophysical properties of mudstone. As a result, the distribution of pay is as much the result of diagenesis as it is of sedimentation. Thus, the mapped patterns of reservoir sandstone thickness do not necessarily define the original channel networks. Maps made assuming traditional channel geometry may overestimate sandstone continuity. Nonetheless, Citronelle Field is an attractive target for $CO_2$-EOR. A careful program that identifies priority areas and includes a detailed assessment of reservoir architecture and internal heterogeneity will be an important key to unlocking its potential.

A component of the effort to interpret and understand the behavior of $CO_2$ during and following injection was the development of nSpyres, the open-source reservoir simulator and productivity environment developed by Eric Carlson at the University of Alabama. With enhancements and improvements implemented during Phase III, large-scale, fine-grid simulations of 50 years of water flooding at the test site were accomplished using a regular grid of 8.2 million cells, each measuring 52.8 x 52.8 x 1 ft. Geostatistical methods were applied to generate permeability distributions leading to high flow capacity zones, consistent with the early breakthrough of $CO_2$ observed in the field. The simulator demonstrated outstanding performance on the benchmark Problem 2 of the SPE Tenth Comparative Solution (Christie and Blunt, 2001).

**Technology Transfer**

Staff members at the Geological Survey of Alabama developed a Core Workshop, for education of interested groups at all levels of expertise, about the geology and resource potential of the Donovan Sand in the Citronelle Field. The workshop focuses on the geologic history of the Donovan and its depositional, diagenetic, and reservoir complexity, as an illustration of how sedimentology can control critical characteristics of that type of hydrocarbon reservoir.

As a result of research performed at the Geological Survey of Alabama in connection with the present project, hundreds of thin sections from the Citronelle Field were added to the Survey's

thin section archive. The archive records are being modernized and standardized to make this resource more accessible to potential users.

The nSpyres open-source framework for simulation of large-scale porous media systems, developed by Eric Carlson at the University of Alabama, is based on the Python programming language, and makes substantial use of numerical and visualization packages that are freely available and are easy to install on multiple platforms. A productivity environment makes it convenient for users to interact with source data and simulation results. The simulator will soon be providing its capabilities on large-scale, fine-grid porous media problems to the entire reservoir engineering community.

Fourteen peer-reviewed papers describing work directly related to the project were published, including comprehensive reviews of the geology of Citronelle Dome and its prospects for $CO_2$-enhanced oil recovery and capacity for $CO_2$ storage (Esposito et al., 2008, 2010). Results of work under the project were presented by members of the project team at seventeen national and international conferences and at twelve regional and local meetings.

**Acronyms, Abbreviations, and Symbols in the Executive Summary**

| | |
|---|---|
| A&M | Agricultural and Mechanical (Alabama A&M University) |
| EOR | enhanced oil recovery |
| LLC | limited liability company |
| NASA | National Aeronautics and Space Administration |
| NETL | National Energy Technology Laboratory |
| N*x*E | compass direction, *x* degrees east of north |
| OOIP | original oil in place |
| ReMi | refraction microtremor |
| TEOR | Tertiary Oil Recovery Project (Gilchrist, 1981, 1982) |
| WAG | water alternating gas recovery technique |

**References in the Executive Summary**


Christie, M. A., and M. J. Blunt, "Tenth SPE Comparative Solution Project: A Comparison of Upscaling Techniques," *SPE Reservoir Evaluation & Engineering*, **2001**, *4*, 308-317.

Esposito, R. A., J. C. Pashin, and P. M. Walsh, "Citronelle Dome: A Giant Opportunity for Multi-Zone Carbon Storage and Enhanced Oil Recovery in the Mississippi Interior Salt Basin of Alabama," *Environmental Geosciences*, **2008,** *15* (2), 53-62.

Esposito, R. A., J. C. Pashin, D. J. Hills, and P. M. Walsh, "Geologic Assessment and Injection Design for a Pilot $CO_2$-Enhanced Oil Recovery and Sequestration Demonstration in a Heterogeneous Oil Reservoir: Citronelle Field, Alabama, USA," *Environmental Earth Sciences*, **2010**, *60*, 431-444.

Esposito, R., R. Rhudy, R. Trautz, G. Koperna, and G. Hill, "Integrating Carbon Capture with Transportation and Storage," *Energy Procedia*, **2011**, *4*, 5512-5519.

Fowler, M. L., L. E. Safley, M. A. Young, R. H. Stechmann, E. S. Blair, and R. E. Crumb, "Reservoir Management Strategy for Citronelle Field, Mobile County, Alabama," Report No.

NIPER/BDM-0353, Prepared for the National Petroleum Technology Office, U.S. Department of Energy, Tulsa, OK, by BDM Petroleum Technologies, Bartlesville, OK, 1998.

Gilchrist, R. E., "Miscibility Study (Repeat 50% P.V. Slug) in Cores, Citronelle Unit, Mobile County, Alabama," unpublished report prepared for the Unit Manager of Citronelle Field, 1981.

Gilchrist, R. E., "Evaluation of Produced Fluids from the Carbon Dioxide Pilot Area in the Citronelle Unit, Mobile County, Alabama," unpublished report prepared for the Unit Manager of Citronelle Field, 1982.

Koperna, G., D. Riestenberg, V. Kuuskraa, R. Rhudy, R. Trautz, G. R. Hill, and R. Esposito, "The SECARB Anthropogenic Test: A US Integrated $CO_2$ Capture, Transportation and Storage Test," *International Journal of Clean Coal and Energy 1*, **2012**, 13-26.

Kovscek, A. R., "Screening Criteria for $CO_2$ Storage in Oil Reservoirs," *Petroleum Science and Technology 20*, **2002**, 841-866.

National Aeronautics and Space Administration, Jet Propulsion Laboratory, California Institute of Technology, AIRS Atmospheric Infrared Sounder, AIRS Carbon Dioxide Data, http://airs.jpl.nasa.gov/ (accessed April 2012).

Roberts, K. A., "Ecological Monitoring and Assessment of Enhanced Oil Recovery ($CO_2$-EOR) for Carbon Storage," Ph.D. Dissertation, Department of Biological and Environmental Sciences, Alabama A&M University, Normal, AL, December 2013.

Roberts, K. A., and X. Chen, "Direct and indirect assessment of vegetation located near $CO_2$-mediated enhanced oil recovery ($CO_2$-EOR) activities," Ecological Society of America, 97th Annual Meeting, Portland, OR, August 5-10, 2012.

# 1. Introduction

## 1.1. Background

The team of Alabama A&M University, Denbury Resources, Inc., Geological Survey of Alabama, Southern Company, University of Alabama, University of Alabama at Birmingham, and University of North Carolina at Charlotte were partners in a Cooperative Agreement with the NETL Strategic Center for Natural Gas and Oil, to evaluate the potential for carbon-dioxide-enhanced oil recovery to increase oil yield and extend the productive life of the Citronelle Oil Field in Mobile County, Alabama. The Citronelle Unit, largest oil producer in the State of Alabama, is operated by Denbury Onshore, LLC, a subsidiary of Denbury Resources, Inc., of Plano, TX.

The geology and history of the Citronelle Oil Field, discovered in 1955, have been described by Eaves (1976), Fowler et al. (1998), and Kuuskraa, Lynch, and Fokin (2004). Oil is produced from the Donovan Sands in the Rodessa Formation (Lower Cretaceous). An estimate of the original oil in place (OOIP) is 378.6 million bbl (Fowler et al., 1998). Production peaked in 1963 at 8,220,364 bbl/year (Alabama State Oil and Gas Board, 2014). Production in 2013 was 538,991 bbl/year, or 6.6% of the peak. Most of the field has undergone water flooding since 1961 (Eaves, 1976; Fowler et al., 1998). Cumulative production, at the end of February 2014, was 173,292,422 bbl, or 46% of OOIP, approaching the ultimate oil recovery expected to be achievable using conventional secondary recovery techniques.

According to the criteria enumerated by Kovscek (2002), the Citronelle Field is a good candidate for both $CO_2$-EOR and $CO_2$ sequestration. From the reservoir engineering prospective, the site is mature and water-flooded, with existing infrastructure, including deep wells, and from the geological prospective, the field consists of fluvial-deltaic sandstone reservoirs in a simple structural dome and, because of the presence of a regionally extensive anhydrite seal, four-way structural closure, and lack of faulting, is naturally stable with respect to $CO_2$ storage (Jack C. Pashin, personal communication, 2006). However, the geology of the heterogeneous siliciclastic rocks in Citronelle Field is quite different from that of the carbonate strata of the Permian Basin in Texas and New Mexico and the Williston Basin in North Dakota and Montana, well-known sites of commercially successful $CO_2$-EOR projects.

Kuuskraa et al., (2004) estimated the oil recoverable from Citronelle Field using $CO_2$-EOR to be 64 million bbl, or 17% of the original oil in place. Denbury Resources' estimate of the Field's EOR potential is 26 million bbl. Assuming 10% of OOIP to be economically recoverable (38 million bbl) using $CO_2$-EOR and a production rate increased to 1.1 million bbl/year (twice present production), the productive life of the field would be extended by 35 years.

A component of the present investigation was an assessment of the capacity of the oil reservoir and adjacent saline formations for sequestration of carbon dioxide, in parallel with $CO_2$-EOR and when tertiary oil recovery operations are complete. Esposito et al. (2008) estimated the capacity of Citronelle Dome for $CO_2$ storage to be 530 to 2100 million short tons, sufficient to store

the $CO_2$ produced from coal-fired generation at nearby Alabama Power Company Plant Barry (12 million tons/year) for at least 40 years.

The objectives of the project were to provide a detailed analysis of Citronelle geology, reservoir simulations, diagnostic and monitoring techniques, and water-alternating-gas injection experience that will assist the operator in designing and implementing a commercial $CO_2$ flood at Citronelle to realize the expected EOR potential of the field and provide a secure sequestration site for $CO_2$ produced from electric power generation for decades to come, should the Country decide that carbon capture and storage is needed to minimize the accumulation of $CO_2$ in the atmosphere and its effect on Earth's climate.

## 1.2. Scope of Work

The technical work to be done under the project was divided into three phases, corresponding to the phases of the $CO_2$ injection in the field: preparation, $CO_2$ injection, and interpretation of the response.

***Phase I (January 1, 2007 to August 31, 2008).*** Work in the field during Phase I was focused on preparation for the injection of $CO_2$, including the following activities:

Selection and preparation of the test site
Interference test
Pre-injection simulation study
Determination of oil-$CO_2$ minimum miscibility pressure
Begin water flood

The estimate of $CO_2$ storage capacity in Citronelle Dome (Esposito et al., 2008) was also performed during Phase I.

***Phase II (September 1, 2008 to December 31, 2010).*** Work in the field during Phase II was focused on the injection of $CO_2$. The original plan was to inject 7500 tons; the actual amount injected was 8036 tons.

The use of the carbon-13 to carbon-12 isotope ratio in the $CO_2$ in produced gas was shown to be an excellent method for distinguishing injected $CO_2$ from $CO_2$ native to the reservoir during Phase II.

***Phase III (January 1, 2011 to January 31, 2014).*** Work in the field during Phase III was focused on monitoring and testing to interpret the response to $CO_2$ injection.

***Phases I, II, and III.*** Other components of the work were the subjects of high levels of activity throughout the project:

Stratigraphy, sedimentology, and petrology of Donovan Sands
Models for reservoir architecture and connectivity
Reservoir simulation and visualization
Seismic surveys and interpretation
Air, soil, and vegetation monitoring
Development of the open-source reservoir simulator

**Acronyms in Section 1**

| | |
|---|---|
| EOR | enhanced oil recovery |
| NETL | National Energy Technology Laboratory |
| OOIP | original oil in place |

**References in Section 1**


Alabama State Oil and Gas Board, 2012, 2014. http://www.gsa.state.al.us/

Eaves, E., "Citronelle Oil Field, Mobile County, Alabama," American Association of Petroleum Geologists Memoir 24, 1976, pp. 259-275. http://egrpttc.geo.ua.edu/reports/citronelle/eaves.html

Esposito, R. A., J. C. Pashin, and P. M. Walsh, "Citronelle Dome: A Giant Opportunity for Multi-Zone Carbon Storage and Enhanced Oil Recovery in the Mississippi Interior Salt Basin of Alabama," *Environmental Geosciences*, **2008,** *15* (2), 53-62.

Fowler, M. L., L. E. Safley, M. A. Young, R. H. Stechmann, E. S. Blair, and R. E. Crumb, "Reservoir Management Strategy for Citronelle Field, Mobile County, Alabama," Report No. NIPER/BDM-0353, Prepared for the National Petroleum Technology Office, U.S. Department of Energy, Tulsa, OK, by BDM Petroleum Technologies, Bartlesville, OK, 1998.

Kovscek, A. R., "Screening Criteria for $CO_2$ Storage in Oil Reservoirs," *Petroleum Science and Technology 20*, **2002**, 841-866.

Kuuskraa, V. A., R. Lynch, and M. Fokin, "Site Selection and Process Identification for $CO_2$ Capture and Storage Test Centers," Summary Report: Geologic Assessment of $CO_2$ Storage Options, Four Proposed Southern Company Power Plants, Prepared under Agreement No. E2-P79/C5887 for the Electric Power Research Institute by Advanced Resources International, Arlington, VA, March 26, 2004.

# 2. Reservoir Geology of the Donovan Sandstone in Citronelle Field

Jack C. Pashin,* David C. Kopaska-Merkel, and Denise J. Hills
Geological Survey of Alabama, Tuscaloosa, Alabama

## 2.1 Citronelle Geology: Introduction

Citronelle Field is Alabama's largest oil field, having produced more than 173 million barrels of oil and nearly 16 billion cubic feet of gas since discovery in 1955. According to the State Oil and Gas Board of Alabama (OGB), 414 wells in the field are active, and annual oil production is on the order of 1 million barrels of light, sweet crude with API gravity of about 42°. The field produces from Lower Cretaceous strata of the Donovan sandstone, which has long been known for a high degree of depositional heterogeneity and low reservoir energy (Wilson and Warne, 1964; Eaves, 1976; Fowler et al., 1988, 1995). Because of this, secondary waterflood operations began early in the life of the field in 1961 to improve oil recovery.

The field had matured and production had declined substantially by the early 1980s. Hence, the Citronelle Unit Manager, with the support of the U.S. Department of Energy, performed a series of tertiary oil recovery experiments (i.e., the TEOR project) to test the viability of $CO_2$-enhanced oil recovery (Gilchrist, 1981, 1982). The records of these experiments are incomplete, but cores of sandstone from the pilot wells were preserved and were donated to the Geological Survey of Alabama (GSA) by Denbury Resources to support the new pilot program. The new pilot program, which is located in the northeastern corner of the Citronelle oil unit (Figure 2.1), began in 2007 and has provided a wealth of new information that provides a fresh perspective on the reservoir geology of Citronelle Field. Additional information from a variety of $CO_2$ sequestration studies, including the SECARB Anthropogenic Test, has provided new geological data from Citronelle Field (Pashin et al., 2008; Esposito et al., 2008, 2010; Petrusak et al., 2009, 2010).

As part of these initiatives, geologists at GSA have developed a new evaluation of Citronelle reservoir geology, and this report summarizes the results of this evaluation. Lower Cretaceous sandstone units similar to the Donovan sandstone are widespread in the Gulf Coast region, yet remarkably little research has been published on these deposits. Accordingly, this research may help optimize operations in fields with similar reservoirs and provide crucial insight on other heterogeneous reservoirs where $CO_2$ flooding may be effective.

This study employed a broad range of analytical methods emphasizing core description, stratigraphy, sedimentology, and petrology. Details of the analytical methods used are given in the section on approach and methodology. Next is a summary of the geologic setting of Citronelle Field that includes delineation of the basic stratigraphic and structural framework of the field. The bulk of the report focuses on the delineation of lithofacies composing the Donovan sandstone

*Current address: Boone Pickens School of Geology, 105 Noble Research Center, Oklahoma State University, Stillwater, OK 74078

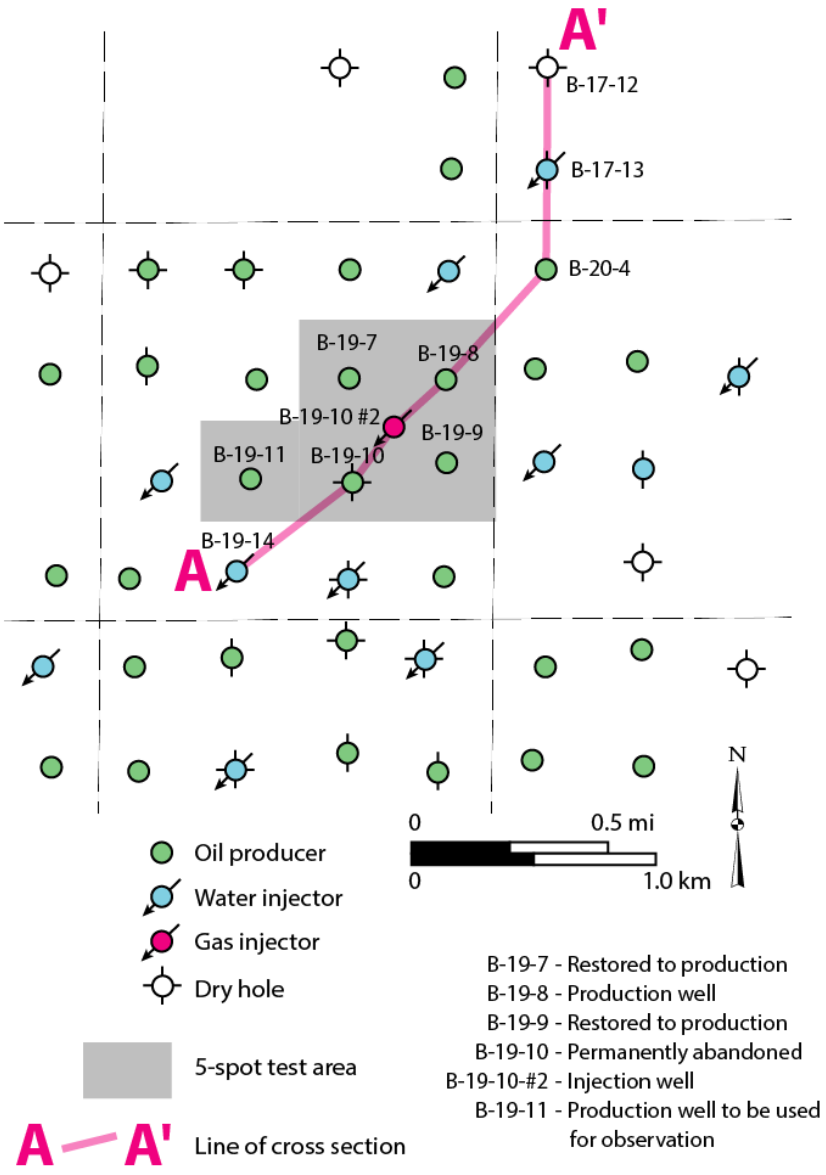


Figure 2.1. Map of northeastern Citronelle Field showing locations of injection and production wells, the inverted five-spot test pattern employed during this study, and a line of stratigraphic cross section.

and interpretation of depositional processes and environments. The petrologic characterization centers on the framework composition of the sandstone, the nature and distribution of porosity and permeability, and the diagenetic factors that influence reservoir quality. The results of stratigraphic, sedimentologic, and petrologic analysis are then synthesized into a sequence stratigraphic model that provides a predictive framework linking basic geologic processes with reservoir architecture and reservoir properties. With this predictive framework in hand, the report turns toward identifying the implications of reservoir geology for field management, and particularly a transition to commercial-scale $CO_2$-enhanced oil recovery (EOR) operations.

## 2.2. Citronelle Geology: Approach and Methodology

Numerous geologic techniques were applied during this study, and this work emphasized sedimentary geology and petrology. Data resources available for study are geophysical well logs, cores, and core analyses. Most geophysical well logs from Citronelle Field are available to the public in the files of the OGB. Where gaps were identified in the OGB holdings, additional well logs were provided by Denbury Resources. Most wells were drilled between 1955 and 1965, and so vintage well logs constitute the vast majority of the available subsurface data. Spontaneous potential (SP), conductivity, resistivity, and microresistivity logs are available for most wells, and many bulk density and neutron logs also are available. Wells drilled as part of the TEOR project have a more modern log suite that includes density porosity and neutron porosity curves. In addition, a new well drilled in the Southeast Citronelle Unit (Well SECU D-9-8 #2) includes advanced petrophysical logs displaying rock composition and fluid saturation.

Electric logs in the northeastern part of the Citronelle Oil Unit, where the recent test was performed, were digitized, and resistivity was plotted on a logarithmic scale, which helped determine the basic relationships between lithofacies and log response. A dense network of stratigraphic cross sections was constructed to enable identification, correlation, and the development of 3-D models of pay zones. Special attention was paid to the 16-2 and 14-1 sandstone units, which were the target sandstone units for the EOR test in the northeastern part of the field. Pay zones in the project area were identified using microresistivity logs (a.k.a. micrologs), and structural contour and net pay isolith maps were made of the pay zones. Well logs and derivative data were assembled, analyzed, and mapped using Petra software. Burial history analysis of a deep well from Citronelle Field was performed as part of research performed by the GSA for the U.S. Minerals Management Service (now the Bureau of Ocean Energy Management) under various agreements.

Cores of the Donovan sandstone are available from several wells in Citronelle Field, and the project team focused on 12 cores that cover a large part of the Donovan section, including a core from the injection well used in this study (Well B-19-10 #2). The oldest core studied (Well C-1-6 #1) is from the center of the field. Ten of these cores were retrieved in the 1980s when the injection wells were drilled for the TEOR project and are scattered throughout the field. A new core was recovered as part of the SECARB Anthropogenic test (Well SECU D-9-8 #2). The TEOR cores had been wrapped in saran, foil, and paraffin and were thus very well preserved; they were slabbed, boxed, and analyzed as part of the current study. One shortcoming of these cores, however, is that most of the mudstone zones in the Donovan were discarded during the TEOR project. Mudstone sections in the C-1-6 #1 and SECU D-9-8 #2 cores, however, were preserved, and the slabs from these cores provide the best windows into the facies and reservoir architecture of the Donovan sandstone.

The cores were described and logged graphically using standard stratigraphic and sedimentologic procedures to characterize rock types, bedding styles, physical sedimentary structures, and fossil content. Grain size was determined with a graphical comparator, and color was determined using a Munsell soil color chart. Cores were photographed digitally to document characteristic lithologic and paleobiologic features. After the cores were logged and photographed, lithofacies were defined, and interpretations of depositional process and depositional environment were made on the bases of the modern and ancient analogs that have been documented in the geological literature. Core analysis data, including porosity, permeability, and fluid saturation, are

available from several of the cores and were used to correlate lithologic characteristics with reservoir quality. After description, analysis, and interpretation was complete, the results were synthesized into a sequence stratigraphic framework that was designed to facilitate prediction of reservoir facies distribution and characteristics.

Petrographic analysis focused on characterization of framework composition and diagenetic processes, and evaluation of porosity and permeability. A total of 323 petrographic thin sections was made from core samples using standard methods. All thin sections were impregnated with blue epoxy to show open pores. The thin sections were stained with Alizarin red S to identify calcite and with cobalt nitrite to identify potassium feldspar (Dickson, 1965; Gabriel and Cox, 1929). The thin sections were examined for framework grain composition, size, fabric, and diagenesis, pore geometry, and pore fillings.

To determine sandstone composition, point counts were conducted on 77 thin sections. Non-overlapping photographs were taken at a common scale, encompassing a representative sample of each thin section. A rectangular grid was laid over each photograph, and the rock constituents at every grid intersection were identified and recorded. At least 100 points were counted for 70 of the 77 thin sections. Comparison of thin sections represented by different numbers of points indicates little difference in the result that can be ascribed to sample size. Proportions of various rock constituents, including open pore space, were calculated for all point-counted thin sections. Standard ternary diagrams of detrital composition were used to classify the sandstone and evaluate provenance.

## 2.3. Geologic Setting

Citronelle Field is located in the Mississippi Interior Salt Basin (Figure 2.2), which is a sub-basin of the Gulf of Mexico sedimentary basin. In the Citronelle area, the Mississippi Interior Salt Basin contains a succession of Mesozoic and Cenozoic strata that is commonly between 18,000 and 20,000 feet thick. These strata accumulated as part of the passive margin along the northern rim of the Gulf of Mexico (e.g., Salvador, 1987, 1991). The sedimentary fill of the salt basin unconformably overlies basement strata of the Paleozoic-age Appalachian-Ouachita orogenic belt. The mid Jurassic Louann Salt unconformably overlies the basement. This unconformity apparently marks the transition from active rifting during Triassic time to passive margin development associated with the opening of the Atlantic and the Gulf of Mexico, which began during the Jurassic (Withjack et al., 1998).

The Louann salt varies greatly in thickness throughout the region as a result of regional salt tectonics. The salt is absent where the younger sedimentary cover is welded to basement, is locally thicker than 1,000 feet in broad salt pillows, and is locally more than 10,000 feet thick where it has flowed into diapiric structures (Hughes, 1968). Indeed, salt-related fold and fault systems occur throughout the salt basin and have played a dominant role in the migration and trapping of oil and gas in the region. Above the Louann is a thick Jurassic section that consists principally of sandstone, carbonate, and evaporite. Early Cretaceous strata in the Citronelle area are thicker than 6,000 feet; they are dominated by siliciclastic redbeds containing thin carbonate and evaporite intervals. Late Cretaceous and Tertiary strata in the Citronelle area are about 7,200 feet thick.

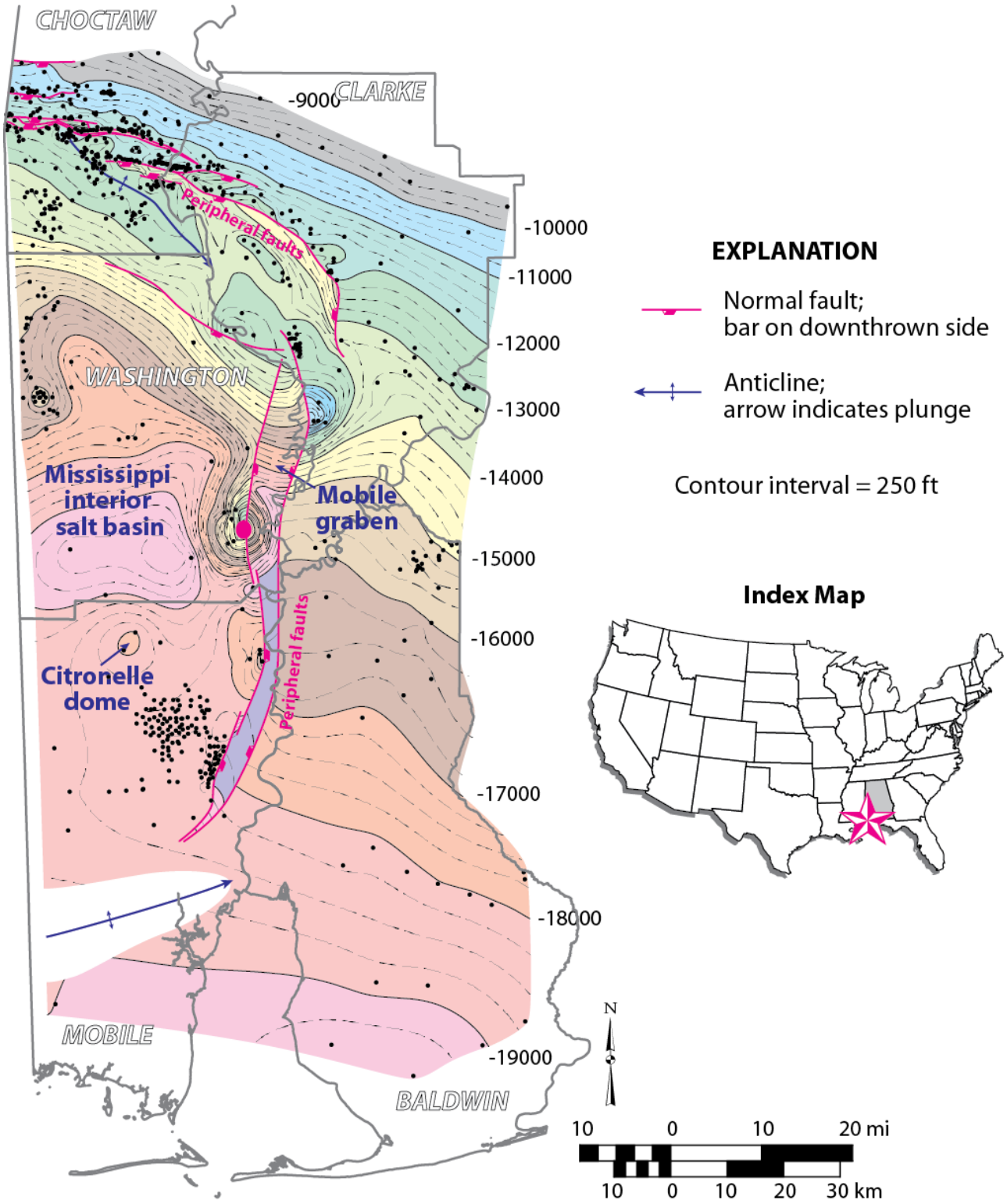


Figure 2.2. Structural contour map of the top of the Smackover Formation (Jurassic) in the eastern Mississippi Interior Salt Basin showing the location of Citronelle dome, which is a salt-cored anticline that hosts the Donovan oil accumulation.

### *2.3.1. Structural Framework*

Citronelle Field is in the southern part of the Mississippi Interior Salt Basin about 15 miles west of the Mobile graben, which is a peripheral fault system that marks the margin of the salt basin (Figure 2.2). The field is developed within an anticlinal structure called Citronelle dome. The dome is a subtle fold with limbs dipping less than 3° (Figure 2.3). The fold is underlain by a broad, thin pillow of Louann Salt, and the origin of the dome has long been linked to regional salt movement (Cottingham, 1988). Strata below the Ferry Lake Anhydrite, including the Donovan sandstone, exhibit no tangible changes of thickness across the dome, indicating that folding post-dates Ferry Lake deposition. All younger strata thin toward the crest of the dome, indicating a prolonged interval of structural growth spanning the last 100 million years.

A structural contour map of the base of the Ferry Lake Anhydrite demonstrates the structural simplicity of Citronelle dome (Figure 2.4). The dome is a simple four-way structural closure that is slightly elongate toward the northwest. The northeast flank of the dome is significantly steeper than the southwest flank (Figures 2.3 and 2.4). The structure has more than 500 feet of structural closure, and a saddle between the dome and a footwall uplift along the western boundary of the Mobile graben defines the spillpoint of the structure. The dense well spacing in the crestal region of the dome follows the general footprint of the oil accumulation (Figure 2.4). The lowest known oil in the dome is about 200 feet above the structural spillpoint, indicating that the Donovan reservoirs are underfilled with hydrocarbons. No faults are known in Citronelle dome, and no macroscopic natural fractures were observed in cores of the Donovan sandstone.

The $CO_2$ flood area employed in this study is in the northeastern corner of Citronelle Field, where Donovan strata dip gently toward the northeast at about 80 feet per mile. A 3-D structural model of the base of the 16-2 sandstone demonstrates the structural simplicity of the area (Figure 2.5). The base of the sandstone strikes approximately N. 47° W., and variability of the contours is modest and probably reflects paleotopographic variation of this surface associated with channeling and other depositional processes as much as structural deformation.

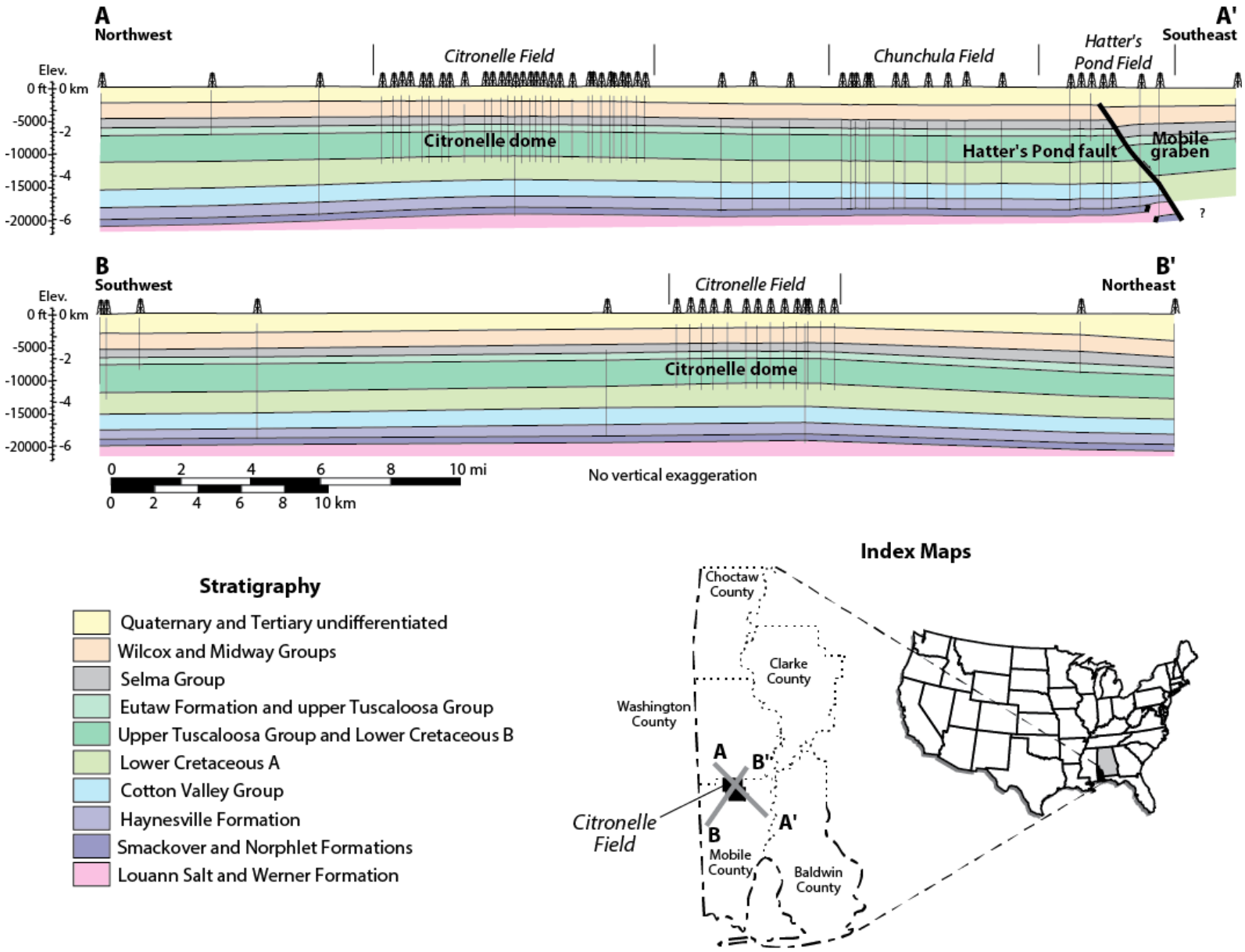


Figure 2.3. Structural cross sections of Citronelle dome showing location of Citronelle Field in the Lower Cretaceous section.

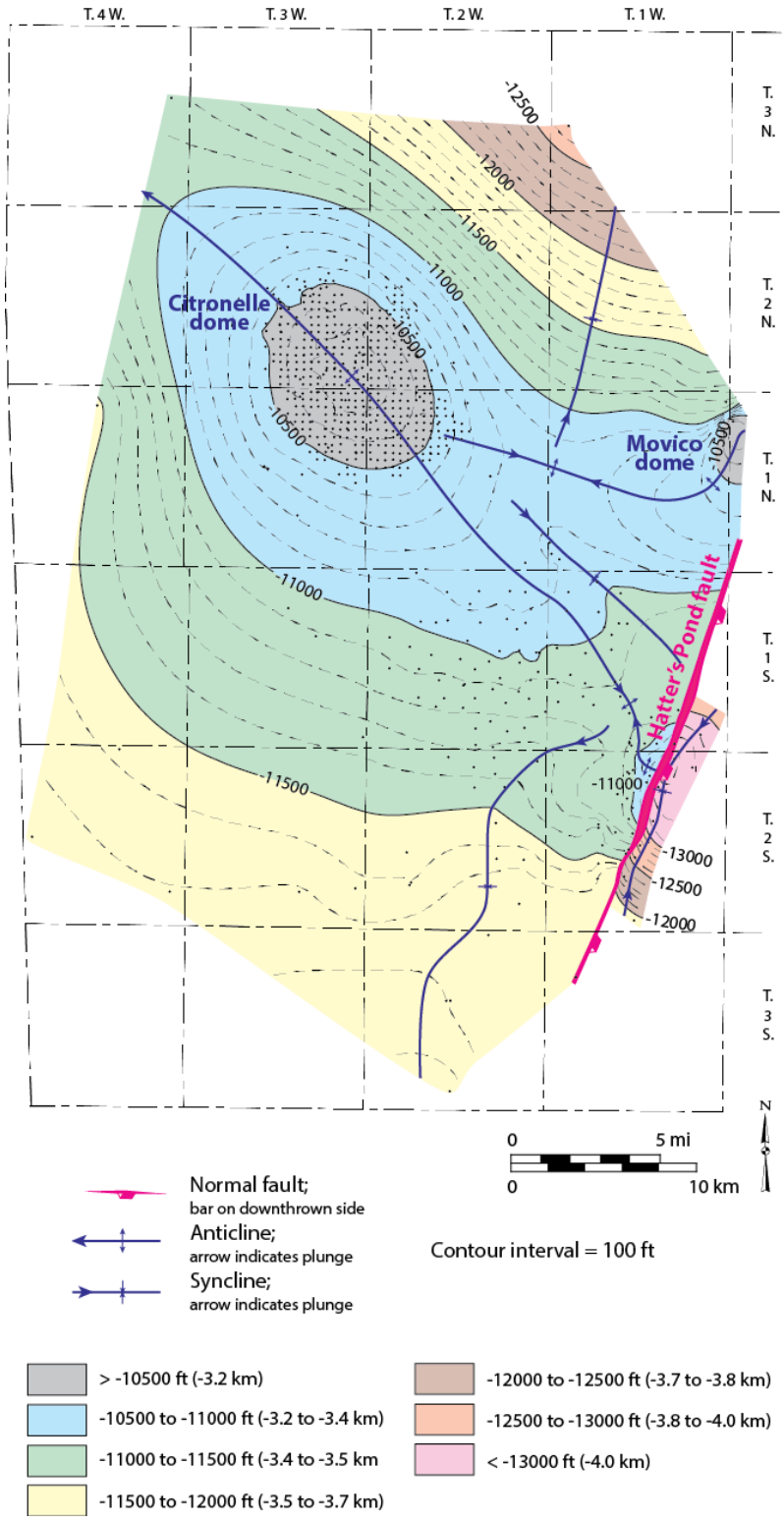


Figure 2.4. Structural contour map of the top of the Donovan sandstone (base of Ferry Lake Anhydrite) showing the areal geometry of Citronelle dome and the footprint of the oil field in the crestal region of the structure.

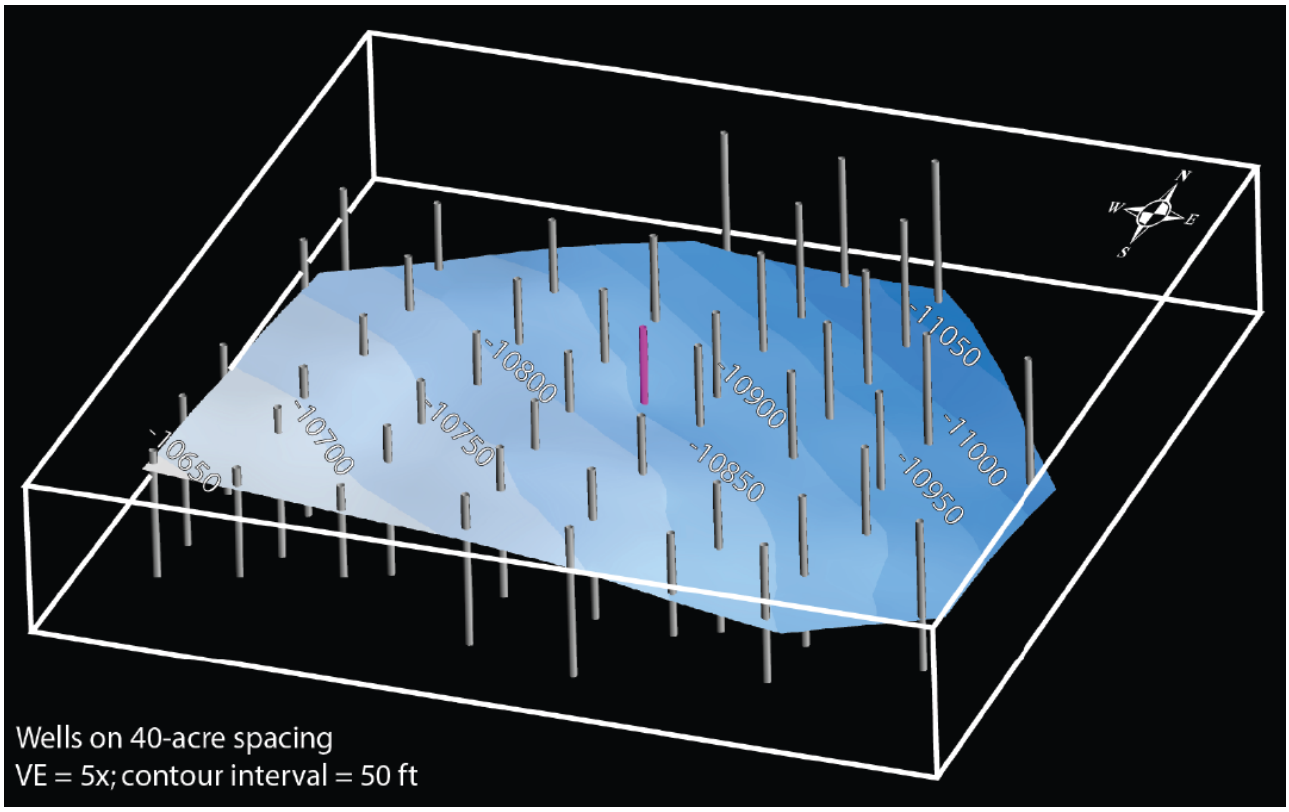


Figure 2.5. Structural model showing uniform northeast dip of the base of the 16-2 sandstone in northeastern Citronelle Field. Location of B-19-10 #2 injection well highlighted in magenta.

### *2.3.2. Burial History*

A burial history curve based on a deep well in Citronelle Field provides some insight into the Donovan petroleum system (Figure 2.6). Post-Louann strata record nearly continuous sedimentation from Jurassic through Miocene time. The overall burial history establishes a decelerating subsidence curve, which is typical of passive margins. Subsidence decelerated markedly near the start of Tertiary time, indicating effective tectonic stability over the past 60 million years. Jurassic strata of the Norphlet Sandstone and Smackover Limestone entered the hydrocarbon maturation window at about 120 million years and reached overmaturity around 30 million years. Today, Upper Cretaceous strata of the Tuscaloosa Group sit at the edge of thermal maturity, and the Donovan sandstone is near the mid-late mature boundary, which is in the heart of the oil generation window and corresponds with the onset of thermogenic gas generation.

The burial history curve suggests that the oil has had significant residence time in Citronelle dome, and the preponderance of light oil in sandstone containing significant pyrobitumen indicates that significant thermal cracking occurred after emplacement of the oil. Although the reservoir may be entering the thermogenic gas window, production and core analysis data indicate that the gas-oil ratio in Citronelle Field is extremely low. Indeed, what little gas is present is dissolved in the oil, thus the reservoir is strongly undersaturated with natural gas.

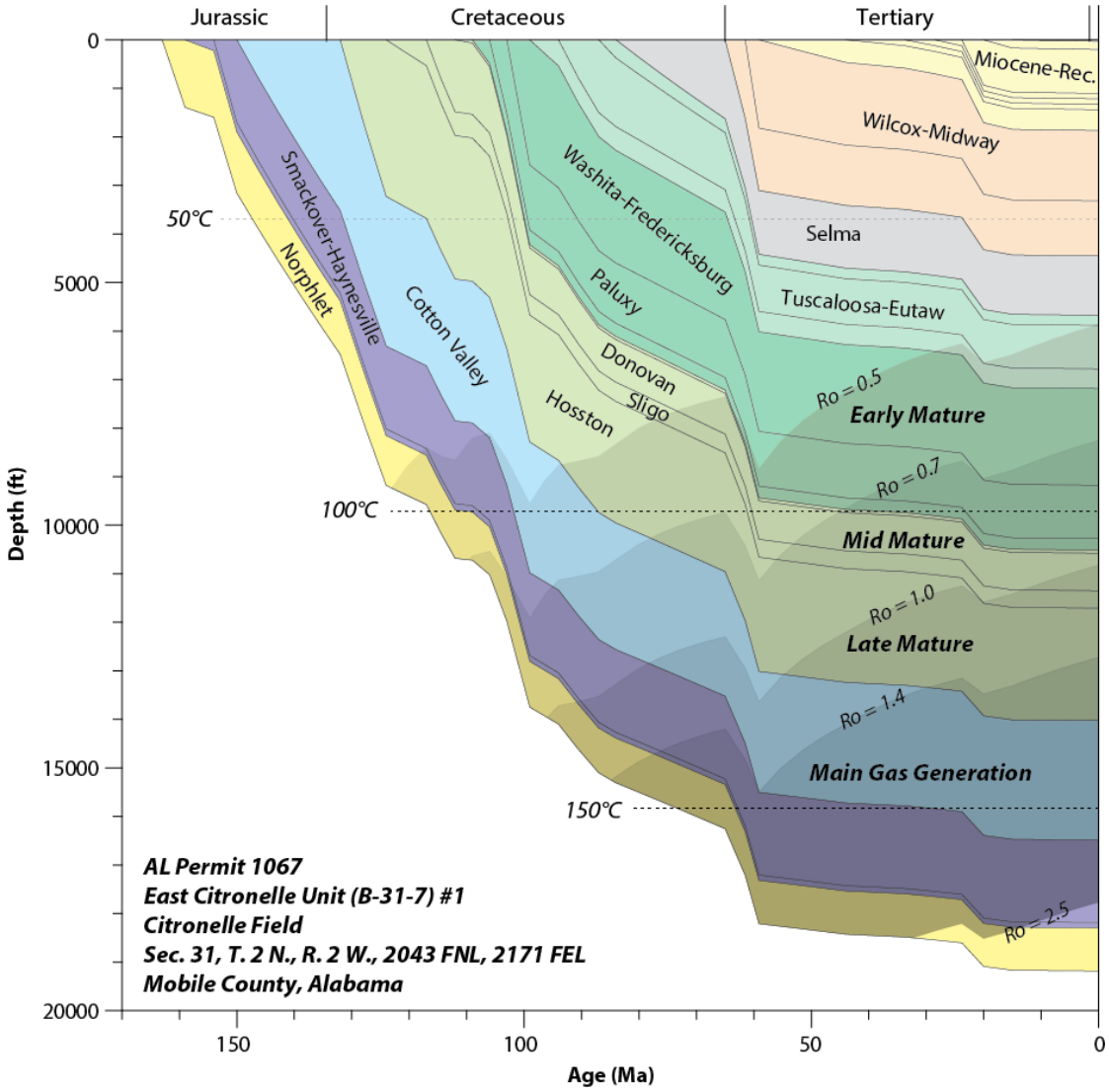


Figure 2.6. Burial history model and hydrocarbon maturation windows based on interpretation of a deep well in the central part of Citronelle Field.

No organic-rich source strata have been identified in the lower Cretaceous section of the eastern Mississippi Interior Salt Basin. Because of this, organic-rich carbonate in the middle part of the Smackover Limestone is considered the principal petroleum source rock in the region (Claypool and Mancini, 1989). Plotting the burial history to highlight source rocks, reservoir rocks, and seals (Figure 2.7) reveals the complexity of the Donovan petroleum system. Smackover strata are very thin in Citronelle dome and are overlain by an extremely thick evaporite seal in the Haynesville Formation. Since no faulting is known in the Citronelle area, it is doubtful that Smackover strata in the dome could have charged the Donovan reservoir. Claypool and Mancini (1989) suggested that oil from Citronelle Field has geochemical affinity with the Smackover Formation. Therefore, remote sourcing of the petroleum accumulation from areas outside the dome is the simplest explanation.

### *2.3.3. Stratigraphic Framework*

The Donovan sandstone is near the middle of the Lower Cretaceous section in the Mississippi Interior Salt Basin and constitutes the upper 1,000 feet of a major redbed interval that spans nearly 3,500 feet of section. The Donovan has traditionally been assigned to the Rodessa Formation (Eaves, 1976), although true Rodessa equivalents of early Albian age are probably restricted only to the uppermost 100 feet of the Donovan interval. The Donovan appears to contain strata equivalent to the James Limestone, which is of late Aptian age (Mancini and Puckett, 2005) (Figure 2.8). The Donovan also may include strata equivalent to the latest Aptian Bexar Formation, which intervene between James and Rodessa strata.

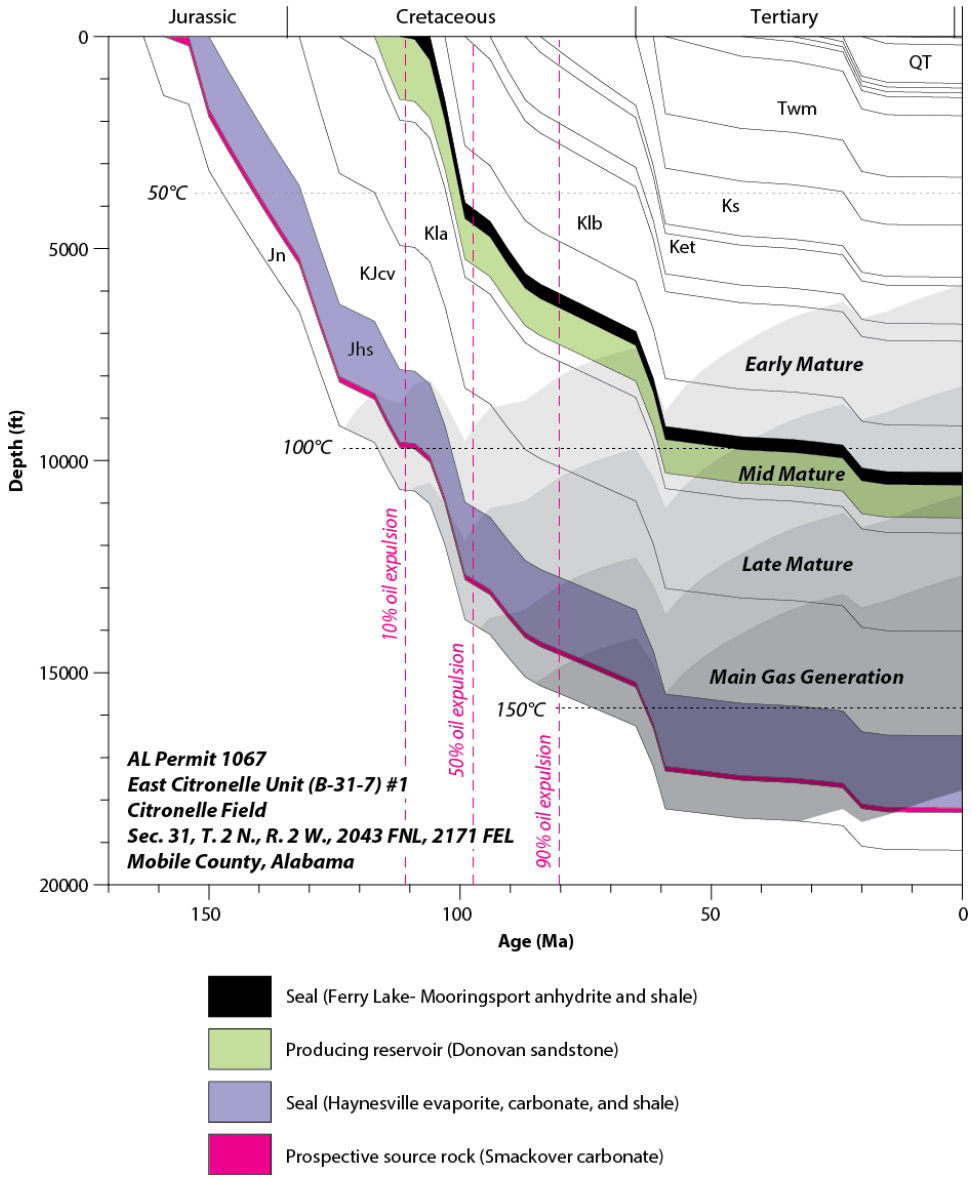


Figure 2.7. Burial history model showing positions of source rocks, reservoir rocks, seals, hydrocarbon maturation windows, and source-rock expulsion events in Citronelle Field. A local petroleum source in the Smackover Limestone is unlikely because a thick evaporite section lacking faults intervenes between potential Smackover source rocks and the Donovan oil accumulation.

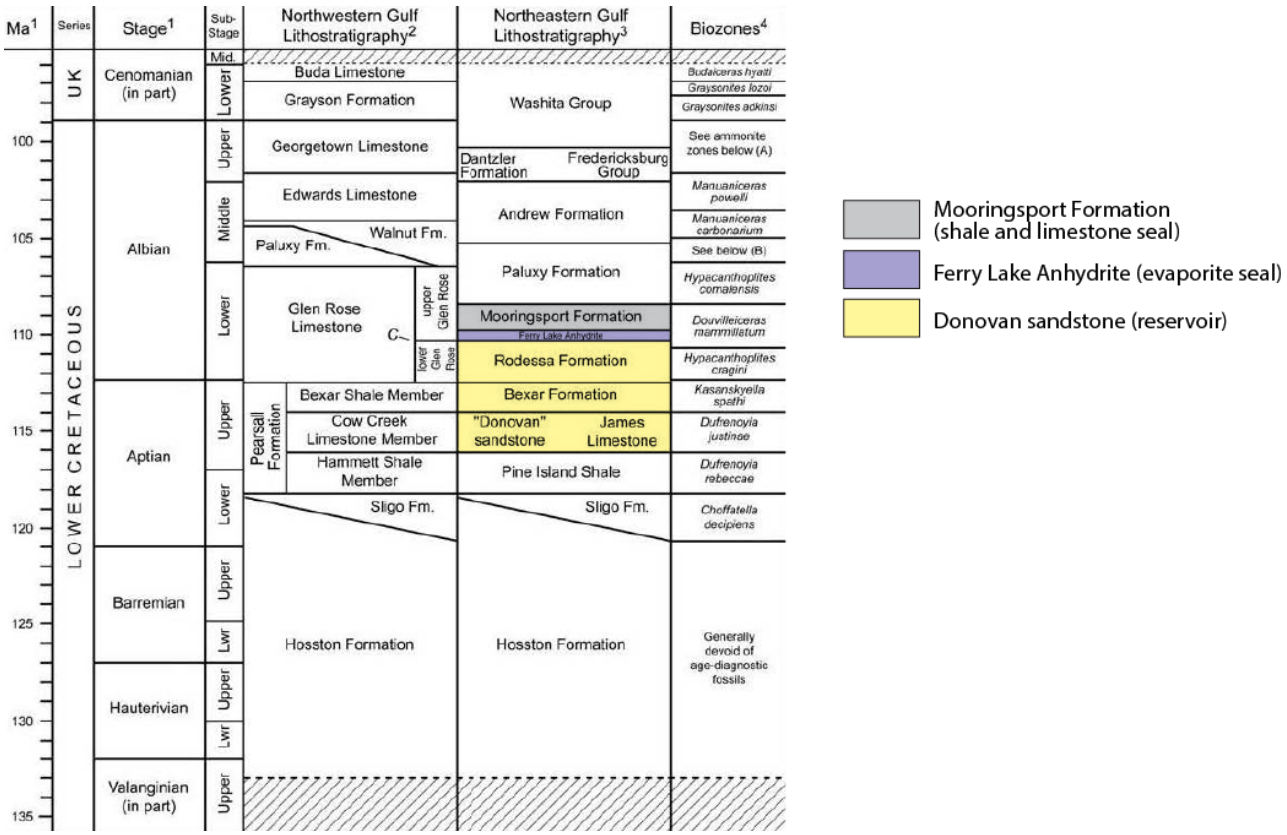


Figure 2.8. Stratigraphic chart showing position of Donovan reservoir strata in Citronelle Field (yellow) relative to formal stratigraphic units in the Gulf of Mexico Basin (modified from Mancini and Puckett, 2005).

Following the work of Mancini and Puckett (2005), the Donovan sandstone is interpreted to overlie mid Aptian redbeds equivalent to the Pine Island Shale. The Donovan is overlain sharply by the Ferry Lake Anhydrite (early Albian), which is composed of interbedded anhydrite and shale. The Ferry Lake, in turn, is overlain by interbedded shale and limestone of the Mooringsport Formation (early Albian).

Only a few exploratory wells penetrate the base of the Donovan sandstone in Citronelle Field because reservoir strata are restricted to the upper 850 feet of the interval. In Well B-31-7 #1, the basal Donovan sharply overlies a shaly section that may be a Pine Island equivalent (Figure 2.9). Internally, the Donovan contains numerous stacked sandstone-mudstone packages that contain some limestone. Individual sandstone and mudstone beds are typically thinner than 30 feet, and limestone beds are generally thinner than 10 feet. The sandstone is very fine- to medium-grained, includes intraclastic conglomeratic, and ranges in color from red to light gray. Oil and pyrobitumen give the reservoir sandstone units a yellowish-brown to very dark gray color. Mudrocks are rich in sand and silt and are of variegated color. Red mudstone predominates, and intervals of dark greenish-gray to dark gray shale are common, especially at contacts with oil-bearing sandstone units. Limestone units in the Donovan range from skeletal calcarenite to oyster calcirudite and locally produce oil.

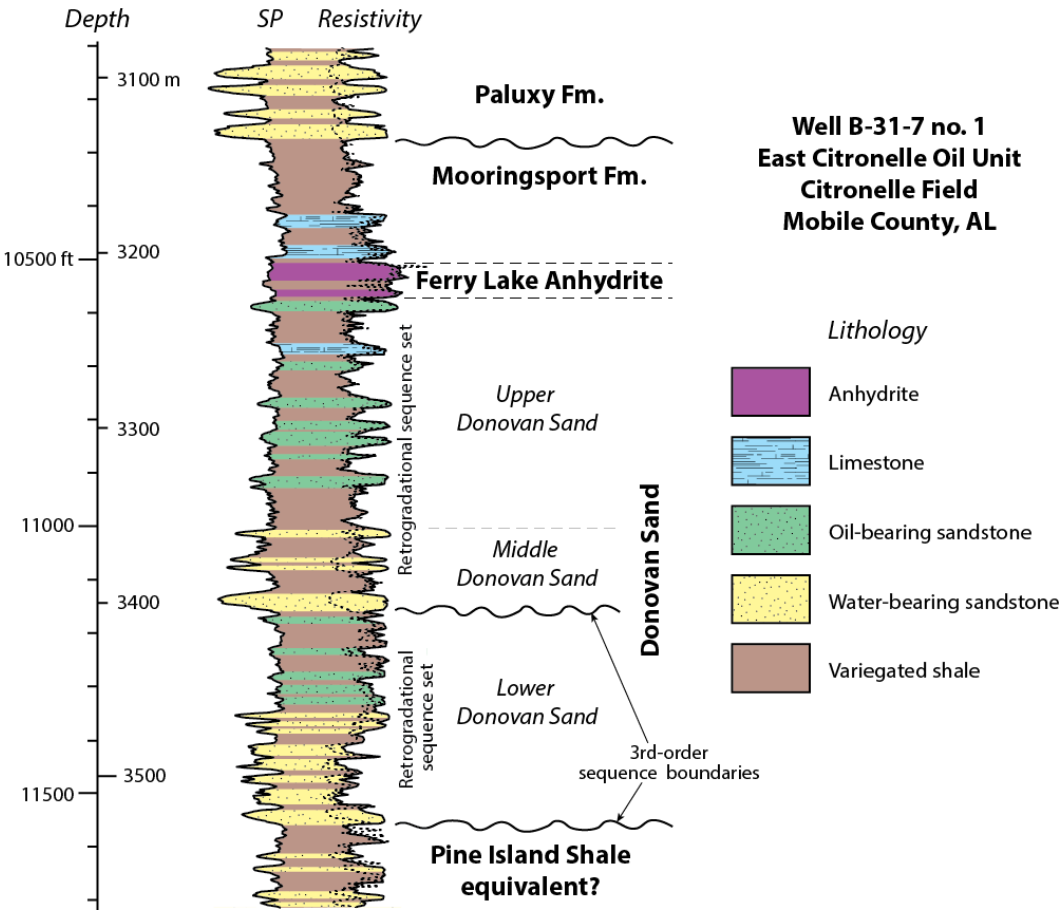


Figure 2.9. Geophysical well log showing stratigraphy and rock types of the Donovan sandstone and adjacent units in Citronelle Field.

The Donovan sandstone is subdivided into three intervals: the lower Donovan, the middle Donovan, and the upper Donovan (Figure 2.9). The lower Donovan is about 400 feet thick and contains sandstone units that tend to fine and thin upward. The lower half of this interval is composed of low-resistivity sandstone exhibiting strong separation between the deep and shallow resistivity curves. Low resistivity reflects iron-bearing minerals in the sandstone, and separation of the resistivity curves indicates that the sandstone units are water-bearing. The upper half of the lower Donovan contains sandstone units with resistivity comparable to shale, and weak separation of the resistivity curves corresponds to oil-bearing sandstone. Lower Donovan sandstone units have produced oil, but most of these reservoirs have been depleted and sit below drillable cement plugs that were set in or above the middle Donovan interval.

The middle Donovan sandstone is less than 200 feet thick and constitutes a series of water-bearing sandstone units that are interbedded with mudstone (Figure 2.9). The basal contact of the middle Donovan is sharp, whereas the upper contact is gradational. Middle Donovan sandstone units are distinguished by high resistivity in shallow induction curves, reflecting relatively low iron mineral content, and very low resistivity in deep induction curves, which indicates saturation with hypersaline formation water. Indeed, the middle Donovan sandstone lacks economically significant oil resources.

The upper Donovan sandstone constitutes the upper 500 feet of the Donovan interval and contains sandstone units with high resistivity comparable to that in the shallow induction curves in the middle Donovan (Figure 2.9). However, the upper Donovan sandstone units typically exhibit minimal separation between the deep and shallow induction curves, which is characteristic of high initial oil saturation that commonly exceeds 50 percent.

The Ferry Lake Anhydrite is about 50 feet thick in Citronelle Field and consists of two anhydrite beds separated by shale that can be correlated throughout the field (Figure 2.9). The anhydrite is generally considered the terminal topseal for the Donovan oil accumulation. Above the Ferry Lake is the Mooringsport Formation, which is about 240 feet thick. The Mooringsport sharply overlies the Ferry Lake Anhydrite and is sharply overlain by sandstone-dominated redbeds of the Paluxy Formation. The basal 75 feet of the Mooringsport contains argillaceous limestone beds that are up to 15 feet thick, and these shale and limestone beds contribute to the integrity of the topseal of the oil reservoir.

Wilson and Warne (1964) and Eaves (1976) interpreted the Donovan sandstone as a fluvial deposit. However, Wilson and Warne noted oysters in parts of the Donovan, indicating a coastal origin for at least part of the section. Northeast of Citronelle Field, strata equivalent to the Donovan sandstone are dominated by redbeds of apparent continental origin. Southwest of the field below the modern continental shelf, the Donovan passes into a thick carbonate succession (Petty, 1999) (Figure 2.10). The southwest margin of the carbonate shelf is fringed by a major barrier reef complex, and so the bulk of the shelf can be characterized as a broad platform lagoon. Accordingly, the Donovan sandstone can be interpreted as a coastal plain deposit that accumulated near the landward fringe of the platform lagoon.

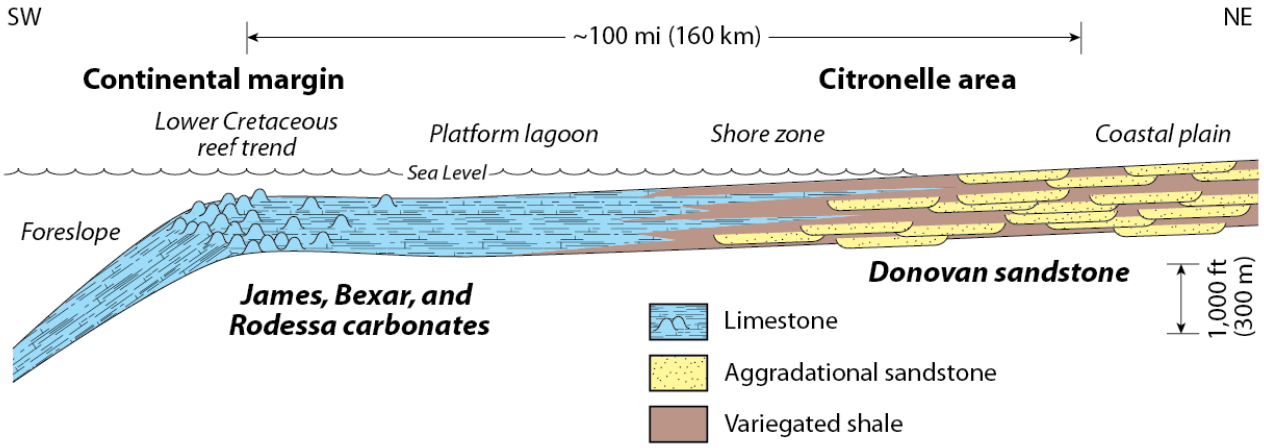


Figure 2.10. Generalized facies diagram showing relationship of the Donovan sandstone to equivalent carbonate deposits of the Gulf of Mexico Region. Regional relationships suggest that the Donovan sandstone was deposited on a coastal plain along the landward fringe of a back-reef platform lagoon.

The Donovan sandstone in Citronelle Field contains more than 43 reservoir sandstone units that have been mapped throughout the field (Eaves, 1976), and numerous other sandstone units are present in the water-bearing intervals of the lower and middle Donovan sandstone (Figures 2.9 and 2.11). The sandstone units are generally organized into two major thinning- and fining-upward intervals, the older of which corresponds with the lower Donovan sandstone, and the younger of which corresponds to the middle and upper Donovan (Figure 2.9). Considering the dominant fluvial origin of the sandstone units, each thinning- and fining-upward succession can be a sequence set with a major depositional sequence boundary at the base. According to Mancini and Puckett (2005), the section from the base of the Donovan sandstone to the base of the Ferry Lake Anhydrite represents a time span of 6 million years (110 to 116 million years; Figure 2.8). Therefore, each sequence set appears to represent 2 to 4 million years and is thus bound at the base by a third-order sequence boundary. Presence of about 60 sandstone-mudstone packages in the Donovan interval indicates high-frequency sequence development. Individual sandstone-mudstone packages therefore have an average frequency of ~100,000 years, which is consistent with changes of base level in the Milankovitch short eccentricity band (i.e., fifth-order depositional sequences).

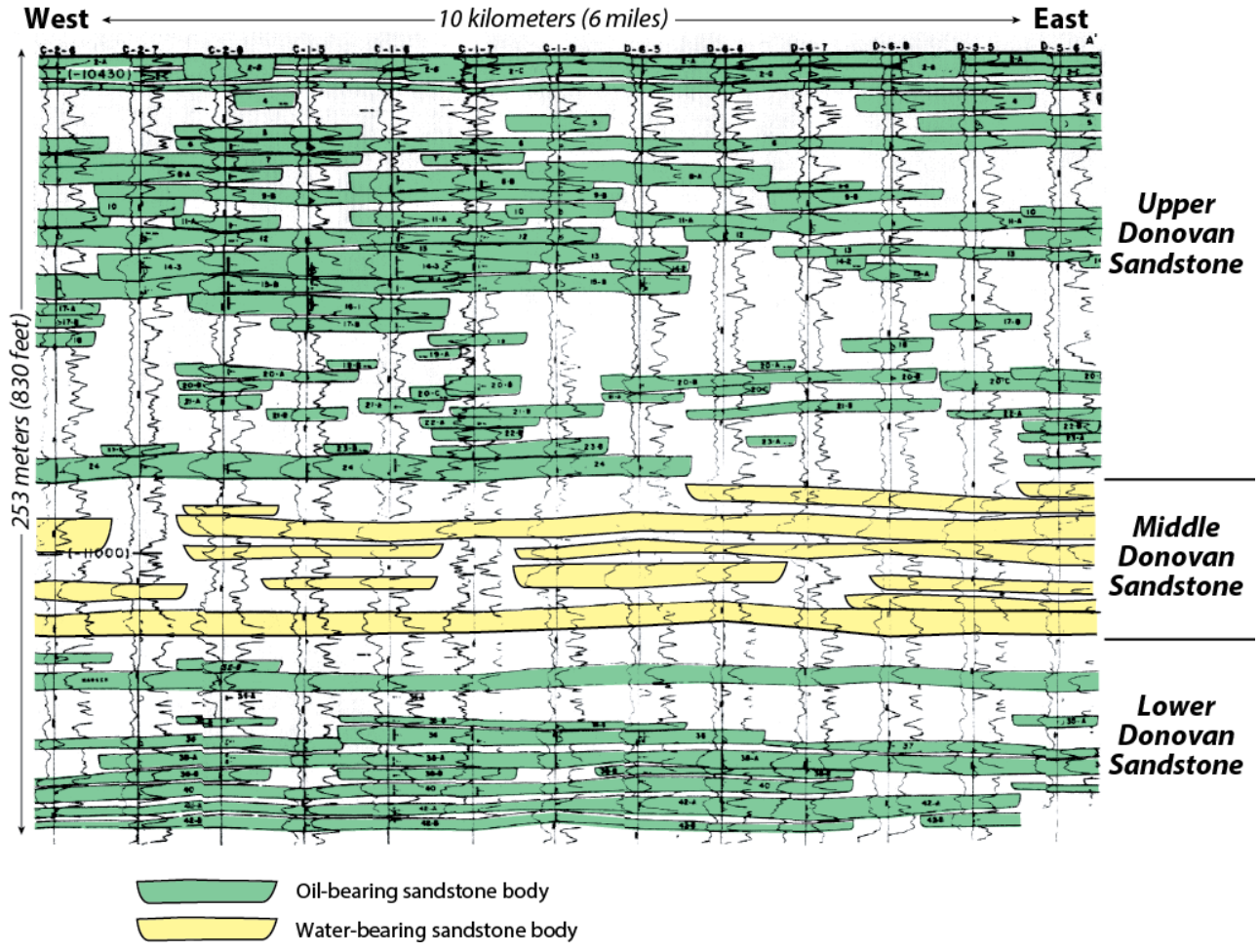


Figure 2.11. Cross section through central Citronelle Field showing the distribution of reservoir and water-bearing sandstone units in Citronelle Field (modified from Eaves, 1976).

## 2.4. Lithofacies and Depositional Environments

The sandstone-mudstone packages that constitute the Donovan sandstone were organized into four lithofacies, each containing a distinctive suite of rock types, physical sedimentary structures, biogenic structures, and diagenetic features. These lithofacies are the (1) conglomerate facies, (2) sandstone facies, (3) heterolithic facies, and (4) mudstone facies. In the following sections we describe the characteristics of each lithofacies and offer interpretations of depositional process and depositional environment that are based on those characteristics.

### *2.4.1. Conglomerate Facies*

***Characteristics.*** A range of conglomeratic deposits occur in the Donovan sandstone that vary in terms of clast type, color, internal sedimentary structures, and grain types. Rock types in the conglomerate facies include conglomerate and conglomeratic sandstone (Figures 2.12 and 2.13). Clasts range in size from granules to cobbles; pebbles are most common, whereas cobbles are few. Clast types are varied and include dolomitic mudstone (Figure 2.13A), argillaceous mudstone (Figure 2.13B), coalified plant debris (Figure 2.13D), oysters (Figure 2.13E), and anhydrite (Figure 2.13C). Conglomerate thickness is highly variable, ranging from pebble layers less than six inches thick to zones of clast-supported conglomerate thicker than three feet.

Dolomitic mudstone pebbles are the most common type of lithoclasts; they are angular to well-rounded and tend to be subspherical (Figure 2.13A). The clasts are commonly coated with clay, and many have faded or bleached rims; calcite-filled septaria also are common within the clasts (Figure 2.14). The pebbles are typically medium gray to brownish-gray in color, although those in the middle Donovan commonly have red hues. The conglomerate is almost universally clast-supported, and the matrix consists of calcite-cemented sandstone. The sandstone matrix is typically fine- to medium-grained, and the cement gives the sandstone pale colors, most typically light to very light gray. In parts of the middle Donovan, however, the sandstone has pink to reddish hues, and calcite cementation is less pervasive.

Argillaceous mudstone clasts are typically platy and are angular to subround (Figure 2.13B). The mudstone is silty and sandy. Color is most commonly dark gray, although clasts in some intervals, including the middle Donovan sandstone, have reddish and greenish hues. Sandstone matrix is commonly calcareous and resembles that described above, although many of the units bearing abundant argillaceous lithoclasts are cross-stratified. Anhydrite pebbles also were observed in some sandstone units and tend to be preserved as isolated clasts supported by sandstone matrix (Figure 2.13C).

Bioclastic material also is common in the conglomerate facies and consists of plant debris and shells (Figures 2.13D, 2.13E, 2.15, and 2.16). Coalified plant material is common and typically occurs as coal clasts associated with pebbles and cobbles of mudstone or as zones of coal spars in sandstone. The plant debris is dominated by woody material derived mainly from angiospermous plants. Conglomeratic strata containing abundant oyster shells (Figure 2.13D) are common near the top of the lower and upper Donovan intervals. The oysters are disarticulated and commonly form shell hash. Some of the shell hash, moreover, lacks significant siliciclastic matrix and thus forms limestone (Figure 2.15). Where large shell fragments are present, the limestone is calcirudite. Where shells have been macerated the limestone is skeletal calcarenite and has a sparry calcite matrix (biosparite; grainstone) containing miliolid foraminifera and algae (Figure 2.17). The fabric

of the limestone layers is complex, with moldic and shelter pores visible in many hand samples. Many of these large pores are filled with pyrobitumen (Figures 2.16 and 2.17).

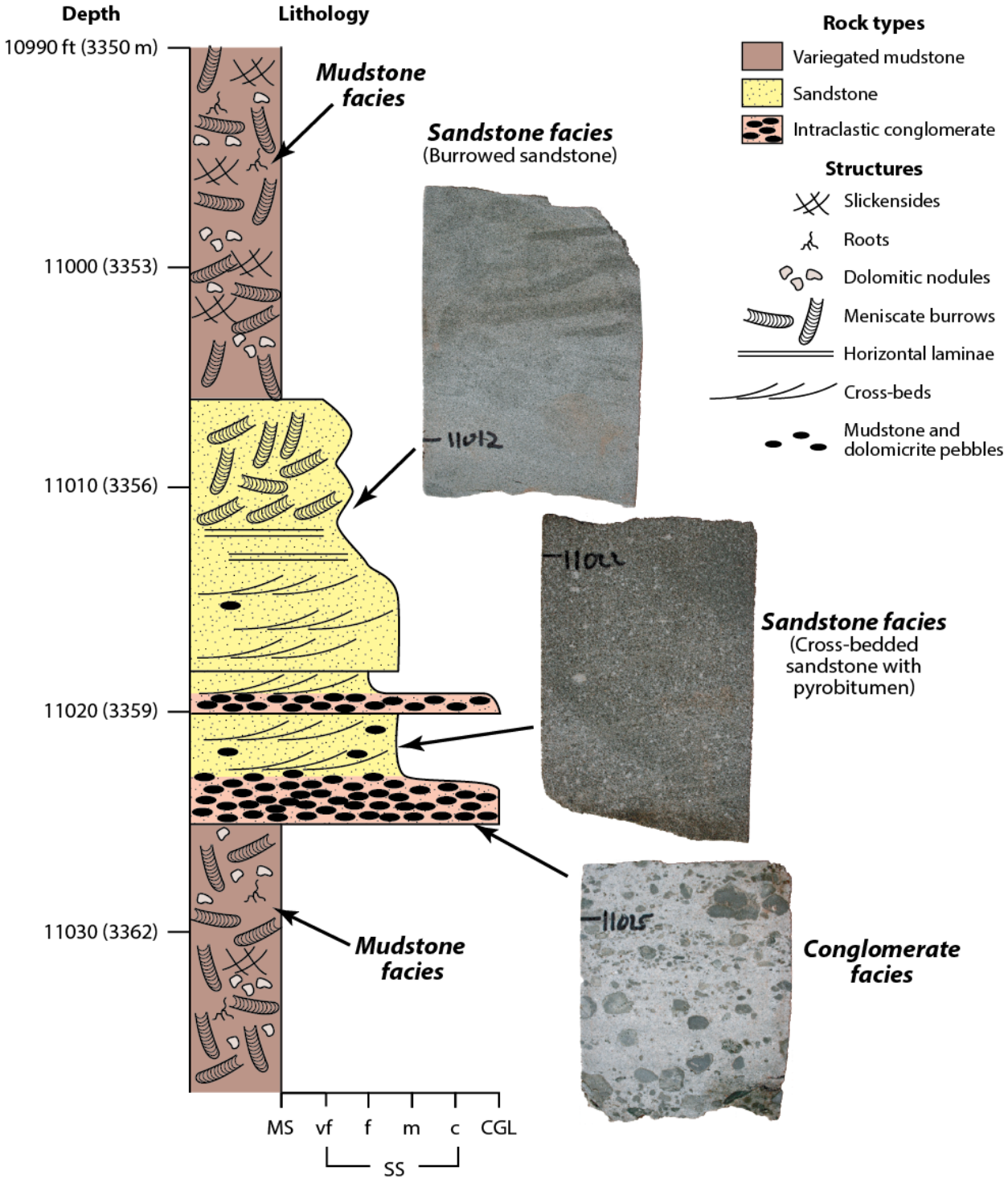


Figure 2.12. Core log and photographs of the 16-2 sandstone and adjacent mudstone units in the B-19-10 #2 injection well showing major lithofacies, rock types, and sedimentary structures in the Donovan sandstone.

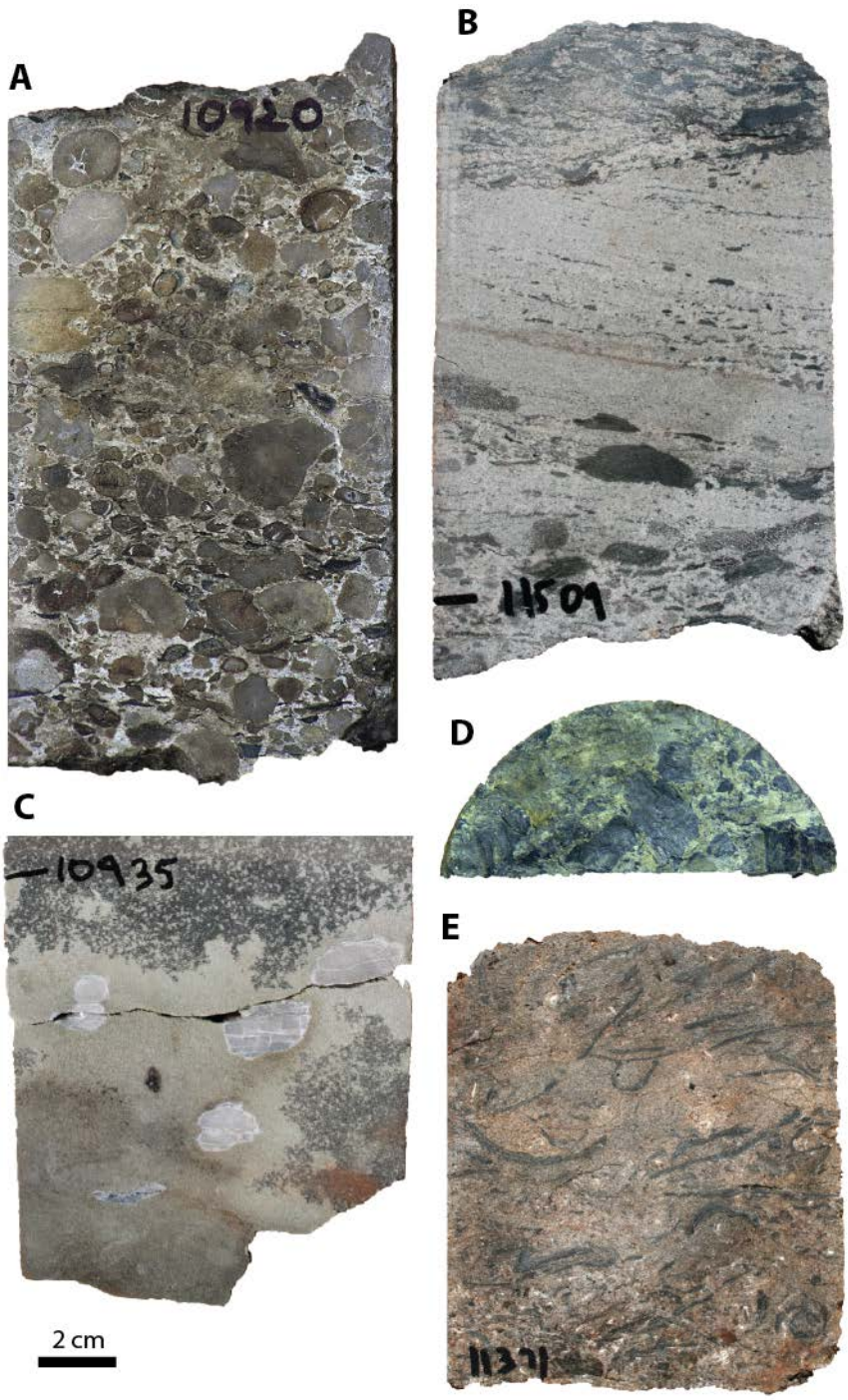


Figure 2.13. Photographs of slabbed core from the conglomerate facies. A. Clast supported conglomerate containing dolomitic mudstone pebbles, Well C-1-6 #1, 10,920 ft. B. Cross-bedded conglomeratic sandstone and conglomerate containing platy shale clasts, Well C-11-15 #2, 11,509 ft. C. Conglomeratic sandstone containing anhydrite clasts, Well C-11-15 #2, 10,935 ft. D. Conglomeratic sandstone containing coalified plant material, Well C-1-6 #1, 10,948 ft. E. Oyster hash in calcareous sandstone matrix, Well C-11-15 #2, 11,371 ft.

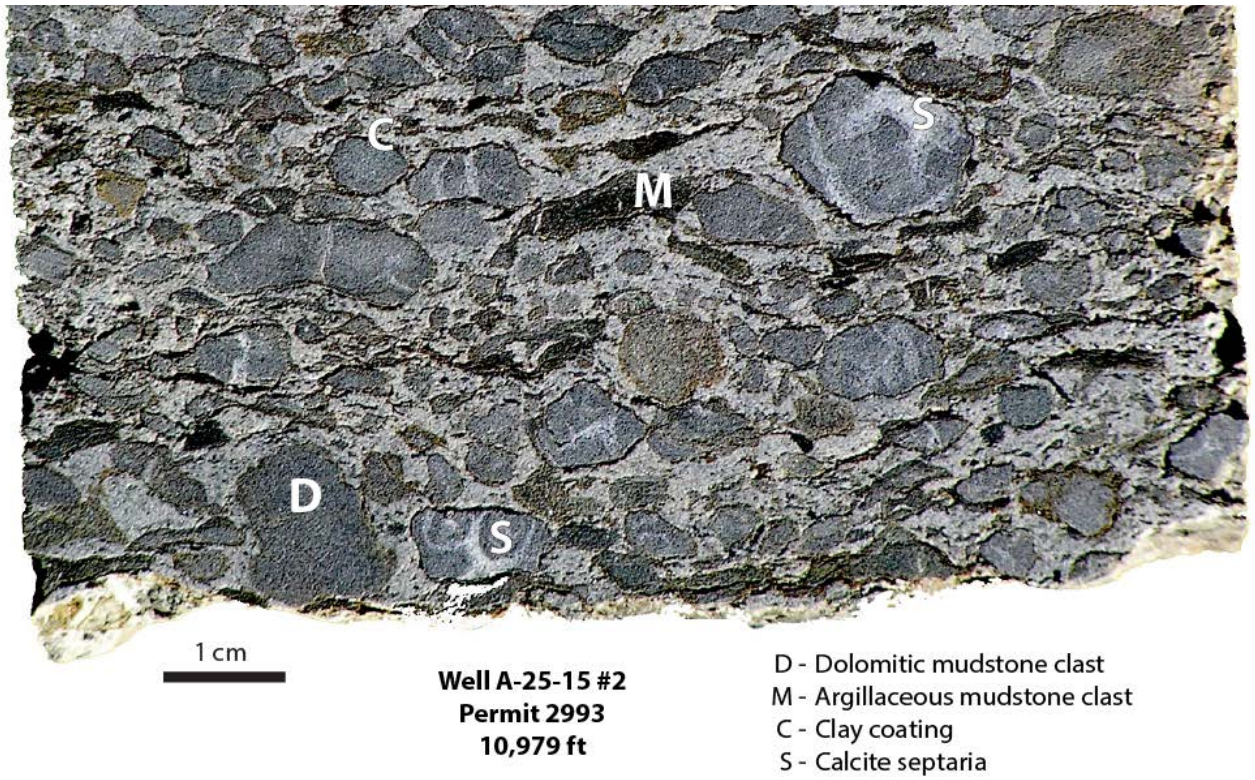


Figure 2.14. Conglomerate containing dolomitic and argillaceous mudstone clasts. Note abundant clay coatings on lithoclasts.

Conglomerate beds have sharp to distinct lower contacts and are commonly present at or near the base of the reservoir sandstone units (Figures 2.12 and 2.18). The upper contacts of the conglomerate intervals, by contrast, are sharp to gradational. The internal bedding structure of the conglomerate beds is complex, and some beds are composites of multiple conglomerate layers separated by sandstone or mudstone (Figure 2.19). In electric logs the conglomerate layers have moderate resistivity and a positive deflection in SP curves (Figure 2.18). Correlation of well logs suggests that some conglomerate beds are traceable among multiple wells and are thus widespread, whereas others cannot be correlated from well to well and thus appear to be localized.

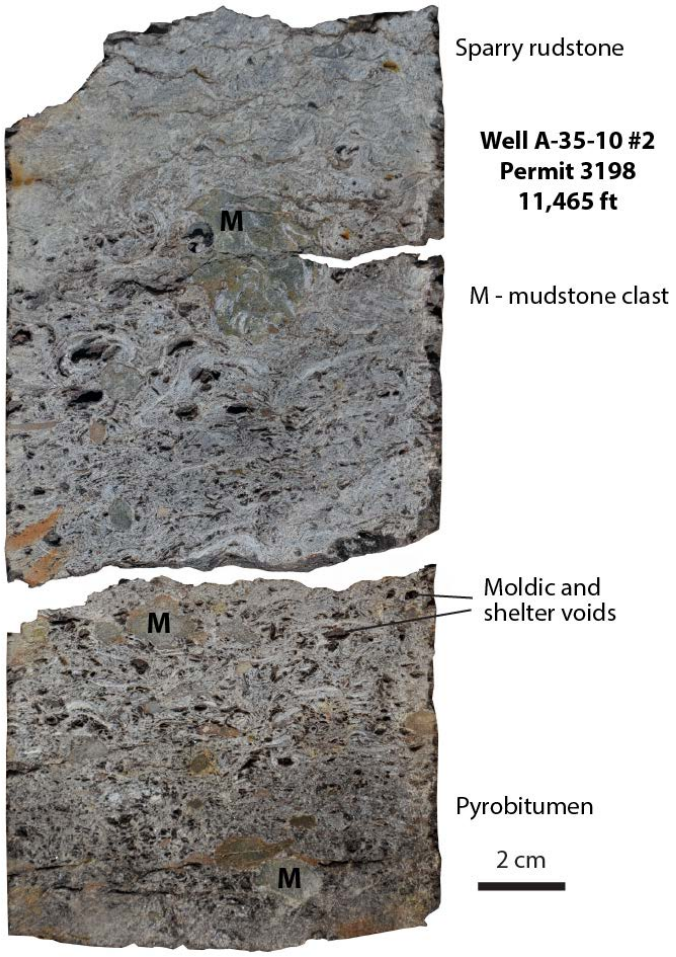


Figure 2.15. Limestone containing oyster hash in the conglomerate facies. Note abundant voids filled with pyrobitumen (black), clasts of oyster-bearing mudstone, and general fining upward.

***Interpretation.*** Lithoclasts in the conglomerate facies are all of sedimentary or biological origin (Figure 2.13), suggesting that they were derived by reworking of nearby sediment. Indeed, most of the clasts can be traced back to the other lithofacies, which are described in the sections below. The sharp bases of the conglomerate layers and the association with the basal contacts of the reservoir sandstone bodies (Figures 2.12 and 2.18) indicates an origin by erosion. Cross-bedding in some of the conglomeratic rocks (Figure 2.13B), moreover, confirms transport by vigorous currents. The variable lateral extent of the conglomerate layers (Figure 2.18) indicates deposition in channel bottoms, and some of the widespread layers may have been deposited on tidal ravinements.

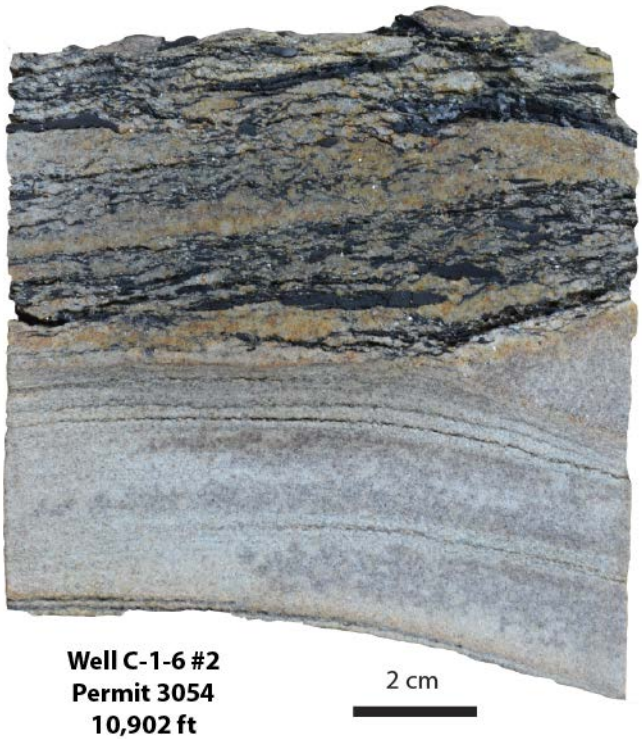


Figure 2.16. Conglomerate layer containing coalified plant material.

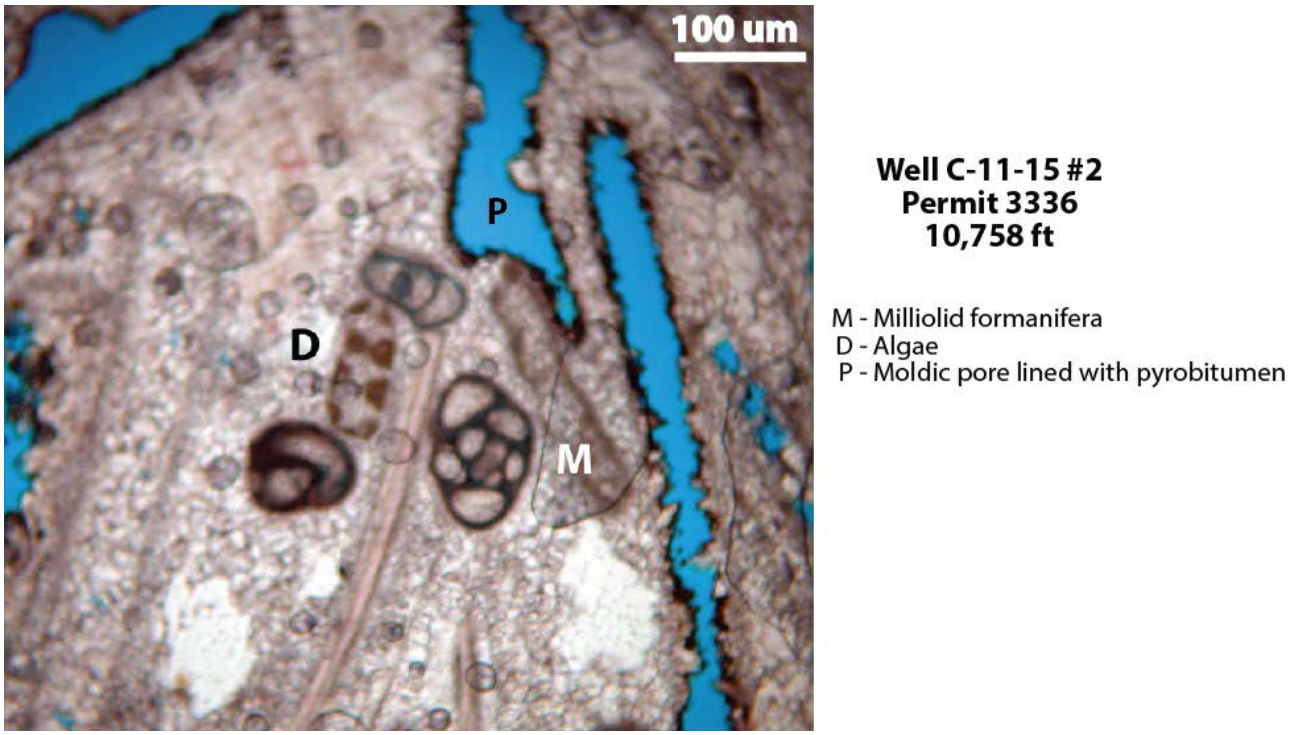


Figure 2.17. Thin section photomicrograph of oyster biosparite containing miliolid foraminifera. Moldic pores formed by dissolution of oyster shells; note pyrobitumen linings on pores.

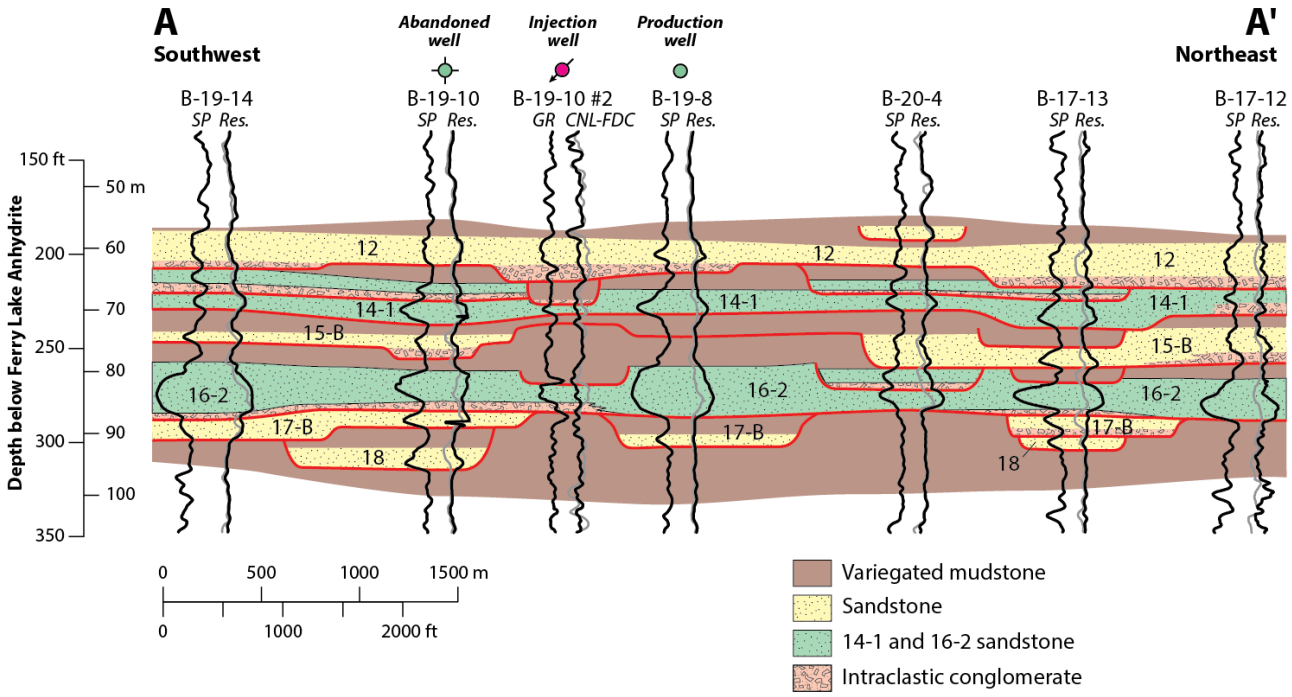


Figure 2.18. Stratigraphic cross section showing facies variation in the Donovan sandstone in the injection project area of northeastern Citronelle Field. See Figure 2.1 for location.

Platy mudstone clasts (Figure 2.13B) were probably derived by simple erosion of the mudstone units that underlie the conglomerate and sandstone layers. Similarly, anhydrite pebbles (Figure 2.13C) appear to be derived from anhydrite nodules that occur in other facies. Abundant coalified plant material in some conglomerate beds (Figures 2.13D and 2.16), alternatively, indicates significant input of plant material derived from vegetated landscapes. Calcite-filled septaria and bleached rims in the dolomitic mudstone clasts, by contrast, suggest a complex origin involving desiccation and weathering of sediment, which was subsequently eroded, transported, and deposited in the conglomerate facies. Clay coatings on the lithoclasts (Figure 2.14) may have multiple origins. Some may be relict clay coatings that formed as argillans in ancient soil profiles (e.g., Retallack, 1990; Pittman et al., 1992), whereas others may have formed by rolling and armoring in mud. Mud-armored clasts form where pebbles roll down muddy slopes or are rolled through mud by currents, such as river currents and tidal currents (e.g., Hall and Fritz, 1984; Knight, 2005). Indeed, presence of shell hash with miliolid foraminifera (Figure 2.16) in parts of the conglomerate facies indicates that marine processes were involved in parts of the Donovan sandstone; some of the shells in mudstone clasts may have been reworked from adjacent marine strata, whereas many of the shells may have been derived from oysters living on channel and ravinement bottoms. Indeed, examination and interpretation of the other lithofacies of the Donovan sandstone demonstrates that these strata were deposited in a broad range of environments in which a spectrum of continental and marine processes were effective.


Figure 2.19. Photograph of core containing two discrete conglomerate beds separated by a thick lamina of mudstone. Intervening mudstone lamina contains internal ripple cross-laminae. This type of bedding demonstrates the extreme variability of paleoflow conditions during deposition of the conglomerate facies.

### *2.4.2. Sandstone Facies*

***Characteristics.*** The sandstone facies constitutes all thick-bedded sandstone units in the Donovan sandstone and thus includes all of the major reservoir sandstone units, as well as the water bearing sandstone units of the lower and middle Donovan intervals. The sandstone is very fine to medium grained and contains a diverse suite of physical and biological sedimentary structures (Figures 2.12, 2.20, and 2.21). As mentioned previously, Donovan sandstone ranges in color from red to light gray, and oil and pyrobitumen give the reservoir sandstone units a yellowish-brown to very dark gray color (Figures 2.12, 2.20A, and 2.20C).

Physical sedimentary structures in the sandstone include cross-beds, subhorizontal laminae, and ripple cross-strata (Figure 2.20). Cross-bedding includes a range of planar and tangential forms, although it is often difficult to conclusively identify cross-bed types in core. Some of the cross-beds have clay- and mica-draped foresets (Figure 2.20B), and normally graded laminae were observed locally (Figure 2.22). Sandstone with horizontal to subhorizontal laminae is present in many Donovan sandstone bodies and constitutes most of the sandstone at the top of the upper Donovan (Figure 2.20C). Micaceous partings are common in the sandstone, as are local layers of

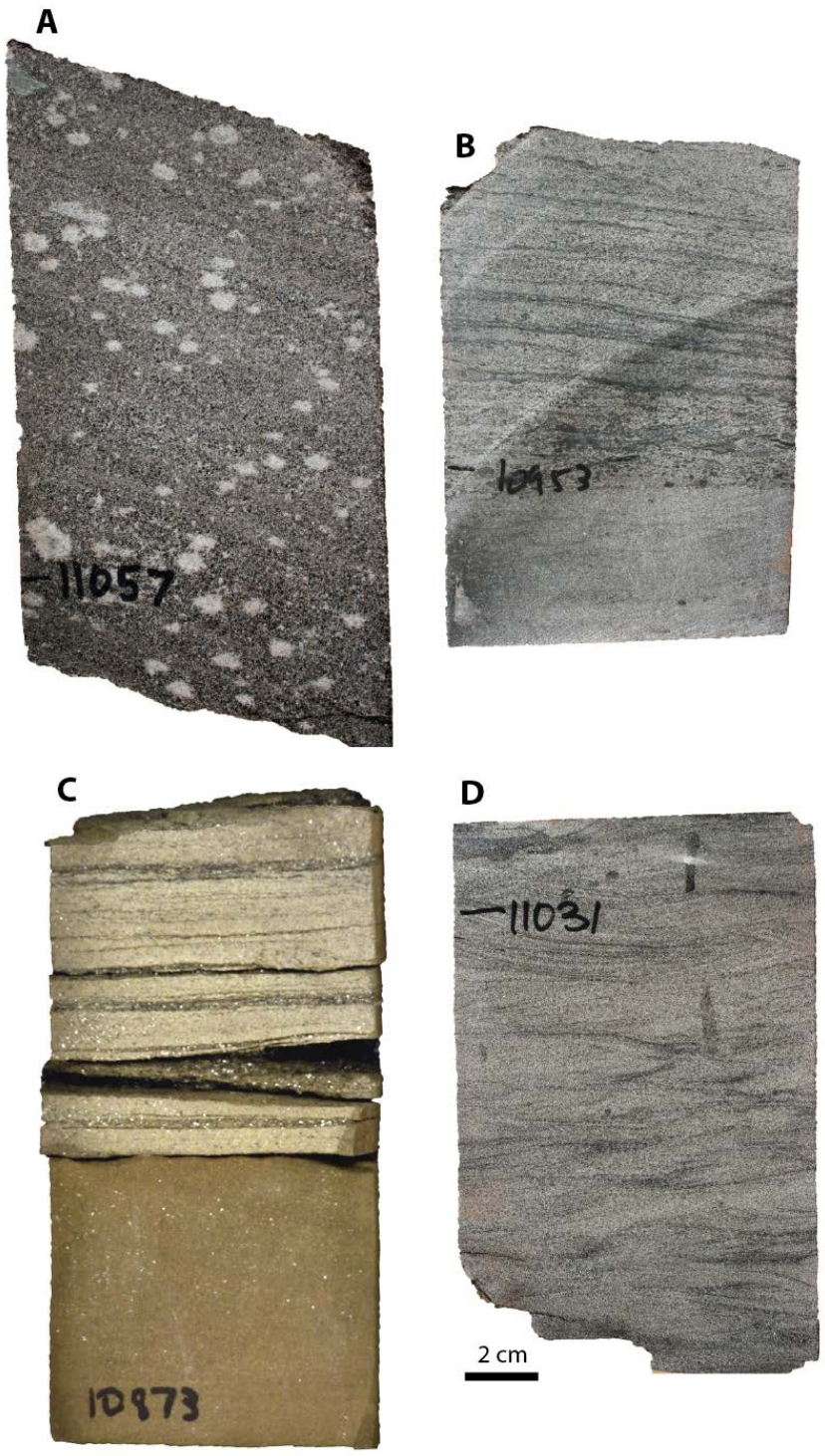


Figure 2.20. Photographs of slabbed core from the sandstone facies. A. cross-bedded sandstone blackened with pyrobitumen, Well C-11-15 #2, 11,057 ft. B. Cross-bedded sandstone with abundant tiny clay chips and clay-draped foresets (Well B-19-10 #2, 10,953 ft. C. Horizontally laminated sandstone stained with oil and containing micaceous laminae, Well C-1-6 #1, 10,873 ft. D. Sandstone containing trough-shaped current-ripple cross-laminae, Well C-11-15 #2, 11,031 ft. Note vertical burrow in upper part of core slab.

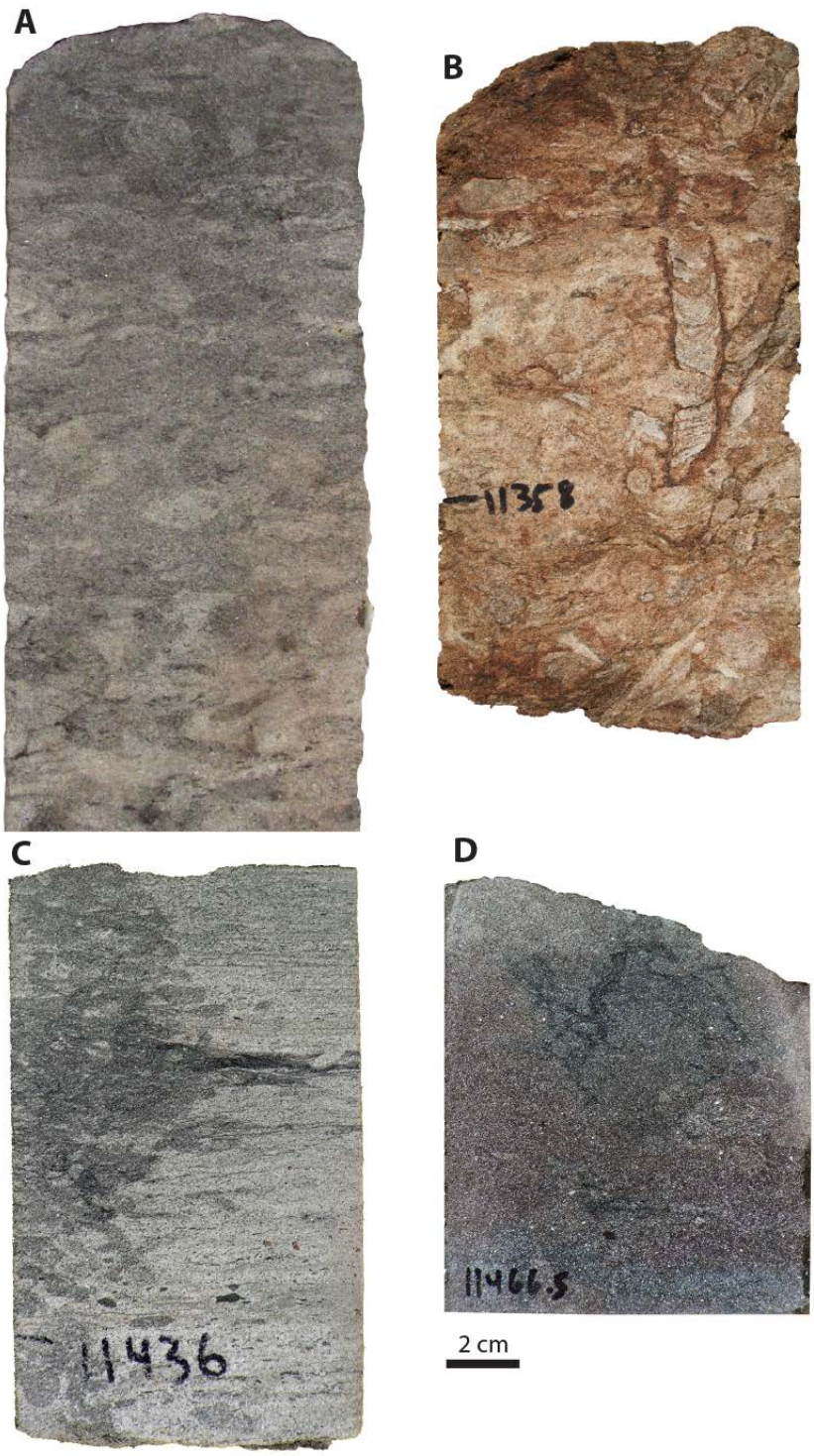


Figure 2.21. Photographs of slabbed core showing bioturbation in the sandstone facies. A. Sandstone mottled with abundant adhesive meniscate burrows, Well D-9-8 #2, 10,986 ft. B. Reddish sandstone contining meniscate burrows outlined by illuvial clay, Well C-11-15 #2, 11,358 ft. C. Abundant meniscate burrows defining margin of nest structure adjacent to laminaed sandstone, Well A-26-8 #2, 11,436 ft. D. Sandstone containing branching carbonized root structure, Well A-26-8 #2, 11,466.5 ft.

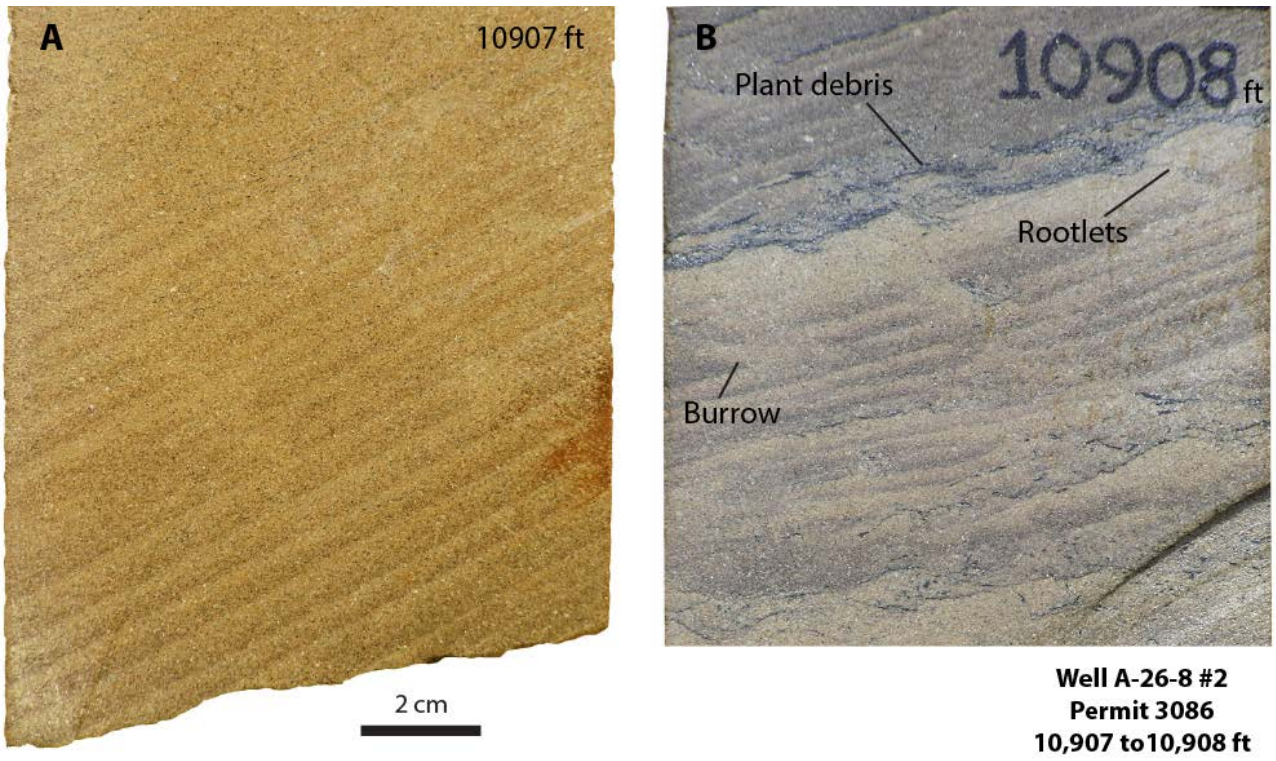


Figure 2.22. Photographs of slabbed core containing cross-strata with normally graded laminae, indicating possible local influence of sedimentation by eolian grainfall. A. Steep cross-strata with faint burrows. B. Cross-strata with normally graded laminae, coalified plant debris, burrows, and rootlet structures.

mudstone chips. Current-ripple cross-strata are common in very fine- to fine-grained sandstone. Several ripple forms are present, including trough-shaped forms (Figure 2.20D) characteristic of linguoid, lunate, and cuspate ripples and simple dipping foresets indicative of straight- to sinuous-crested ripples (Figure 2.23). Climbing ripples were observed in some intervals (Figure 2.23), and most ripples in the sandstone facies indicate dominant unidirectional flow, at least at the scale of hand samples.

Biogenic structures are abundant in many parts of the sandstone facies and include burrows and plants (Figure 2.21). Burrow mottling is especially abundant in the upper parts of the Donovan sandstone bodies (Figures 2.12 and 2.21A). Meniscate burrows up to 0.5 inch in diameter are the most common forms (Figure 2.21B). In some layers intense burrowing passes laterally into weakly bioturbated strata, which is suggestive of nest structures (Figure 2.21C). In addition to plant debris, moreover, branching carbonized root networks are preserved in some sandstone intervals (Figure 2.21D).

Diagenetic structures in the sandstone units include concretionary calcite and anhydrite cement (Figures 2.12 and 2.20A). Calcite cement is pervasive where sandstone forms the basal contacts of sandstone bodies and where the sandstone facies is in contact with the conglomerate facies. These pervasively cemented zones are typically less than one foot thick. Calcite cement


Figure 2.23. Photograph of very fine-grained sandstone with climbing current ripples. Ripple foresets draped with mica and organic matter. Note consistent foreset dip orientation.

also occurs as dispersed granule- to pebble-size concretionary bodies that typically have diffuse boundaries. Similarly, anhydrite cement occurs as granule- to pebble-size concretionary bodies with diffuse boundaries. Stylolites also are common in the sandstone.

Donovan sandstone units tend to fine upward, have gradational to sharp upper contacts, and are vertically and laterally heterogeneous. In core, fine- to medium-grained cross-bedded sandstone is most common near the bases of sandstone bodies above the conglomeratic intervals (Figure 2.12). By contrast, fine- to very-fined grained sandstone containing subhorizontal laminae, ripple cross-strata and bioturbation predominates in the upper parts of the sandstone intervals. In terms of lateral heterogeneity, many sandstone units can be correlated with ease across large parts of the field, whereas others are difficult to correlate from well to well (Eaves, 1976) (Figures 2.11 and 2.18). Where sandstone units are easily correlated, however, variable log signatures demonstrate that each sandstone body exhibits significant interwell heterogeneity (Figure 2.18). SP and resistivity curves typically have blocky signatures reflecting little variation of grain size and porosity or Christmas-tree-type signatures that reflect fining upward and vertically decreasing porosity. The magnitude of the negative deflection in SP and shallow resistivity curves is roughly proportional to reservoir quality. Indeed, the cross section A-A' demonstrates the strong SP response of the 14-1 and 16-2

sandstone units, which account for the vast majority of Donovan production in the northeastern part of Citronelle Field and were the targets of the $CO_2$-EOR test.

Examination of core analysis data and micrologs indicates that, with the exception of some limestone in the conglomerate facies, pay zones are restricted to the sandstone facies. Pay zones are readily identified in micrologs as intervals where micro-inverse resistivity is substantially lower than micro-normal resistivity. In the case of the 14-1 and 16-2 pay zones, the micro-inverse curve sits around 2.5 to 3.0 ohm $m^2/m$ and the micro-normal curve sits around 4.0 to 5.0 ohm $m^2/m$ (Figure 2.24). Models of the $CO_2$ flood area indicate that net pay thickness ranges from 0 to 14 feet in the 14-1 sandstone and from 0 to 20 feet in the 16-2 sandstone (Figure 2.25). The map patterns indicate irregular patterns of pay thickness and that pay thickness in both target sandstone units increases away from the injection point within the inverted five-spot well pattern. In the B-19-10 #2 injection well, net pay is less than three feet thick in the 14-1 sandstone and is 10 feet thick in the 16-2 sandstone. Pay-quality sandstone is absent in the 14-1 sandstone northwest of the inverted five-spot used in this study. Within the inverted five-spot well pattern, pay is thickest in the southeastern and southwestern wells. Prominent maxima of pay thickness in the 16-2 sandstone are northeast and west of the injection well.

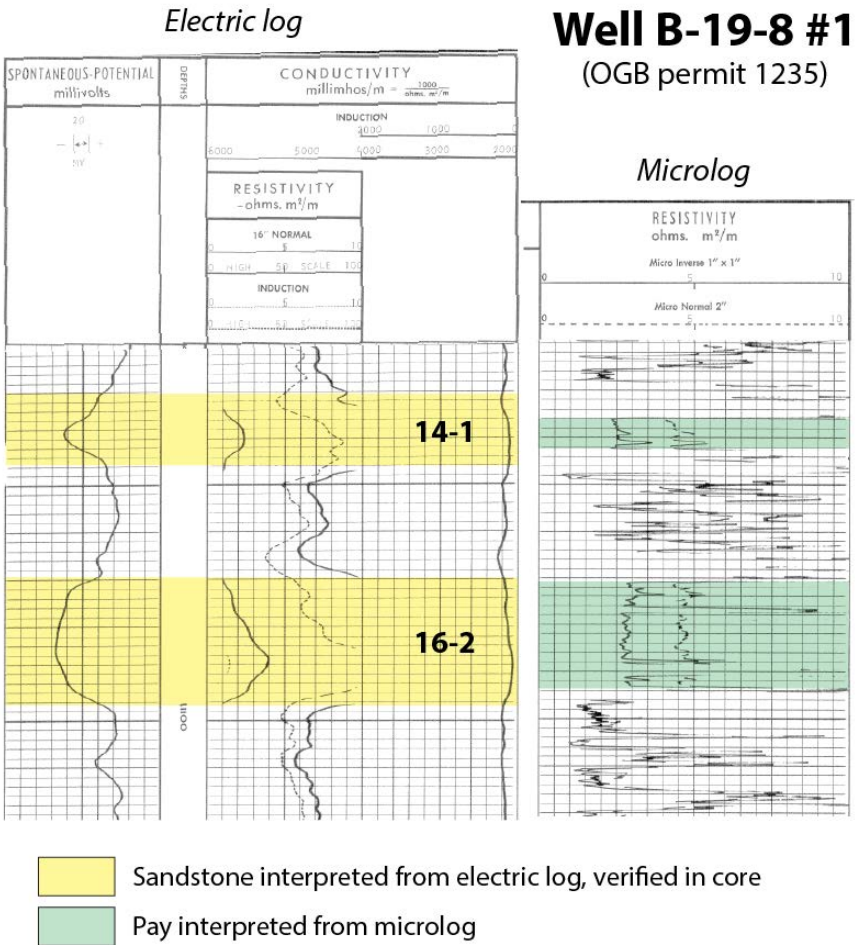


Figure 2.24. Geophysical well logs showing relationships between SP-resistivity logs and micrologs. Pay zones were interpreted from micrologs, and models of net pay thickness were constructed in the northeastern part of Citronelle Field.

**A. 14-1 Sand**

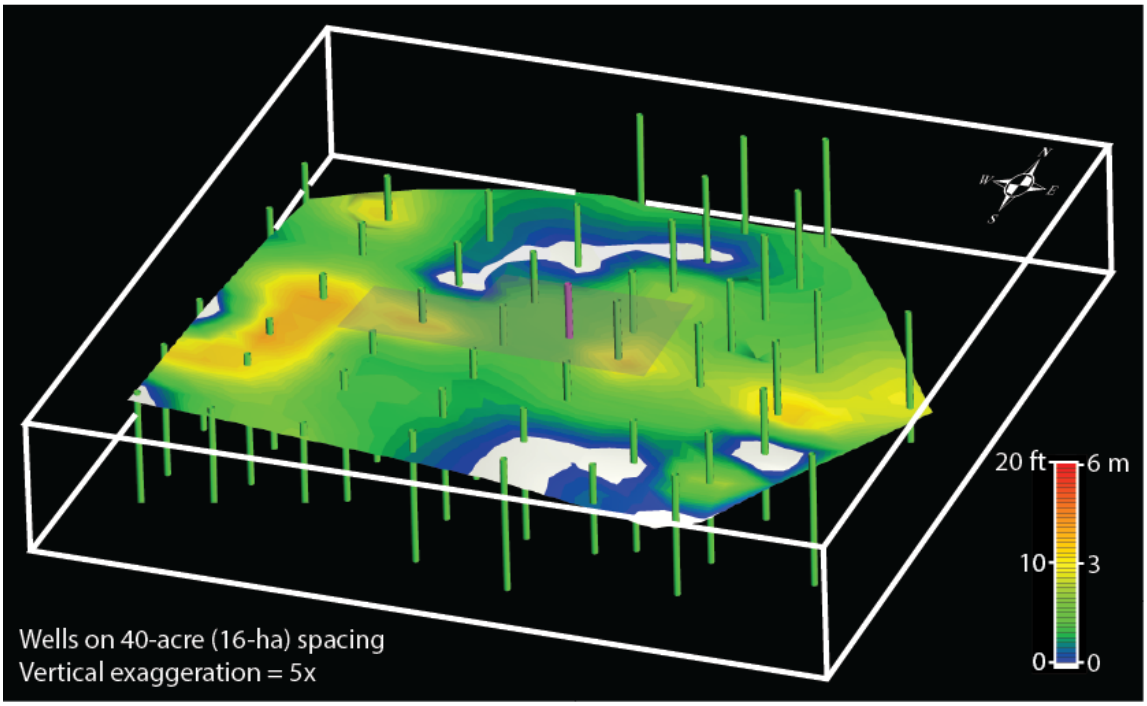


**B. 16-2 Sand**

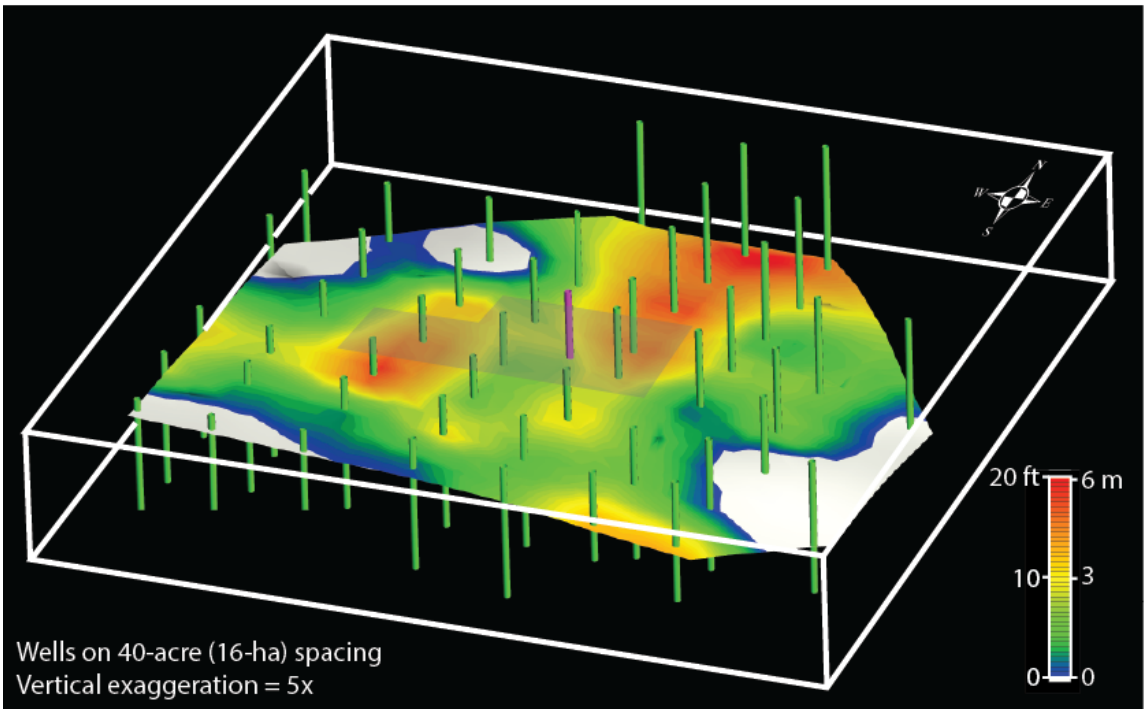


Figure 2.25. Three-dimensional models of net pay thickness in the northeastern part of Citronelle Field. Color contoured pay thickness is draped on structural models of the base of each sandstone. EOR experiment area shaded gray, and B-19-10 #2 injection well is highlighted in magenta.

***Interpretation.*** The sandstone facies has many characteristics of fluvial, estuarine, and beach deposits. The general vertical progression from medium- to fine- grained sandstone with cross-beds to fine- to very fine-grained sandstone with subhorizontal laminae and ripple cross-strata (Figure 2.12) is suggestive of waning flow, and the variable lateral extent of the sandstone bodies is suggestive of channel systems (Figures 2.12, 2.18, and 2.26). Most of the cross-bedded sand (Figures 2.12 and 2.20A) was transported as bedload, whereas much of the ripple cross-laminated sandstone (Figures 2.20D and 2.23) was deposited from suspended load. The consistent ripple orientation in the cores suggests that unidirectional flows predominated, suggesting a dominant fluvial origin. However, mud draping of some cross-strata (Figure 2.20B) indicates periodic waxing and waning of flow, which is typical of tidal systems (e.g., Terwindt, 1981). At the other end of the spectrum, the association of normally graded laminae with roots and plant fragments (Figure 2.22) is possibly the product of eolian grainfall sedimentation (e.g., Hunter, 1977), which has been observed in dryland river systems (Shepherd, 1987; Tooth, 2000).

Trace and plant fossils in the sandstone (Figure 2.21) appear to be dominantly terrestrial. Meniscate burrows are abundant in many continental deposits and are commonly the product of insect and other animal activity in abandoned stream beds and alluvial plains (e.g., Hasiotis, 2002). The occurrence of fossil root systems indicates that some sandy landscapes were vegetated. Clearly, the sandstone facies represented a very wide spectrum of depositional processes and environments, but some generalizations can be made. Grain size indicates a dominance of bedload fluvial sedimentation, and so the fluvial deposits may represent sandy braided streams of Platte type following the classification of Miall (1977). Cross-bedded sandstone thus probably accumulated mainly in transverse bars, whereas the gravel beds represented by the conglomerate facies accumulated in longitudinal bars. Climbing ripples indicate that suspended load sedimentation was locally effective, but these types of deposits are scarce and probably were deposited in minor sinuous channel segments amidst the longitudinal and transverse bars that predominate in braided systems. Indeed, a lack of evidence for significant levee, flood-basin, and crevasse-splay deposits in the Donovan sandstone suggests that the fluvial systems had low sinuosity and were confined largely to valleys.

Local evidence for tidal processes, such as mud-draped cross-strata (Figure 2.20B) indicates episodic incursion of marine water at the landward fringe of the platform lagoon and thus formation of estuaries. However, these types of deposits are rare in most of the Donovan sandstone, indicating that most sedimentation occurred in a continental dryland setting. The most prominent examples of coastal sedimentation occur in the uppermost sandstone units of the lower Donovan and upper Donovan intervals (Figure 2.26). In these parts of the section, sandstone beds are very widespread, and the associated strata of the conglomerate facies include oyster hash. The sandstone in these intervals is dominated by subhorizontal laminae (Figure 2.20C), which are suggestive of the low-angle, wedge planar cross-strata that are diagnostic of beach deposits and shoreface. Similar deposits are widespread in the Cretaceous strata of North America (e.g., McCubbin, 1982). Channel fills associated with the beach-shoreface deposits, which contain most of the oyster hash (Figures 2.15 and 2.17), are interpreted as inlet deposits. Hence, the distribution of fluvial and marine deposits is consistent with overall rising sea level and a long-term transition from fluvial to shoreline environments during deposition of each Donovan sequence set.

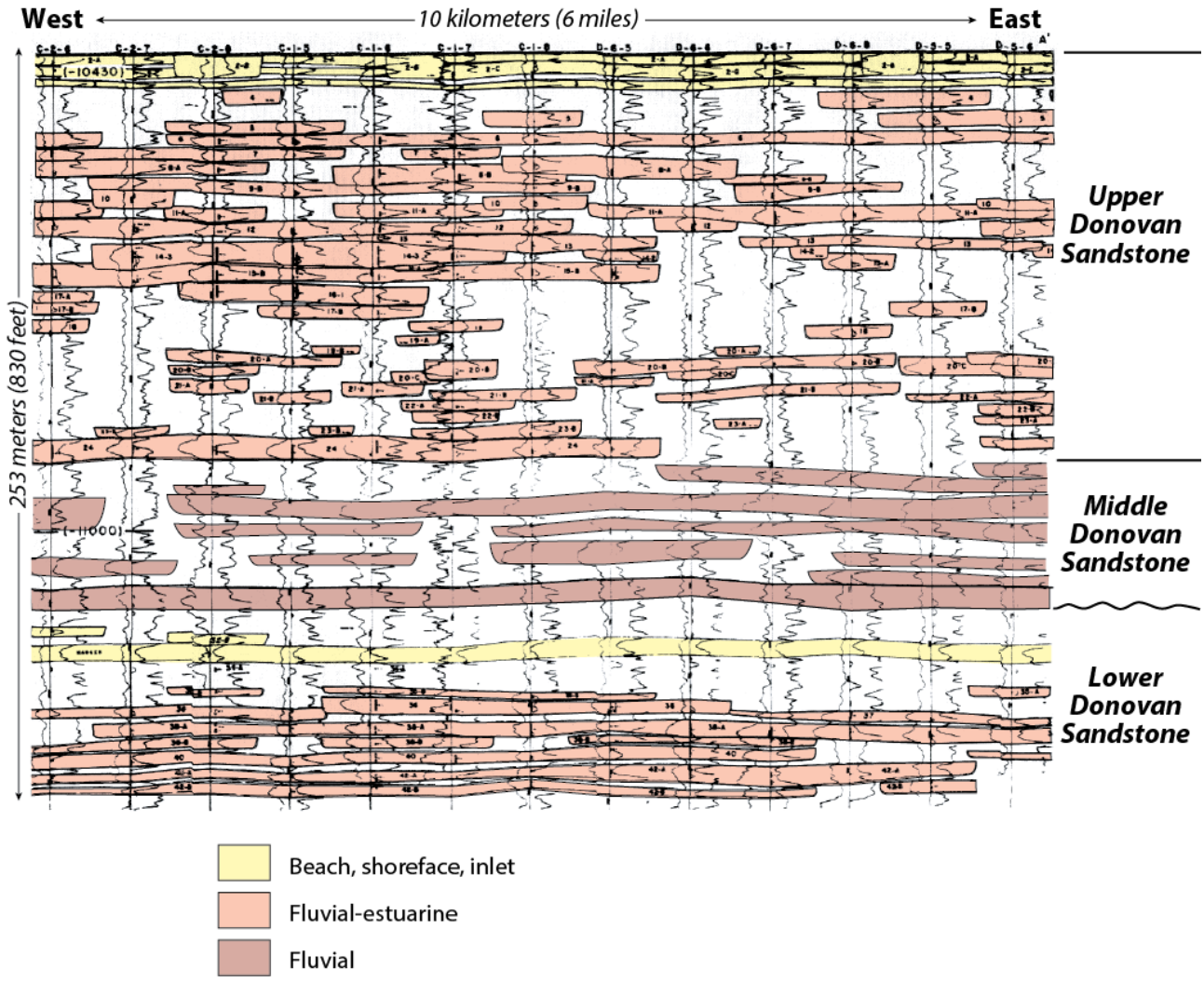


Figure 2.26. Cross section traversing central Citronelle Field showing generalized interpretations of sandstone depositional environments (modified from Eaves, 1976).

### *2.4.3. Heterolithic Facies*

***Characteristics.*** The heterolithic facies is the least common lithofacies of the Donovan sandstone (Figure 2.27) and occurs primarily in the upper portions of the lower Donovan and upper Donovan intervals. The heterolithic facies constitutes parts of the Donovan sandstone that contain thinly interbedded shale, siltstone, and sandstone. These strata are variegated, with most of the shale being dark gray and most of the siltstone and sandstone being medium gray to light gray. These strata commonly have red hues, and the arenaceous layers have brownish to dark gray shades where they are stained with oil and pyrobitumen.

Bedding styles in the heterolithic facies include flaser, wavy, lenticular, and pinstripe bedding (Figure 2.27). Thin layers containing dolomitic mudstone, mudstone, and anhydrite clasts resembling those in the conglomerate facies occur locally (Figure 2.28). Physical sedimentary structures include load casts, current-ripple cross strata, and horizontal laminae (Figure 2.27).

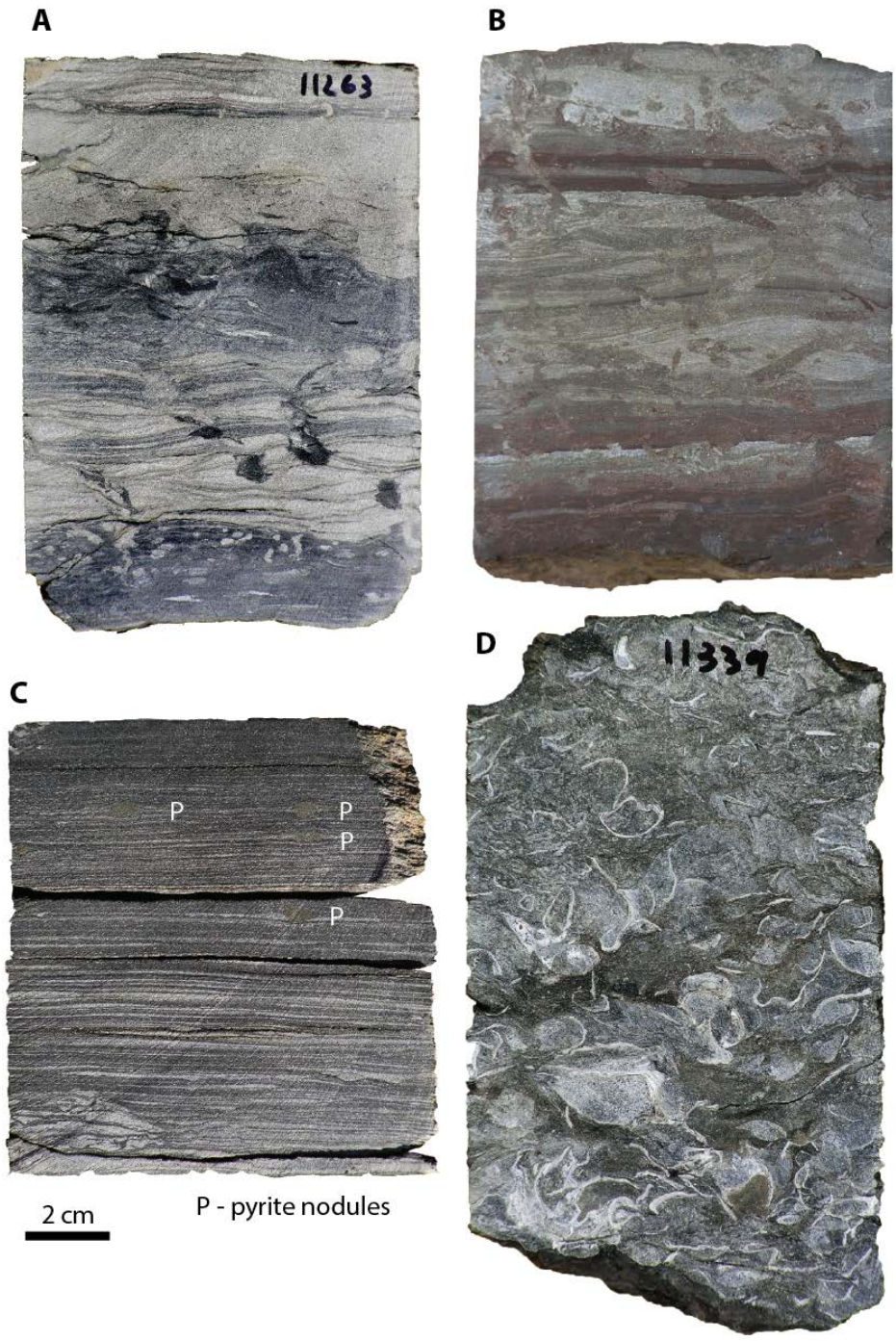


Figure 2.27. Photographs of slabbed core from the heterolithic facies. A. Interbedded shale, siltstone, and sandstone with load casts, current ripples, and burrows, Well C-2-16 #2, 11,263 ft. B. Variegated shale, siltstone, and sandstone with wavy and lenticular bedding and abundant burrows, including inclined burrows of *Rhizocorallium*, Well C-1-6 #1, 10,935 ft. C. Pinstripe-laminated shale, siltstone, and sandstone with pyrite nodules and burrow fills, Well C-1-6 #1, 11,339 ft. D. Bioturbated mudstone and sandstone containing abundant oyster shells, many of which are articulated and uncompacted, Well C-1-6 #1, 11,339 ft.


Figure 2.28. Core photograph showing wavy bedded conglomerate, sandstone, and mudstone in the heterolithic facies, Well C-1-6 #1, 10,720 ft.

Ripple foreset orientation is less uniform than in the sandstone facies (Figure 2.27B). Desiccation cracks were observed locally, particularly where the shale and sandstone bear red hues (Figure 2.29A), and trace fossils are common throughout the lithofacies. Parts of the lithofacies are calcareous, and some beds contain abundant oyster shells. Some of these intervals constitute hashes of disarticulated shells that are flattened, whereas others contain articulated shells that are filled with sediment (Figure 2.27D).

Biogenic structures in the heterolithic facies are quite varied. Meniscate burrows are common, particularly where the facies has red hues and where desiccation cracks are present (Figure 2.29A). Overall, the trace fossil assemblage is much more diverse than in the sandstone facies and includes specimens of *Rhizocorallium* (Figure 2.28B) and *Teichichnus* (Figure 2.29B), as well as conical burrows resembling *Conostichus* (Figure 2.29C). Pyrite nodules are common in these strata and in places appear to fill horizontal burrows (Figure 2.27C).

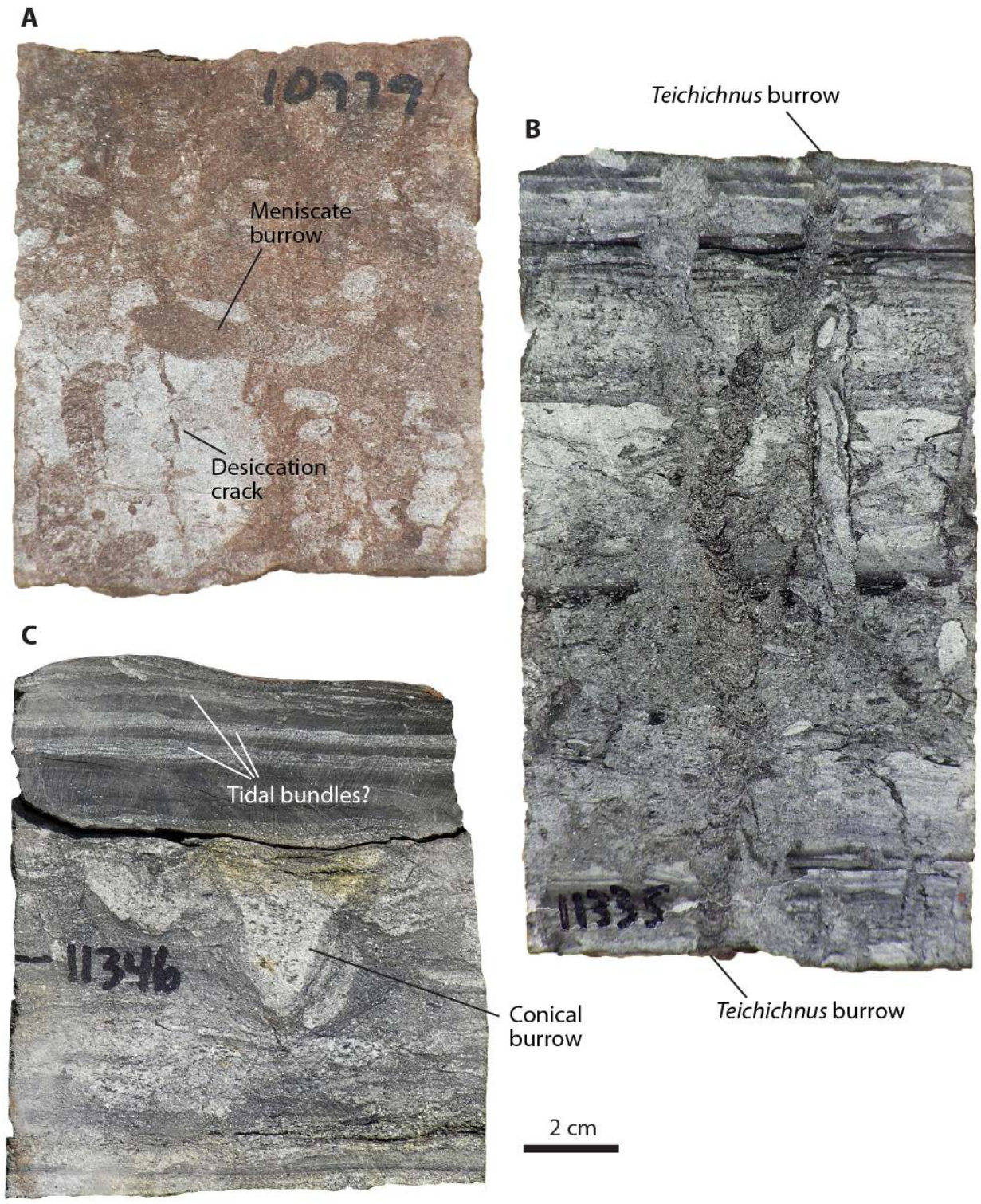


Figure 2.29. Photographs of biogenic structures in slabbed core of the heterolithic facies. A. Meniscate burrows and desiccation cracks in interbedded sandstone and red mudstone, Well C-1-6 #1, 10,979 ft. Note well-defined meniscae in horizontal burrow. B. Specimen of *Teichichnus* in interbedded sandstone, siltstone, and shale of the heterolithic facies, Well C-6-1, #1, 11,335 ft. C. Conical burrows and possible tidal bundles in interbedded shale, siltstone, and sandstone, Well C-2-16 #2, 11,346 ft.

Strata of the heterolithic facies tend to be associated with the upper parts of the Donovan sandstone bodies, particularly in the transition zone where sandstone grades into mudstone. The precise thickness and distribution of the heterolithic facies is uncertain because of spotty core coverage in mudstone-bearing intervals. Based on the available evidence, heterolithic strata tend to be less than two feet thick in most of the lower Donovan and upper Donovan. Reddish hues are common in these strata, and typical sedimentary structures include mud cracks and a meniscate burrow assemblage similar to that in the sandstone facies. In the upper 100 feet of each interval, by contrast, heterolithic strata are commonly thicker than two feet, and strata with red hues are relatively scarce. It is here that the trace fossil assemblage is more diverse than that in the sandstone facies, and this is the part of the section where oyster shells are abundant.

***Interpretation.*** Most strata assigned to the heterolithic facies have the classic characteristics of tidal deposits. These characteristics include wavy, flaser, lenticular, and pinstripe bedding (Figure 2.27), which have long been associated with tidal flat settings (e.g., van Straaten, 1954; Klein, 1977). Oyster assemblages (Figure 2.27D) and burrows like *Teichichnus* (Figure 2.29B) are the clearest indicators of marine to brackish water (e.g., Seilacher, 2007). The disarticulated oysters forming hashes have been transported, but zones with articulated shells (Figure 2.27D) may represent in situ assemblages. Desiccation cracks (Figure 2.29A) indicate episodic exposure, and the meniscate burrows in this facies (Figure 2.29A) arguably represent the same terrestrial insect communities that are interpreted to have dominated bioturbation in the sandstone facies. Thus, it is possible, if not likely, that trace fossil assemblages of continental affinity have been superimposed on marine and marginal marine fossil assemblages in the heterolithic facies.

This is especially apparent where thin intervals of the heterolithic facies are in the parts of the Donovan sandstone that contain principally fluvial deposits. Some of these zones may represent minor marine incursions into the river valleys and the formation of estuaries. Alternatively, deposits containing only mud cracks and meniscate burrows could be interpreted as continental sheet flood deposits. Therefore, the simplest interpretation is that the heterolithic facies tends to have a continental signature in the lower part of each sequence set. The frequency and extent of estuarine tidal flat deposits increases upward in section, culminating in widespread shoreline sedimentation along the landward fringe of the platform lagoon at the top of the sequence sets (Figure 2.26).

### *2.4.4. Mudstone Facies*

***Characteristics.*** The mudstone facies constitutes all thick-bedded mudstone intervals in the Donovan sandstone (Figures 2.12, 2.30, and 2.31). In general, the mudstone facies has thickness and continuity that is similar to the sandstone facies (Figures 2.18 and 2.26). The signature rock type of the mudstone facies is reddish, non-fissile mudstone. Variegated mudstone is common and rock colors include a range of gray and greenish hues. The mudstone tends to be rich in silt and sand and can in places be classified as muddy sandstone.

Although the mudstone appears massive at first glance, close examination reveals several types of physical and biogenic sedimentary structures. Much of the mudstone has a blocky appearance and contains slickensides with variable orientation (Figure 2.30A). This type of mudstone is quite friable, breaking readily into blocky pieces smaller than two inches. Dolomitic mudstone nodules are abundant in the mudstone facies and weather to pale colors (Figure 2.30B).

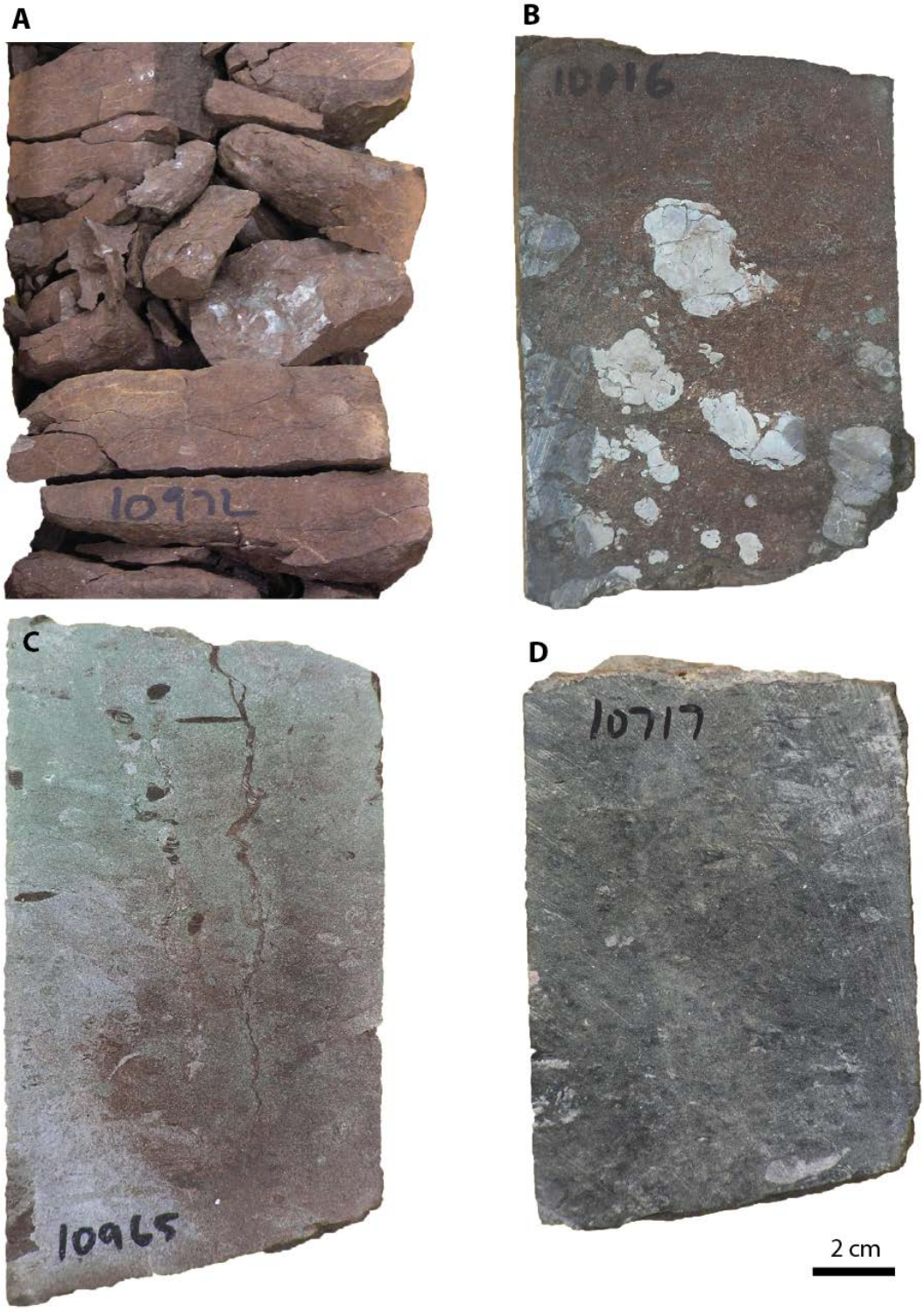


Figure 2.30. Photographs of slabbed core of the mudstone lithofacies in Well C-1-6. A. Mudstone containing pedogenic slickensides and blocky peds, 10,972 ft. B. Mudstone containing dolomitic mudstone nodules with cracks, 10,816 ft. C. Variegated sandy mudstone with desiccation crack and meniscate burrows, 10,965 ft. D. Gray mudstone with intense burrow mottling, 10,717 ft.

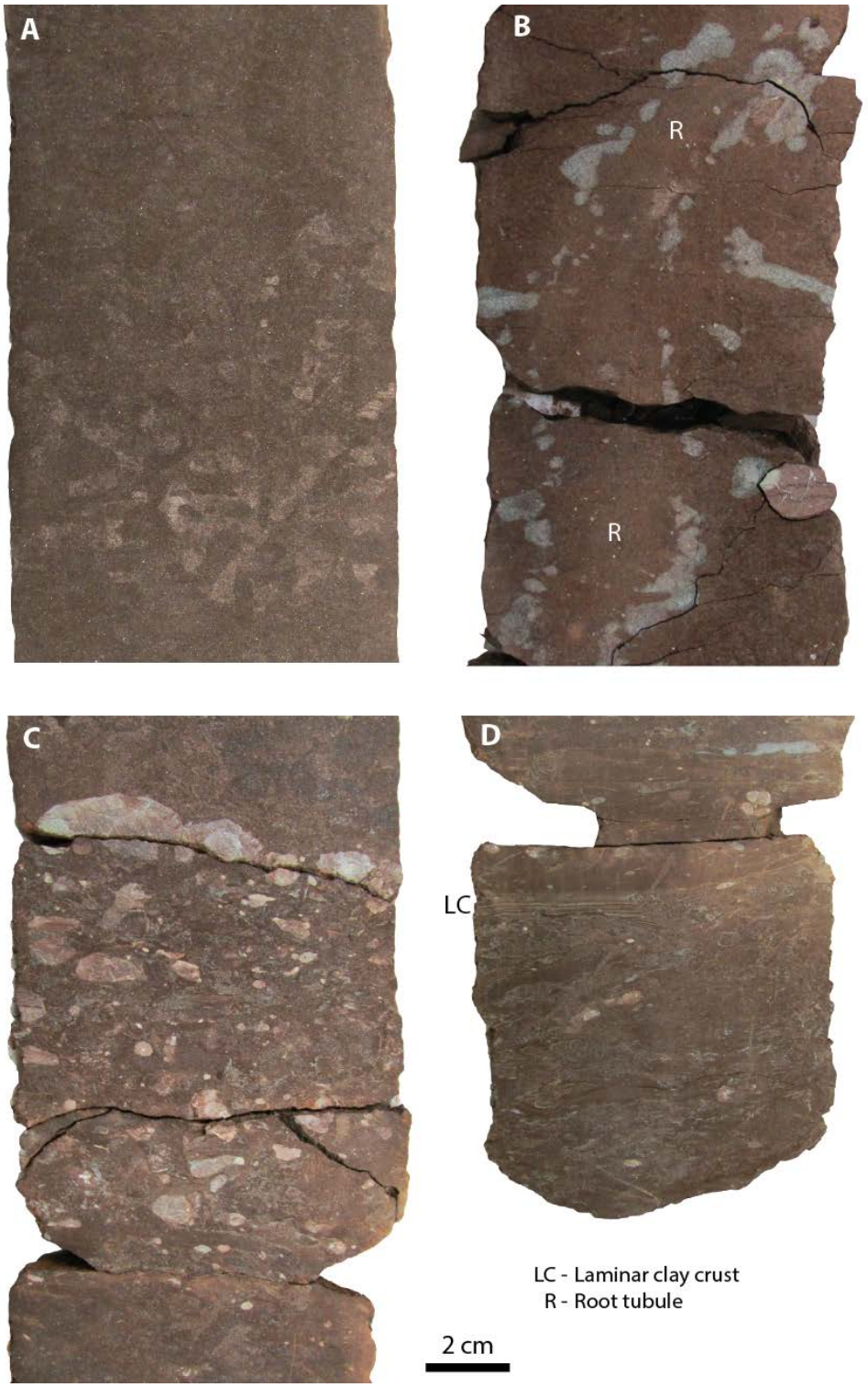


Figure 2.31. Photographs of slabbed core from the mudstone facies, Well D-9-8 #2. A. Sandy mudstone with abundant meniscate burrows, 10,970 ft. B. Fossil root tube with gray halo suggesting reduction of mud by decay of organic matter, 11,034 ft. C. Conglomeratic layer within mudstone facies composed of dolomitic and argillaceous mudstone clasts, 11,153 ft. D. Layer of mudstone pebbles overlain by crust of thinly laminated claystone, 11,154 ft.

Anhydrite nodules also were identified in some samples. The nodules range in size from granules to cobbles. Internally the nodules are extremely fine-grained and can be indistinct from the host mudstone matrix where fresh. The nodules are commonly cracked, and the cracks are commonly filled with clay or form calcite-filled septaria. Larger desiccation cracks also have been observed in the mudstone (Figure 2.30C). Some of the nodules have clay coatings that resemble the coatings on the dolomitic mudstone clasts in the conglomerate facies. Conglomeratic layers are preserved locally in the mudstone and include accumulations of mudstone and dolomitic mudstone clasts (Figures 2.31C and 2.31D). Conglomeratic layers in the mudstone facies have mudstone matrix and are thus readily distinguished from those in the conglomerate facies, which have sandstone matrix. Thin, laminated clay layers that appear as laminar crusts also are present in the mudstone facies and are commonly associated with conglomeratic intervals (Figure 2.31D).

Most of the mudstone has a mottled texture, which is mainly the product of intense burrowing (Figures 2.30D and 2.31A). The trace assemblage is dominated by meniscate burrows like those in the sandstone facies. Some traces of plant life are preserved in the mudstone facies. Large tubular structures with gray rims are suggestive of mud-filled root cavities (Figure 2.31B). Coalified root systems are preserved locally and are characterized by irregular vitrain linings surrounded by halos of gray mudstone.

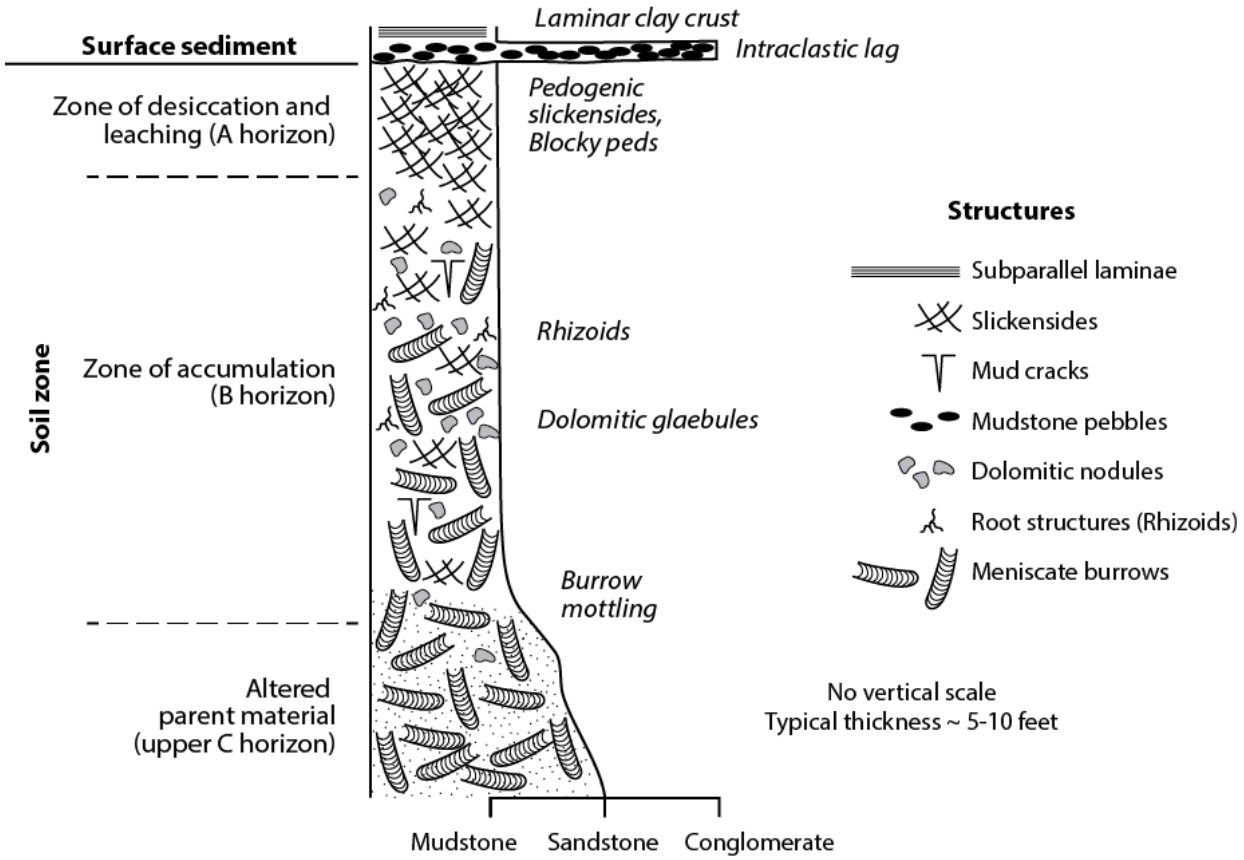


Figure 2.32. Idealized vertical succession and paleoenvironmental interpretation of rock types and sedimentary structures in the mudstone lithofacies.

Strata in the mudstone facies display a distinctive vertical succession of rock texture, sedimentary structures, and biogenic structures (Figure 2.32). This succession, moreover, can be repeated multiple times within a single mudstone unit. The base of the succession is gradational with either the sandstone facies or the heterolithic facies, and the zone of gradation can approach three feet in thickness. The lower part of the mudstone facies is intensely burrow-mottled and is very sandy (Figure 2.31A). Sand content decreases upward, and dolomitic mudstone nodules (Figure 2.30B) increase upward in frequency and size. Higher in the succession, the frequency and size of the nodules decreases, sand content continues to decrease, and burrowing becomes less distinct. It is in this part of the succession that root traces are most common (Figure 2.31B). Slickensides and desiccation cracks (Figure 2.30A, C) become increasingly common in the upper few feet of the vertical succession, and friability of the mudstone increases. Slickensided and cracked mudstone typically forms the top of the succession. Alternatively, some successions are capped by conglomeratic mudstone (Figure 2.31C) or laminar clay crusts (Figure 2.31D).

***Interpretation.*** The mudstone facies is interpreted as the product of intense oxidation and soil formation. Intensely oxidized and desiccated soil profiles with abundant pedogenic slickensides are characteristic of vertic soil profiles, or vertisols, which form today in arid to semi-humid regions (e.g., Retallack, 1990). The idealized vertical succession (Figure 2.32) shows the architecture of a typical soil profile in the mudstone facies. The abundant meniscate burrows (Figure 2.31A) in the lower part of the profile indicate that the landscape supported animal life, and the intensity of burrowing reflects the cumulative effect of biotic activity during formation of the soil profile.

The dolomitic mudstone nodules (Figure 2.30B) represent precipitation of carbonate leached from higher in the soil profiles. Carbonate nodules in soil profiles are called glaebules by soil scientists. Dolomitic glaebules are uncommon in modern soil profiles (Retallack, 1990) and may thus be a product of exchange of magnesium with clay during burial diagenesis. The abundance of cracks and septaria in the nodules indicate desiccation and hence alternating episodes of wetting and drying, and the presence of anhydrite suggests that the climate was semi-arid to arid. Clay coatings on some of the nodules indicates illuviation of clay from higher in the soil profiles and accumulation around nodules as argillans (argillaceous cutans).

Root traces (Figure 2.31B) provide evidence for a vegetated landscape, although the abundance of pedogenic slickensides (Figure 2.30A) indicates that desiccation, swelling, and compaction dominated the fabric of the upper part of the soil profile. The slickensides are interpreted as stress cutans, which are coatings of aligned clay that form where drying and wetting shrink and swell soil, causing slippage among soil particles. Soil particles are called peds, which are the fundamental units of soil structure. The shape and size of the desiccated and slickensided bodies in the mudstone facies indicate that the upper parts of the soil profiles were dominated by blocky peds (Figure 2.32).

The conglomeratic layers and the thinly laminated clay layers (Figures 2.31C and 2.31D) indicate that some surface features are preserved in the mudstone facies (Figure 2.32). The conglomeratic layers constitute thin accumulations of pebbles formed from mudstone and glaebules atop the soil profiles. The abundance of similar clasts in the conglomerate facies, moreover, indicates that the vast majority of the intraclastic material was derived locally from the vertic soil. The thinly laminated clay layers that locally overlie the conglomeratic layers in the mudstone facies, moreover, are interpreted as laminar clay crusts that probably accumulated in shallow puddles that

remained after storms and floods. Examination of the mudstone facies indicates that soil formation was a major process during Donovan sedimentation. Indeed, the section that follows on petrology and diagenesis demonstrates that soil-forming processes exerted significant control on Donovan reservoir characteristics.

## 2.5. Petrology and Diagenesis

Petrologic analysis is used to analyze the composition and fabric of sedimentary rocks and is valuable for determining the effects of geologic and geochemical processes, from the time of deposition to deep burial and reservoir formation, on rock composition and reservoir quality. This section begins with a discussion of framework sandstone composition, which provides vital information on the provenance, or source, of sediment. A discussion follows on diagenetic factors, which are low-temperature alteration processes, that influence the characteristics and quality of Donovan sandstone reservoirs. The discussion concludes with porosity and permeability, which are the principal rock properties affecting the storage and mobility of reservoir fluid.

### *2.5.1. Framework Sandstone Composition*

Examination of thin sections reveals that the Donovan sandstone is of variable compositional and textural maturity. A quartz-feldspar-lithic fragment (QFL) diagram indicates that point-counted samples cluster near the quartz-feldspar axis, with feldspar content ranging from 5 to 50% by volume (Figure 2.33). According to the widely used sandstone classification of Folk (1980), framework composition ranges from arkose to subarkose, although some lithic arkose and sublitharenite are present. The feldspar fraction includes substantial amounts of plagioclase and potassium feldspar, and total feldspar content averages 16% of the rock volume. Mica, including muscovite and biotite (Figure 2.34) constitutes about 4% of the rock volume, which is unusually high for sandstone. Mica is present chiefly in the form of large, platy flakes (Figure 2.34A) and is in places concentrated in laminae up to a few millimeters thick (Figure 2.34B). Minor framework constituents include chert, sedimentary rock fragments, polycrystalline quartz, and fossil debris.

The sedimentary rock fragments are of local origin, having been derived mainly from the mudstone facies. These grain types, however, yield little information on the ultimate provenance of the sandstone. Plotting the non-sedimentary material on the provenance diagram of Dickinson and Suczek (1979) and Dickinson et al. (1983) reveals that the provenance indicators are dominated by quartz and feldspar and that igneous-metamorphic rock fragments form an insignificant part of the sandstone (Figure 2.33). Accordingly, the sandstone plots mainly in the transitional continental field, suggesting an origin from denudation of feldspar-rich basement provinces. This indicates that the sediment is far-traveled, since these types of sediment sources form only a minor fraction of the nearby Appalachian highlands, which plunge underneath the Gulf of Mexico coastal plain in eastern and central Alabama. However, the unusually high abundance of mica in the sandstone (Figure 2.34B) suggests significant input from metamorphic rocks, which are abundant and widespread in the Appalachian Piedmont Province.

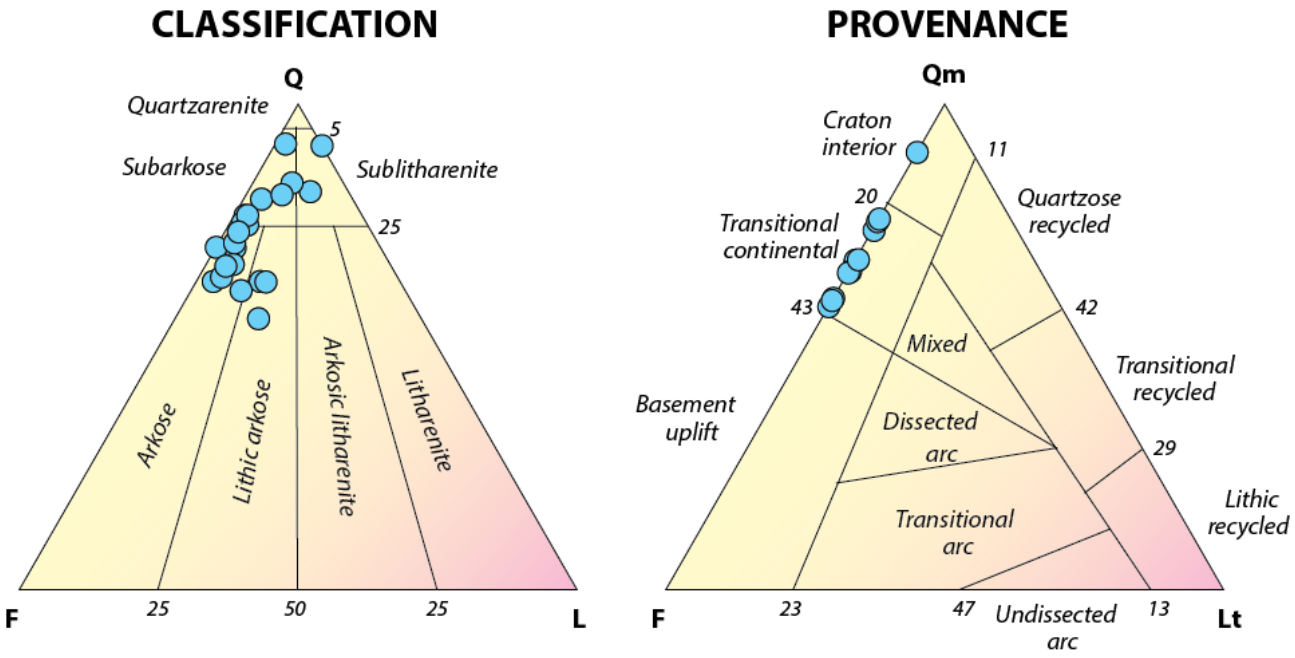


Figure 2.33. Ternary diagrams showing classification and provenance of the Donovan sandstone in Citronelle Field.

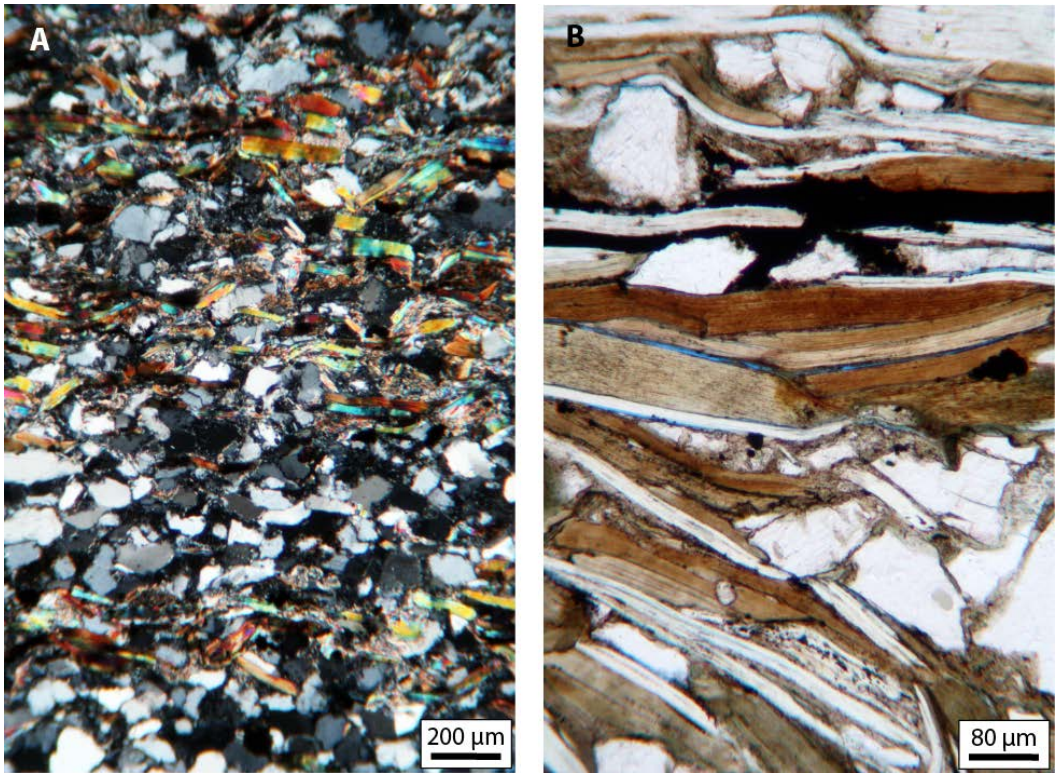


Figure 2.34. Photomicrographs of Donovan sandstone, Well A-25-15. A. Micaceous siltstone. Platy grains with high birefringence are mica; most equant grains with low birefringence are quartz and feldspar, 11,424 ft. B. Micaceous lamina showing major concentration of platy muscovite, biotite, and phlogopite grains, 11,439 ft.

### *2.5.2. Diagenesis*

A number of diagenetic features were observed in the Donovan sandstone that provide crucial insight into the geochemical processes that operated from early burial to the emplacement of oil in the reservoir. Key processes that have affected the fabric and quality of the sandstone include dissolution, fluid transport, and mineral precipitation. The effects of dissolution are readily apparent in many samples of reservoir sandstone in Citronelle Field. Many feldspar grains have been vacuolized, leaving skeletons of mineral inclusions and grain-size pores where the feldspar has been dissolved (Figure 2.35). Examination of thin sections, moreover, indicates that feldspar dissolution is an important source of porosity in the Donovan sandstone.

Weathering and dissolution of feldspar yields clay, which has clearly evacuated some pores (Figure 2.35) while accumulating in others (Figure 2.36). Some of the products of feldspar dissolution include pore-filling kaolinite (Figure 2.36A), and it is not clear whether the pore-filling kaolinite formed in situ or was transported. The paleosols of the mudstone facies provide evidence for deep weathering in the Donovan sandstone, and many thin sections reveal that much of the sandy mudstone is the product of infiltration of clay into weathered sandstone (Figure 2.36B). Hence, while weathering and meteoric flushing of clay increased the porosity of some sand layers, illuviation and accumulation of clay by vertical percolation of water through the soil profile occluded porosity in many sand layers.

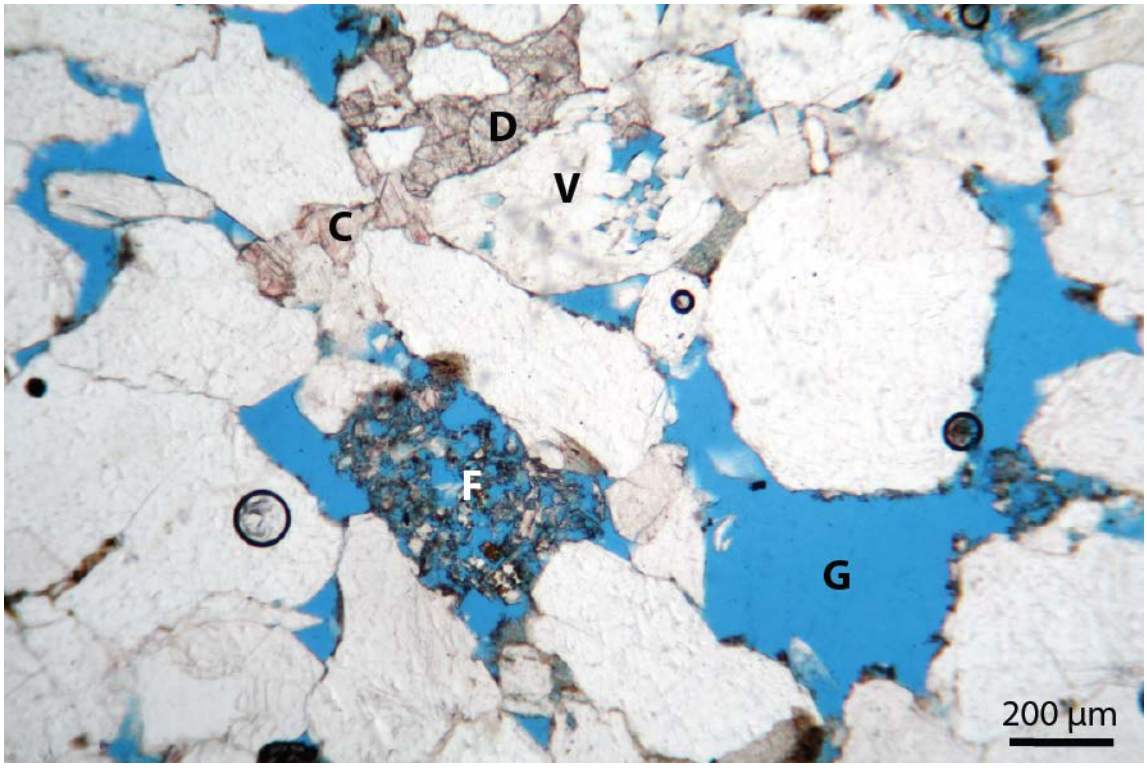


Figure 2.35. Photomicrograph of Donovan sandstone showing grain-size pores (G), vacuolized feldspar grains (F), interparticle calcite cement (C), and interparticle dolomite cement (D), Well A-25-15, 11,420 ft.

Carbonate minerals constitute the major burial cements in the Donovan sandstone. Calcite is the most common cement and is present as large, poikilotopic bodies that occlude porosity (Figure 2.37). As mentioned in the discussion of the sandstone and conglomerate facies, calcite cement is pervasive near the contacts of the sandstone bodies and in many conglomerate beds and forms pebble-size concretionary masses in the interior of the reservoir sandstone units. Some dolomite cement also occurs in the reservoir (Figure 2.35), and cement-stratigraphic relationships indicate that it is a late-stage cement that formed during deep burial. Quartz overgrowths are not obvious in thin sections of the sandstone, although faceted and interlocking grain boundaries of quartz grains (Figure 2.35), including stylolites, indicate that pressure solution and quartz overgrowth were significant processes during burial.

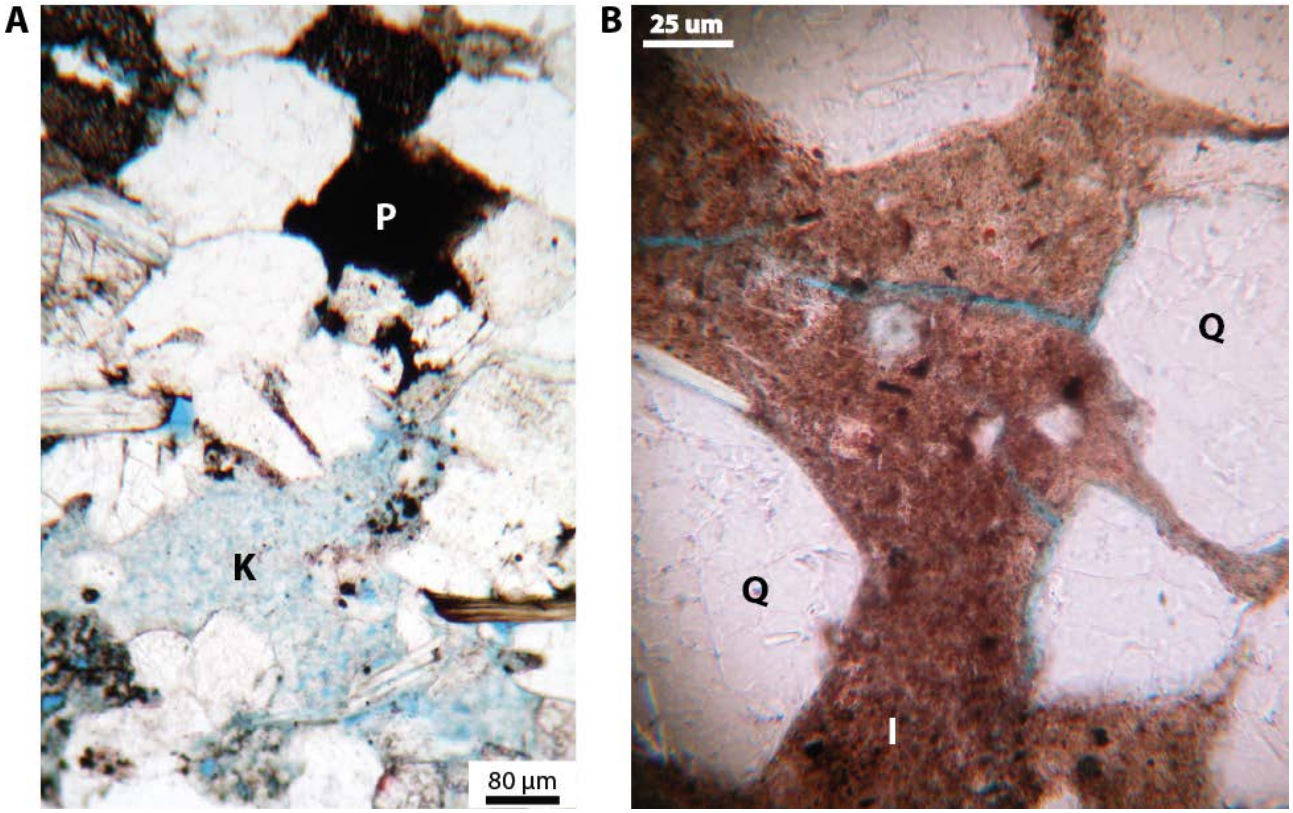


Figure 2.36. Thin section photomicrographs showing petrographic expression of clay and pyrobitumen in Donovan sandstone. A. Pore-filling kaolinite (K) and pyrobitumen (P), Well A-25-15, 11,421 ft. B. Pervasive intergranular clay in muddy sandstone of the mudstone facies, interpreted to be of illuvial origin, Well C-11-15 #2, 11,356 ft. Q = quartz, I = illuvial clay matrix.

Donovan sandstone records a transition from the diagenetic processes associated with burial to catagenetic processes associated with the generation, migration, trapping, and alteration of oil. Reduction fingers in red sandstone are preserved in the SECU D-9-8 #2 core (Figure 2.38), which provides crucial information on the evolution of the sandstone bodies and the emplacement of hydrocarbons. The core preserves fingers of yellowish-gray sandstone in red sandstone, and the sandstone in the lower part of the photograph is darkened with pore-filling pyrobitumen. This indicates that the sandstone was originally red but was intruded by reducing pore fluids containing oil. The pattern of reduction provides evidence for viscous fingering between the oil-bearing fluid

and the brine in the red sandstone near the contact. Considering the intense oxidation represented by the red hues of most non-reservoir strata in the Donovan interval, it is probable that the Donovan interval was by and large a redbed succession and that the gray to yellowish colors of the reservoir sandstone units formed by secondary reduction during emplacement of the oil. The gray mudstone intervals by the contacts of sandstone bodies, furthermore, is thus interpreted as the product of reduction halos formed by intrusion of reducing fluid into the sandstone intervals.

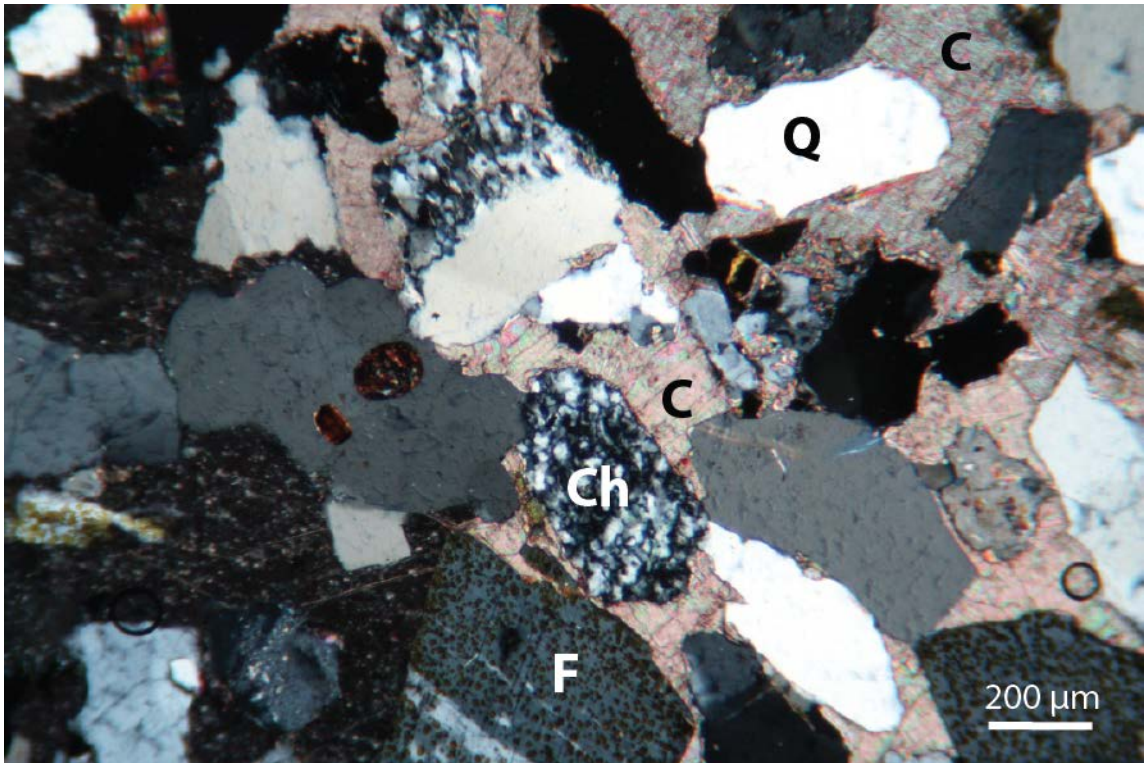


Figure 2.37. Photomicrograph showing calcite cement in the Donovan sandstone, Well A-25-15, 11,465 ft. Q = quartz grain, Ch = chert grain, F = feldspar grain, and C = poikilotopic calcite cement.

Pore-filling pyrobitumen is extremely common in the sandstone (Figures 2.12 and 2.36A) and indicates alteration of the Citronelle oil accumulation. Pyrobitumen is a residual product that can be formed by in situ thermal cracking of oil or by late-stage microbial activity (e.g., Hunt, 1979; Tissot and Welte, 1984). The temperature limit for major subsurface microbial activity in a sedimentary basin is typically between 80 and 100 °C, and thus the Donovan sandstone has been beyond this temperature range since the end of the Cretaceous (Figures 2.6 and 2.7). Burial history analysis suggests that the Citronelle oil accumulation had been trapped by that time and that the oil accumulation has been maturing thermally ever since. Indeed, the reservoir is just now reaching the edge of the thermogenic gas window. Hence, the preferred interpretation is that the pyrobitumen is a residue from in situ thermal cracking, which is in part responsible for the high quality of the oil produced from Citronelle Field today.


Figure 2.38. Pyrobitumen and fluid reduction fingers in Donovan sandstone showing evidence of intrusion of reducing oil-bearing fluids into red sandstone, Well D-9-8 #2, 11,139 ft.

### *2.5.3. Porosity and Permeability*

Porosity and permeability of sandstone can be controlled by depositional factors, diagenetic factors, or a combination of the two. In the Donovan reservoir sandstone, porosity is typically lower than 20 percent and averages 10 percent. Reservoir permeability is generally lower than 100 mdarcy and is typically on the order of 10 mdarcy, and some generalizations can be made about the permeability of strata in the various Donovan lithofacies. Strata in the conglomerate facies have permeability values lower than 0.1 mdarcy, indicating no significant reservoir potential. Comparison of core analysis data with samples of the sandstone facies indicates that permeability is typically higher than 10 mdarcy in cross-bedded sandstone and is on the order of 1 mdarcy in strata containing current ripples and intense bioturbation. Permeability was determined in two samples from the mudstone facies and is on the order of 0.0002 mdarcy, indicating that the mudstone intervals form significant seals, baffles, and barriers.

Within the sandstone facies, grain size has a significant impact on permeability. Finer rocks are, on average, less permeable than coarser ones (Figure 2.39). However, permeability ranges greatly in each grain size class, indicating that other factors are effective. Diagenesis is certainly an

important factor, considering that porosity is enhanced in some samples by feldspar dissolution (Figure 2.35) and is occluded by accumulation of clay (Figure 2.36).

Donovan pore systems at Citronelle are mixtures of primary interparticle pores and secondary dissolution pores (Figure 2.35). We make the conservative assumption that interparticle pores are primary if they contain no trace of cement, but dissolution pores can mimic primary pores where calcite has been dissolved (Kugler and McHugh, 1990; Kugler and Mink, 1999). That being said, the observable dissolution porosity in the Donovan sandstone is exclusively related to feldspar dissolution and typically accounts for 50 to 60 percent of total porosity. Considering that mean porosity is only 10 percent, it is clear that dissolution porosity is among the most important determinants of reservoir quality in Citronelle Field.

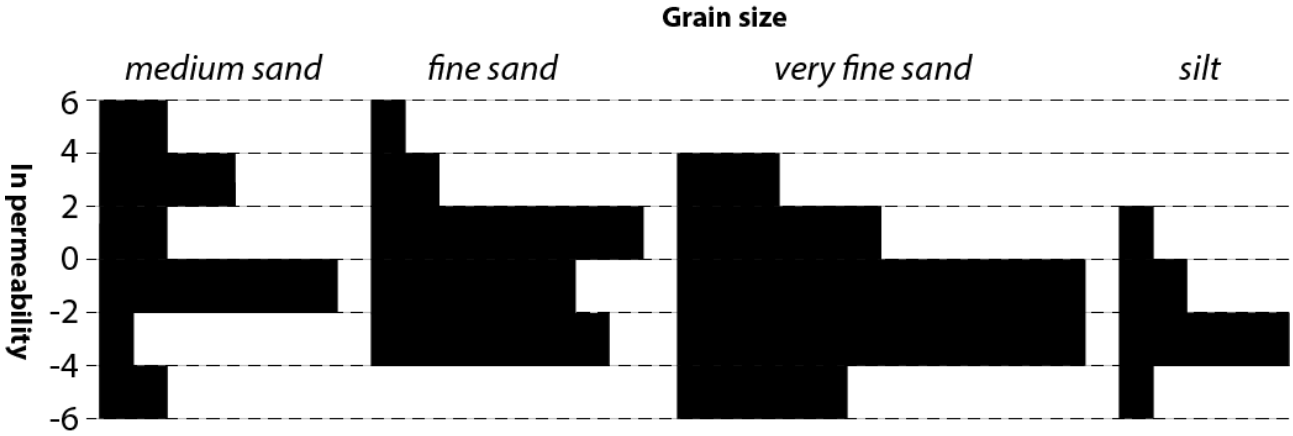


Figure 2.39. Frequency histograms showing relationship between grain size and permeability in the Donovan sandstone in Citronelle Field. Permeability generally decreases with decreasing grain size, although a high degree of variability suggests strong diagenetic influence on reservoir properties.

## 2.6. Sequence Stratigraphic Model

The results of sedimentologic and petrologic analysis can be synthesized into a sequence stratigraphic model (e.g. Vail, 1987; Wilgus et al., 1988; Catuneau, 2006) that provides a predictive framework for reservoir distribution and reservoir quality. As mentioned in the section on stratigraphic framework, the Donovan sandstone constitutes two distinct retrogradational sequence sets that record long-term landward shifts of coastal onlap (Figure 2.9). Facies analysis indicates that these shifts are expressed as transitions from bedload-dominated fluvial deposition to estuarine and beach sedimentation (Figure 2.26). Stacking of about 60 conglomerate-sandstone-mudstone packages in the Donovan sandstone suggests that sedimentation was cyclic, with each package representing about 100,000 years. This time span is on the order of the Milankovitch short eccentricity cycle, and so cyclicity within the Donovan sandstone is interpreted to have been driven by climatic changes associated with ellipticity of the earth's orbit around the sun. These changes include not only variation of rainfall during each cycle, but eustatic changes of sea level and associated changes of base level on the alluvial plain. These are the primary factors that would have regulated the frequency of marine flooding along the fringe of the Donovan platform lagoon (Figure 2.10), as well as the frequency of soil formation, valley incision, deposition of fluvial-estuarine sediment, and beach formation (Figure 2.40).

The proposed model is a basic valley filling model (Figure 2.40) that is similar to other sequence stratigraphic models designed for strata dominated by nonmarine sediment (e.g., Plint et al., 2001; Martino, 2004; Currie, 2007). The abundant paleosols of the mudstone facies represent widespread exposure, weathering, and erosion, which led to the incision of river valleys during lowstands of sea level (Figure 2.40A). Following basic sequence stratigraphic procedure, the contacts between the mudstone units and the overlying conglomerate-sandstone-mudstone successions can be characterized as lowstand surfaces of erosion, or sequence boundaries.

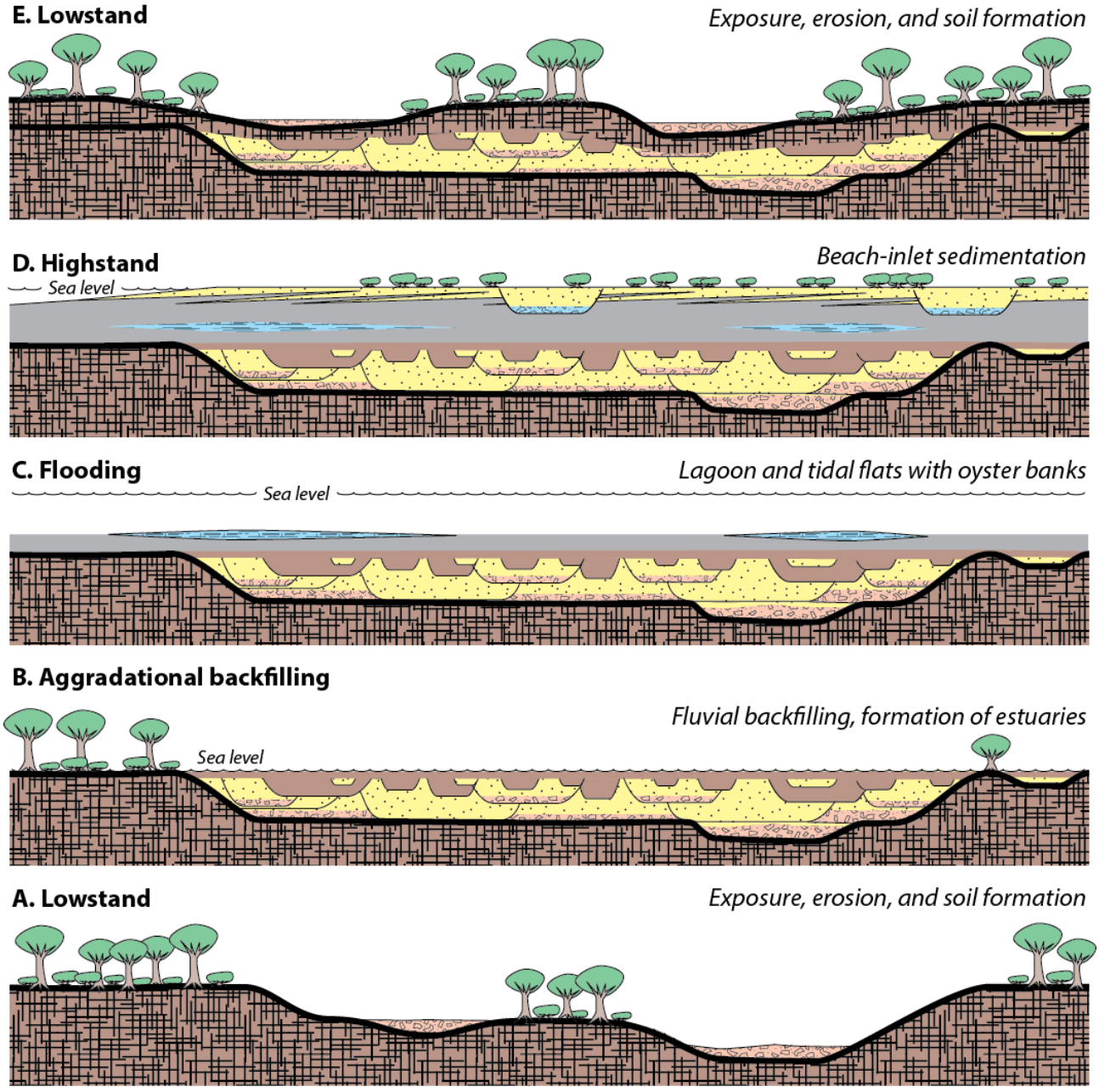


Figure 2.40. Idealized sequence stratigraphic model for the Donovan sandstone. This model depicts the range of depositional events thought to have influenced Donovan sedimentation and diagenesis during a single 100,000-year depositional sequence. About 60 such depositional sequences are preserved in the Donovan interval in Citronelle Field.

The initial stages of valley filling are recorded by the strata of the conglomerate facies, which form channel lags at the base of the conglomerate-sandstone-mudstone successions. Some conglomerate may have accumulated in topographic lows during lowstand (Figure 2.40A). The major sandstone units are interpreted to record aggradational infilling of the valley systems as base level rose (Figures 2.12, 2.18, and 2.40B). Sea-level rise may have been an important factor contributing to aggradational infilling, although subsidence of the coastal plain may have been equally important. Correlation of well logs indicates that many Donovan sandstone bodies are composed of nested channels that decrease upward in size (Figure 2.18). Many of the channels atop the sandstone units are plugged with mud, which results in a high degree of facies heterogeneity at the top of the sandstone bodies.

Most of the muddy channel fills have been altered by weathering, whereas some preserve estuarine deposits, signaling episodic marine flooding (Figure 2.40B). Widespread marine flooding, however, is only apparent in the upper parts of each sequence set, where the tidal deposits and oyster hashes of the heterolithic facies predominate (Figure 2.40C). At the top of the lower Donovan sandstone, widespread deposition of muddy strata formed reservoir seals, helping explain the occurrence of water-bearing middle Donovan sandstone above oil-bearing lower Donovan sandstone (Figures 2.11 and 2.26). Highstand deposits are preserved only in the uppermost sandstone units of each sequence set, which are interpreted to contain beach deposits (Figures 2.26 and 2.40D). Throughout most of Donovan time, however, whatever sediment may have been deposited during marine flooding and highstand had very low preservation potential, and regional exposure, soil formation, and valley incision marked the start of the next 100,000 year depositional sequence (Figure 2.40D).

Soil formation, moreover, had a major impact on reservoir quality. Indeed, nearly all pay zones in the Donovan sandstone are in sandstone where at least half of the porosity is the result of feldspar dissolution and meteoric flushing of the dissolution products. Where the dissolution products accumulated, such as in sandy parts of the soil profile containing illuvial clay (Figure 2.36B), reservoir quality was destroyed. Hence, the final geometry of many Donovan reservoir sandstone bodies may be more a reflection of soil forming processes than a reflection of sandstone geometry at the time of deposition.

## 2.7. Geological Implications for Field Management

Although Citronelle Field is structurally simple (Figures 2.3 and 2.4), analysis of depositional architecture reveals extreme facies heterogeneity (Figures 2.18 and 2.26). With so many productive sandstone units to consider in Citronelle Field, perhaps the greatest challenge for designing waterflood and $CO_2$-EOR programs is managing this heterogeneity. Stratigraphic cross sections indicate that reservoir sandstone bodies tend to occur in clusters (Figures 2.11, 2.18, and 2.26), thus initial planning should perhaps focus on assessment of these clusters in specific focus areas.

Experience from the $CO_2$ flood area employed in this study indicates that, although several productive sandstone units may be present in a given area, most production comes from only a few of those units (i.e., the 14-1 and 16-2 sandstone units; Figure 2.18). Consequently, identifying the most productive sandstone units and assessing heterogeneity and oil-in-place appears to be an important element of long-term planning. Another factor for consideration when designing injection programs is stratigraphic isolation and hydraulic confinement of the target sandstone

bodies. Keeping injectate in zone may be a significant problem where numerous sandstone bodies are stacked and amalgamated into multi-storey successions, and this may limit the predictability of reservoir sweep, as well as predictability of the location and timing of $CO_2$ breakthrough.

Interwell heterogeneity is another key consideration in Citronelle Field. Although some sandstone units have great lateral continuity, each well may have a substantially different geophysical log signature, reflecting major variation of reservoir properties among wells (Figure 2.18). Original well spacing in the field was 40 acres, and downspacing when the TEOR injection wells were drilled indicates that the original well pattern undersampled reservoir heterogeneity. Indeed, correlations based on the original well pattern have limited value for predicting the thickness and continuity of productive sandstone units in infill wells.

The most important sources of this heterogeneity appear to be primary facies heterogeneity and diagenetic processes associated with pedogenesis. Primary facies heterogeneity is expressed as isolated channel fills in discontinuous sandstone units and nesting of multiple channel fills within the more widespread sandstone units (Figure 2.18). Fining upward and plugging of upper-tier channels with mud is a source of significant relief at the tops of the sandstone bodies that may exceed relief at the bases of the sandstone units. Because of this, high potential exists for oil and injected $CO_2$ to be stranded in the sandstone between mud-plugged channels.

It is important to keep in mind that two conditions must be met for pay development in the Donovan sandstone. The first is porosity enhancement by dissolution of feldspar during pedogenesis (Figures 2.35 and 2.36). The second is flushing of the dissolution products out of the sandstone. Where those products have accumulated, moreover, the sandstone is plugged with clay matrix and has the petrophysical properties of mudstone. As a result, it is important to keep in mind that the mapped distribution of pay (Figures 2.24 and 2.25) is as much the result of diagenesis as it is of sedimentation. Thus, a cautionary note is that the mapped patterns of reservoir sandstone thickness do not necessarily define the original channel networks and that maps made assuming traditional channel geometry may overestimate sandstone continuity. Accordingly, Citronelle Field is an attractive target for $CO_2$-EOR, and a careful program that identifies priority areas and includes a detailed assessment of reservoir architecture and internal heterogeneity is an important key to unlocking this potential.

## 2.8. Summary and Conclusions

Citronelle Field is the product of a complex geologic history that is tied to the evolution of the Mississippi Interior Salt Basin. The field is trapped structurally in a simple domal structure that formed above a broad salt pillow. The Donovan sandstone is of Early Cretaceous age and constitutes a heterogeneous assemblage of sandstone reservoirs in which conglomerate and mudstone units form baffles and barriers to flow and is ultimately sealed by impermeable evaporites of the Ferry Lake Anhydrite. The burial history of the field is consistent with the decelerating extensional subsidence associated with the development of the Gulf of Mexico passive margin. Oil has been trapped within Donovan sandstone for more than 60 million years and now sites in a thermal window that is conducive to hydrocarbon cracking and accumulation of pyrobitumen.

Donovan sandstone bodies are organized into two retrogradational sequence sets, and individual depositional sequences are about 30 feet thick and have a frequency of about 100,000 years, suggesting climatic control of sedimentation by Milankovitch orbital processes. Facies

analysis of the Donovan sandstone indicates that reservoir facies were deposited primarily in incised valleys containing dryland fluvial and associated estuarine deposits that accumulated along the landward fringe of an extensive platform lagoon. Widespread lagoonal and beach barrier deposits are preserved at the top of each sequence set and record two episodes of marine flooding in the Citronelle region.

Reservoir quality in Citronelle Field is influenced by a variety of depositional and diagenetic processes associated with soil formation and valley incision. Most sedimentation occurred as incised valleys were backfilled during rises of base level, and diagenesis was driven in large part by pedogenic processes. The Donovan sandstone was deposited primarily as a redbed succession, and intrusion of reducing fluids associated with oil emplacement resulted in the gray and yellowish-brown colors that are characteristic of the reservoir sandstone units.

Feldspar dissolution during pedogenesis was a fundamental control on reservoir quality in the Donovan sandstone and effectively differentiates pay zones from baffle and barrier strata. Accordingly, many pay zones are as much the product of diagenetic processes as they are of primary sedimentation. The interplay of depositional and diagenetic processes resulted in a multitude of reservoir sandstone bodies in which reservoir heterogeneity occurs at numerous scales. This heterogeneity is an important consideration for identifying and prioritizing $CO_2$ injection targets and understanding reservoir confinement and subsurface flow pathways.

**Acronyms and Abbreviations in Section 2**

| | |
|---|---|
| API | American Petroleum Institute, Washington, DC |
| EOR | enhanced oil recovery |
| GSA | Geological Survey of Alabama, Tuscaloosa, AL |
| OGB | State Oil and Gas Board of Alabama, Tuscaloosa, AL |
| QFL | quartz-feldspar-lithic (ternary diagram) |
| SECARB | Southeast Regional Carbon Sequestration Partnership |
| SECU | Southeast Citronelle Unit |
| SP | spontaneous potential (well log) |
| TEOR | Tertiary Oil Recovery Project (Gilchrist, 1981, 1982) |

**References in Section 2**

Catuneau, O., 2006, Principles of Sequence Stratigraphy: Amsterdam, Elsevier, Developments in Sedimentology, 386 p.

Claypool, G. E., and Mancini, E. A., 1989, Geochemical relationships of petroleum in Mesozoic reservoirs to carbonate source rocks of Jurassic Smackover Formation, southwestern Alabama: American Association of Petroleum Geologists Bulletin, v. 73, p. 904-924.

Cottingham, J. P., 1988, A kinematic model for interpreting the structural evolution of the Citronelle dome, Mobile County, Alabama: Tuscaloosa, Alabama, University of Alabama, unpublished Master's thesis, 94 p.

Currie, B. S., 2007, Sequence stratigraphy of nonmarine Jurassic-Cretaceous rocks, central Cordilleran foreland-basin system: GSA Bulletin, v. 109, p. 1206-1222.

Dickinson, W. R., Beard, S. L., Brakenridge, G. R., Erjavec, J. L., Ferguson, R. C., Inman, K. F., Knepp, R. A., Lindberg, F. A., and Ryberg, P. T., 1983, Provenance of North American Phanerozoic sandstones in relation to tectonic setting: GSA Bulletin, v. 94, p. 222-235.

Dickinson, W. R., and Suczek, C. A., 1979, Plate tectonics and sandstone compositions: AAPG Bulletin, v. 63, p. 2164-2182.

Dickson, J. A. D., 1965, A modified staining technique for carbonates in thin section: Nature, v. 205, p. 587.

Eaves, E., 1976, Citronelle Oil Field, Mobile County, Alabama: AAPG Memoir 24, p. 259-275.

Esposito, R. A., Pashin, J. C., and Walsh, P. M., 2008, Citronelle Dome: A giant opportunity for multi-zone carbon storage and enhanced oil recovery in the Mississippi Interior salt basin of Alabama: Environmental Geosciences, v. 15, p. 53-62.

Esposito, R. A., Pashin, J. C., Hills, D. J., and Walsh, P. M., 2010, Geologic assessment and injection design for a pilot $CO_2$-enhanced oil recovery and sequestration demonstration in a heterogeneous oil reservoir: Citronelle Field, Alabama: Environmental Earth Sciences, v. 60, p. 431-444, DOI: 10.1007/s12665-010-0495-5.

Folk, R. L., 1980, Petrology of Sedimentary Rocks: Austin, Hemphill Publishing Company, 184 p.

Fowler, M. L., Safley, L. E., Young, M. A., Stechmann, R. H., Blair, E. S., and Crumb, R. E., 1988, Reservoir Management Strategy for Citronelle Field, Mobile County, Alabama: U.S. Department of Energy, Office of Fossil Energy, NIPER/BDM-0353.

Fowler, M. L., Rawn-Schatzinger, S. P., Salamy, M. A., Young, S. R., Jackson, E. L., Cole, M. P., Madden, H., and Sarathi, P., 1995, Reservoir Characteristics, Petroleum Characteristics, and Research Needs for Fluvial/Alluvial Reservoirs in the United States: U.S. Department of Energy, Office of Fossil Energy, NIPER/BDM-0133, 387 p.

Gabriel, A., and Cox, E. P., 1929, A staining method for the quantitative determination of certain rock minerals: American Mineralogist, v. 37, p. 337-340.

Gilchrist, R. E., 1981, Miscibility Study (Repeat 50% P.V. Slug) in Cores, Citronelle Unit, Mobile County, Alabama: unpublished report prepared for Unit Manager of Citronelle Field.

Gilchrist, R. E., 1982, Evaluation of Produced Fluids from the Carbon Dioxide Pilot Area in the Citronelle Unit, Mobile County, Alabama: unpublished report prepared for Unit Manager of Citronelle Field.

Hall, A. M., and Fritz, W. J., 1984, Armored mud balls from Cabretta and Sapelo barrier islands, Georgia: Journal of Sedimentary Research, v. 54, p. 831-835.

Hasiotis, S. T., 2002, Continental trace fossils: SEPM Short Course Notes 51, 132 p.

Hughes, D. J., 1968, Salt tectonics as related to several Smackover fields along the northeast rim of the Gulf of Mexico basin: Gulf Coast Association of Geological Societies Transactions, v. 18, p. 320-330.

Hunt, J. M., 1979, Petroleum Geochemistry and Geology: Freeman, San Francisco, 617 p.

Hunter, R. E., 1977, Basic types of stratification in small eolian dunes: Sedimentology, v. 24, p. 361-387.

Klein, G. deV., 1977, Clastic Tidal Facies: Dordrecht, D. Reidel Publishing, 119 p.

Knight, J., 2005, Processes of soft-sediment clast formation in the intertidal zone: Sedimentary geology, v. 181, p. 207-214.

Kugler, R. L., and McHugh, A., 1990, Regional diagenetic variation in Norphlet sandstone: implications for reservoir quality and the origin of porosity: GCAGS Transactions, v. 40, p. 411-424.

Kugler, R. L., and Mink, R. M., 1999, Depositional and diagenetic history and petroleum geology of the Jurassic Norphlet Formation of the Alabama coastal waters area and adjacent federal waters area: Marine Georesources and Geotechnology, v. 17: p. 215-232.

Mancini, E. A., and Puckett, T. M., 2005, Jurassic and Cretaceous transgressive (T-R) cycles, northern Gulf of Mexico, USA: Stratigraphy, v. 2, p. 31-48.

Martino, R. L., 2004, Sequence stratigraphy of the Glenshaw Formation (middle-late Pennsylvanian) in the central Appalachian basin, in J. C. Pashin and R. A. Gastaldo, eds., Sequence stratigraphy, paleoclimate, and tectonics of coal-bearing strata, AAPG Studies in Geology 51, p. 1-28.

McCubbin, D. G., 1982, Barrier-island and strand-plain facies: AAPG Memoir 31, p. 247-279.

Miall, A. D., 1977, A review of the braided-river depositional environment: Earth Science Reviews, v. 13, p. 1-62.

Pashin, J. C., McIntyre, M. R., Grace, R. L. B., and Hills, D. J, 2008, Southeastern Regional Carbon Sequestration Partnership (SECARB) Phase III: Final Report prepared for Advanced Resources International, 57 p.

Petrusak, R., Riestenberg, D., Goad, P., Schepers, K., Pashin, J. C., Esposito, R. A., and Trautz, R., 2009, World class $CO_2$ sequestration potential in saline formations, oil and gas fields, coal and shale: The U.S. Southeast Regional Carbon Sequestration Partnership has it all: San Diego, SPE International Conference on $CO_2$ Capture, Storage and Utilization, paper SPE 126619, 18 p.

Petrusak, R., Cyphers, S., Baumgardner, S., Hills, D., Pashin, J. C., and Esposito, R. A., 2010, Saline reservoir storage in an active oil field: extracting maximum value form existing data for initial site characterization; Southeast Regional Carbon Sequestration Partnership (SECARB) Phase III "anthropogenic $CO_2$" test at Citronelle Field: New Orleans, SPE International Conference on $CO_2$ Capture, Storage, and Utilization, paper SPE 139700, 25 p.

Petty, A. J., 1999, Petroleum exploration and stratigraphy of the Lower Cretaceous James Limestone (Aptian) and Andrew Formation (Albian): Main Pass, Viosca Knoll, and Mobile Areas, northeastern Gulf of Mexico: Gulf Coast Association of Geological Societies Transactions, v. 49, p. 441-450.

Pittman, E. D., Larese, R. E., and Heald, M. T., 1992, Clay coats: occurrence and relevance to preservation of porosity in sandstones: SEPM Special Publication 47, p. 241-255.

Plint, A. G., McCarthy, P. J., and Faccini, U. F., 2001, Nonmarine sequence stratigraphy: updip expression of sequence boundaries and systems tracts in a high-resolution framework, Cenomanian Dunvegan Formation, Alberta Foreland Basin, Canada: AAPG Bulletin, v. 85, p. 1967-2001.

Retallack, G. J., 1990, Soils of the Past—An Introduction to Paleopedology: Boston, Unwin–Hyman, 520 p.

Salvador, A., 1987, Late Triassic-Jurassic paleogeography and origin of the Gulf of Mexico basin: American Association of Petroleum Geologists Bulletin, v. 71, p. 419-451.

Salvador, A., 1991, Triassic-Jurassic, *in* Salvador, A., ed., The Gulf of Mexico Basin: Boulder, Colorado, Geological Society of America, The Geology of North America, v. J, p. 131-180.

Seilacher, A., 2007, Trace Fossil Analysis: Berlin, Springer, 226 p.

Shepherd, R. G., 1987, Lateral accretion surfaces in ephemeral-stream point bars, Rio Puerco, New Mexico, in F. G. Ethridge, R. M. Flores, and M. Harvey (eds.), Recent developments in fluvial sedimentology: SEPM Special Publication 39, p. 93–98.

Terwindt, J. H. J., 1981, Origin and sequences of sedimentary structures in inshore mesotidal deposits of the North Sea, in Nio, S.-D., ed., Holocene sedimentation in the North Sea Basin: International Association of Sedimentologists Special Publication 5, p. 4-26.

Tissot, B. P., and Welte, D. H., 1984, Petroleum Formation and Occurrence (2nd Edition): Berlin, Springer-Verlag, 699 p.

Tooth, S., 2000, Process, form, and change in dryland rivers: a review of recent research: Earth Science Reviews, v. 51, p. 37-107.

Vail, P. R., 1987, Seismic stratigraphy interpretation procedure: American Association of Petroleum Geologists, Studies in Geology 27, v. 1, p. 1-10.

van Straaten, L. J. M. U., 1954, Sedimentology of Recent tidal flat deposits and the psammites du Condroz (Devonian): Geologie en Mijnbouw, v. 15, p. 1-11.

Wilgus, C. K., Hastings, B. S., Kendall, C. G. St. C., Posamentier, H. W., Ross, C. A., and Van Wagoner, J. C., eds., 1988, Sea-level changes: an integrated approach: SEPM Special Publication 42, 407 p.

Wilson, M. D., and Warne, J. R., 1964, Sand continuity study, Citronelle Oil Field, Mobile County, Alabama: unpublished report prepared for Unit Manager of Citronelle Field.

Withjack, M. O., Schlische, R. W., and Olsen, P. E., 1998, Diachronous rifting, drifting, and inversion on the passive margin of central eastern North America: an analog for other passive margins: AAPG Bulletin, v. 82, p. 817-835.

# 3. Minimum Miscibility Pressure of Citronelle Oil

César A. Turmero and Peter E. Clark*
University of Alabama, Tuscaloosa, Alabama

## 3.1. Rolling Ball Viscometer

A rolling ball viscometer was built by Peter Clark and Graduate Research Assistant César Turmero at the University of Alabama for the present project. A photograph of the viscometry laboratory and viscometer is shown in Figure 3.1. A diagram of the rolling ball instrument is shown in Figure 3.2. The viscometer detects changes in the viscosity of $CO_2$-oil mixtures by measurement of the speed with which a magnetized steel ball rolls down an inclined tube filled with oil under $CO_2$ pressure and temperature representative of the reservoir of interest. The passage of the ball is detected at three locations using Hall effect transducers.

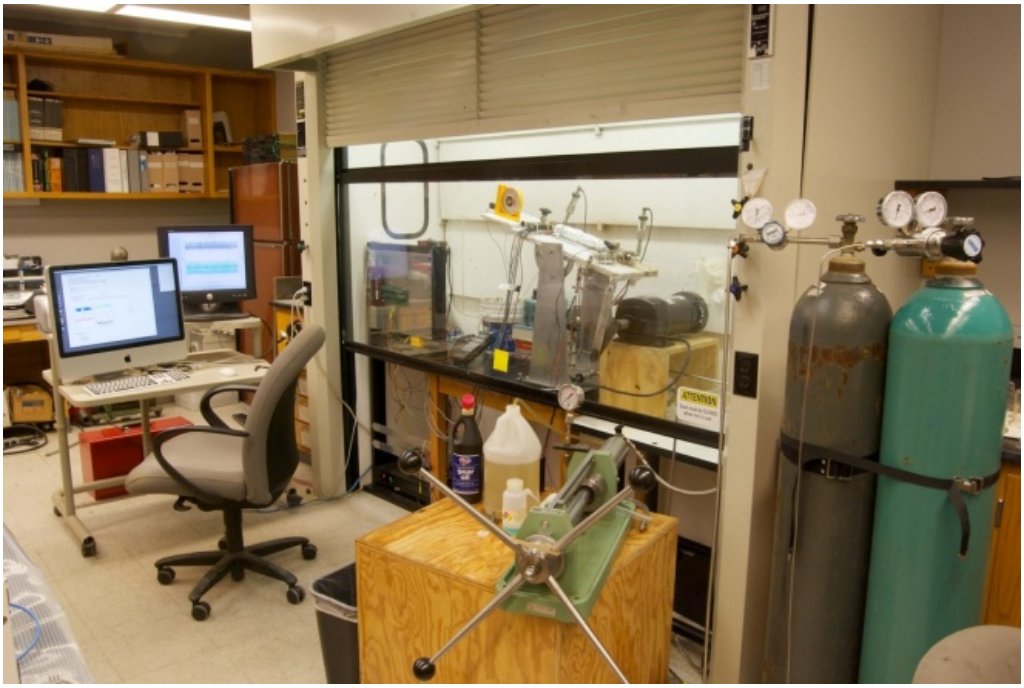

Figure 3.1. Viscometry laboratory at the University of Alabama. The rolling ball viscometer is in the fume hood near the center of the photograph.

Many improvements to the apparatus, signal processing techniques, and data analysis software were made over the life of the project, to minimize the error in identifying the time associated with the center of a pulse from the Hall effect transducers and improve the reproducibility of the measurements.

*Peter Clark is now in the Department of Chemical Engineering at Oklahoma State University in Stillwater, where he holds the Sampson and Ward Chair in Petroleum Engineering.

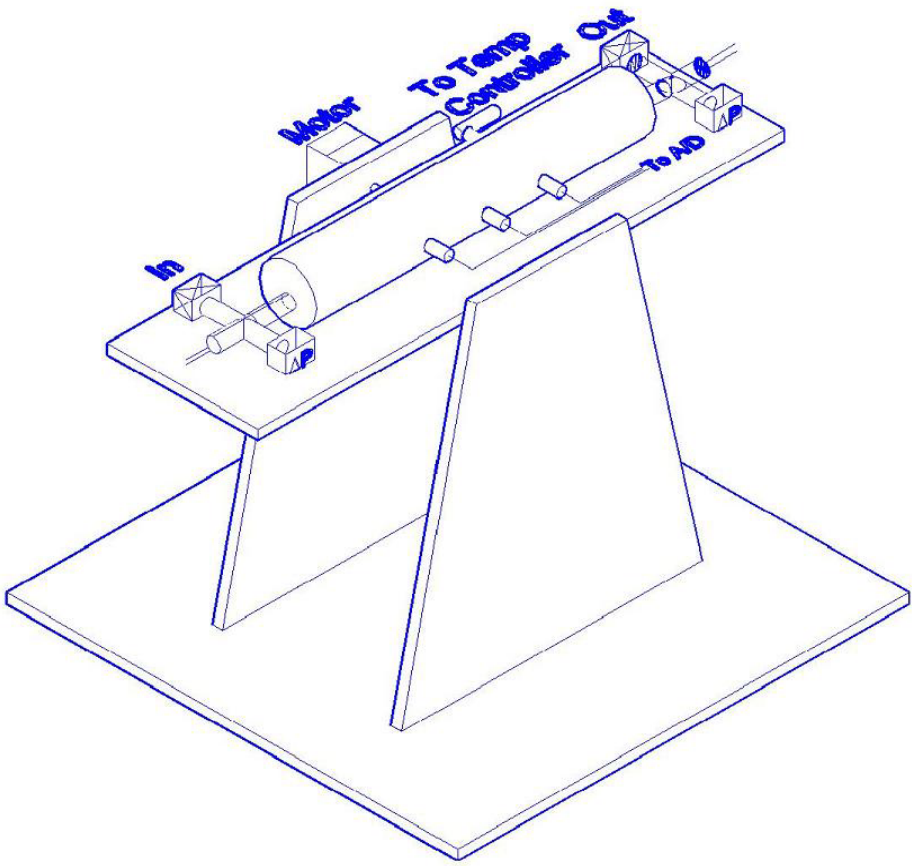


Figure 3.2. Rolling ball viscometer.

### 3.2. Minimum Miscibility Pressure

The minimum miscibility pressure for mixtures of Citronelle oil with carbon dioxide was determined using the rolling ball apparatus. Tests were run in triplicate and at three different angles. A representative set of measurements of transit times of the ball between transducers, at an angle of $30^{o}$, is shown in Figure 3.3. Each data point in the figure is an average of three runs. The measurements at other angles exhibit similar behavior. The minimum miscibility pressure was determined as 2340 ± 160 psi, well below the hydrostatic pressure in the Upper Donovan Sands at depths near 11,000 ft. A miscible $CO_2$ flood in the target reservoirs was therefore assured.

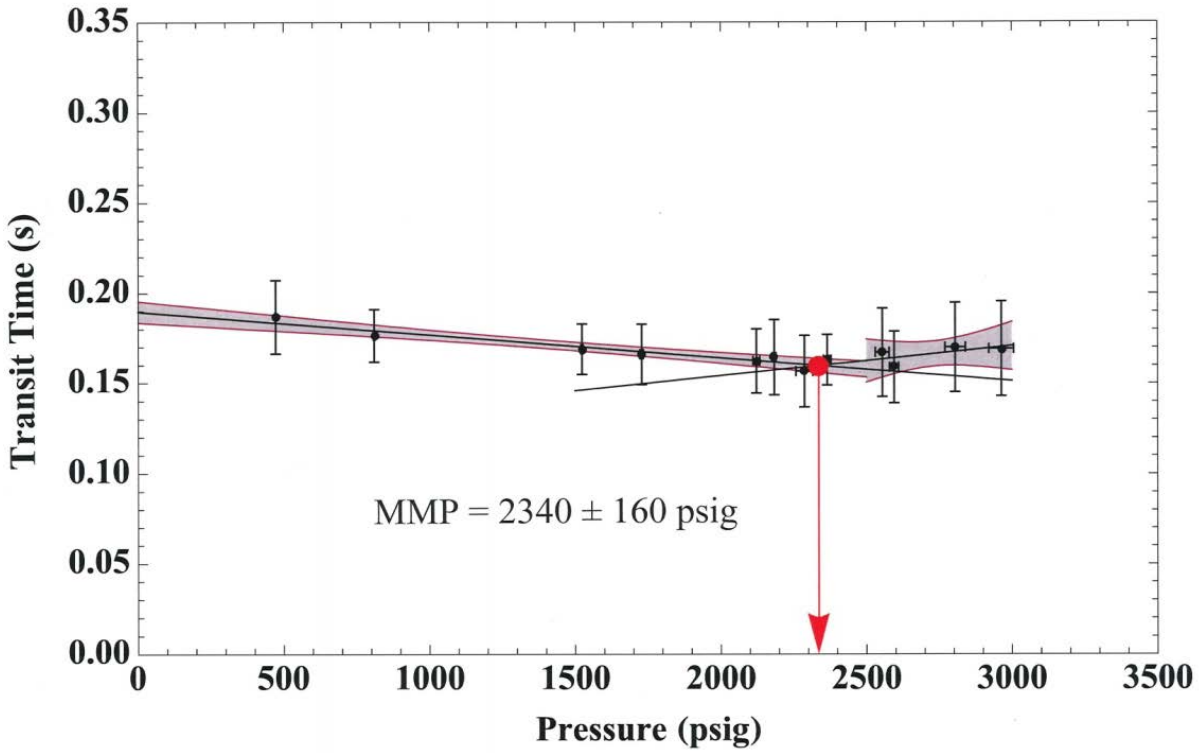


Figure 3.3. Measurements of transit time versus $CO_2$ pressure in the rolling ball viscometer, for a Citronelle oil sample at an angle of $30^o$. The minimum miscibility pressure (MMP) was established as 2340 ± 160 psig.

# 4. Well Tests and Reservoir Simulation

Eric S. Carlson
University of Alabama, Tuscaloosa, Alabama

## 4.1. Pre-Injection Interference Test

An interference test was run at the project well pattern between April 17, 2008 and May 23, 2008. Pressure gauges were placed in the shut-in Wells B-19-9 and B-19-7, while injection of water occurred in Well B-19-10 #2. The pressure measurements are shown in Figure 4.1. Well B-19-9 is about 822 ft southeast of the injector, while Well B-19-7 is about 1049 ft to the northwest. Injection commenced on May 3, 2008. The injection rate was variable, but stayed close to approximately 140 STB/day of water.

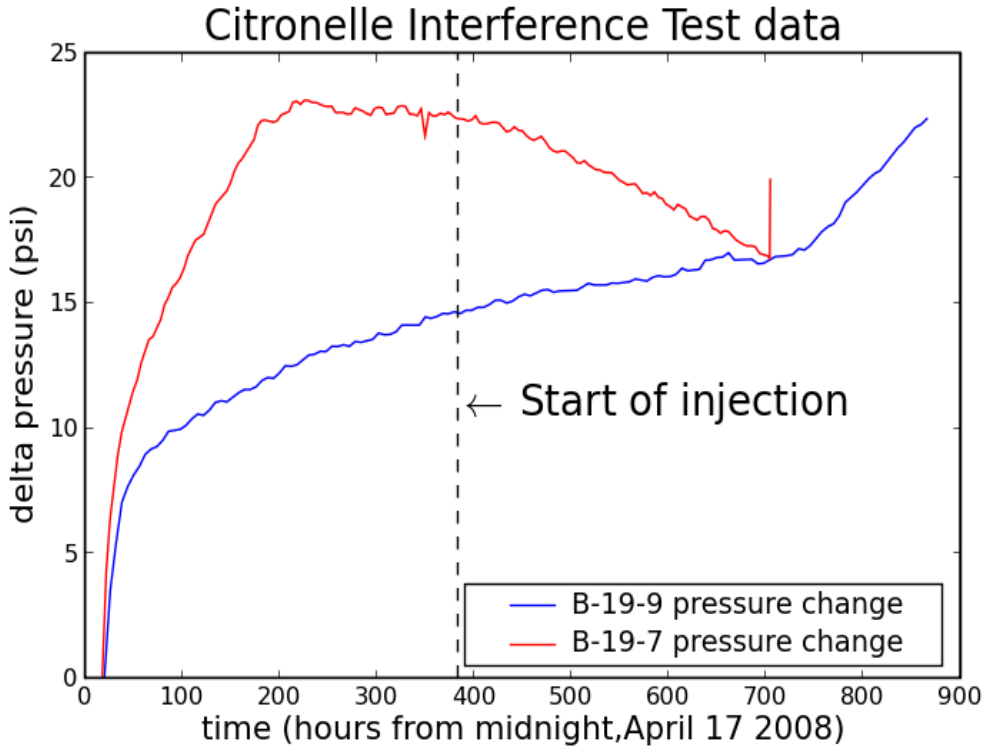


Figure 4.1. Pressure responses relative to an "initial" pressure.

An analysis of the interference test provided some clear evidence of communication between the injector and Well B-19-9. A fit of the data, shown in Figure 4.2, gave a total mobility, $\lambda_T = k\,(k_{ro}/\mu_o + k_{rw}/\mu_w)$, of approximately 0.61 mdarcy/cP, and an average production thickness, $h$, of approximately 20 ft, assuming a porosity of 15.5%, total compressibility of 10 x $10^{-6}$/psi, and average reservoir injection rate of 140 bbl/day.

Due to unforeseen difficulties at the injection well, leading to a delay in the start of water injection, the pressure gauge in Well B-19-7 was pulled before it could show a response. At this

point, no "cause-and-effect" could be performed with the data from this well because the observed pressure response could be explained by a multitude of causes. In fact, the gauge was pulled before the closer well, B-19-9, had responded to injection. If the reservoir properties determined for B-19-9 apply, then it would have taken another five days to get an initial response in Well B-19-7 to the injection started on May 3.

The good news from these initial assessments:

1. Confirmation that the injector is in communication with at least one nearby producer.
2. No obvious "short circuits" between the injector and either of the two production observation wells.
3. There was no evidence of significant layering (at least for the duration of the test).
4. The higher pressure of 5500 psi in Well B-19-9 versus the lower pressure of 5130 psi in Well B-19-7, suggests reasonable levels of communication between some of injectors and producers in the vicinity. B-19-7 is closer to low-pressure producers and B-19-9 is closer to high-pressure injectors.

The ambiguous:

1. Could not say for certain that Well B-19-7 was in communication with the injector.
2. The low permeability of 0.6 mdarcy/cP versus 20 to 40 mdarcy/cP from cores suggests either low-permeability baffles between the injector and producer and/or some mobile water and mobile oil (near the average water saturation where $\lambda_T$ is minimized).

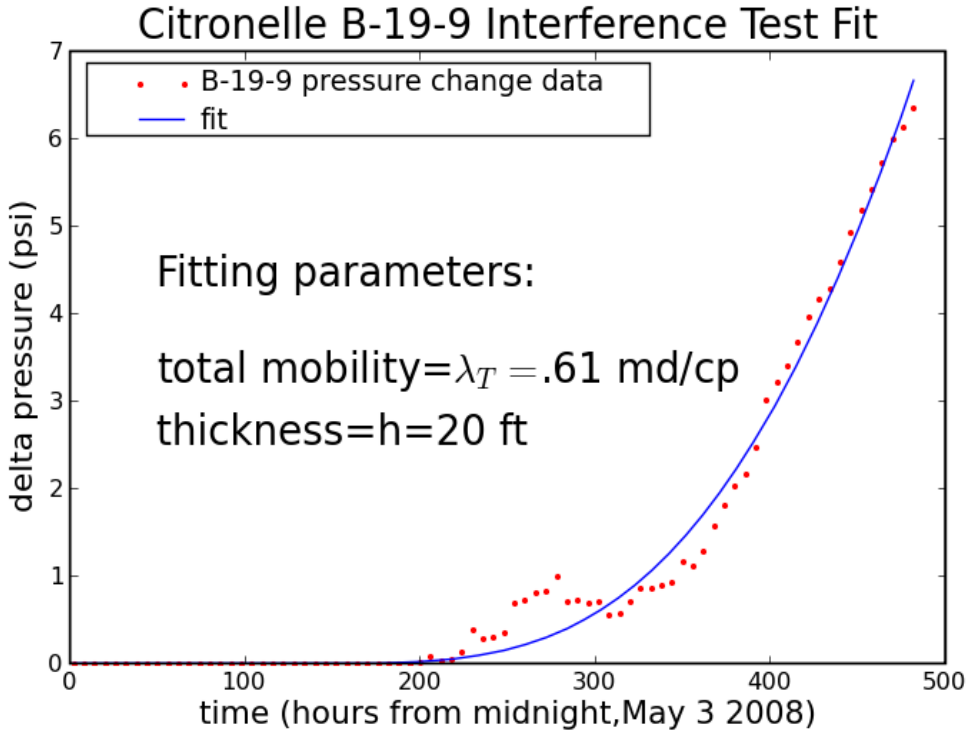


Figure 4.2. Curve fit results for Well B-19-9.

A fitting program performed a least-squares match of the pressure changes to the equation

$$p(r,t) - p_i = \frac{70.6qB\mu}{kh} \cdot E_1\left(\frac{\phi\mu c_t r^2}{.00105kt}\right) \tag{4.1}$$

where

$$E_1(x) = \int_x^\infty \frac{\exp(-u)}{u} du$$

$$\frac{k}{\mu} \approx \lambda_T = k(k_{ro}/\mu_o + k_{rw}/\mu_w)$$

for multiphase flow conditions (mdarcy/cP), and

| | |
|---|---|
| $h$ | average thickness, ft |
| $qB$ | the reservoir flow rate (assume 140 bbl/day) |
| $\phi$ | average porosity (assume 0.155) |
| $c_t$ | average total compressibility (assumed 10 x $10^{-6}$/psi) |
| $r$ | distance from the injector, = 822 ft for Well B-19-9 |
| $t$ | time, hours. |

The pressures were changing due to injection and production at other wells in the vicinity of the test. This change had to be filtered out of the results, so the prevailing pressure at the observation well when the initial response to injection at Well B-19-10 #2 occurred was subtracted from the actual pressure. Although superposition theory could have been applied, no attempt was made to do this because the rate data at the injection well were not detailed, nor did we have any information regarding what was inducing the background pressure changes.

Despite these assumptions, a few considerations make the analysis credible. First, the time at which the initial response to injection occurs at the observation well depends primarily on the total mobility. The change of the initial response by as much as ± 2 days has little impact on the calculated mobility. Second, the amplitude of the pressure change is most influenced by $\lambda_T h/qB$. The rate appears to be good to roughly ± 20%, so the fact that the calculated thickness comes close to those estimated from geological studies means that the calculated $\lambda_T$ is probably okay. Finally, our simulation studies assumed a single-phase permeability of around 10 mdarcy, but relative permeability effects severely impacted injection rates so that the calculated rates were comparable to the rates observed during the interference test and the effective mobility was comparable to that derived from the interference test results.

## 4.2. Pre-Injection Simulation Study

### *4.2.1. Model*

Simulations of $CO_2$ injection into the inverted five-spot well pattern chosen for the test were performed using the SENSOR (System for Efficient Numerical Simulation of Oil Recovery) reservoir simulator from Coats Engineering, Inc. (http://www.coatsengineering.com/). The construction of the model, assumptions, and properties of the reservoir used to describe the test well pattern were as follows.

Quarter inverted five-spot
Area = 800 ft by 800 ft
Average thickness = 20 ft
10 layers, using a 10 by 10 by 10 grid (cell block size of 2 x 80 x 80 ft)
Injector and producer in opposite corners
No impediment to vertical flow
Different layers have different permeabilities, but permeability is uniform within each layer
Porosity = 0.154
Initial average water saturation = 0.6
Irreducible water saturation = 0.21
"Irreducible" oil saturation = 0.25
Capillary pressure neglected
Reservoir temperature = 210 $^{o}$F (results are not very sensitive to temperature)
Viscosity of water at 5000 psi = 0.4 cP
Injection pressure of 7500 psia and producing pressure of 3000 psia
SENSOR default productivity indices for each well
No allowance for $CO_2$ dissolution in water
No interaction of $CO_2$ with the formation

### *4.2.2. Summary of Cases*

Five cases were constructed having different distributions of permeability over the ten layers, as specified in Table 4.1. Case PW most closely approximates the distribution of permeabilities in the two sands that were the targets of the test injection, according to data in a report on previous reservoir engineering in the Citronelle Field. However, Case PW suffers from its inability to account for heterogeneity and lack of continuity within each layer. Of the cases considered, Case LN was best at reproducing the effective permeability of the formation in an interference test using downhole pressure sensors, run by Denbury Resources between the injector and one of the producers in the five spot, described in Section 4.1. However, even with the layering and adjustment of the permeabilities to account for heterogeneity, the simulation is a highly idealized description of the reservoir.

Six different $CO_2$ and water injection scenarios, described in Table 4.2, were run for each of the permeability distribution cases. The calculated injection and production histories for the permeability distribution of Case LN and all six injection scenarios are shown in Figure 4.3.

Table 4.1. Assumed Distributions of Permeability of the Ten Layers.

| Case Name | Permeability Distribution, top to bottom (millidarcy) |
|---|---|
| Homogeneous | 7, all layers the same |
| H2L | 19 10 9 8 7 6 5 3 2 1 |
| L2H | 1 2 3 5 6 7 8 9 10 19 |
| LN | 6 7 5 7 19 7 10 8 7 9 |
| PW | 161 48 0.7 1.1 8.6 1.9 1.5 2.0 4.6 2.9 |

Several features of the injection and production histories shown in Figure 4.3 are worth noting: (1) cumulative oil production steadily increases with increasing total amount of $CO_2$ injected (figure at top left), (2) a significant increase in oil production rate occurs approximately 400 days after the start of $CO_2$ injection, accompanied by $CO_2$ breakthrough (figures at top right and third from the top on the right), and (3) there is not a great difference in the cumulative oil produced by a single injection of 15,000 tons of $CO_2$, compared with the oil produced by two $CO_2$ slugs of 7500 tons each separated by water injection (10% of pore volume).

Table 4.2. WAG Scenarios Run for each of the Permeability Distributions.

| Short Name | Description |
|---|---|
| waterflood | Continuous water injection only |
| 2x7500 | 7500 tons $CO_2$, then 10% of pore volume water, then 7500 tons $CO_2$, then continuous water |
| 1x15000 | 15000 tons $CO_2$, then continuous water |
| 1x22500 | 22500 tons $CO_2$, then continuous water |
| 1x30000 | 30000 tons $CO_2$, then continuous water |
| $CO_2$ only | Continuous $CO_2$ injection only, up to a maximum of 2 billion scf |

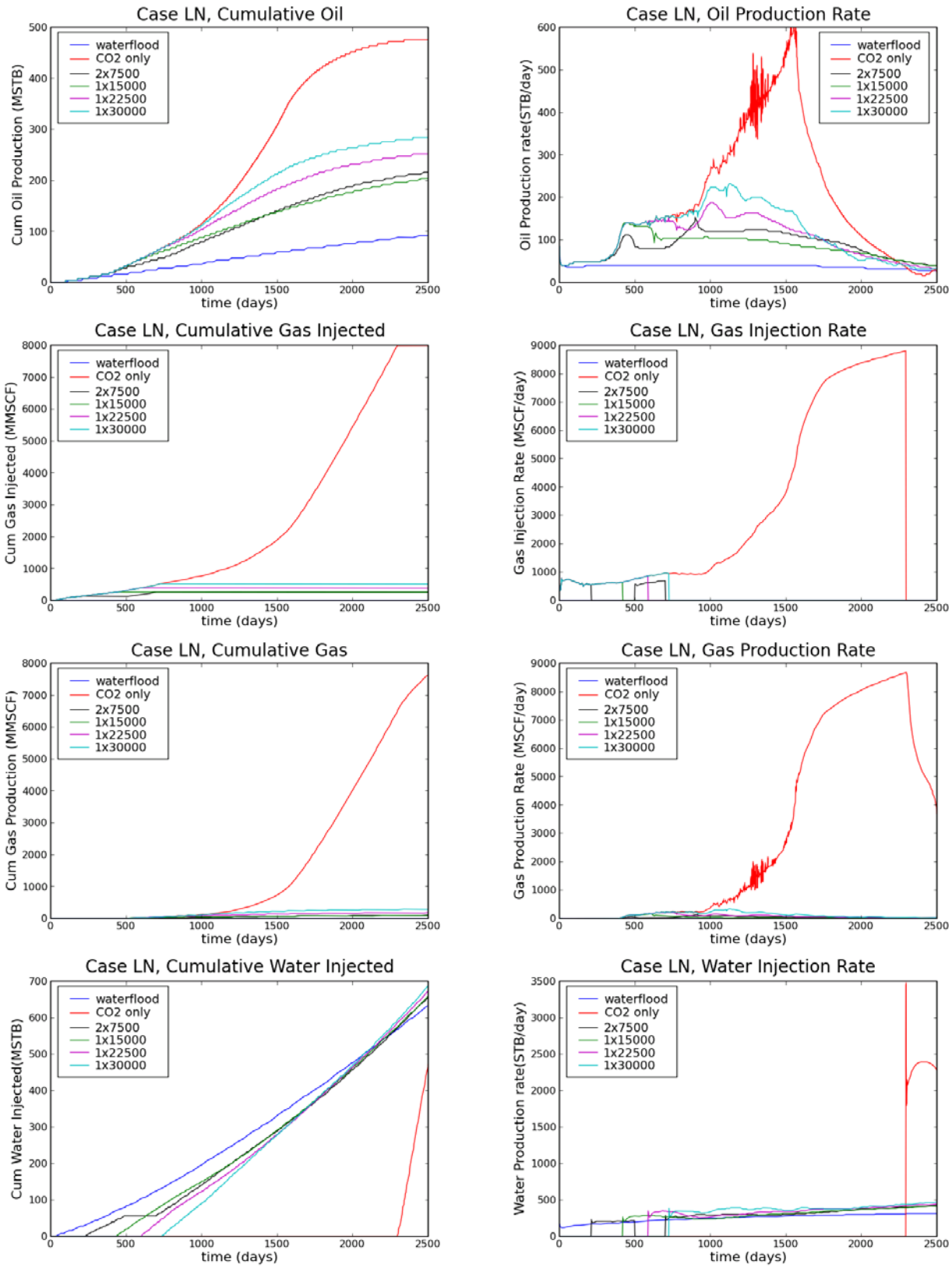


Figure 4.3. Injection and production histories calculated using SENSOR for the permeability distribution of Case LN (Table 4.1) and six different $CO_2$ and water injection scenarios (Table 4.2).

### *4.2.3. Expanded Analysis of Case LN*

This section expands on the results for Case LN presented in the previous section, examining oil recovery versus $CO_2$ slug size. Based on the fits of the present section, a useful comparative analysis of project economics can be performed, and it was shown that it is possible to find the optimum $CO_2$ slug size for various pricing scenarios.

The results of Case LN were analyzed more closely to provide comparative results for different slug sizes. Prior to this analysis, three more slug-size simulation cases were performed, including runs for 7500 tons, 60,000 tons, and 90,000 tons of $CO_2$. Under the assumptions made here about the system, it turned out that the cumulative oil versus time for the water-injection-only case could be fit with a straight line [= (*t* days)(37.8 STB/day)]. Using this as a baseline, it was assumed that the production above this value was the incremental oil due to $CO_2$ injection. This cumulative incremental production, shown in Figure 4.4, was fit as a function of time and $CO_2$ slug size using the following (Gnu Octave) function:

```
function y = thefit(slug,t)
%slug size in tons, t in days
u = log10(slug);
tau = -81.928*u^2+1020.545*u-1795.586;
A = 48.97*(1-exp(-2.13E-05*slug))*4 %MSTB;
y=A*(1+tanh(0.00211*(t-tau)));
end
```

Although the fit to the curves in Figure 4.4 is not perfect, the correlation provides a simple and convenient continuous representation of incremental oil recovery versus $CO_2$ slug size and time that can be used for comparative analysis. Total cumulative oil recovery, including oil that would have been produced by waterflood, without injection of $CO_2$, is shown in Figure 4.5.

Other functions useful for the economic analysis were also generated. Cumulative incremental oil recovery at 1800 days from the start of $CO_2$ injection is shown as a function of the total amount of $CO_2$ injected in Figure 4.6. The cumulative amount of $CO_2$ injected is shown as a function of time in Figure 4.7. The smoothed rate of $CO_2$ injection versus time, obtained by differentiating the function describing the cumulative $CO_2$, is shown in Figure 4.8.

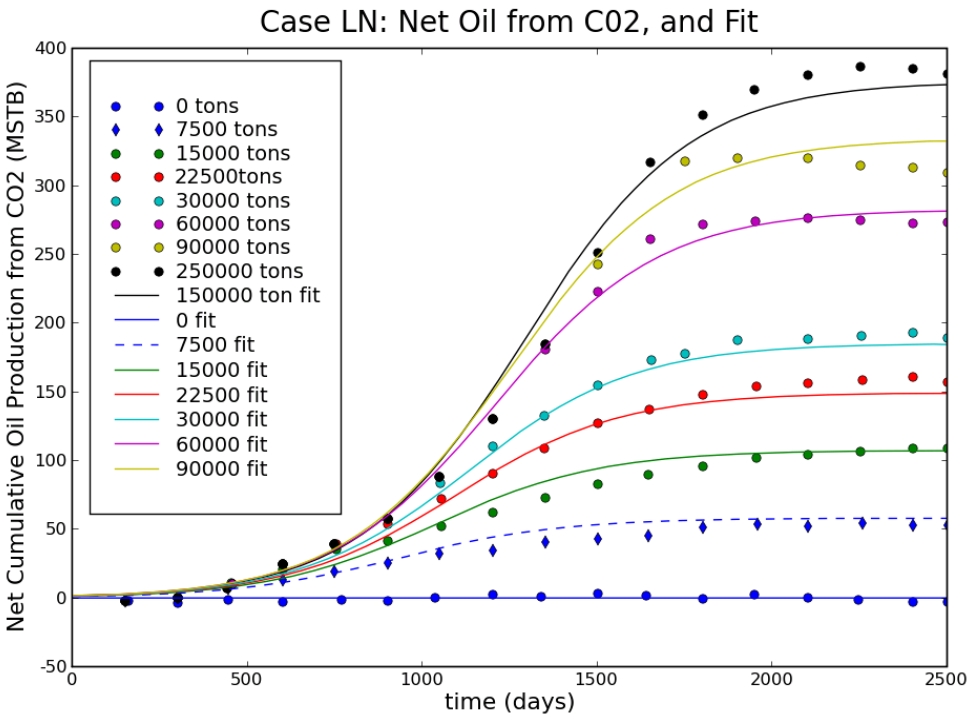


Figure 4.4. Simulation results for incremental oil production due to $CO_2$ injection, and the approximate fit to each data set using the function given in the text.

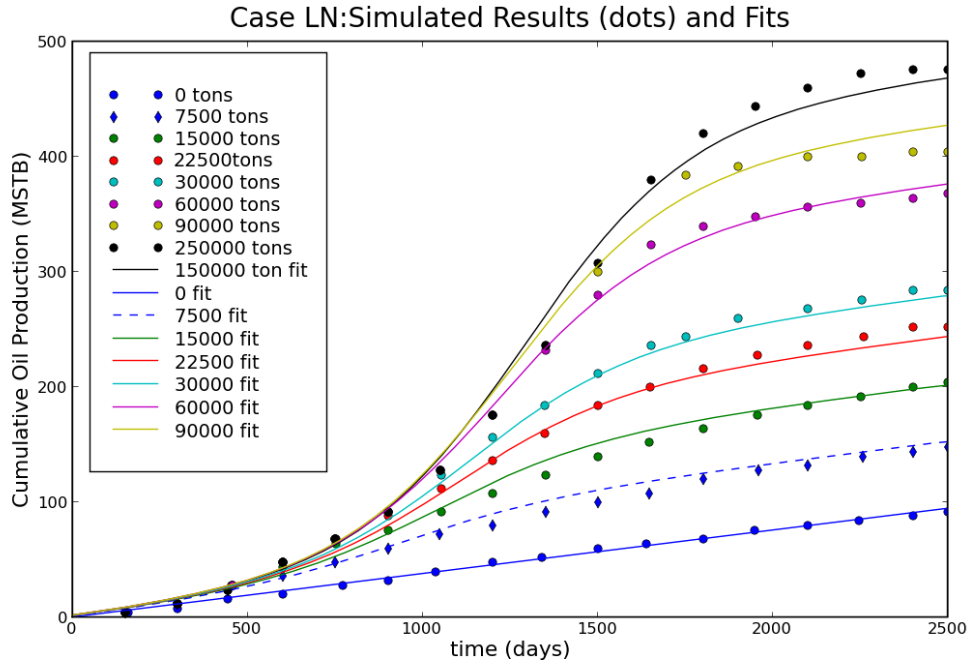


Figure 4.5. Total produced oil and corresponding fits, obtained by adding the production by waterflood only [(*t* days)(37.8 STB/day)] to the curves of Figure 4.4.

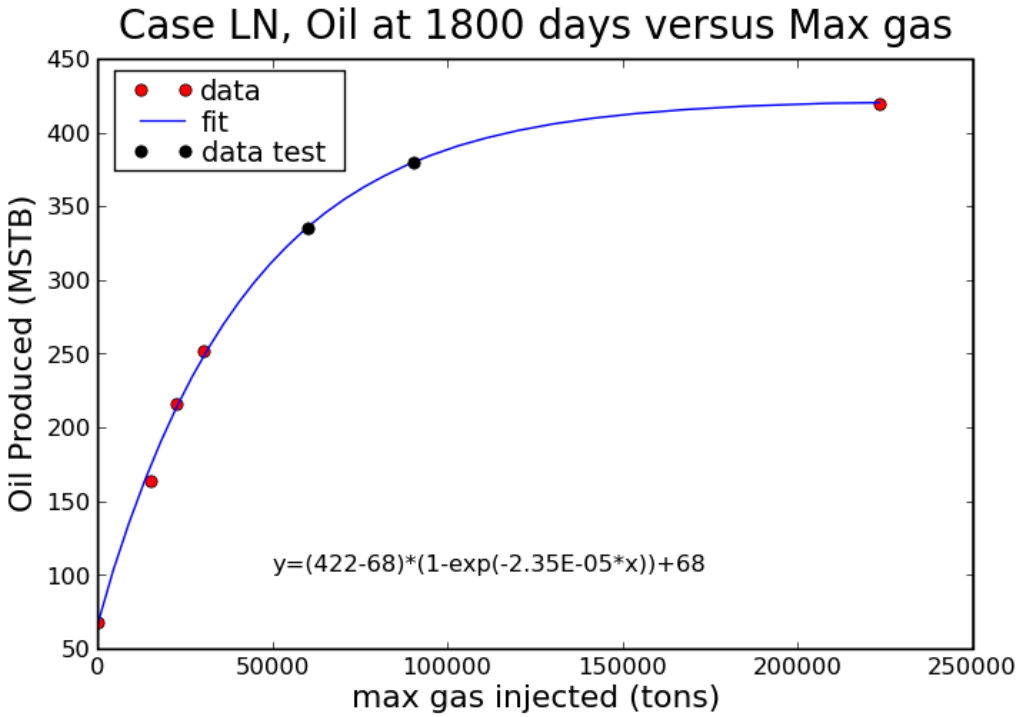


Figure 4.6. Simulation results for cumulative oil recovery at 1800 days from the start of injection versus the $CO_2$ slug size. The curve was fit using the red dots. The black dots are the results of simulation runs made to test the accuracy of the correlation.

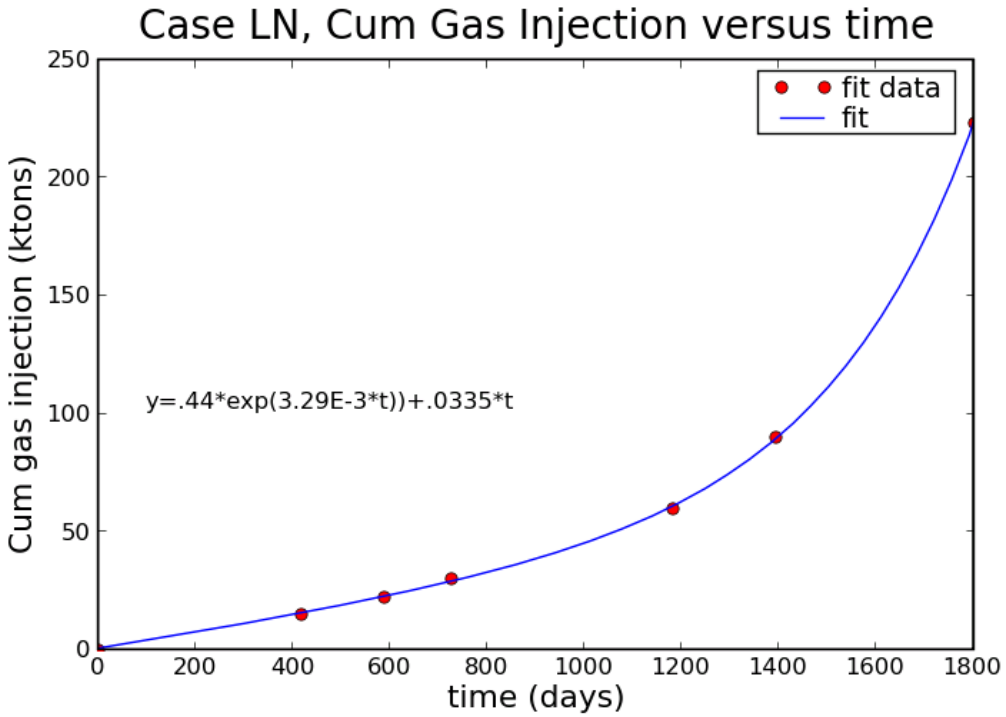


Figure 4.7. Cumulative $CO_2$ injection versus time. The red dots here indicate the endpoints for 15,000, 22,500, 30,000, 60,000, and 90,000 tons of $CO_2$, from left to right.

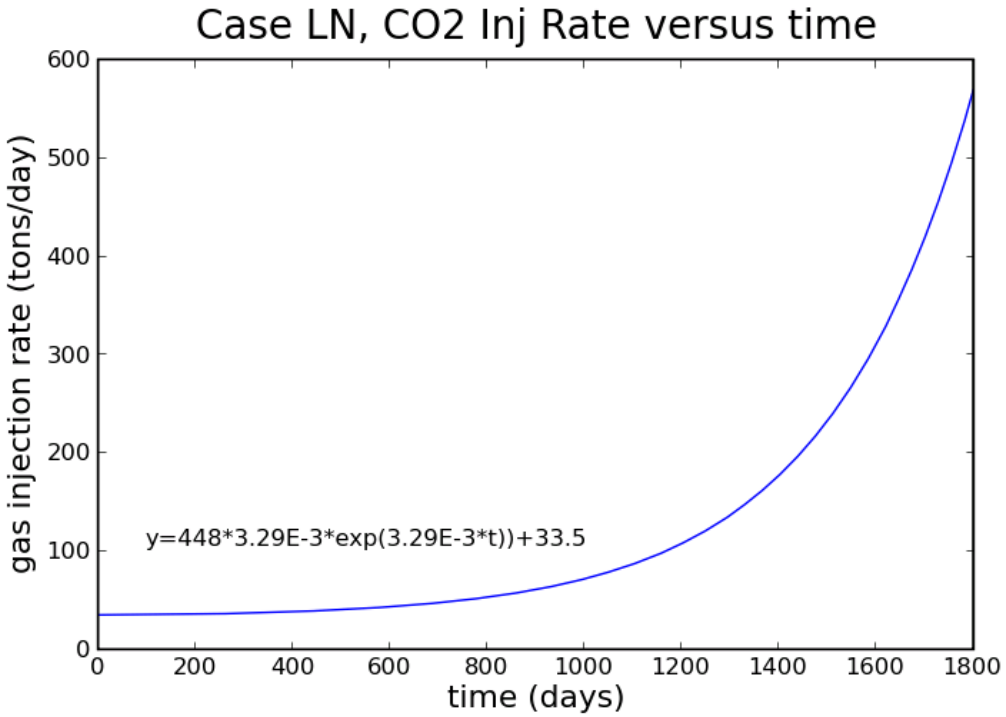


Figure 4.8. Smoothed $CO_2$ injection rate obtained by taking the derivative of the cumulative $CO_2$ injection versus time (Figure 4.7).

## 4.3. Post-Injection Pressure Buildup Test

This section provides a detailed analysis of the data from a pressure-transient test run on the injection well (B-19-10 #2) after $CO_2$ injection ceased. The operator report, the test data and the analysis of the data are presented in Figures 4.9 to 4.15. Table 4.3 contains a brief description and summary of the significance of each figure. Analysis of the test data strongly suggests that:

The well has a substantial hydraulic fracture, with a total length of perhaps 600-1000 ft.

The permeability of the zone tested is on the order of 0.4 millidarcy.

One of the zones, most likely the upper (14-1) sand, is completely plugged off.

The fracture length and permeability magnitudes are approximate, but the results are probably conclusive about the presence of a large, high-conductivity fracture in a very tight zone. That the upper zone is plugged is an inference from previous flow profile measurements showing 60% to 80% of injected fluid going into the upper zone during and prior to $CO_2$ injection, combined with the reduction in the sustained injection rate (from 170 bbl/day to 70 bbl/day), and the lack of any evidence of layering from the pressure test.

Table 4.3. Summary of Well Test Figures.

| Figure Number | Type | Significance |
|---|---|---|
| Figure 4.9 Upper middle | Pressure versus time | Bottom-hole pressure during the test, shows the various stages |
| Figure 4.9 Lower left | Pressure versus time | Pressure before first shut-in period -- note the nearly constant pressure for 30 hours prior to shut-in |
| Figure 4.9 Lower right | Pressure versus time | Pressure after the end of the first shut-in period, before last shut-in -- note the lack of constant pressure here |
| Figure 4.10 | log(dp) versus log(dt) | This log-log plot of the early shut-in period has a slope of ½ for most of the plot, a strong indication of a fractured well |
| Figure 4.11 | dp versus sqrt(dt) | Straight-line behavior on this plot of the early shut-in period suggests a fracture. The slope can be used to estimate fracture length |
| Figure 4.12 | dp versus log(dt) | The slope at the later times of the early shut-in period MIGHT be able to give permeability |
| Figure 4.13 | log(dp) versus log(dt) | This log-log plot of the last shut-in period has a slope of nearly ½ for most of the plot, strong corroboration for a fractured well |
| Figure 4.14 | dp versus sqrt(dt) | Straight-line behavior on this plot of the second shut-in period corroborates the presence of a fracture. The slope can be used to estimate fracture length, but rate is uncertain |
| Figure 4.15 | Test Summary | Chronology of the test, with rate snapshots |

Figure 4.15 summarizes the procedures used for the various stages of the test, and provides rates on various days. The plan was to shut the well in, run the pressure gauge to the bottom of the hole, run at constant rate for 3 days, shut in for 7 days, run at constant rate for another three days, then shut in and pull the gauge. The test log (Figure 4.15) and pressure versus time data (Figure 4.9) indicate some injection difficulties early in the test. Figure 4.9 clearly shows a 30+-hour period of nearly constant pressure injection. The extended constant pressure period was long enough, immediately prior to the shut-in period, that it makes the shut-in-time analysis identical to a constant-rate injection test. That is, we can analyze the response to the change of rate from 73 bbl/day to 0 bbl/day without considering previous information.

Figures 4.10 through 4.12 show standard plots for the shut-in period analysis. The data for dp was calculated by subtracting pressure from the pressure at shut-in time. The values for dt were calculated by subtracting initial shut-in time from the time. The extended period where $\log_{10}(dp)$ versus $\log_{10}(dt)$ is a straight line with a slope of ½ indicates a fractured well. Under these circumstances, a plot of dp versus sqrt(dt) should have a straight line at early times, the slope of which can help estimate fracture length. Figure 4.11 presents this plot, and shows straight line behavior until the pressure change reaches about 250 psi. Under ideal circumstances, it should be possible to use radial flow theory, once the pressure change is roughly twice the pressure change at the deviation time, which means we need dp greater than 500 psi for the radial flow analysis. Figure 4.12 is a dp versus $\log_{10}(dt)$ plot, and a straight-line fit to the late data is shown.

After the first shut-in period, the rate is restarted and injection occurs for another three days. The pressure versus time data of Figure 4.9 shows that well pressure was not constant. Nevertheless, an analysis using the same methodology as was used for the first shut-in time was performed, as illustrated in Figures 4.13 and 4.14. These figures show results that are not as convincing as those from the previous analysis, but they are still quite consistent with the first data set. The lack of detailed rate versus time data makes a more rigorous multirate analysis of the late pressure data impossible, so Figures 4.13 and 4.14 are probably as good as possible for this portion of the test.

The assumptions used for the analysis are summarized in Table 4.4, and the results are given in Table 4.5. The permeability estimate agrees surprisingly well with those from the interference test run in 2009. In that case, average mobility for the combination of Sands 14-1 and 16-2 was estimated to be 0.6 mdarcy/cP, compared to about 0.4 mdarcy from this test. The first test had a substantial oil phase to consider (having higher viscosity) and relative permeability effects, so the results are very close.

Finally, the fracture lengths calculated from the two separate stages of the test agree closely (within the accuracy of the rates), and overall seem very reasonable. The presence of a long fracture at the well could explain the unusual breakthrough behavior of the injected $CO_2$. This would be particularly true if the fracture were oriented SW-NE, with the fracture slightly longer toward the southwest than to the northeast. Future simulation runs could provide some insight into this.

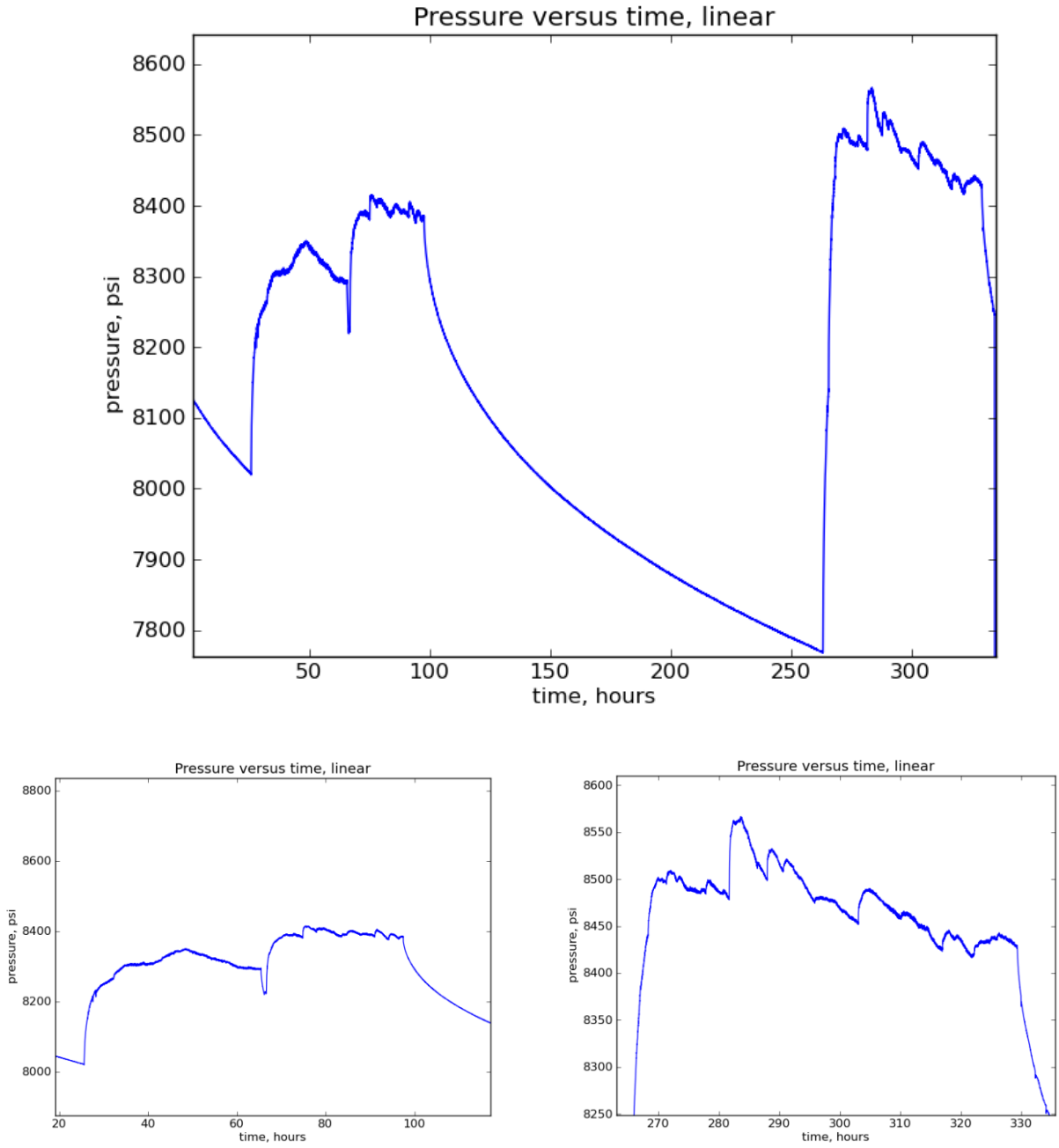


Figure 4.9. Pressure versus time behavior for the pressure-transient test run at Well B-19-10 #2. The top figure shows the entire data set. The figure at lower left highlights the nearly constant pressure injection prior to the first shut-in period and the figure at lower right shows the not-so-constant pressure prior to the second shut-in period.

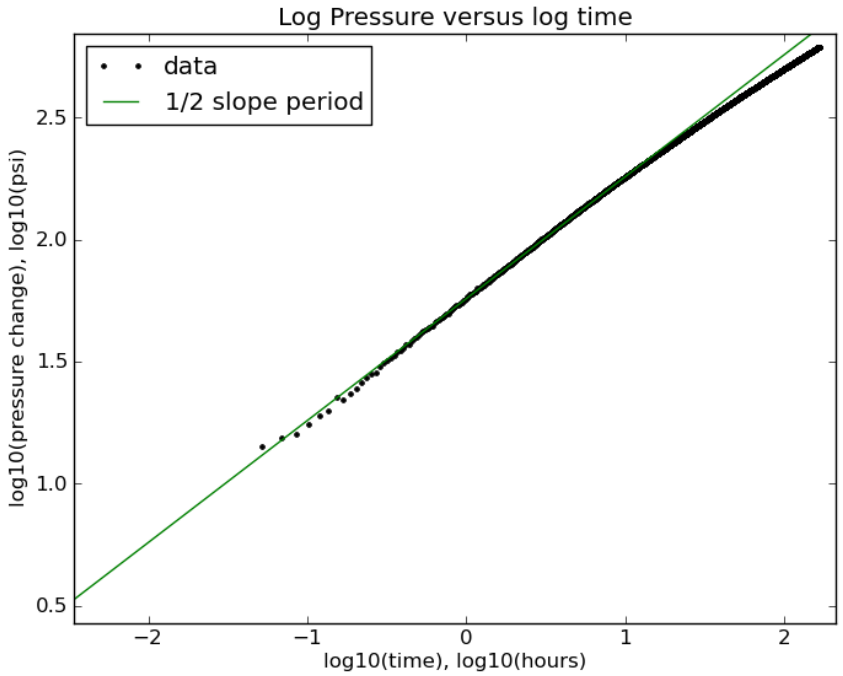


Figure 4.10. Plot of log pressure change versus log shut-in time behavior for the test run at Well B-19-10 #2, during the first shut-in period. Note the extended period when the slope is ½.

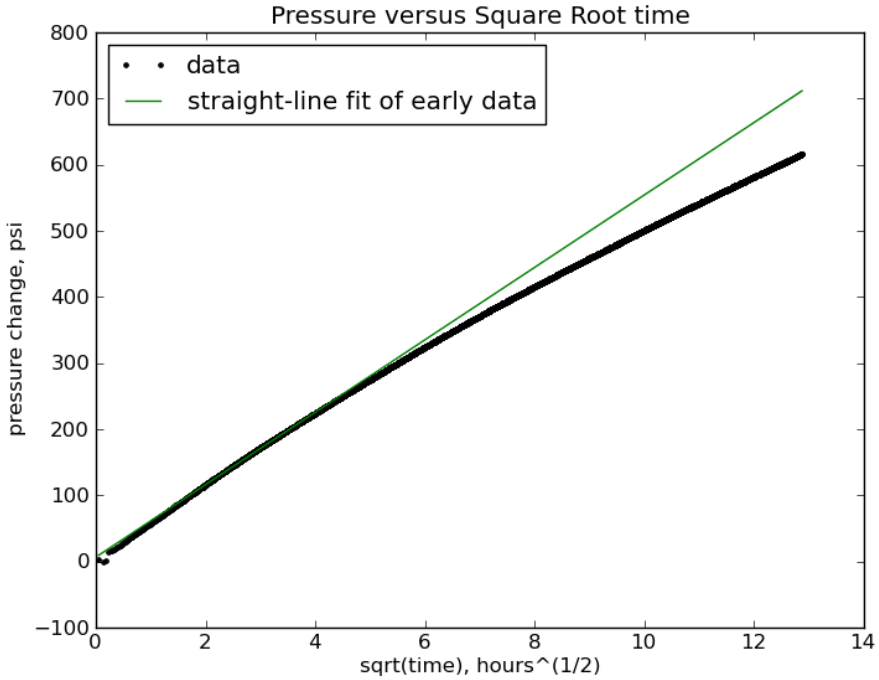


Figure 4.11. Plot of pressure change versus the square root of shut-in time behavior for the test run at Well B-19-10 #2, during the first shut-in period. The slope of the line fit to the data at early times is 55 psi/hr$^{½}$.

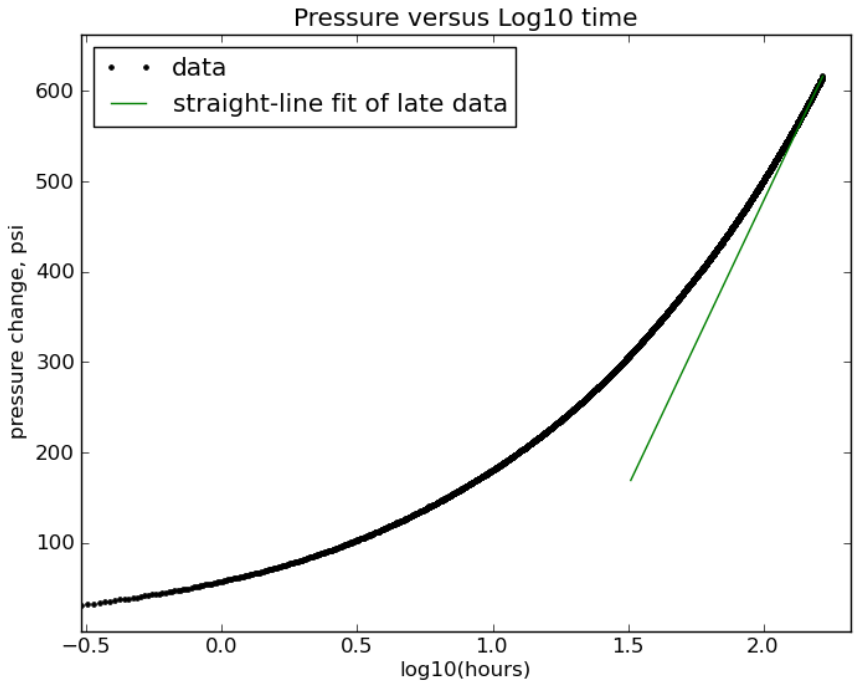


Figure 4.12. Plot of pressure change versus log shut-in time behavior for the test run at Well B-19-10 #2, during the first shut-in period. The slope of the line fit to the data at long times is 631 psi/cycle.

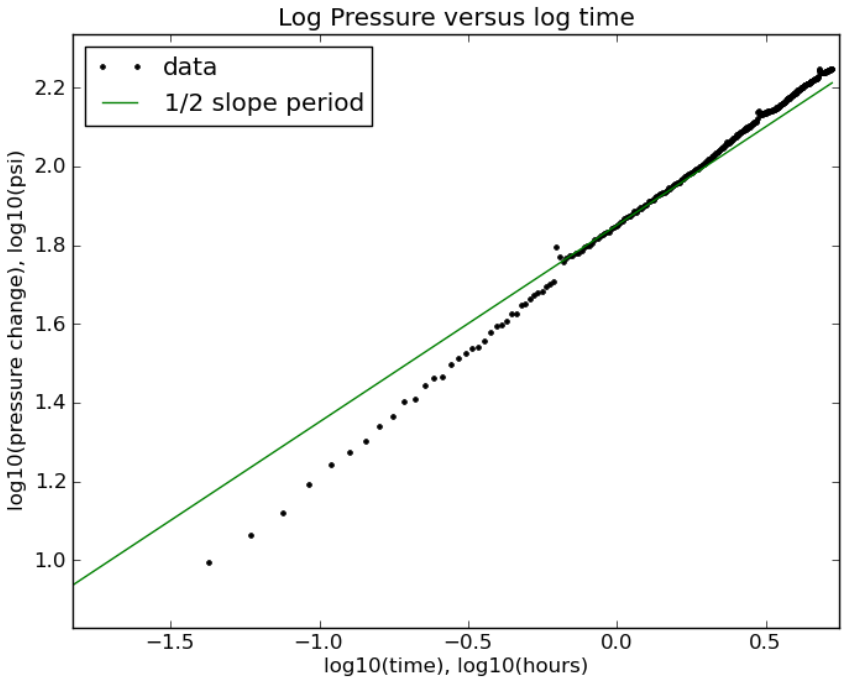


Figure 4.13. Plot of log pressure change versus log shut-in time behavior for the test run at Well B-19-10 #2, during the second shut-in period. The line having slope of ½ is still a good approximation, despite the non-constant pressure prior to shut-in, but not as good as during the first shut-in period.

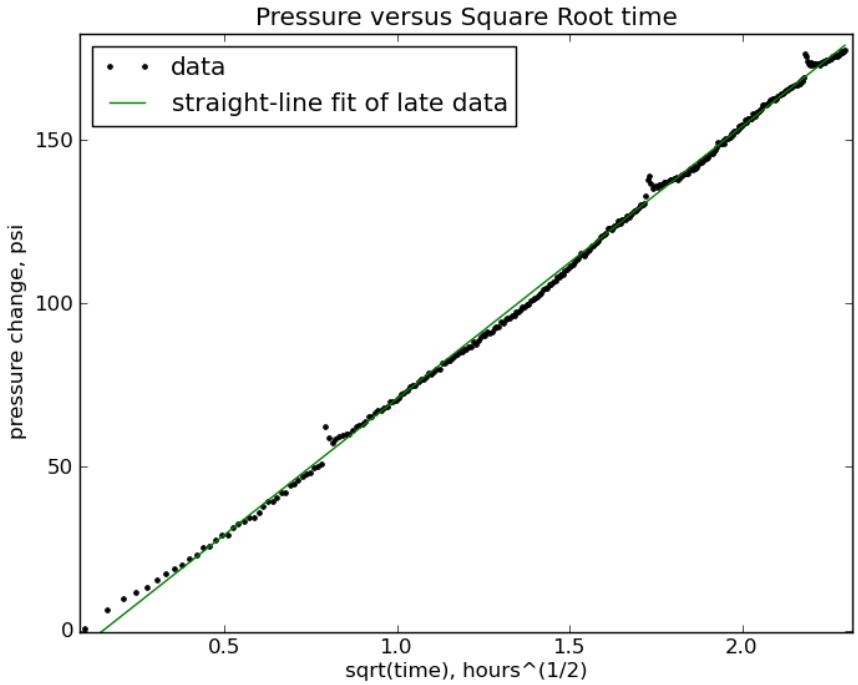


Figure 4.14. Plot of pressure change versus square root of shut-in time behavior for the test run at Well B-19-10 #2, during the second shut-in period. The slope of the line fit to the data is 83 psi/hr$^{½}$.

| Table 4.4. Assumed or Inferred Parameter Estimates. | | |
|---|---|---|
| **Parameter** | **Value** | **Source** |
| $q_1$ = average rate prior to first shut-in period | 73 bbl/day | Figure 4.15, discussion of rates prior to first shut-in period |
| mu = viscosity | 0.4 cP | Brine viscosity at 240 $^{o}$F, fresh water would be 0.3 |
| $c_t$ = total compressibility | 5.0 x $10^{-6}$/psi | Guess at sum of water compressibility and formation compressibility |
| phi = porosity | 0.15 | Estimated, could be as low as 0.08 for Sand 16-2 |
| h = thickness | 20 ft | Estimated from geological studies for Sand 16-2 |
| $q_2$ = average rate prior to second shut-in period | Low: 74 bbl/day<br>High: 117 bbl/day | Figure 4.15, discussion of rates near the end of the test |

| Table 4.5. Calculated from the Data. | | |
|---|---|---|
| **Parameter** | **Value** | **Source/Formula** |
| $m\_sqrt_1$ = dp versus sqrt(dt) slope | 54.8 psi/hr$^{½}$ | Figure 4.11, at early times, see line on graph |
| m_log = dp vs. log t slope | 630.5 psi | Figure 4.12, very late times, see line on graph |
| k = permeability | 0.4 mdarcy | $162.6*q_1*mu/m\_log10/h$ |
| $L_{f1}$ = fracture length | 645 ft | $2*4.064*(q_1/h)*sqrt(mu/(k*phi*c_t))/m\_sqrt_1$ |
| $m\_sqrt_2$ = dp versus sqrt(dt) slope | 83 psi/hr$^{½}$ | Figure 4.14, see line on graph |
| $L_{f2}$ = fracture length from second shut-in period | 430 ft (q = 74)<br>680 ft (q = 117) | $2*4.064*(q_2/h)*sqrt(mu/(k*phi*c_t))/m\_sqrt_2$<br>(low rate 74 bbl/day, high rate 117 bbl/day) |

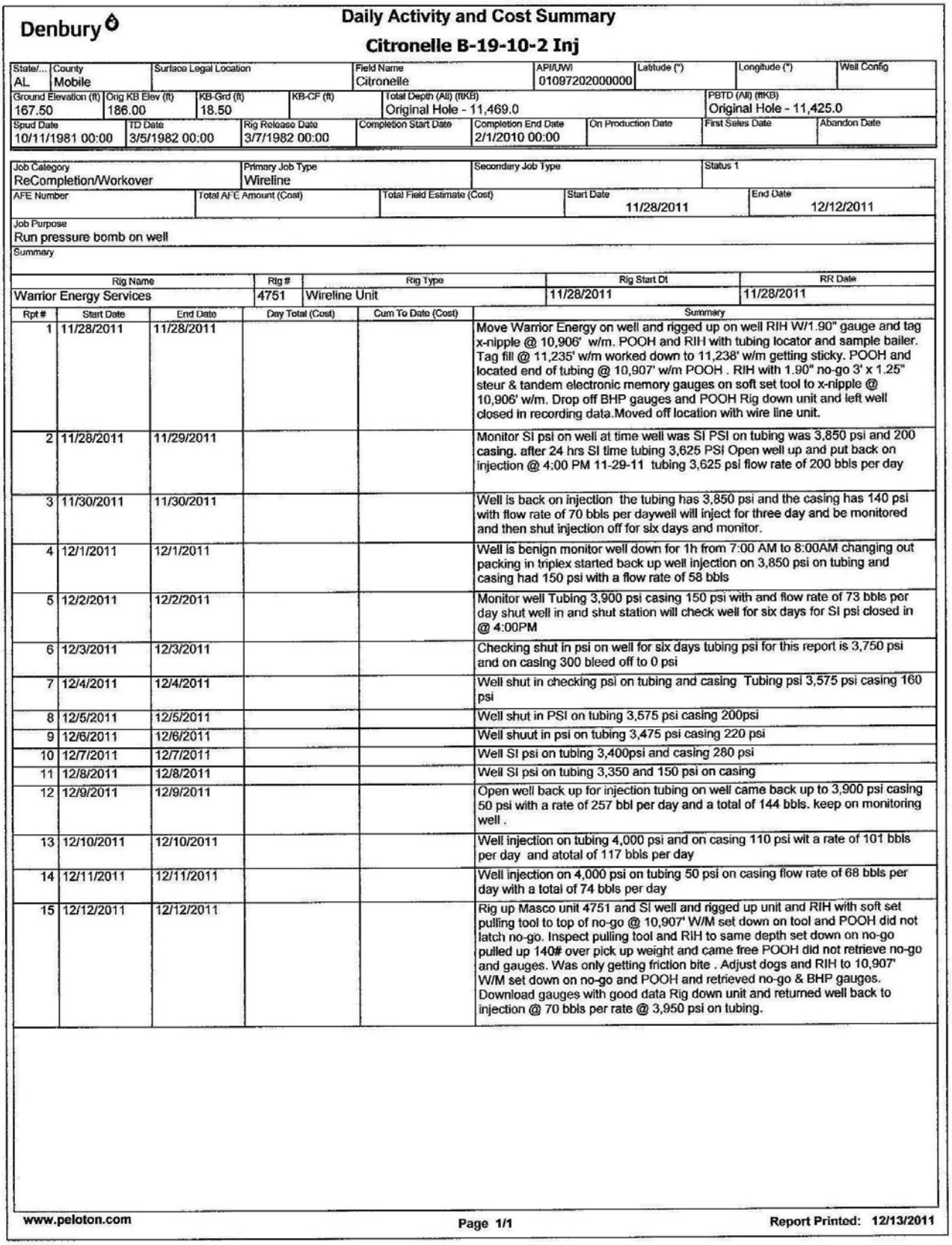

Denbury

## Daily Activity and Cost Summary

### Citronelle B-19-10-2 Inj

| State/... | County | Surface Legal Location | Field Name | API/UWI | Latitude (°) | Longitude (°) | Well Config |
|---|---|---|---|---|---|---|---|
| AL | Mobile | | Citronelle | 01097202000000 | | | |

| Ground Elevation (ft) | Orig KB Elev (ft) | KB-Grd (ft) | KB-CF (ft) | Total Depth (All) (ftKB) | PBTD (All) (ftKB) |
|---|---|---|---|---|---|
| 167.50 | 186.00 | 18.50 | | Original Hole - 11,469.0 | Original Hole - 11,425.0 |

| Spud Date | TD Date | Rig Release Date | Completion Start Date | Completion End Date | On Production Date | First Sales Date | Abandon Date |
|---|---|---|---|---|---|---|---|
| 10/11/1981 00:00 | 3/5/1982 00:00 | 3/7/1982 00:00 | | 2/1/2010 00:00 | | | |

| Job Category | Primary Job Type | Secondary Job Type | Status 1 |
|---|---|---|---|
| ReCompletion/Workover | Wireline | | |

| AFE Number | Total AFE Amount (Cost) | Total Field Estimate (Cost) | Start Date | End Date |
|---|---|---|---|---|
| | | | 11/28/2011 | 12/12/2011 |

Job Purpose: Run pressure bomb on well

Summary

| Rig Name | Rig # | Rig Type | Rig Start Dt | RR Date |
|---|---|---|---|---|
| Warrior Energy Services | 4751 | Wireline Unit | 11/28/2011 | 11/28/2011 |

| Rpt # | Start Date | End Date | Day Total (Cost) | Cum To Date (Cost) | Summary |
|---|---|---|---|---|---|
| 1 | 11/28/2011 | 11/28/2011 | | | Move Warrior Energy on well and rigged up on well RIH W/1.90" gauge and tag x-nipple @ 10,906' w/m. POOH and RIH with tubing locator and sample bailer. Tag fill @ 11,235' w/m worked down to 11,238' w/m getting sticky. POOH and located end of tubing @ 10,907' w/m POOH . RIH with 1.90" no-go 3' x 1.25" steur & tandem electronic memory gauges on soft set tool to x-nipple @ 10,906' w/m. Drop off BHP gauges and POOH Rig down unit and left well closed in recording data.Moved off location with wire line unit. |
| 2 | 11/28/2011 | 11/29/2011 | | | Monitor SI psi on well at time well was SI PSI on tubing was 3,850 psi and 200 casing. after 24 hrs SI time tubing 3,625 PSI Open well up and put back on injection @ 4:00 PM 11-29-11 tubing 3,625 psi flow rate of 200 bbls per day |
| 3 | 11/30/2011 | 11/30/2011 | | | Well is back on injection the tubing has 3,850 psi and the casing has 140 psi with flow rate of 70 bbls per daywell will inject for three day and be monitored and then shut injection off for six days and monitor. |
| 4 | 12/1/2011 | 12/1/2011 | | | Well is benign monitor well down for 1h from 7:00 AM to 8:00AM changing out packing in triplex started back up well injection on 3,850 psi on tubing and casing had 150 psi with a flow rate of 58 bbls |
| 5 | 12/2/2011 | 12/2/2011 | | | Monitor well Tubing 3,900 psi casing 150 psi with and flow rate of 73 bbls per day shut well in and shut station will check well for six days for SI psi closed in @ 4:00PM |
| 6 | 12/3/2011 | 12/3/2011 | | | Checking shut in psi on well for six days tubing psi for this report is 3,750 psi and on casing 300 bleed off to 0 psi |
| 7 | 12/4/2011 | 12/4/2011 | | | Well shut in checking psi on tubing and casing Tubing psi 3,575 psi casing 160 psi |
| 8 | 12/5/2011 | 12/5/2011 | | | Well shut in PSI on tubing 3,575 psi casing 200psi |
| 9 | 12/6/2011 | 12/6/2011 | | | Well shuut in psi on tubing 3,475 psi casing 220 psi |
| 10 | 12/7/2011 | 12/7/2011 | | | Well SI psi on tubing 3,400psi and casing 280 psi |
| 11 | 12/8/2011 | 12/8/2011 | | | Well SI psi on tubing 3,350 and 150 psi on casing |
| 12 | 12/9/2011 | 12/9/2011 | | | Open well back up for injection tubing on well came back up to 3,900 psi casing 50 psi with a rate of 257 bbl per day and a total of 144 bbls. keep on monitoring well . |
| 13 | 12/10/2011 | 12/10/2011 | | | Well injection on tubing 4,000 psi and on casing 110 psi wit a rate of 101 bbls per day and atotal of 117 bbls per day |
| 14 | 12/11/2011 | 12/11/2011 | | | Well injection on 4,000 psi on tubing 50 psi on casing flow rate of 68 bbls per day with a total of 74 bbls per day |
| 15 | 12/12/2011 | 12/12/2011 | | | Rig up Masco unit 4751 and SI well and rigged up unit and RIH with soft set pulling tool to top of no-go @ 10,907' W/M set down on tool and POOH did not latch no-go. Inspect pulling tool and RIH to same depth set down on no-go pulled up 140# over pick up weight and came free POOH did not retrieve no-go and gauges. Was only getting friction bite . Adjust dogs and RIH to 10,907' W/M set down on no-go and POOH and retrieved no-go & BHP gauges. Download gauges with good data Rig down unit and returned well back to injection @ 70 bbls per rate @ 3,950 psi on tubing. |



Figure 4.15. Summary of the well test operator report.

## 4.4. Open Source Simulation Development

We succeeded in the task of establishing a stable and accurate reservoir simulation algorithm for nSpyres, our open-source simulator, for two-phase flow in porous media. Furthermore, even using a highly non-optimized, strictly single-core solution, the simulator is competitive in solution speeds with the fastest simulators and simulation technologies in the world. Part of the reason for the high speed is the use of an open-source version algebraic multigrid solver, AGMG (Notay, 2011). That said, the primary improvement in speed comes from a very stable method for solving the nonlinear implicit saturation equation system, which converges quickly and reliably, regardless of the time step size. In the latest version of nSpyres, selection of time step size depends entirely on desired solution accuracy/resolution, with no consideration to stability. As long as we have only two mobile phases, the framework will be almost trivial to extend for systems with multiple components or species. The simulator is officially ready to apply to the problems in our project, with vastly more flexibility than any commercial simulator available for our use.

A substantial effort was expended to develop methodologies that would allow for a robust and accurate solution to Problem 2 of the SPE Tenth Comparative Solution (Christie and Blunt, 2001). This problem concerns the performance of a highly heterogeneous, elongated five spot (injector at center, producers on corners). The system has dimensions 2200 feet by 1200 feet by 170 feet. The cell block sizes are uniformly 10 feet by 20 feet by 2 feet, so the simulation runs use a grid with dimensions of (220,60,85) for 1,122,000 cells. The original data set had just shy of 30,000 cells having zero porosity that were intended to be non-active cells, but we changed their porosity to 0.001. The problem was originally meant to examine results from various upscaling methods, but the paper provided several fine-grid solutions that many studies have used for reference. At the fine-grid level, the problem is highly pathological. Few standard linear solvers can handle the pressure solution efficiently because of the extreme permeability variability, and the saturation solution is difficult because of high rates and high variability in porosity. Therefore, the problem has become a benchmark for new solvers and algorithms.

Sample results of our latest runs are shown in Figure 4.16. In the figure, one or more of the original reference solutions is shown, along with three nSpyres cases. The most noteworthy characteristics from the figure are:

nSpyres solutions are extremely close to the original “Landmark” case.

There is virtually no difference between the 5-day time step results and the 20-day time step results.

A run with 10 total steps and maximum step size of 300 days gave results very consistent with those using smaller time steps.

Not apparent from the figure is the fact that the 10-step solution is better than any of the upscaled solutions from the original paper. Also, we have confirmed that the differences between the “Landmark” and “Chevron” cases are due to the Chevron run having placed the production wells at the centers of the corner cells, while the Landmark run places the wells in the corners of the cells. Although increased numerical dispersion is unavoidable with large time steps, part of the apparent differences of the 10-step run results from the other runs can be rectified by using a more sophisticated interpolation, instead of plotting results at time step midpoints.

Some specific performance details are summarized in Table 4.6. In the past few years, nSpyres has evolved from using implicit pressure, explicit saturation (IMPES) to its current use of implicit pressure, implicit saturation (sequential implicit, also known as SEQ). Timing for the solution decreased from 4 days, with large material balance errors, to 22 hours, with smaller material balance errors, to as little as 148 seconds, with small material balance errors on older hardware.

The table provides a breakdown of where each run spends its time, and various trends for solution behaviors as time step size is increased. With sequential implicit, at each time step a pressure equation system is generated using flow properties based on current saturations and pressures, then solved for the next time level. A velocity field is generated from the new pressures, and a nonlinear system of equations is generated for saturations. The saturation equation system must be solved iteratively, and at each iteration a linear system must be solved. From the table, one can see that a 5-day-step solution required 401 pressure equation solutions, and 815 linear system solutions. As the time steps get larger, the number of nonlinear iterations per step, the average time per pressure solve, and the average time per saturation solve increases. On the other hand, the total oil recovered from the pattern after 2000 days is only slightly different.

For the sake of timing comparison, Table 4.7 provides a summary of reported timings for solution of the full SPE 10 Problem. Since the results were published in different years and were obtained on different systems, Figure 4.17 provides an approximate trend over the past 16 years for single-core (sequential, non-parallel) floating point speeds. Even after accounting for CPU-speed trends, most of the runs are not even close to as fast as the run times reported in Table 4.6. An optimized 13-step streamline simulation took 170 seconds in 2009, and a 64-CPU run took 620 seconds in 2007 (no information on the simulation type). In neither of the close cases is there discussion of the quality of the results.

Table 4.6.
Performance Results for 2000-day Solutions for SPE 10 using nSpyres.
Timing for single thread on Xeon 3.33 GHz X5680 Processor.

| Max time step (days) | Steps | Nonlinear iterations | Total Run time (seconds) | Pressure Solve time (seconds) | Saturation Solve time (seconds) | Saturation tolerance | Pattern Oil at 2000 days ($10^6$ STB) | Oil Material Balance error |
|---|---|---|---|---|---|---|---|---|
| 5 | 401 | 815 | 3610 | 1097 | 373 | 7.0E-04 | 2.872 | 0.005% |
| 10 | 202 | 422 | 1837 | 574 | 201 | 1.0E-03 | 2.876 | 0.01% |
| 20 | 102 | 275 | 1062 | 301 | 128 | 2.0E-03 | 2.881 | 0.02% |
| 50 | 43 | 134 | 500 | 133 | 71 | 4.0E-03 | 2.889 | 0.03% |
| 100 | 24 | 81 | 304 | 76 | 61 | 6.0E-03 | 2.887 | 0.04% |
| 200 | 15 | 57 | 209 | 47 | 45 | 8.0E-03 | 2.877 | 0.15% |
| 300 | 10 | 39 | 148 | 32 | 36 | 8.0E-03 | 2.872 | 0.2% |

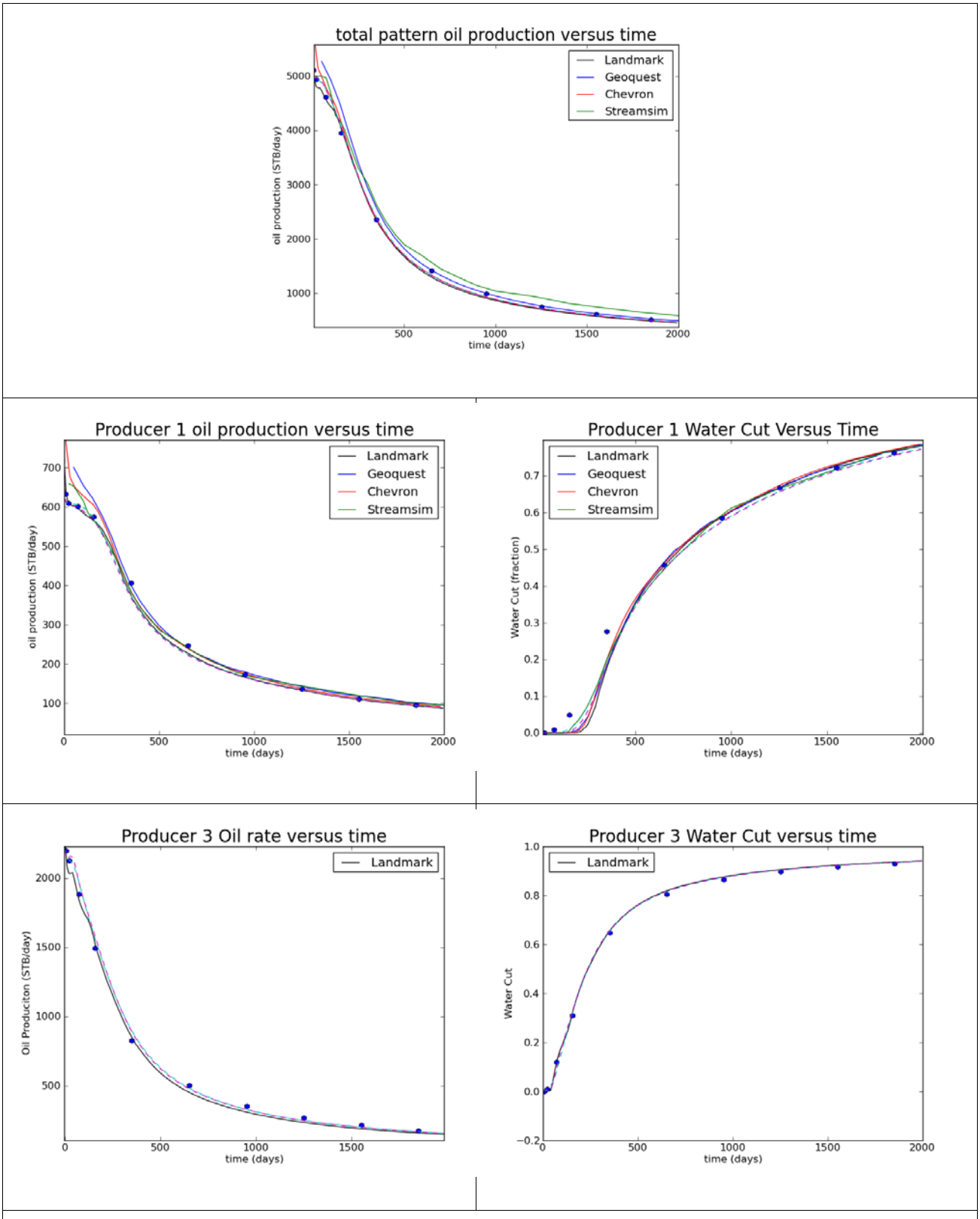


Figure 4.16. Selected results for SPE 10 comparative solution simulation runs. The solid lines are published results from the original 2001 paper, the dashed lines are for the 5- and 20-day time step solutions, and the markers (solid circles) are for the 10-total-steps solution.

| Table 4.7. Summary of Available Benchmark Times for SPE 10 Solutions. | | | | |
|---|---|---|---|---|
| Reference | Year | Source type | Time | Notes |
| Hammersley and Ponting | 2008 | Conference paper | 328 minutes | 128 time steps, 542 non-linear iterations |
| Gong | 2011 | Workshop slides | 4.5 hours | General-Purpose Research Simulator (GPRS), 1 CPU |
| Gong | 2011 | Workshop slides | 5 hours | Eclipse on 8 CPUs, though no specification of cores versus CPU |
| Esler et al. | 2012 | Conference presentation | 27 minutes | In-house simulator, uses operator split, pressures solved with 20-day steps, saturation propagated with 1000's of independent explicit steps, uses Tesla GPU and single precision for saturations |
| Esler et al. | 2012 | Conference presentation | 24+ hours | In-house simulator, uses operator split, pressures solved with 20-day steps, saturation propagated with 1000's of independent explicit steps, uses sequential solver, single CPU |
| Kwok | 2007 | Stanford Univ. Dissertation | 16558 seconds | 53 steps |
| Gratien et al. | 2007 | Conference paper | 7169 (1 CPU) 620 (64 CPU) seconds | 2 processes per node |
| Lu | 2008 | Univ. of Texas Dissertation | 52 minutes | 150 processors, using Hypre |
| Natvigand et al. | 2009 | Conference paper | 170 seconds | Parallel streamline simulator, “highly optimized commercial simulator,” 13 time steps |

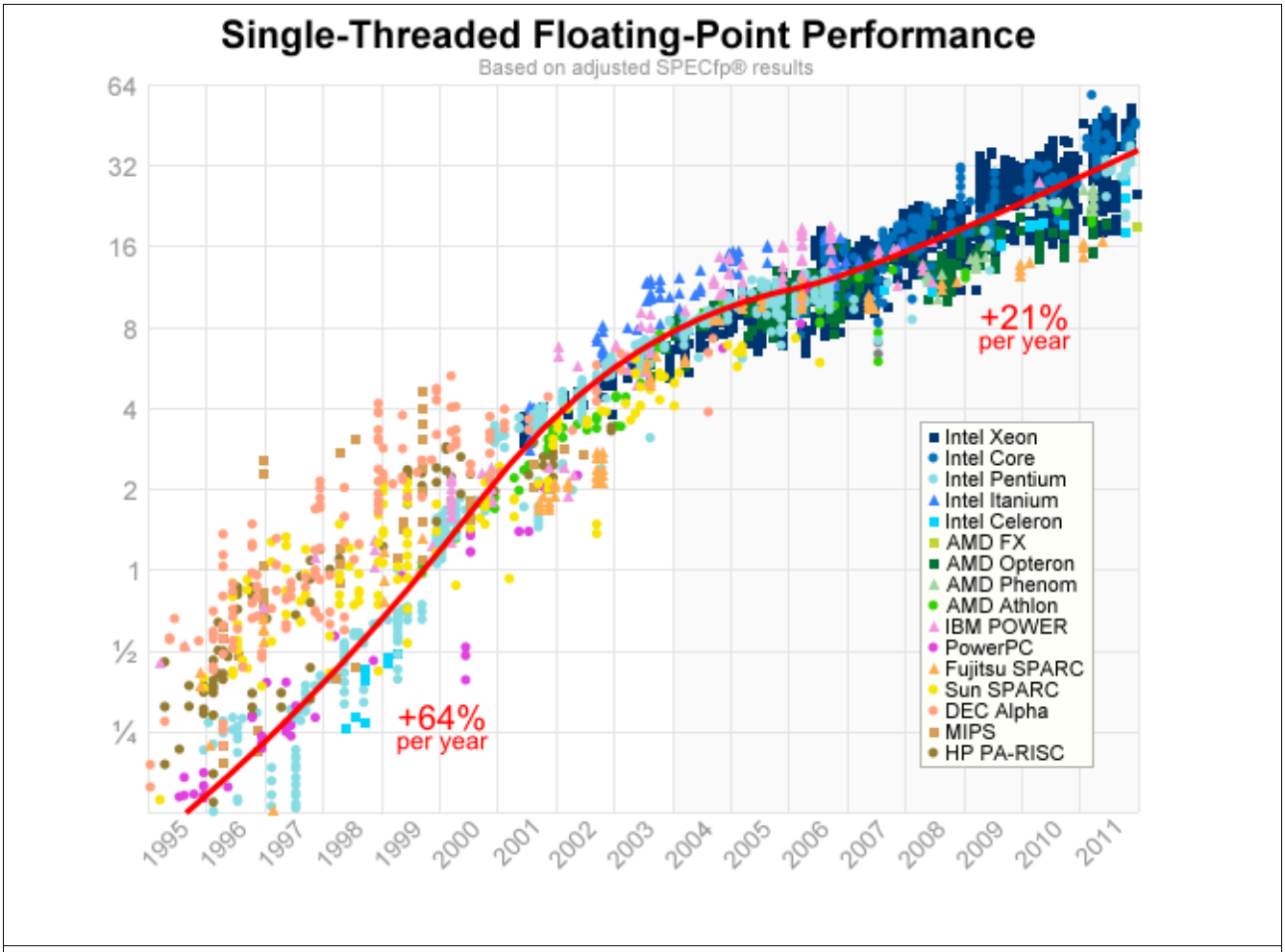


Figure 4.17. Results of an analysis of single-core performance for floating-point benchmarks as a function of year, as suggested by historical data harvested by a public domain program written by Jeff Preshing in February 2012, available from https://github.com/preshing/analyze-spec-benchmarks

## 4.5. Detailed Simulation

We ran 12 very-high-resolution simulations of waterflooding in the pilot region. Despite the fact that these runs were tests, the results of the runs have already provided substantial useful information about the test region. Additionally, these tests have helped to confirm some strengths of the simulator and to flag some areas that need to be modified. In particular, the code will need to include some adaptive implicitness in well rate and saturation calculations to allow for larger time steps.

The identification of perforation zones was extremely challenging because perforation depths are reported without identifying the "zero" reference. These reference depths can vary by as much as thirty feet. To accommodate this big oversight, we needed to make sometimes-large adjustments to the depths. After making these adjustments, an additional small depth adjustment, +/- 3 feet, was made for each well so that the perforation interval corresponded as closely as possible to the depth-corrected stratigraphic pay zones identified by the Geological Survey of Alabama (GSA). Once all of these adjustments were made, a program was written to look at the overlap between pay and perforation zones to identify which grid cells should be opened. All of the final information is summarized in Figure 4.18.

The actual subsea elevation of each zone was one of the adjustments required for aligning the perforations with the stratigraphic zones. The elevation is also information required for proper calculation of flow potential in the simulations. Figure 4.19 shows the structural elevation, where the "zero" reference was a POSSIBLE water contact relative to the top of the GSA stratigraphy interpretation. The top of Figure 4.19 also shows a triangulation of the wells used for the mapping, and includes 8 fake wells added to the outside boundary to assure elevation estimates for the entire simulation grid.

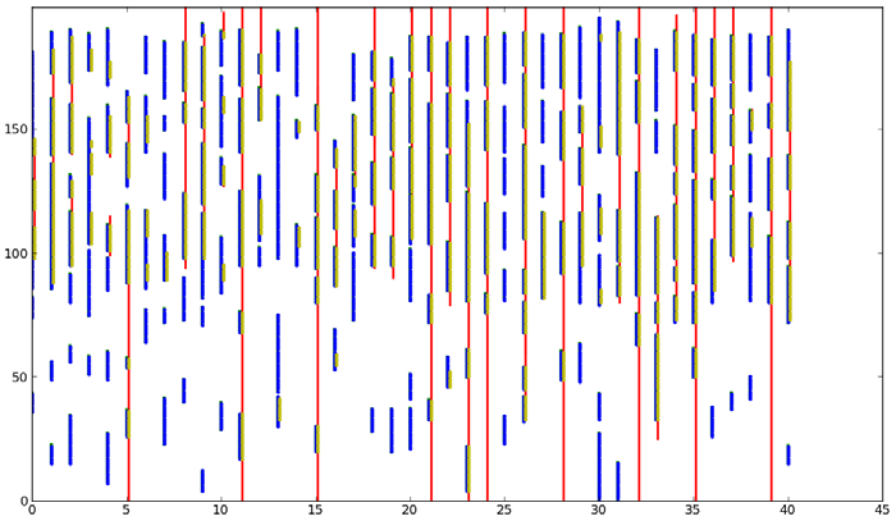


Figure 4.18. Figure summarizing, without any location considerations, possible pay zones (blue), perforated intervals as summarized in well files (red), and the zones opened for the simulation runs (yellow).

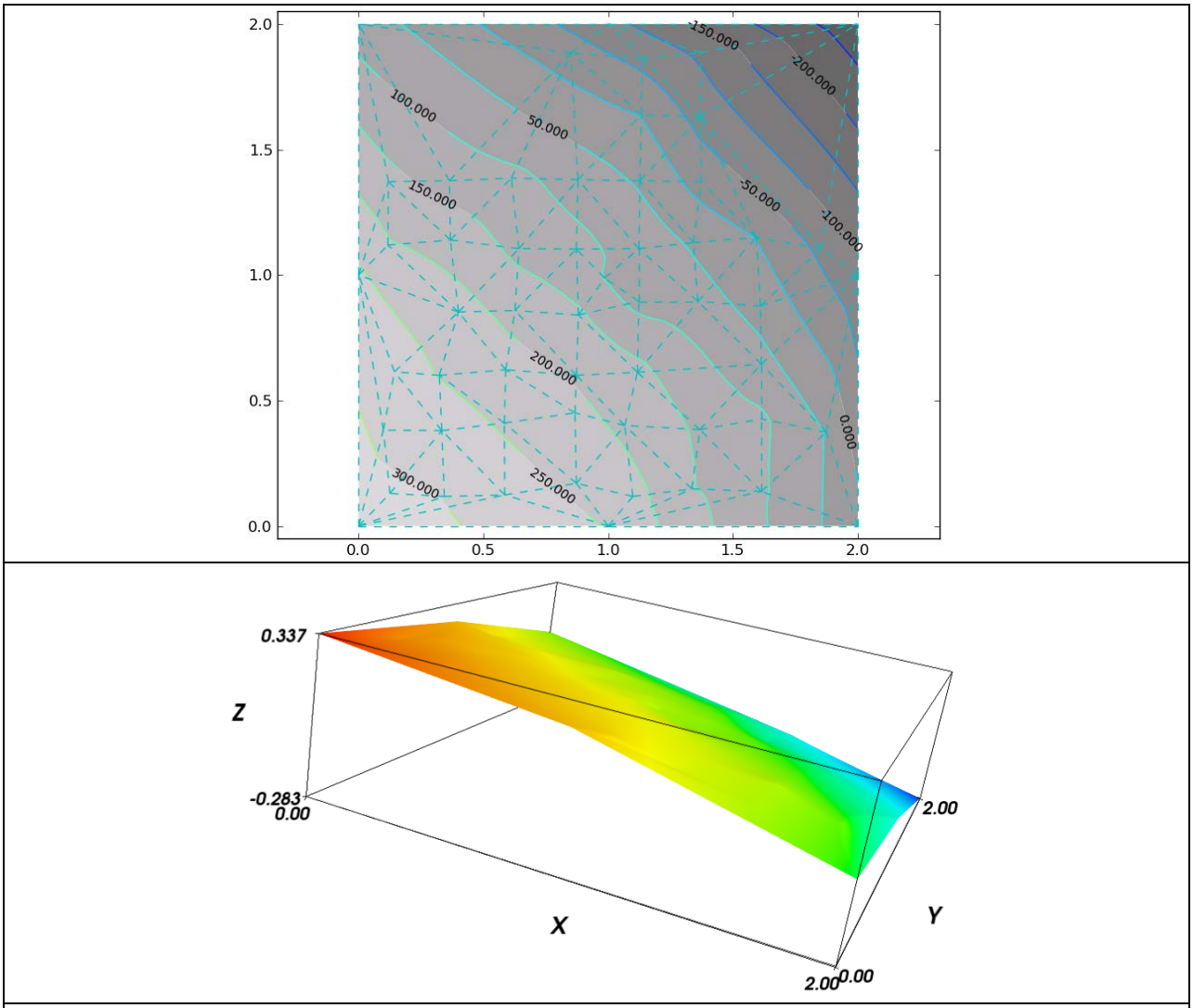


Figure 4.19. Top: Contour map of structure in the pilot region based on the top of the Ferry Lake Anhydrite formation. Bottom: The same information, but shown as a color-coded surface, with blue on low and red on high elevations.

Once the elevations were calculated, these were applied to the simulation grid. Three representations of the depth-adjusted pay volume are shown in Figure 4.20. Throughout Citronelle Field, structural relief is almost a nonissue. In our pilot test region, however, structural elevations vary much more than they do elsewhere in the field. The figure also shows how discontinuous the pay zones are in the pilot region.

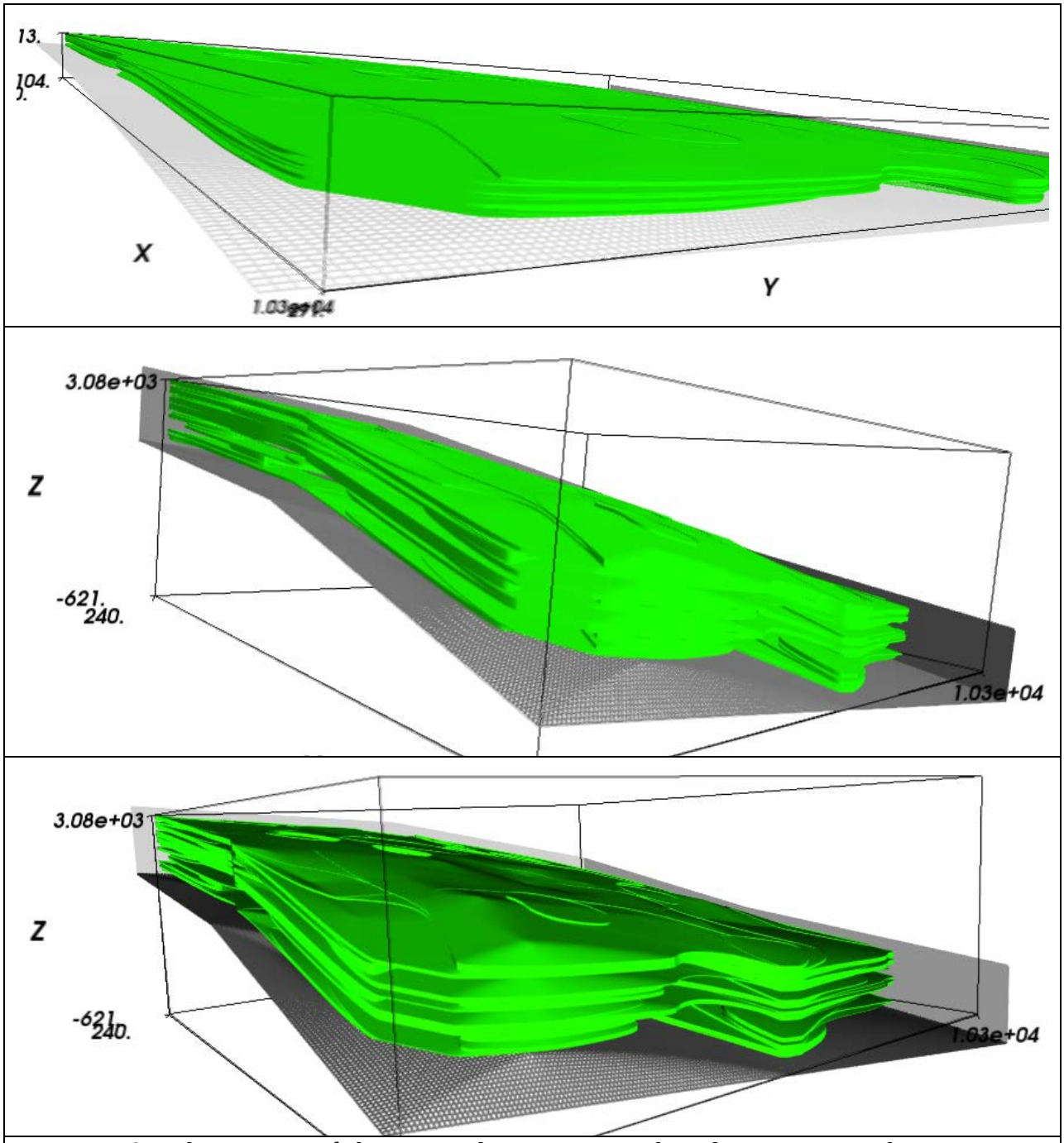


Figure 4.20. Three views of the potential pay zones in the pilot test area. The top view is uniformly scaled in all directions, while the bottom view has the vertical, Z direction, exaggerated by a factor of 5. The middle and bottom figures are roughly the same, but with different lighting to highlight slightly different features.

The base case used for the simulation tests involved 205 x 200 x 200 = 8.2 million cells having the same dimensions of 26.8 ft by 26.8 ft by 1 ft thick. 2.94 million of the cells were in pay-quality zones. Horizontal permeability in the pay zones was set to a uniform 7 mdarcy, vertical permeability to 10% of the horizontal values, and porosity was set to a uniform 0.154. The initial/connate water saturation was 0.21, and residual oil saturation was 0.25. Porosity in the non-pay zones was set to 0.01, and permeability was either zero or 1 x $10^{-6}$ mdarcy, and initial water saturation was 0.5. Cell elevations were as depicted in Figure 4.20. Production wells produced at constant well pressure of 3000 psi, constrained to a maximum of 400 psi pressure drop between cell block and well. Injection wells injected at constant pressure of 7000 psi, also with a maximum difference of 400 psi.

The primary purposes of the simulation tests were to assess performance and stability of the base simulator using realistic well distributions and reservoir geometry, and with varying well rates. The tests showed that for a given time step, the serial (single-core) performance is very fast and accurate.

Even with the simplified rock properties, these test produced some very useful results. The discussion will focus on the results of the longest run, which achieved ten years of activity. In this case, the water and oil relative permeabilities were the "better" case shown on the left side of Figure 4.21, and the non-pay zones had zero permeability. For comparison, one image will be shown that is related to a shorter run with the "leaky" water relative permeability of Figure 4.21. The right side of Figure 4.21 shows the theoretical displacement behavior of these two cases, and indicates that the "leaky" case bypasses far more oil than the "better" case.

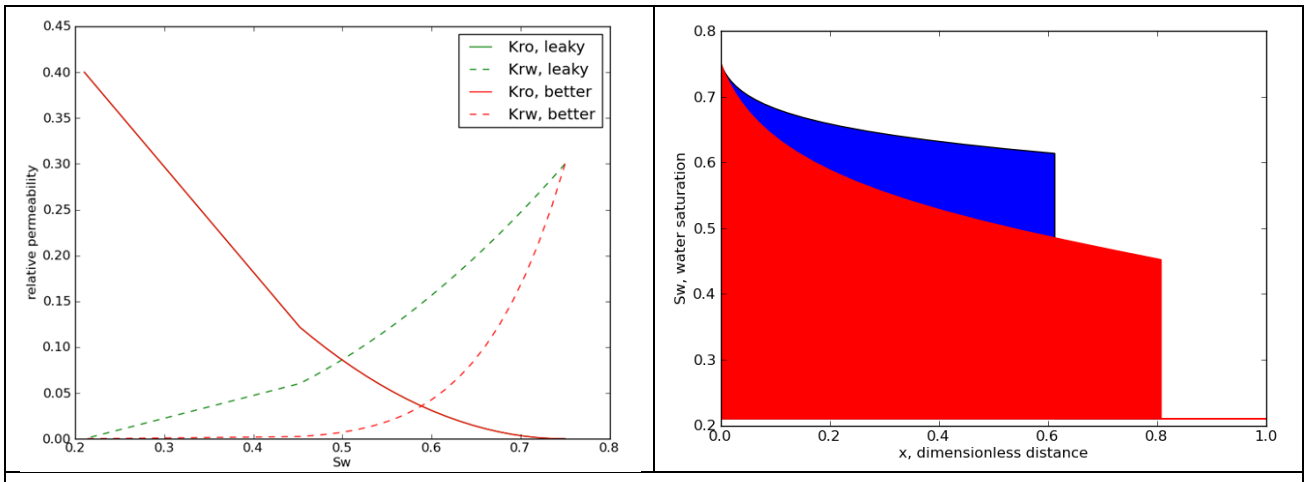


Figure 4.21. Left: The extremes of relative permeability behaviors used in the simulation runs (constant oil relative permeability, variable water relative permeability). Right: The ideal frontal advance behavior of the extremes of relative permeability at 0.5 moveable pore volumes injected. The red zone on the right corresponds to the green (leaky) curve on the left, and suggests a vastly less efficient displacement efficiency than the blue region.

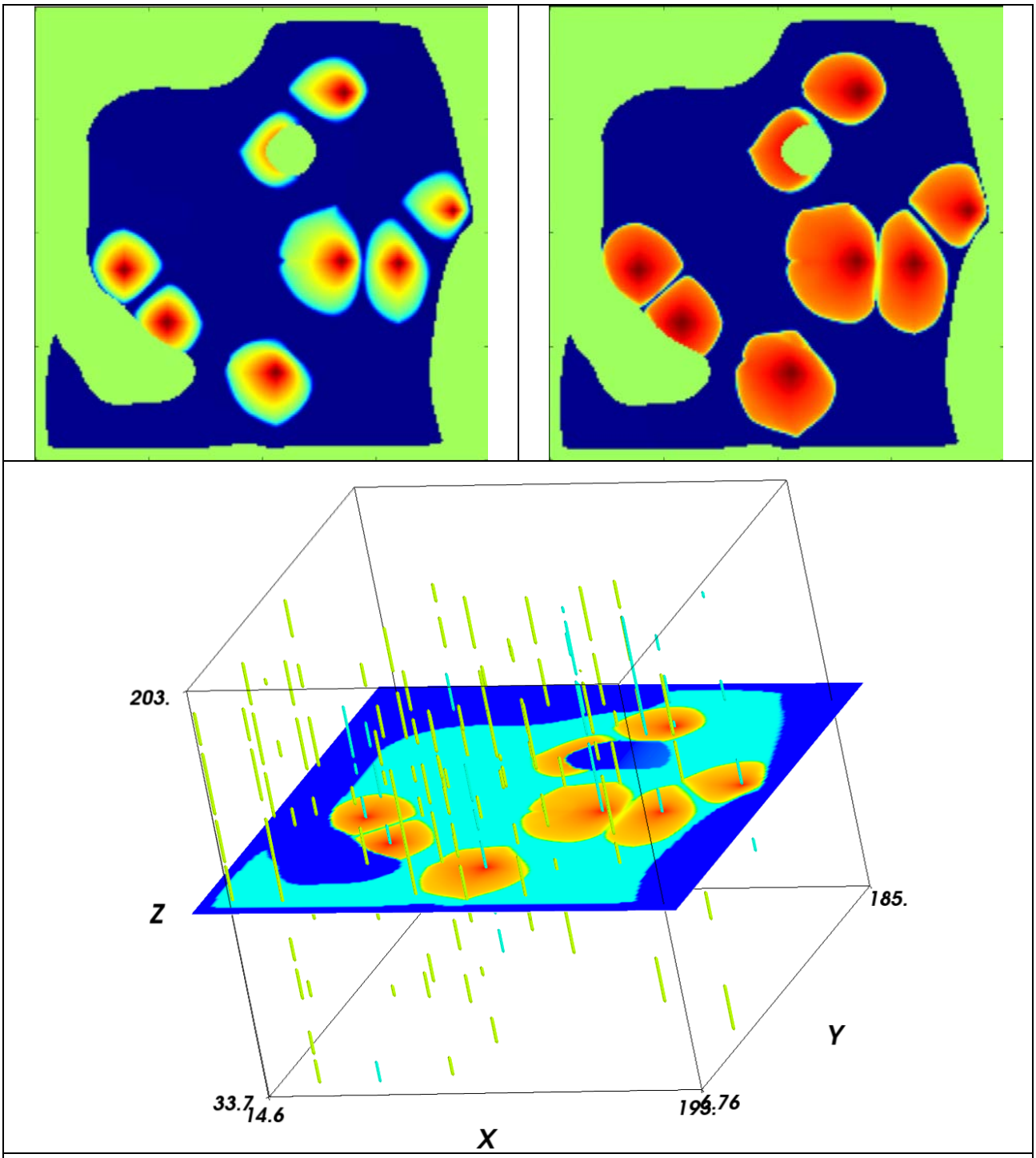


Figure 4.22. All of these images concern water saturation, where red indicates high water saturation and blue indicates low water saturation. In the top two figures, the light green, and in the bottom figure the dark blue, all indicate non-reservoir zones. The figure at top left shows water saturation for the "leaky" case of Figure 4.21, and the other two figures show water saturation for the "better" case of Figure 4.21. The bottom figure also shows the perforated zones, where yellow indicates production zones, and cyan indicates injection zones. There are many more producers than injectors.

The results shown in Figure 4.22 provide contrast between the "leaky" and "better" cases. The image at the top left shows the spatial distribution of water saturation for the "leaky" case after three years of injection, while the image at the top right shows the distribution of water saturation after ten years of injection in the "better" case. The red and orange tones indicate high water saturations, while the blue and light colors indicate low water saturations. The light green areas in the top figures are all non-pay cells. The image on the left clearly indicates a high level of front smearing, while that on the right shows very sharp changes in water saturation. The proper front behavior and strict honoring of no flow within the non-pay zones shown in these figures provide strong evidence that the simulator handles frontal advance properly.

The lower image in Figure 4.22 shows the location of the horizontal cross sections, and also provides the locations of perforated zones at each well. Close inspection of the images shows a non-pay area near their centers. In the lower figure the non-pay area is dark blue; in the upper figures it is green. This area is surrounded by a region of water saturation, even though there is no injection in the layer at this location. Despite reduced vertical permeability, injected water from a different layer has no problem migrating to a productive region.

The level of communication among the pay-quality cells depends strongly on the interpolation method used, and on the thresholds, perforated intervals, and ultimate assignment of rock properties. The determination of which cells were of pay quality was based on one threshold value, with the simplest interpolation routine possible. Given the geological realizations used for the simulation tests, some interesting continuity results emerged. In Figure 4.23, three types of volumes are represented, including those shown in yellow, having high water saturation, those shown in blue, having low pressures, and production wells, shown in light green. The blue regions are significant, because they suggest poor communication with the injectors in the studied area, though they could have good communication with injectors outside the pilot test area. The yellow volumes show the regions where the amount of oil recovered from the test area is greatest, after 10 years of injection. The light green well surfaces suggest good pressure support, but show that the water fronts have not yet advanced to those wells.

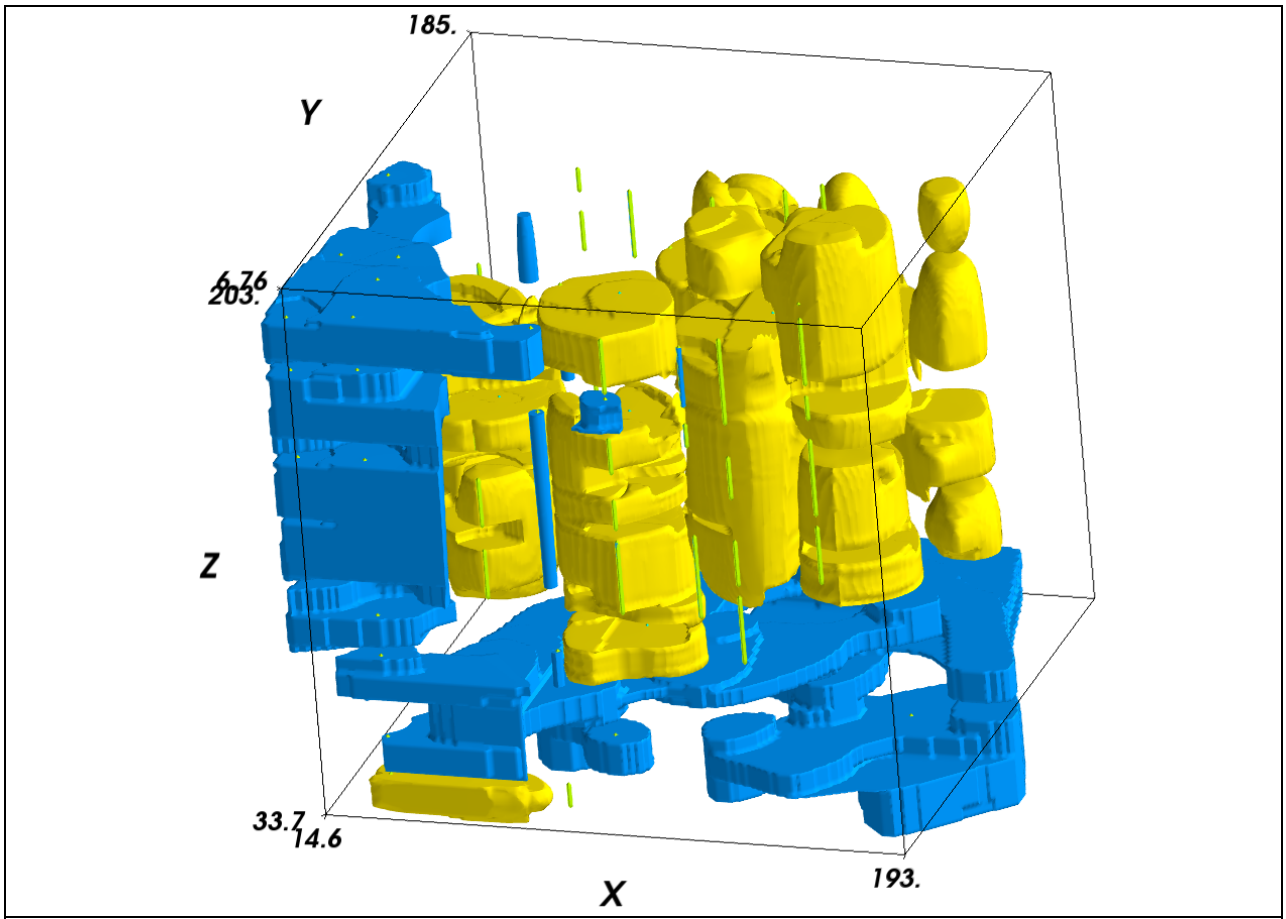


Figure 4.23. The volumes enclosed by the different color surfaces represent completely separate characteristics. The blue volumes are low pressure regions, and the yellow volumes are (mutually exclusive) high-water-saturation zones that only occur around injection wells. The thin green surfaces are production wells, probably in good communication with injectors.

We developed a methodology to allow us to automatically estimate porosity and permeability at each cell of a simulation grid, if we have porosity as a function of depth at various locations in the formation. The method uses multidimensional interpolation, and it is set up specifically to honor the well data. All of the grid data can be geostatistically perturbed, but at this point we are more concerned with assessing potential for continuity. Figure 4.24 shows isosurfaces generated from the output of a generic nine-well system. The image sequence starts with identification of the bounding volumes of all possible pay zones and works it way through various bounding zones of progressively better quality. In this case, it is possible to identify high porosity/permeability zones having extended volumes and others that are clearly local volumes around wells. At this point, we must use the generic example because we do not yet have even hypothetical distributions for porosity and permeability at wells, including in our pilot test area.

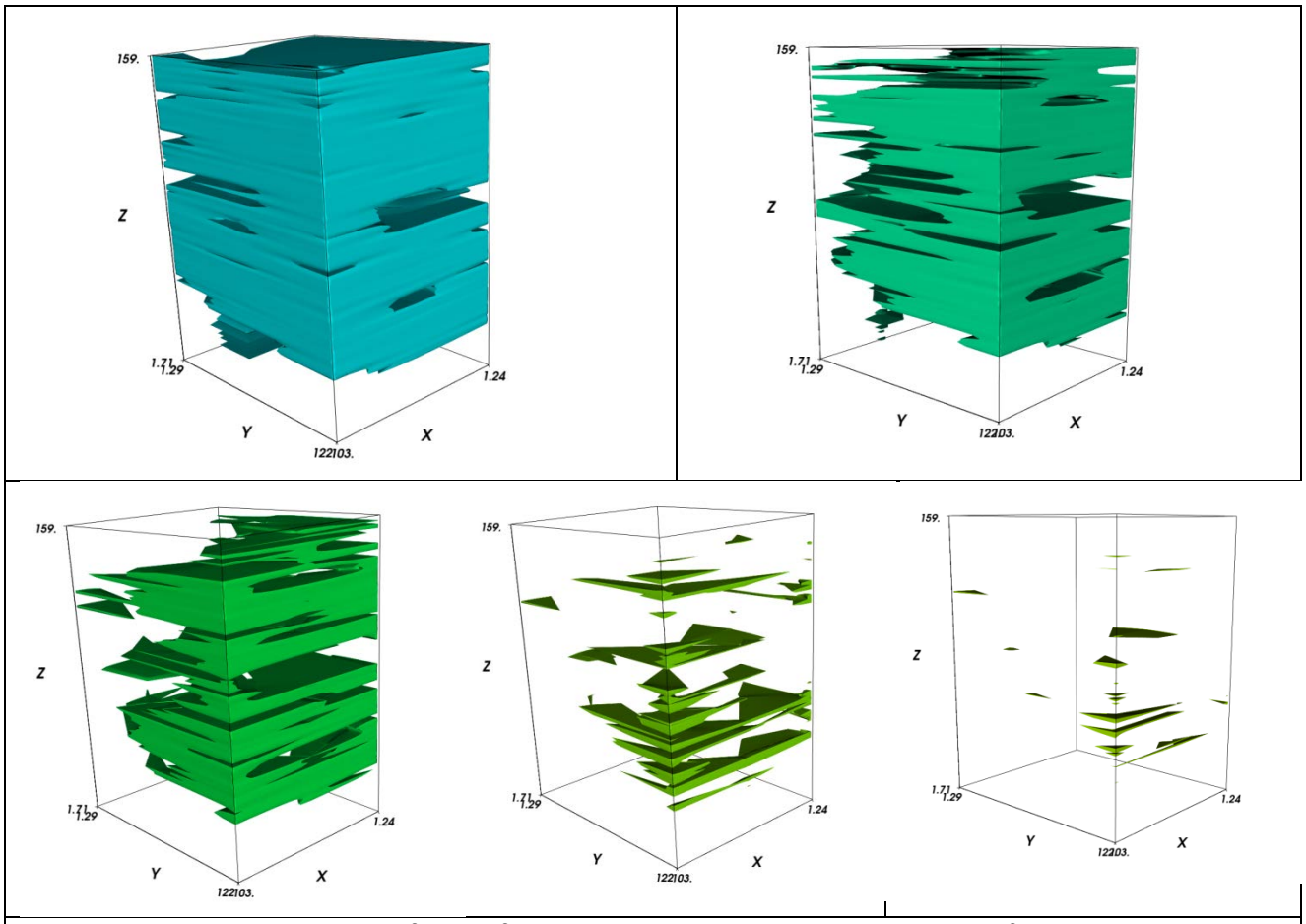


Figure 4.24. Bounding isosurfaces of various minimum qualities generated from the interpolation methodology by a sample calculation performed for 9 wells. The porosities at the isosurfaces shown in the figures are: upper left, porosity > 0.06; upper right, porosity > 0.08; lower left, porosity > 0.10; lower middle, porosity > 0.12; and lower right, porosity > 0.13.

Figure 4.25 shows the full field production for the Citronelle Field throughout its life, and Figure 4.26 gives a close-up view of the oil production and a decline curve fit to the data over the past 27 years. The equation

$$\text{Monthly oil} = 163{,}400 \exp\left(-0.046\,(t - 30)\right), \tag{4.2}$$

gives a very reasonable fit for the oil rates on average for the past 27 years, where $t$ is the time in years since the beginning of production. Using this fit, Citronelle could produce 11 million more barrels of oil over the next 50 years, compared with the 166 million barrels already produced. The additional recovery of 11 million barrels is a small fraction of the conservatively estimated 200 million barrels of oil remaining in place.

The full-field data indicate an average of about 75 bbl of fluid per day per well, which is not too far out of line with the rate related to the 7-mdarcy results from the test runs for the pilot area made with nSpyres, shown in Figure 4.27. Although the total fluid rate is not bad, the simulated water fractions shown in Figure 4.28 are way off: 30% calculated versus 85% actual. Since, in a homogenous reservoir, volumetric recovery depends so much on the total pore volumes of injected fluid, the water cut variation between the three different formation permeability cases presented in Figure 4.28 only reflects the differences caused by injection rate. Since the calculated rates, in the presence of low permeability, are comparable to those observed in the field, we have strong evidence for channeling due to permeability variation (not just from crazy variation of reservoir geometry).

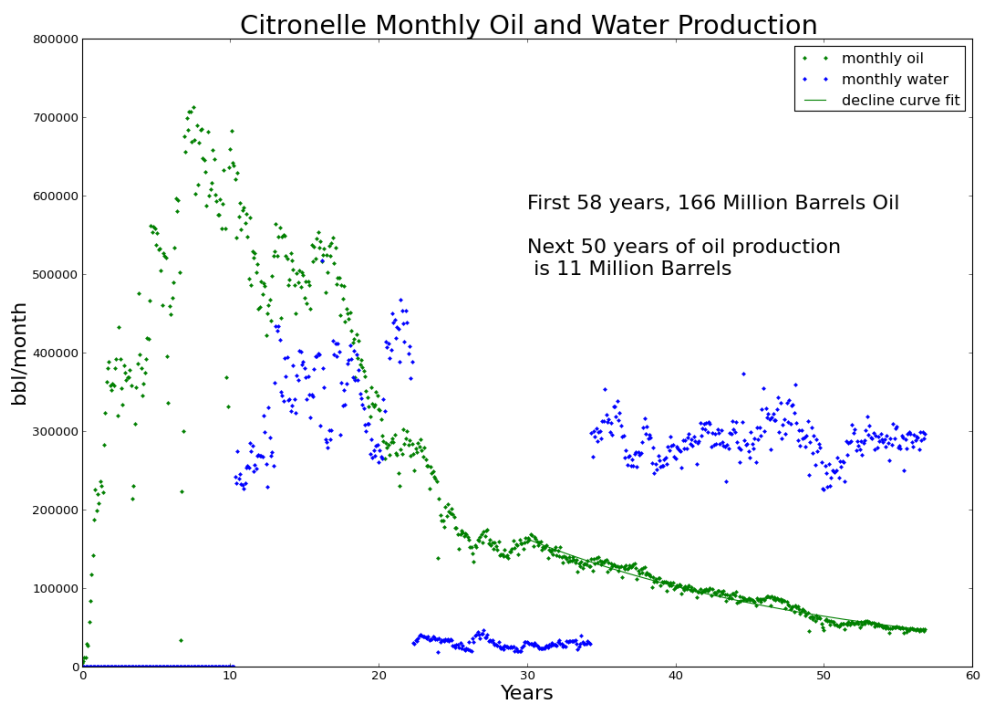


Figure 4.25. Production of oil and water from the Citronelle Oil Field throughout its lifetime.

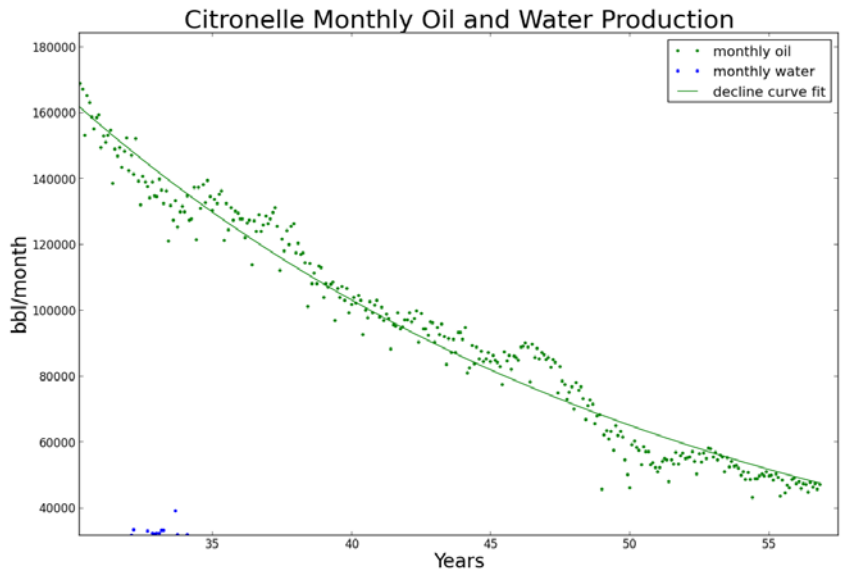


Figure 4.26. Decline curve fit to monthly oil production from the Citronelle Field for the past 27 years. Monthly oil = $1.6343 \times 10^5 \exp(-0.0459603636\,(t - 30))$, with $t$ in years since the start of production from the field.

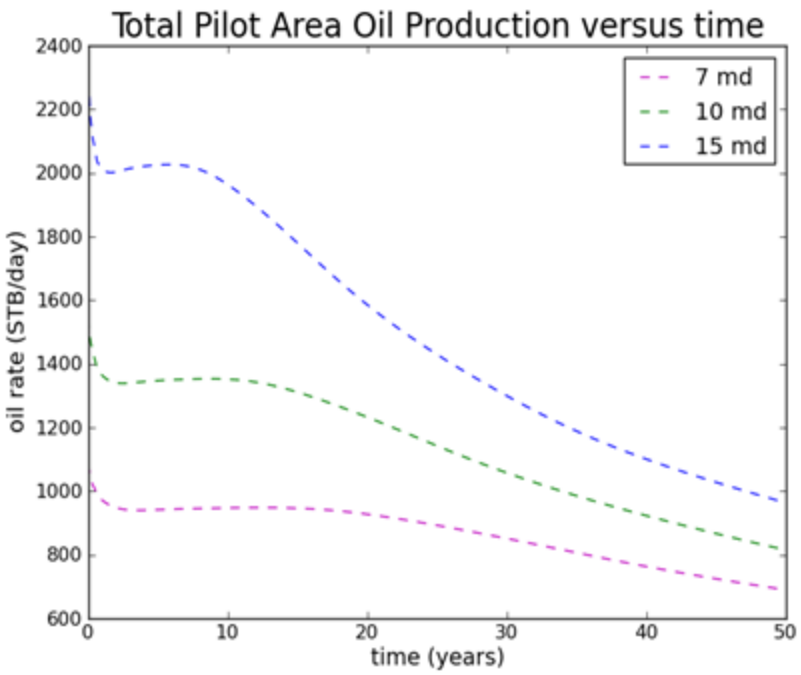


Figure 4.27. Fine-grid simulation results for 50 years of oil production from the pilot region. The simulations used nSpyres and assumed uniform permeability distributions, but highly irregular geometry.

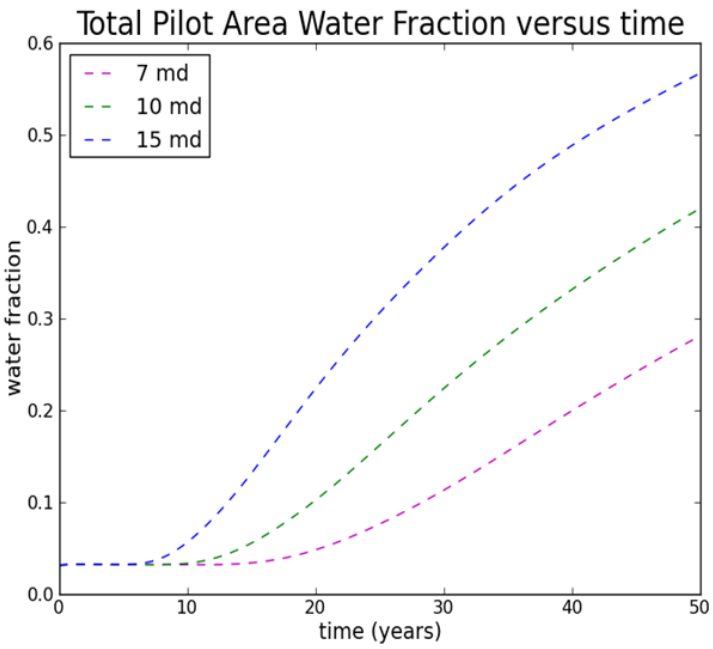


Figure 4.28. Fine-grid simulation results over 50 years, for the produced water fraction from the pilot region. The simulations used nSpyres and assumed uniform permeability distributions, but highly irregular geometry.

One important observation from these simulation results is the clear trends of vertical migration of water, even with restrictive vertical permeability. Unfortunately, as detailed as these simulations were regarding local connectivity, the zones that were considered are actually in communication with the rest of the field. We have been developing a parallel version of nSpyres that will allow us to create a detailed simulation (500 million cells) of the entire field. We have succeeded with much of this effort (for example, a 6-core, single-workstation solution to the SPE 10 Problem in 21 seconds), but still need a few additional capabilities, such as the ability to handle discrete fractures, before applying the simulation to the entire field. With this tool, we think it would be possible to apply the results of the pilot injection for assessment and optimization of designs for full-field recovery.

**Acronyms, Abbreviations, and Symbols in Section 4**

| | |
|---|---|
| AGMG | aggregation-based algebraic multigrid method (Notay, 2011) |
| $c_t$ | average total compressibility, $psi^{-1}$ |
| CPU | central processing unit |
| *dp* | pressure at shut-in minus instantaneous pressure, psi |
| *dt* | time since shut-in, hours |
| GPRS | General-Purpose Research Simulator (Gong, 2011) |
| GSA | Geological Survey of Alabama, Tuscaloosa, AL |
| *h* | average thickness, ft |

| | |
|---|---|
| IMPES | implicit pressure, explicit saturation |
| $k$ | absolute permeability, mdarcy |
| $k_{ro}$ | relative permeability to oil, dimensionless |
| $k_{rw}$ | relative permeability to water, dimensionless |
| $L_f$ | length of fracture, ft |
| $m$ | slope, psi/hr$^{½}$ or psi |
| $p$ | pressure, psi |
| $q$ | water injection rate, bbl/day |
| $qB$ | reservoir flow rate, bbl/day |
| $r$ | distance from the injector, ft |
| SENSOR | System for Efficient Numerical Simulation of Oil Recovery (Coats Engineering, Inc., http://www.coatsengineering.com/) |
| SEQ | sequential implicit |
| SPE | Society of Petroleum Engineers, Richardson, TX |
| STB | stock tank barrel |
| $t$ | time, hours, days, or years |
| WAG | water-alternating-gas recovery |
| $\lambda_T$ | total mobility, mdarcy/cP |
| $\mu$ | viscosity, cP |
| $\mu_o$ | viscosity of oil, cP |
| $\mu_w$ | viscosity of water, cP |
| $\phi$ | average porosity, dimensionless |

**References in Section 4**


Christie, M. A., and M. J. Blunt, "Tenth SPE Comparative Solution Project: A Comparison of Upscaling Techniques," *SPE Reservoir Evaluation & Engineering*, **2001**, *4*, 308-317.

Coats Engineering, Inc., 2009, http://www.coatsengineering.com/

Esler, K., V. Natoli, A. Samardžić, S. Atan, and B. Ramírez, "Accelerating Reservoir Simulation and Algebraic Multigrid with GPUs," Presentation S0140, GPU Technology Conference, San Jose, CA, May 2012.

Gratien, J. M., T. Guignon, J. F. Magras, P. Q. Quandalle, and O. R. Ricois, "Scalability and Load Balancing Problems in Parallel Reservoir Simulation," Paper SPE 106023, SPE Reservoir Simulation Symposium, 2007.

Gong, B., "A General Purpose Research Simulator (GPRS) for Numerical Simulation on $CO_2$ Sequestration," Slides from China Australia Geological Storage of $CO_2$ (CAGS) Workshop 3, Session 4.3 presentation, Changchun, China, 11-14 July 2011.

Hammersley, R. P., and D. K. Ponting, "Solving Linear Equations in Reservoir Simulation Using Multigrid Methods," Paper SPE 115017, 2008 SPE Russian Oil & Gas Technical Conference and Exhibition held in Moscow, Russia, 28-30 October 2008.

Kwok, W. H. F., "Scalable Linear and Nonlinear Algorithms for Multiphase Flow in Porous Media," Ph.D. Dissertation, Stanford University, December 2007.

Lu, Bo, "Iteratively Coupled Reservoir Simulation for Multiphase Flow in Porous Media," Ph.D. Dissertation, University of Texas at Austin, 2008.

Natvigand, J. R., B. Skaflestad, F. Bratvedtand, K. Bratvedt, K.-A. Lie, V. Laptevand, and S. K. Khataniar, "Multiscale Mimetic Solvers for Efficient Streamline Simulation of Fractured Reservoirs," Paper SPE119132, SPE Reservoir Simulation Symposium, 2009.

Notay, Y., "Aggregation-Based Algebraic Multigrid for Convection-Diffusion Equations," Report GANMN 11-01, Université Libre de Bruxelles, Brussels, Belgium, 2011.

# 5. Carbon Dioxide Injection

Gary N. Dittmar, Tommy Chatfield, Thomas Boelens, Caroline Donlon, Pete Guerra, Jack Harper, Rick Jolly, Keith Murphy, Stephen Pennell, Mark Rainer, Dylan Sheppard, Steve Walker, and William C. Williams, Denbury Resources, Inc.

Tommy Miller, Tommy Henderson, Michael Sullivan, Franklin Everett, Bartley Lambeth, Paul Stanley, Alec Bailey, Danny Beasley, and Steven Brewer, Denbury Onshore, LLC

Peter M. Walsh, University of Alabama at Birmingham

---

## 5.1. Site Preparation and $CO_2$ Storage

The injection well for the test was B-19-10 #2 (Permit No. 3232). The producers monitored most closely were B-19-7 (Permit No. 1215), B-19-8 (Permit No. 1235), B-19-9 (Permit No. 1205), and B-19-11 (Permit No. 1209). What was originally intended to be a more symmetric inverted five-spot well pattern became distorted by substitution of Well B-19-11 for the plugged and abandoned Well B-19-10 (Permit No. 1206), which, in spite of a heroic attempt at workover by Denbury Onshore, could not be returned to production. An aerial photograph of the oil field in the vicinity of the test pattern, with the wells identified by number, is shown in Figure 5.1.

Produced fluids from Wells B-19-7, B-19-8, and B-19-9 are collected at Tank Battery B-19-8, and fluids from Well B-19-11 go to Tank Battery B-19-11. The locations of the tank batteries are identified in the caption of Figure 5.1. Both tank batteries were equipped with gas-liquid cylindrical cyclone separators, to separate produced oil and water from gas. Because the gas yield from Citronelle oil is very low, the gas was simply vented. The flow meters installed to measure power oil and produced fluid flow rates going to and from the production wells were found not to have sufficient resolution to distinguish the power oil and produced fluid flow rates (4-9 bbl/day of produced oil versus 450-500 bbl/day of power oil per well).

Carbon dioxide for the project was provided by Denbury Onshore from its wells in the natural $CO_2$ reservoir at Jackson, MS. During the $CO_2$ injection, Airgas Carbonic received the $CO_2$ from Denbury Onshore, liquefied it, and transported it to Citronelle.

A refurbished 50-ton liquid $CO_2$ tank was purchased from TOM$CO_2$ Equipment Co. (Loganville, GA), moved to the test site in December 2008, and set on a reinforced concrete pad prepared by Denbury Onshore at Tank Battery B-19-8. The liquid $CO_2$ was stored at approximately 0 $^{o}$F and 300 psig in the refrigerated tank. A charge pump and triplex plunger positive displacement pump were also located at the Tank Battery B-19-8.

The first shipment of $CO_2$ was delivered to the test site by Airgas Carbonic on March 2, 2009. The $CO_2$ arrived in tank trucks, each carrying ~19 tons of $CO_2$. At the average injection rate of 31 tons per day, the 50-ton tank provided 1.6 days of storage capacity and delivery of 1.6 truckloads, on average, were required each day. To keep up, two loads were delivered every other day and, when the level in the storage tank was low, on successive days. Toward the end of the injection period, injection rates increased to more than 40 tons per day, so two truckloads were required nearly every day, and three truckloads on some days.

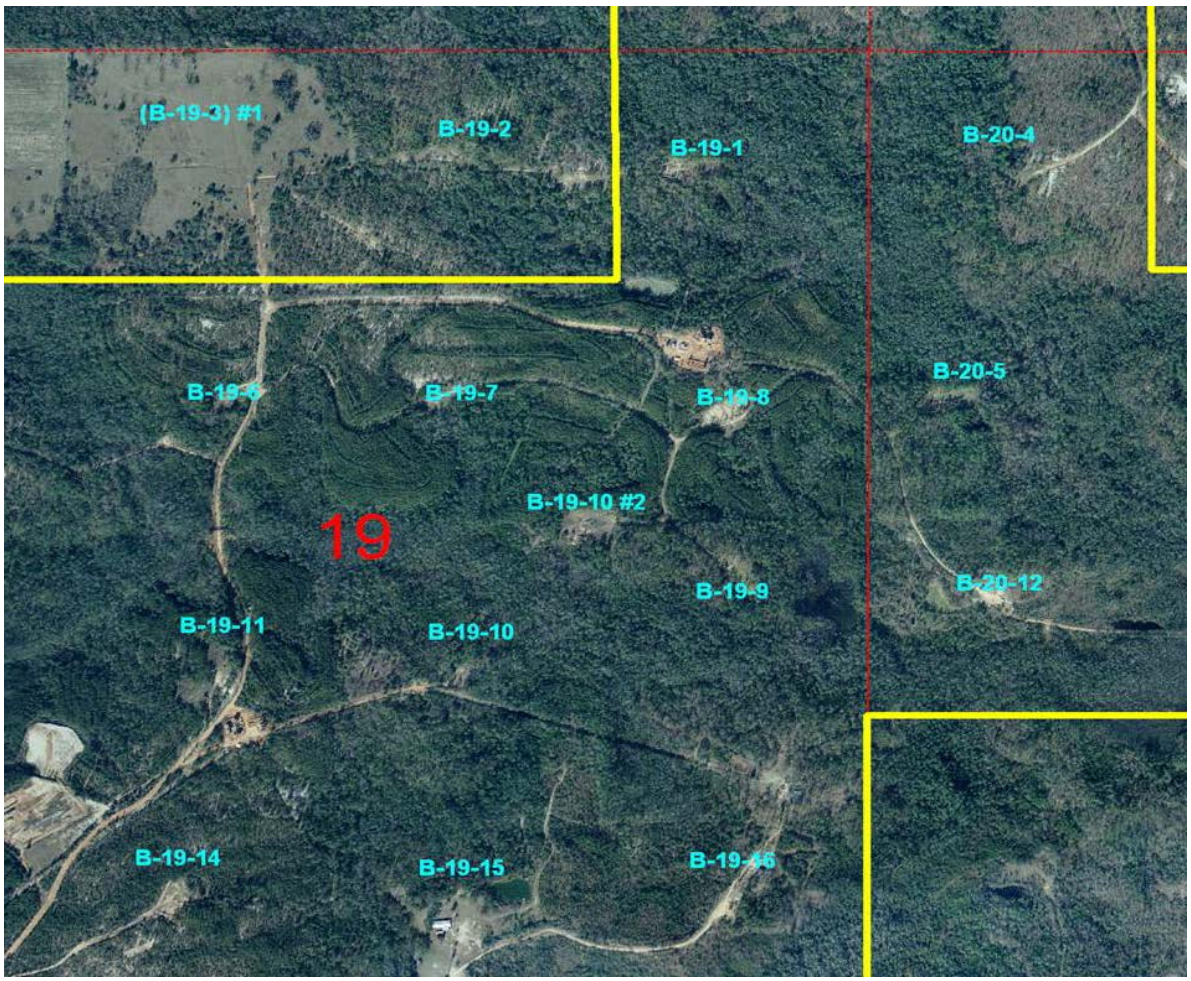


Figure 5.1. Aerial photograph of the Citronelle Oil Field in the vicinity of the test well pattern. The top edge of the photograph faces North. The test pattern consists of injector B-19-10 #2 and producers B-19-7, B-19-8, B-19-9, and B-19-11. Tank Battery B-19-8 is visible just to the Northwest of Well B-19-8. Tank Battery B-19-11 is to the South of Well B-19-11, between the roads.

## 5.2. Record of Water and $CO_2$ Injection Rates, May 2008 to April 2014

The entire history of water and $CO_2$ injection, over the life of the project, is shown in Figure 5.2, beginning with the first steady injection of water following conversion of Well B-19-10 #2 from producer to injector in early 2008. The complete record of injection is introduced here, so it will be available for reference during the discussion of oil production to follow.

Water injection into Well B-19-10 #2, to establish the baseline for oil production, began on March 25, 2008. Some interruptions in water injection followed, while the last of the equipment for the test was installed, the interference test was run, the production wells were brought on line, and preparation of the site was completed. Steady, continuous water injection began on July 4, 2008, at an average rate of 160 ± 18 bbl/day, with Wells B-19-7 and B-19-9 each producing 4 to 5 bbl/day of oil and Wells B-19-8 and B-19-11 each producing 8 to 9 bbl/day of oil. Water injection at this rate continued, without interruption, to March 4, 2009, when preparation began for injection of $CO_2$.

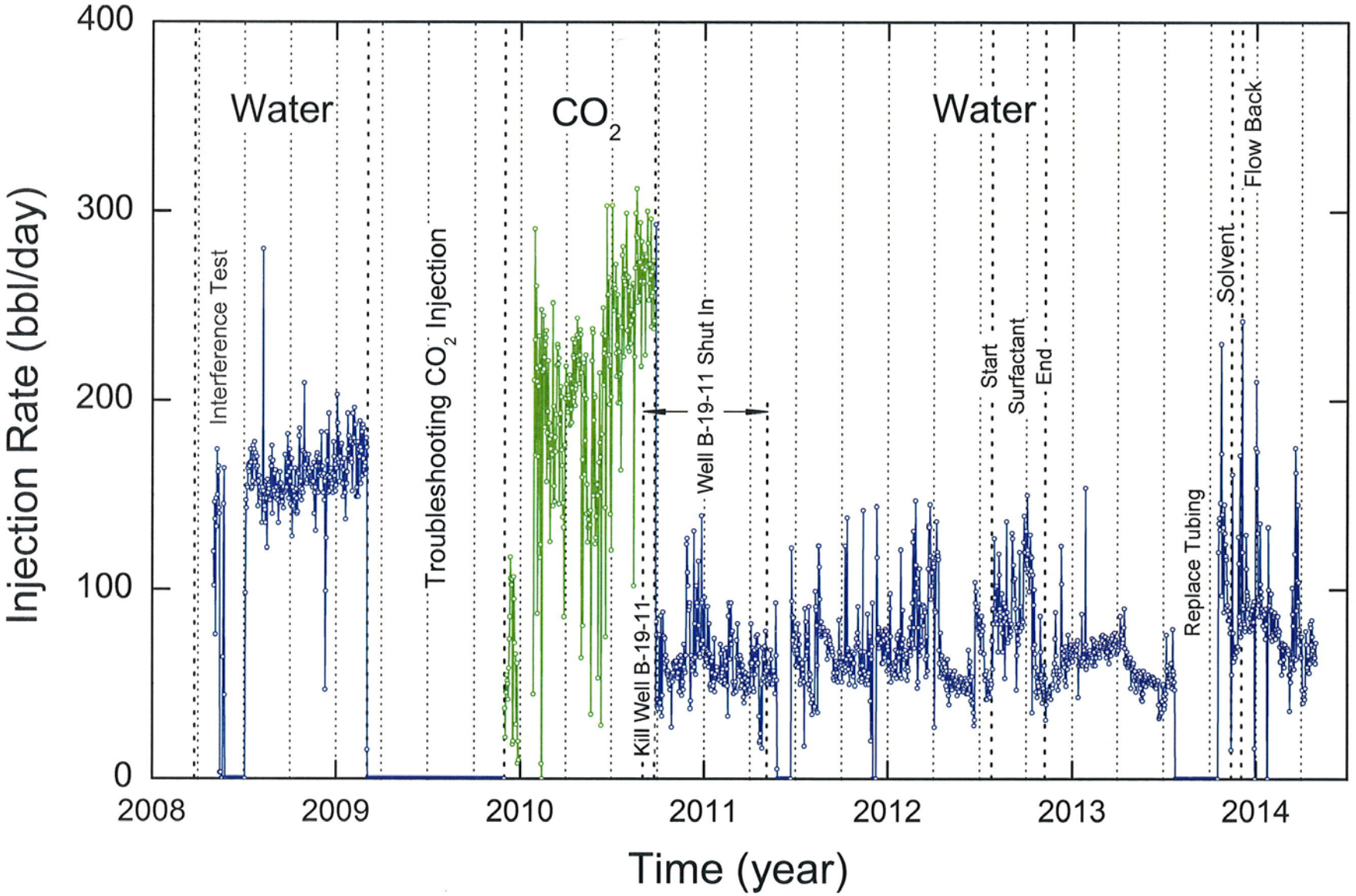


Figure 5.2. History of the rates of water and $CO_2$ injection into Well B-19-10 #2 from May 2, 2008, to April 30, 2014. The tic marks on the time axis correspond to January 1 of the year indicated.

Injection profile tests were run to determine the distribution of water and $CO_2$ between the two injection targets, Sands 14-1 and 16-2. The tests were conducted before, during, and following the $CO_2$ injection, with the results shown in Table 5.1. Comparison of water flow rates in the two columns on the far right in the table shows that during the initial period of water injection the flow rate into the upper Sand 14-1 was 4.5 times the flow into the lower Sand 16-2. The record of injection rates in Figure 5.2 shows that there was a marked change in the water flow rate, before and after the injection of $CO_2$. The distribution of water between the two sands after $CO_2$ injection, in the third row of Table 5.1, shows that the change in total water injection rate was due to loss of flow into Sand 14-1, with the flow into Sand 16-2 unchanged.

## 5.3. $CO_2$ Injection

After the arrival of $CO_2$ at the test site in early March 2009, problems were encountered during attempts to begin $CO_2$ injection. In spite of several rounds of improvements to the pumping system during this early period, steady, continuous $CO_2$ injection could not be maintained for more than a short time. At the end of a project review meeting at the Geological Survey of Alabama on August 12, 2009, Project Manager Chandra Nautiyal and Olayinka Ogunsola, from DOE Headquarters, recommended that advice be sought from organizations having experience in handling and injecting liquid $CO_2$. On returning to his office following the meeting, the Principal Investigator contacted Reliant Gases, who had conducted the successful pilot injection of $CO_2$, supported by U.S. DOE through the Southeast Regional Carbon Sequestration Partnership, into a saline formation at Mississippi Power Company's Plant Daniel, near Pascagoula, MS. In spite of his being on vacation, Vance Vanderburg at Reliant kindly offered to look at the diagram of the pumping system to see if he could identify potential problems. Vance's conclusion, from inspection of the diagram, was that the system was properly configured. In his opinion, the most likely source of problems was the positive displacement pump, which, in his experience, can be quite temperamental when pumping liquid $CO_2$.

Denbury Resources then retained Steve Wegener, a senior engineer from Jacobs Linder Engineering (Metarie, LA) to study the system and make recommendations. A meeting of Steve Wegener with all those concerned with the performance of the injection system was held at Denbury Onshore's offices and at the test site in Citronelle on October 15, 2009. A follow-up meeting of the Denbury group with Steve Wegener was held in Citronelle on November 18, 2009, to witness a test of the $CO_2$ pumping system. That test was not successful, but based on the information and analysis that Steve Wegener provided, and observations during the test, Pete Guerra of Denbury designed a retrofit of the triplex positive displacement pump, which resulted in the following report by Pete to the research team on November 25th:

> We were successful pumping $CO_2$ into the well at Citronelle today. We pumped against 1800 psig for 20 minutes at 150 bbl/day. We also pumped against the choke to 3000 psi at 160 bbl/day. The solution was to fill the dead volume inside the pump cylinders with custom-made Teflon inserts. The dead space was around the plunger and between the inlet and outlet valves. The dead space was allowing the $CO_2$ to compress, which created a temperature spiral until eventually the $CO_2$ vaporized between the valves and would stop pumping around 1500 psig. The pump efficiency increased (the flow rate increased) as the discharge pressure increased, so I'm confident that we have the vapor-lock issue solved.

Table 5.1.
Distribution of Fluid Flow from Injection Well B-19-10 #2 into Sands 14-1 and 16-2,
Determined from Injection Profile Tests before, during, and following $CO_2$ Injection.

| Date | Fluid | Condition | - Fraction of Flow (%) - | | Total flow | - Flow Rate (bbl/day) - | |
|---|---|---|---|---|---|---|---|
| | | | Sand 14-1 | Sand 16-2 | (bbl/day) | Sand 14-1 | Sand 16-2 |
| Sept. 22, 2008 | Water | Baseline | 82 | 18 | 249 | 204 | 45 |
| June 10, 2010 | $CO_2$ | EOR | 60 | 40 | 170 | 102 | 68 |
| January 19, 2012 | Water | WAG | 35 | 65 | 69 | 24 | 45 |
| May 16, 2013 | Water | Following surfactant treatment and reduced injection pressure | 44 | 56 | 68 | 30 | 38 |

The next steps are as follows.

1. Re-sheave the pump maximum speed – to get our rate up.
2. Add a flow switch with shutdown on low flow – to protect against vapor lock.
3. Run the pump to low level in the tank to determine whether or not we'll need to lower the charge pump to achieve sufficient net positive suction head.

This successful modification ended the nine-month period, from March through November 2009, labeled "Testing $CO_2$ Injection" in Figure 5.2, during which little injection of either water or $CO_2$ took place.

The Denbury group in the field at Citronelle replaced the sheave and implemented the low-flow shut-down system needed to protect the triplex pump and began around-the-clock $CO_2$ injection at the test site on December 22, 2009. The injection rate settled at 46.5 tons $CO_2$/day, the exact center of the range of 35 to 58 tons/day anticipated from reservoir simulations by Eric Carlson and Dino Theodorou and Denbury's experience in carbonate reservoirs.

However, after a short period of trouble-free operation at the injection rate of 46.5 tons $CO_2$/day, problems with the triplex pump surfaced again, as damage to the Teflon inserts, described in Pete Guerra's message above, that had been installed to minimize dead volume in the pump. In spite of these problems, Michael Sullivan and Franklin Everett, leading the work in the field, were able to continue injection, with constant attention and maintenance to the pump, for about 11 hours each day. Twenty-four tons of $CO_2$ were typically injected per day; equal to approximately 70% of the anticipated minimum rate (35 tons/day). Then, on December 29th, a tubing leak was detected, requiring a complete shut-down for repair. $CO_2$ in the ground at that point stood at 380 tons. A workover rig was brought in to replace the tubing as quickly as possible. While the tubing was being replaced some improvements were made in the design of the Teflon inserts.

Replacement of the tubing in the injector was completed on January 25, 2010, and pumping and injection of $CO_2$ resumed on January 27. The average rate of $CO_2$ injection, including down time for maintenance, then stabilized at 31 tons/day. The history of $CO_2$ injection, beginning on December 1, 2009, is shown in Figure 5.3. At the average rate of 31 tons/day, injection of the 7500 tons allocated for the test was expected to be complete in September 2010. To allow some additional time for trouble shooting, observation of response, and analysis of data, an 8-month no-cost extension of Phase II, from April 30 to December 31, 2010, was requested by UAB and approved by NETL.

Continuous injection of $CO_2$ was maintained at the average rate of 31 tons/day from January 27 to the end of the planned injection. The original injection target of 7500 tons $CO_2$ was reached on September 12, but because the contract with Airgas Carbonic, the provider of the liquefaction and transportation services, provided for an extra 5 to 10% of $CO_2$, to allow for possible losses during processing and trucking, the injection was continued to 8036 tons, which was reached on September 25th, concluding the $CO_2$ injection.

The record of the $CO_2$ injection is compared, in Figure 5.3, with the reservoir simulation performed by Eric Carlson using SENSOR (Coats Engineering, Inc.). The average injection rate of 31 tons/day is in good agreement with the average rate of 35 tons/day anticipated by the simulation. As mentioned in Section 5.1 and shown in Figure 5.3, the injection rate gradually increased toward

the end of the $CO_2$ injection, often exceeding 40 tons/day during the final months. The upward trend can also be seen in the daily record of the $CO_2$ injection rate in Figure 5.2.

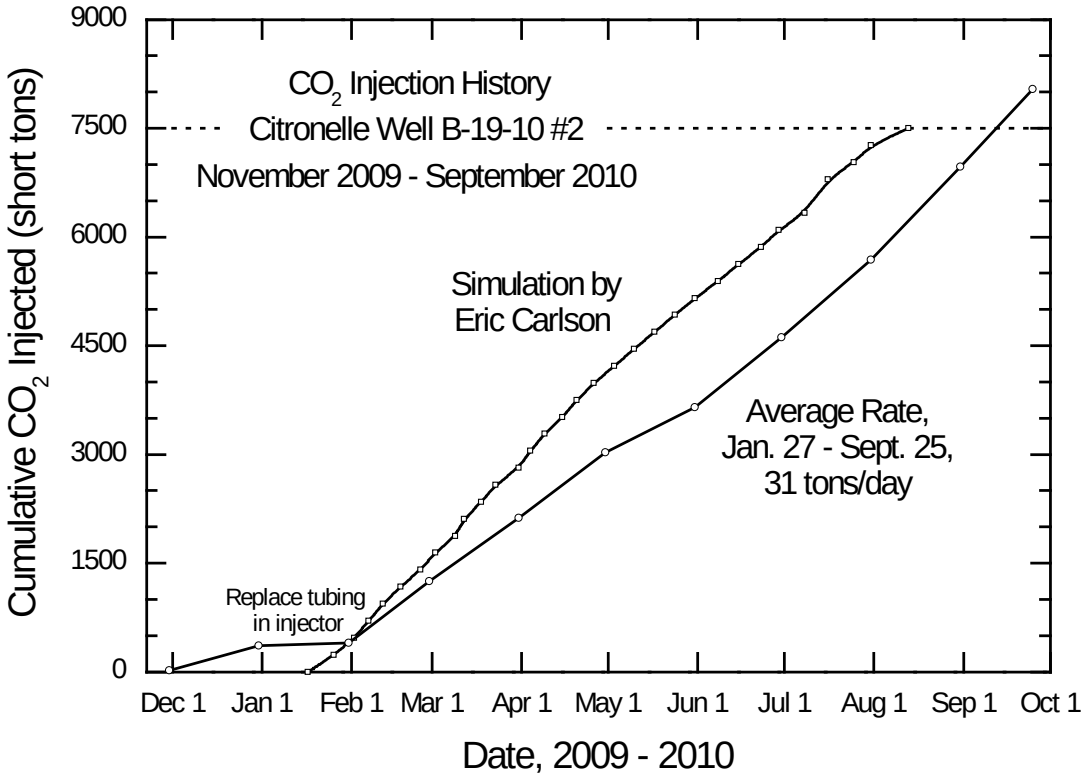


Figure 5.3. Record of the $CO_2$ injection and comparison with the reservoir simulation by Eric Carlson using SENSOR (Coats Engineering, Inc.). The average injection rate from January 27 to the end of the injection on September 25, including down time for maintenance, was 31 tons/day. The total amount of $CO_2$ injected was 8036 tons.

### 5.4. Response to $CO_2$ Injection

Oil produced from three wells in the test pattern (B-19-7, B-19-8, and B-19-9) is gathered, along with production from five other wells to the north and east, at Tank Battery B-19-8. Produced oil from well B-19-11 in the test pattern goes to Tank Battery B-19-11, along with production from three other wells to the west and south.

The record of oil production at Tank Battery B-19-8 during the period from January 2008, almost two years before the start of $CO_2$ injection, through April 2014, is shown in Figure 5.4a. During the initial water injection, from July 2008 to March 2009, oil production had increased, but that tend reversed during the period when no water or $CO_2$ was injected, and oil production then declined, from March to December 2009. Beginning in January 2010, coinciding with the start of continuous $CO_2$ injection, the decline in production was reversed, and, from January to September 2010, when the $CO_2$ injection was complete, oil production increased at the average rate of 18 bbl/day/year.

However, in October 2010, following the return to water injection, oil production began to decline. The decline accelerated in subsequent months, dropping, by March 2011, to only 36% of

the rate at the September 2010 peak and to less than half of the rate just before the start of $CO_2$ injection. One reason for the decline is apparent in Figure 5.4b, which shows the frequency with which the power oil pumps in wells whose fluids are gathered at Tank Battery B-19-8 had to be pulled because of excessive wear due to contamination of the power oil with particles mobilized by $CO_2$ and water. The frequency of pump pulls had begun to increase in August 2010, just before the end of the $CO_2$ injection, and increased by approximately a factor of ten from July 2010 to January and February 2011, when oil production approached its lowest point. As they were pulled, the pumps were replaced by new ones having longer stroke and parts made from harder material, so the frequency of pump maintenance began to decline in February 2011 and there was a corresponding increase in oil production over the next 12 months, to 44 bbl oil/day in March 2012. The subsequent rates of 33-43 bbl/day are lower than the peak rate of 59 bbl oil/day recorded in September 2010 and lower than the rate of 45 bbl oil/day just before the start of $CO_2$ injection in December 2009.

A second reason for the decline in oil production at Tank Battery B-19-8, beginning at the end of the $CO_2$ injection and return to water injection in September 2010, is that the water injection rate, which had been 170 bbl water/day just before $CO_2$ injection was begun, decreased dramatically, from 259 and 293 bbl/day on the first and second full days of water injection, respectively, following the $CO_2$ injection, to an average rate of 67 ± 21 bbl/day on the following days and remained, except for occasional spikes, at this low level, as shown in Figure 5.2.

The response to $CO_2$ injection at Tank Battery B-19-11, where oil from the fourth producer in the inverted five-spot is collected, shown in Figure 5.5a, was quite different from that observed at Tank Battery B-19-8. In contrast to the immediate increase in oil production observed at Tank Battery B-19-8 at the onset of $CO_2$ injection, production at Tank Battery B-19-11 continued for four months on the declining trajectory that it had been following for the previous 10 months. Then, coinciding with breakthrough of $CO_2$ at Well B-19-11 in May 2010, production at the battery abruptly decreased, by approximately the typical production from Well B-19-11 (8 to 9 bbl/day), then continued its steady decline over the next two years to production in the range from 21 to 30 bbl oil/day. Produced gas at Well B-19-11 was so excessive that the well was killed on September 2, 2010, three weeks before the end of $CO_2$ injection, and remained shut in until May 5, 2011. Because Well B-19-11 was shut in during the transition from $CO_2$ back to water injection, the power-oil pumps in wells on Tank Battery B-19-11 were not subject to the erosion-corrosion experienced in the wells on Tank Battery B-19-8, as shown by the record of pump pulls from wells on Tank Battery B-19-11, in Figure 5.5b.

## 5.5. Diagnostic Testing During and Following $CO_2$ Injection

### *5.5.1. $CO_2$ Breakthrough*

***Detection of $CO_2$ in Produced Gas.*** On May 25, 2010, five months after continuous $CO_2$ injection began, high pressure was detected in the vertical oil/water separator at Tank Battery B-19-11, where produced fluids from Well B-19-11 are collected. Well B-19-11 is the producer in the southwest corner of the test pattern, farthest from the injector. Tommy Miller and Michael Sullivan tested the gas in the head space of the power oil tank using a Draeger tube and detected a high level of $CO_2$. Produced gas samples, for detailed analysis, were collected by Peter Walsh on the same day. Close agreement of the delta carbon-13 isotope ratio in $CO_2$ ($\delta^{13}CO_2$) in the sample of produced gas with the isotope ratio in the injected $CO_2$, showed that the $CO_2$ in produced gas at

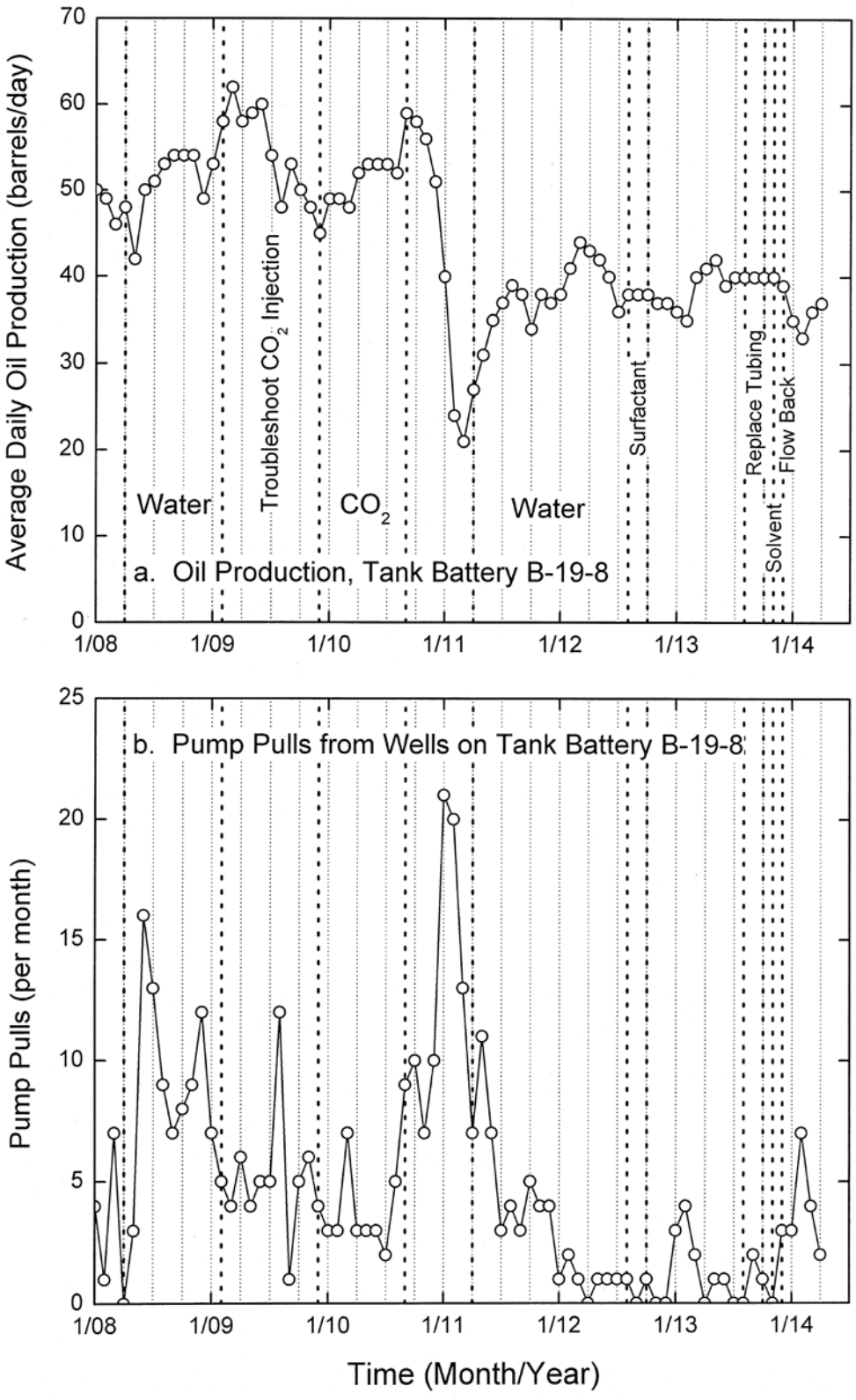


Figure 5.4. Response to $CO_2$ injection at Tank Battery B-19-8. a. Oil production at Tank Battery B-19-8, which receives fluids from Wells B-19-7, B-19-8, and B-19-9, from January 2008 to April 2014. b. Number of times per month that power oil pumps in wells on Tank Battery B-19-8 had to be pulled for maintenance or replacement, from January 2008 to April 2014.

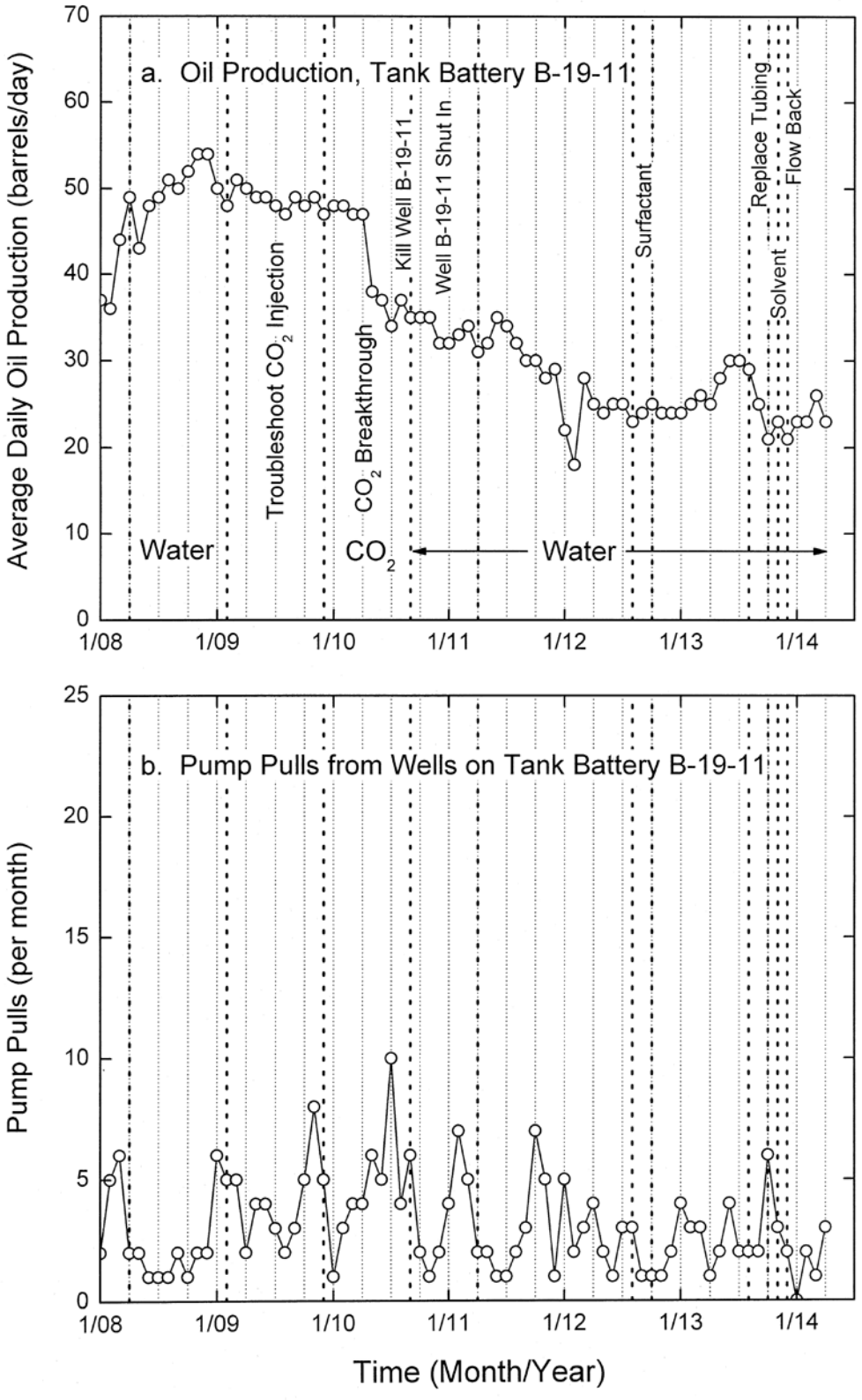


Figure 5.5. Response to $CO_2$ injection at Tank Battery B-19-11. a. Oil production at Tank Battery B-19-11, which receives fluids from Well B-19-11, from January 2008 to April 2014. b. Number of times per month that power oil pumps in wells on Tank Battery B-19-11 had to be pulled for maintenance or replacement, from January 2008 to April 2014.

Well B-19-11 was breakthrough from $CO_2$ injection at B-19-10 #2.* Rapid breakthrough of $CO_2$ was a great surprise, because no evidence of natural fractures had ever been seen in all of the work with drill core from Citronelle sands by Jack Pashin and his coworkers at the Geological Survey of Alabama. The records also indicate that Well B-19-10 #2 had never been intentionally hydraulically fractured.

Another set of produced gas samples was collected on August 4, 2010. The composition of produced gas from all four producers in the test pattern and the analysis of the injected $CO_2$, from the storage tank, are compared in Table 5.2. The gas from one well, B-19-7, has approximately the same $CO_2$ content as gas from all of the wells before $CO_2$ injection began, and its low value (large

Table 5.2.
Analyses of Samples of Produced Gas and Injected $CO_2$ Collected on August 4, 2010.

| Well Name | B-19-11 | B-19-11 | B-19-7 | B-19-8 | B-19-9 | CO2 Tank |
|---|---|---|---|---|---|---|
| **Gas Composition** | | | | | | |
| C1 | 0.66 | 0.67 | 20.57 | 29.02 | 36.17 | 0.02 |
| C2 | 0.45 | 0.44 | 5.50 | 5.58 | 6.26 | 0.01 |
| C2H4 | 0.00 | 0.00 | 0.00 | 0.00 | 0.00 | 0.00 |
| C3 | 1.13 | 1.05 | 8.27 | 7.59 | 7.14 | 0.06 |
| iC4 | 0.67 | 0.62 | 3.18 | 2.85 | 2.46 | 0.03 |
| nC4 | 1.24 | 1.14 | 5.53 | 5.07 | 4.11 | 0.09 |
| iC5 | 0.41 | 0.38 | 1.12 | 1.06 | 0.80 | 0.03 |
| nC5 | 0.87 | 0.80 | 1.99 | 1.93 | 1.40 | 0.06 |
| C6+ | 1.21 | 1.07 | 1.98 | 1.46 | 1.12 | 0.08 |
| H2S | 0.00 | 0.00 | 0.00 | 0.00 | 0.00 | 0.00 |
| He | 0.00 | 0.00 | 0.05 | 0.12 | 0.12 | 0.00 |
| H2 | 0.01 | 0.02 | 0.03 | 0.08 | 0.09 | 0.00 |
| Ar | 0.00 | 0.00 | 0.43 | 0.25 | 0.06 | 0.00 |
| O2 | 0.01 | 0.02 | 0.83 | 0.42 | 0.02 | 0.03 |
| N2 | 0.14 | 0.19 | 47.49 | 30.96 | 11.60 | 0.14 |
| CO | 0.02 | 0.02 | 0.00 | 0.00 | 0.00 | 0.00 |
| CO2 | 93.18 | 93.58 | 3.03 | 13.61 | 28.65 | 99.45 |
| Units | % | % | % | % | % | % |
| **Gas Isotope** | | | | | | |
| † δ13CO2 | -2.8 | -2.8 | -19.9 | -8.2 | -6.8 | -2.9 |

† $\delta^{13}CO_2 = [(^{13}C/^{12}C)_{sample}/(^{13}C/^{12}C)_{reference} - 1] \times 1000$

*We are indebted to Jack C. Pashin for suggesting the use of the carbon-13 to carbon-12 isotope ratio to distinguish injected $CO_2$ from native $CO_2$.

negative number) for $\delta^{13}CO_2$ is characteristic of solution gas. The $CO_2$ and $\delta^{13}CO_2$ analyses for the other wells show that the order of $CO_2$ breakthrough at the producers was B-19-11, B-19-9, then B-19-8.

Produced gas from wells both inside and outside the test pattern was then monitored for increased $CO_2$ using Draeger Tubes. The record of $CO_2$ in produced gas in April 2011 is summarized in Table 5.3. Breakthrough at Well A-25-10, far to the southwest of the injector, is very surprising and provides evidence for distant travel of $CO_2$ across depositional trends.

Table 5.3.
$CO_2$ Content of Produced Gas from Wells
in and near the Test Pattern, April 12, 2011.

| Well | $CO_2$, volume %[a] |
|---|---|
| A-25-8 | ~ 0 |
| A-25-10 | 15 |
| B-19-7 | ~ 0 |
| B-19-8 | 25 |
| B-19-9 | ~ 0 |
| B-19-11 | 57 |
| B-20-4 | ~ 0 |
| B-20-5 | 10 |
| B-30-4 | ~ 0 |

a. ~ 0 indicates a level of $CO_2$ not significantly greater than the 3 vol% typical of Citronelle solution gas.

***$CO_2$ Breakthrough and Direction of Maximum Horizontal Compressive Stress.**** Early breakthrough of $CO_2$ to wells A-25-10, B-19-11, and B-20-5 indicates major extension of the $CO_2$ plume toward the east-northeast and the west-southwest, as shown in Figure 5.6. Accordingly, breakthrough occurred in wells outside the original inverted five-spot pattern employed in this study. All production wells in the area have been hydraulically fractured, whereas the injection well has not, to our knowledge, been hydraulically fractured. Observations from cores indicate that natural fractures in the Donovan Sand are extremely rare, and so induced fractures are the only known fractures that could affect the $CO_2$ flood. The maximum horizontal compressive stress in the subsurface of Alabama is typically between an azimuth of 70 to 80°, and plume extension may have been close to this direction. One explanation of the early breakthrough is that the plume extended along induced fractures and was captured by wells favorably located along the maximum horizontal stress. Whether a fracture was induced in the injection well during water or gas injection is unclear, although the lack of natural fractures in the reservoir may indicate that the reservoir is under

*Contributed by Jack C. Pashin, then at the Geological Survey of Alabama, now at Oklahoma State University.

significant stress and can be fractured easily when pore pressure is increased. Regardless of the precise causes, unexpected plume extension has strong implications for the applicability of $CO_2$-enhanced recovery in Citronelle Field and should be considered when selecting injection and production wells for enhanced recovery operations.

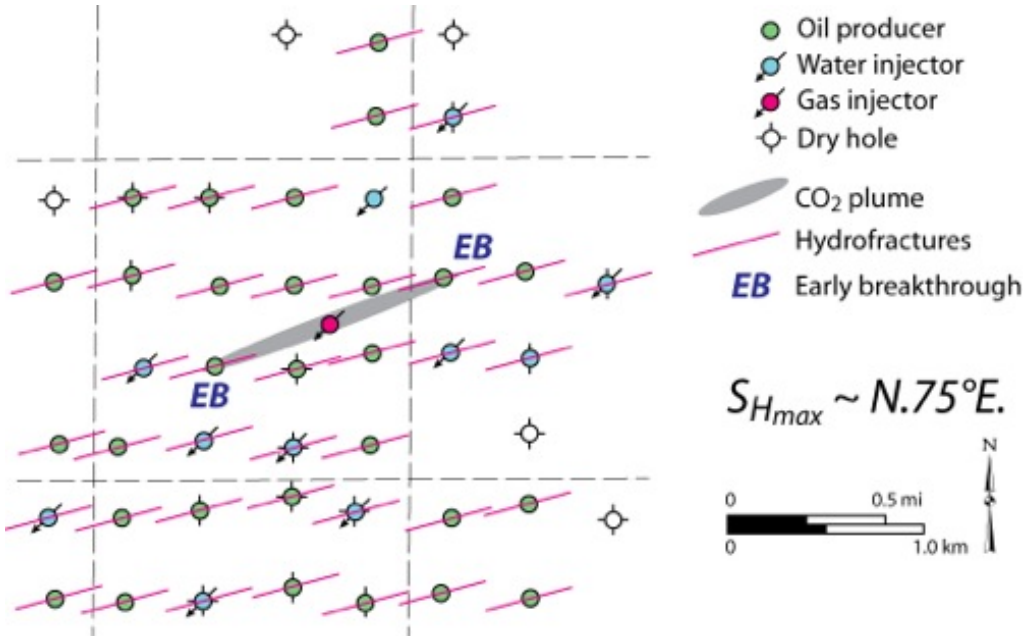


Figure 5.6. Wells in the vicinity of the $CO_2$ injection pilot test (the injector, Well B-19-10 #2 is indicated by the red-filled circle near the center), showing the likely orientation of hydraulic fractures in the direction of maximum horizontal compressive stress, ~ North 75° East, the preferential migration of the $CO_2$ plume in the direction of the fractures, and the location of wells where early breakthrough of $CO_2$ was observed (Jack C. Pashin, Oklahoma State University).

### *5.5.2. Pressure-Transient Injection and Fall-Off Test*

Diagnostic testing continued with a pressure-transient injection and fall-off test, from November 28 to December 12, 2011. The analysis, by Eric Carlson, of the results from that test is presented in Section 4.3. Dr. Carlson concluded that there is a substantial hydraulic fracture originating at the injector, having a total length of 600 to 1000 ft. The pressure-transient test does not provide any information about the direction of the fracture, but the most likely direction is that of maximum horizontal compressive stress in the Southeastern U.S., typically N70E to N80E, as described by Jack Pashin, in the subsection just above. In view of this evidence, the following are likely outcomes: (1) A hydraulic fracture along the direction of maximum horizontal compressive stress was opened by water or $CO_2$ injection into Well B-19-10 #2, and (2) The fracture provided a preferential pathway for $CO_2$, explaining the early breakthrough and excessive produced gas at Well B-19-11, and compromising the sweep efficiency of $CO_2$ in the pilot test.

### *5.5.3. Loss of Injectivity to Water and Properties of the Injection Targets*

Well B-19-10 #2, the injector in the inverted five-spot well pattern for the $CO_2$-EOR pilot test, experienced a marked decrease in injectivity on returning to water injection in September 2010,

following injection of the 8036-ton slug of $CO_2$. The problem can be seen in the injection data for Well B-19-10 #2 during the pilot test, shown in Figure 5.2. The earliest measurements of the water injection rate began in May 2008, shortly after conversion of Well B-19-10 #2 from producer to injector. The average injection rate during the long period of steady water injection from July 2008 to March 2009, toward the left in Figure 5.2, was 160 ± 18 bbl/day (mean and standard deviation). Following that observation of baseline performance, there was little injection of either water or $CO_2$ for approximately 9 months, during trials and trouble-shooting of the $CO_2$ pumping and injection system. The 8036 tons of $CO_2$ were injected from December 2009 to September 2010.

The $CO_2$ injection was completed on September 25, 2010, and water injection began 4½ hours later. On September 26, 259 bbl of water were injected, followed by 293 bbl on September 27. However, on September 28, the injection rate dropped to just 40 bbl/day, and remained at low levels, averaging 67 ± 21 bbl/day from September 28, 2010, to July 24, 2012, as shown in the record of water injection following the $CO_2$ injection in Figure 5.2.

The results from the injection profile tests, summarized in Table 5.1, show that the change in water injection rate before and after injection of $CO_2$ was due to loss of flow into Sand 14-1, with the flow into Sand 16-2 unchanged. David Kopaska-Merkel, at the Geological Survey of Alabama, who performed the analysis of thin sections from the sands, made the following observations regarding the 14-1 and 16-2 Sands:

> The 14-1 Sand is much thinner than the 16-2 Sand and much finer grained. The one thin section from the 14-1 Sand is very fine. Thin sections from the 16-2 Sand indicate that it grades upward from conglomerate to silty very fine sand. The 14-1 Sand appears to contain less carbonate cement than the 16-2 Sand, so I don't think this could be a significant part of the problem. Because it is much finer grained, it wouldn't take much to clog the pores; I suspect this is what is going on. The thicker 16-2 unit is normally graded and parts of it aren't very permeable. However, it contains plenty of rock that is coarser and more permeable than any of the 14-1 Sand. It contains a fair amount of carbonate cement, but obviously this has not been remobilized in any deleterious fashion, because this is not the unit that is experiencing problems. Mineralogically there is not much difference between the two sand units, beyond the difference in carbonate cement abundance.

### *5.5.4. Surfactant Treatment*

A possible explanation for the large and rapid loss in injectivity to water, following the injection of $CO_2$, was thought to be capillary blocking of water flow by supercritical $CO_2$ trapped in what had previously been conducting pores.

Denbury Onshore's chemicals supplier was contracted to treat the water at the injector with surfactant, to evaluate the importance of capillary blocking. The injection rate data are shown on expanded scales in Figure 5.7, along with wellhead pressure measurements. The average injection rate during the period beginning at the left in Figure 5.7, up to the start of surfactant injection, from October 15, 2011 to July 24, 2012 was 67 bbl water/day.

Injection of surfactant began on July 25, 2012 at the initial rate of 4 gallons/day. As is standard practice, the high initial rate was reduced one week later, on August 1, to 2 quarts/day.

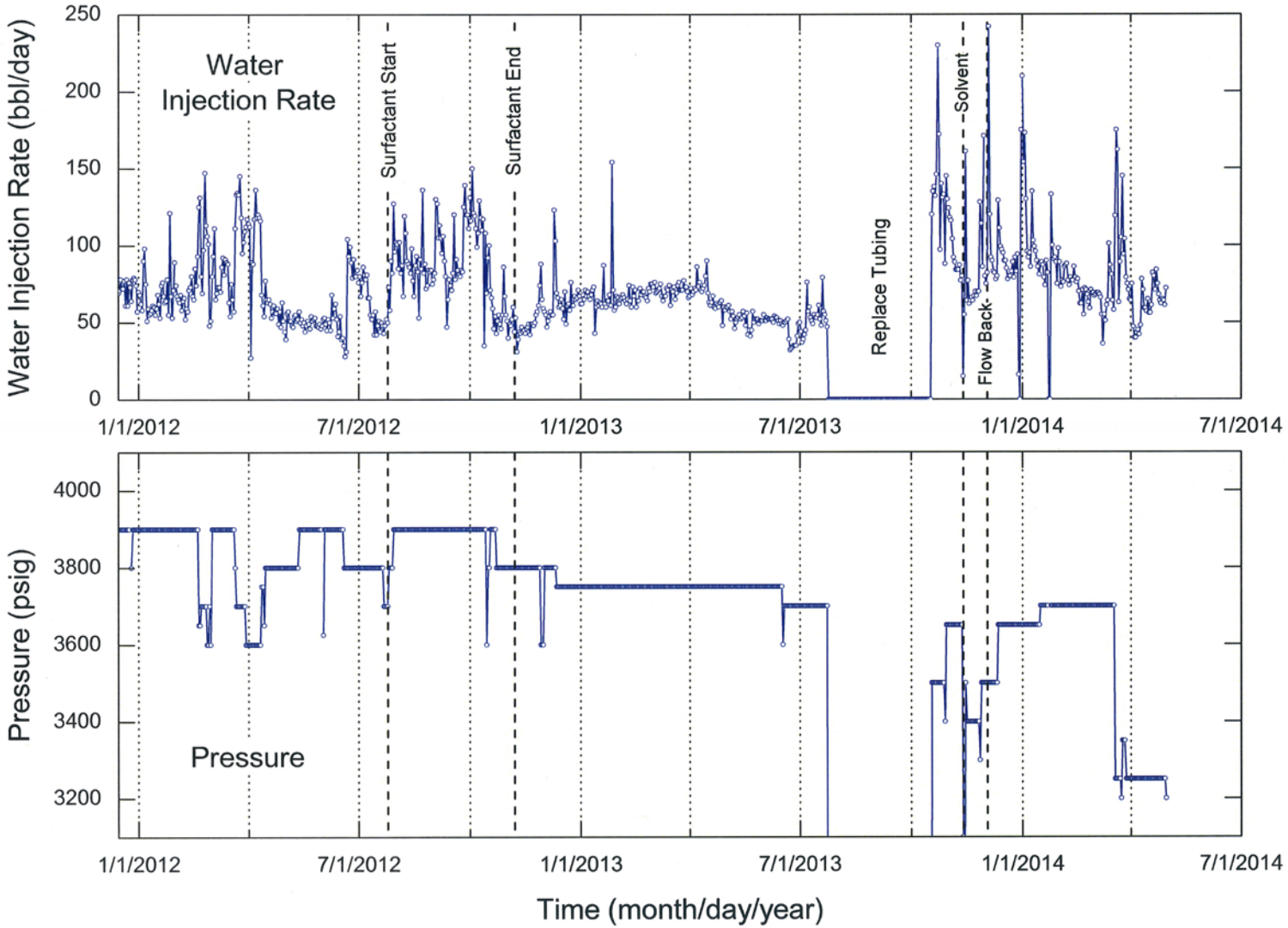


Figure 5.7. Rates (top) and pressures (bottom) of water injection into Well B-19-10 #2 in the inverted five-spot test pattern at Citronelle, from December 15, 2011, to April 30, 2014. Surfactant treatment began on July 25, 2012 and ended on November 7, 2012. Treatment with hydrocarbon solvent and asphaltene dispersant was attempted on July 24, 2013, but was interrupted by a tubing leak. The well was shut in for repair of the tubing from July 25 to October 17, 2013. Treatment with the solvent and dispersant was successful on November 13, 2013. The well was flowed back on December 3, 2013.

The water injection rate responded almost immediately, increasing from 50 bbl water/day on July 23-25 to 80-120 bbl water/day from August 8 to 14. The injection rate continued to increase, reaching 100 to 150 bbl water/day from September 26 to October 12, with an average of 120 bbl water/day.

In mid-October, the Denbury group in Citronelle began an effort to increase the pressure and water injection rates on other wells. The higher pressure resulted in some line leaks, requiring that those lines be shut in and that a pump be shut down to prevent blowing out other lines. The pressure at the injector during this period, beginning on October 15, 2012, was first unstable, then settled down at a value 100 psi lower than before. Surfactant treatment was stopped shortly thereafter, on November 7, 2012. The reduction in pressure provides an explanation for the low injection rates observed from October 23 to November 7.

The water injection rate during surfactant injection, when the pressure was constant at 3900 psig, from July 30 to October 14, 2012, averaged 95 bbl water/day. During the period following $CO_2$ injection but before the surfactant treatment, from September 26, 2010 to July 24, 2012, on the days when the pressure was 3900 psig, the average water injection rate was 63 bbl water/day. The surfactant treatment was therefore associated with a 50% increase in injection rate. Though certainly significant, the increase accompanying surfactant injection did not come close to restoring the injection rate to the average level of 160 bbl water/day before $CO_2$ injection, when the average pressure was only 3600 psig. Interestingly, after stopping the surfactant treatment on November 7, the water injection rate began a consistent upward trend, which continued even after a further reduction in pressure from 3800 to 3750 psig on December 12, 2012. That upward trend reversed, however, during April, May, and June 2013, and the injection rate returned to its previous low level, leaving no significant lasting effect of the surfactant treatment.

The period during which injected water was treated with surfactant is indicated on the records of oil production at Tank Batteries B-19-8 and B-19-11 in Figures 5.4 and 5.5. We note that, with the start of surfactant treatment in July 2012, the decline in production experienced at Tank Battery B-19-8 from March to July 2012 was halted, but only temporarily. At Tank Battery B-19-11, injection of surfactant coincided with the end of a long period of decline in oil production that began with $CO_2$ breakthrough and the abrupt drop in production during $CO_2$ injection, in May 2010.

The conclusions from the surfactant treatment is that while capillary blocking of water injection may have been significant, it is not the principal effect responsible for the loss in injectivity experienced on returning to water injection following the $CO_2$ slug, and the treatment with surfactant had no permanent effect on injectivity to water.

### *5.5.5. Treatment with Hydrocarbon Solvent and Asphaltene Dispersant*

Another possible cause of the loss in injectivity to water was thought to be precipitation of paraffins or asphaltenes left near the well bore by the extraction and outward migration of lighter hydrocarbons with the injected supercritical $CO_2$. Treatment of the injector, Well B-19-10 #2, with hydrocarbon solvent and asphaltene dispersant, to mobilize precipitated heavy ends, was begun on July 24, 2013. In the midst of the treatment with solvent, a leak developed in the tubing, interrupting the test. The tubing was replaced and the well was brought back on line with water injection on October 18, 2013. The treatment with hydrocarbon solvent and asphaltene dispersant

was done on November 13, 2013. The timing of replacement of the tubing and treatment with solvent and dispersant are identified in Figure 5.7 by the labels "Replace Tubing" and "Solvent." Treatment with the solvent and dispersant had only a very short-lived transient effect on water injectivity.

### *5.5.6. Flow-Back of the Injector to Remove Fragments of Internal Plastic Coating and Particles of Scale*

While pulling the tubing, following the development of the leak in July 2013, it was found that the internal plastic coating (IPC) of the tubing had been flaking off. Problems with the integrity of IPC were being experienced by Denbury Resources throughout its oilfield operations at around that time. The cause of the problem was thought to be a lapse in quality control on the part of the tubing supplier. The coated tubing was replaced with regular bare steel tubing.

While replacing the tubing in the injector, a sample of particles was recovered from the well. The sample was separated into three particle size fractions using sieves. Photographs of the three samples are shown in Figure 5.8. All of the particles, including the flakes of IPC with attached scale, in the largest size cut, are magnetic. Plugging by the finest particles, smaller than 0.3 mm (0.012"), is expected to have been the principal cause of the loss in injectivity to water of the finer-grained sand following the injection of $CO_2$. The particles of scale are thought to have been mobilized by the combined action of $CO_2$ and water. An attempt was made to flush out the particles by flowing back the injector.

Well B-19-10 #2 was flowed back on December 3, 2013, with ~250 bbl of water collected. On the following day, 242 bbl of water were injected, the second-highest water injection rate experienced during the entire pilot test. The only higher rate, 280 bbl/day, was recorded in August 2008, before the $CO_2$ injection. Following the flow-back, water injection rates rapidly declined, but remained at an average rate of 88 ± 31 bbl/day for the rest of the month, an unusually high average rate for the post-$CO_2$-injection period. Particles of oxide scale are suspected to have been the principal cause of the loss in injectivity to water following the $CO_2$ injection. Flow-back was not able to dislodge and remove them.

### *5.5.7. Summary of Results from the Diagnostic Tests and Oil Production*

Each of the attempts to restore injectivity to water: treatment with surfactant, treatment with hydrocarbon solvent and asphaltene dispersant, and flow-back, has resulted in transient improvement in the water injection rate, but none of them has had a lasting effect on injectivity. The recent average rate, in March and April 2014, was 72 ± 26 bbl water/day, not significantly higher than the average rate of 67 ± 21 bbl/day observed from the end of the $CO_2$ injection on September 28, 2010, to the beginning of surfactant treatment on July 24, 2012.

Plugging of the finer-grained Sand 14-1 by particles of scale, mobilized by the combined effects of $CO_2$ and water on oxide scales and difficult to dislodge and remove by flow-back, is thought to have been the principal cause of the loss in injectivity to water following the injection of $CO_2$.

a. Larger than ~1.3 mm (0.050").

b. 0.3 to ~1.3 mm (0.012 to 0.050").

c. Smaller than 0.3 mm (0.012").

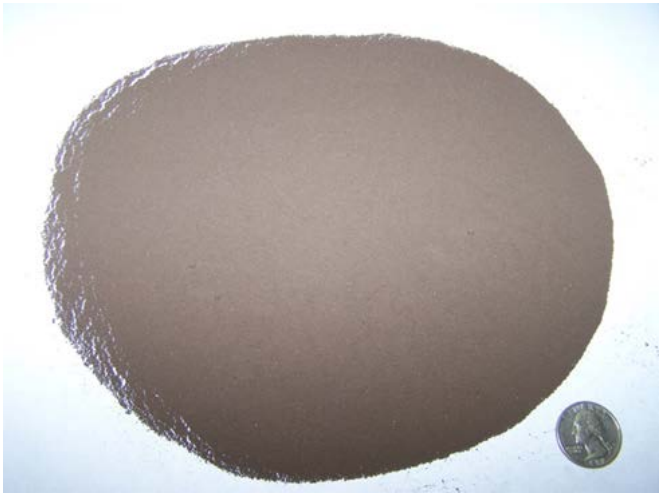

Figure 5.8. Particles of internal plastic coating and oxide scale recovered from the injector, Well B-19-10 #2, during repair of a tubing leak, separated into three size fractions. The internal plastic coating is concentrated in the largest size fraction. All of the particles, including the internal plastic coating with its attached scale, are attracted to a magnet.

Uncertainty introduced into the baseline oil production at both tank batteries, during the troubleshooting of $CO_2$ injection, undermined the ability to make a reliable estimate of the incremental gain or loss in production associated with the $CO_2$ injection.

**Acronyms, Abbreviations, and Symbols in Section 5**

| | |
|---|---|
| IPC | internal plastic coating |
| $S_{Hmax}$ | direction of maximum horizontal compressive stress, degree |
| SENSOR | System for Efficient Numerical Simulation of Oil Recovery (Coats Engineering, Inc., http://www.coatsengineering.com/) |
| $\delta^{13}CO_2$ | delta carbon-13 isotope ratio in $CO_2$ = $[(^{13}C/^{12}C)_{sample}/(^{13}C/^{12}C)_{reference} - 1] \times 1000$ |

# 6. Soil Surface $CO_2$ Fluxes

Ermson Z. Nyakatawa, Latasha J.-T. Lyte, Loutrina T. Staley, and Rogers Atugonza
Department of Biological and Environmental Sciences
Alabama A&M University, Normal, Alabama

## 6.1. Background and Objectives

Geological sinks offer a huge potential for sequestration of carbon dioxide worldwide, to reduce emissions to the atmosphere of this greenhouse gas from anthropogenic sources. Carbon sequestration in terrestrial sinks presents an opportunity to mitigate the adverse effects of global warming by controlling atmospheric $CO_2$ enrichment. The National Energy Technology Laboratory (2012) estimated that oil and gas reservoirs in North America alone have the capacity for storage of 225 billion metric tons of $CO_2$.

The purpose of the studies reported herewith was to examine the possibility that $CO_2$ injected into oil wells for EOR might migrate upward to the ground surface and the atmosphere rather than being retained in the oil-bearing formation at the project site. The present section summarizes the findings from field and laboratory measurements which were undertaken in conjunction with the pilot injection of $CO_2$ at Citronelle Field, to address this question. The objectives of this component of the investigation were:

1. To measure baseline, pre-injection, and post-injection $CO_2$ fluxes around selected oil wells in the study area, before and after the pilot injection of $CO_2$ for EOR in the Citronelle Field.

2. To investigate the relationships between measured $CO_2$ fluxes and physical and chemical properties of the soils near wells used for injection of $CO_2$ and production of oil during the pilot test of $CO_2$-EOR in the Citronelle Field.

## 6.2. Methodology and Instrumentation

### *6.2.1. Study Location*

We conducted this study in a forest ecosystem in the Citronelle Oil Field in Mobile County, Southwest Alabama (Figure 6.1). The sampling plan included five oil wells, consisting of three producers, Wells B-19-7, B-19-8, and B-19-9, a plugged and abandoned well, B-19-10 #1, and an injector, Well B-19-10 #2, arranged as shown schematically in Figure 6.2. The wells are in the small clearings next to their labels, at the center of the aerial photograph in Figure 6.1. Gas samples, soil samples, and measurements of soil moisture and temperature were taken at three locations around each well, labelled A, B, and C in Figure 6.2.

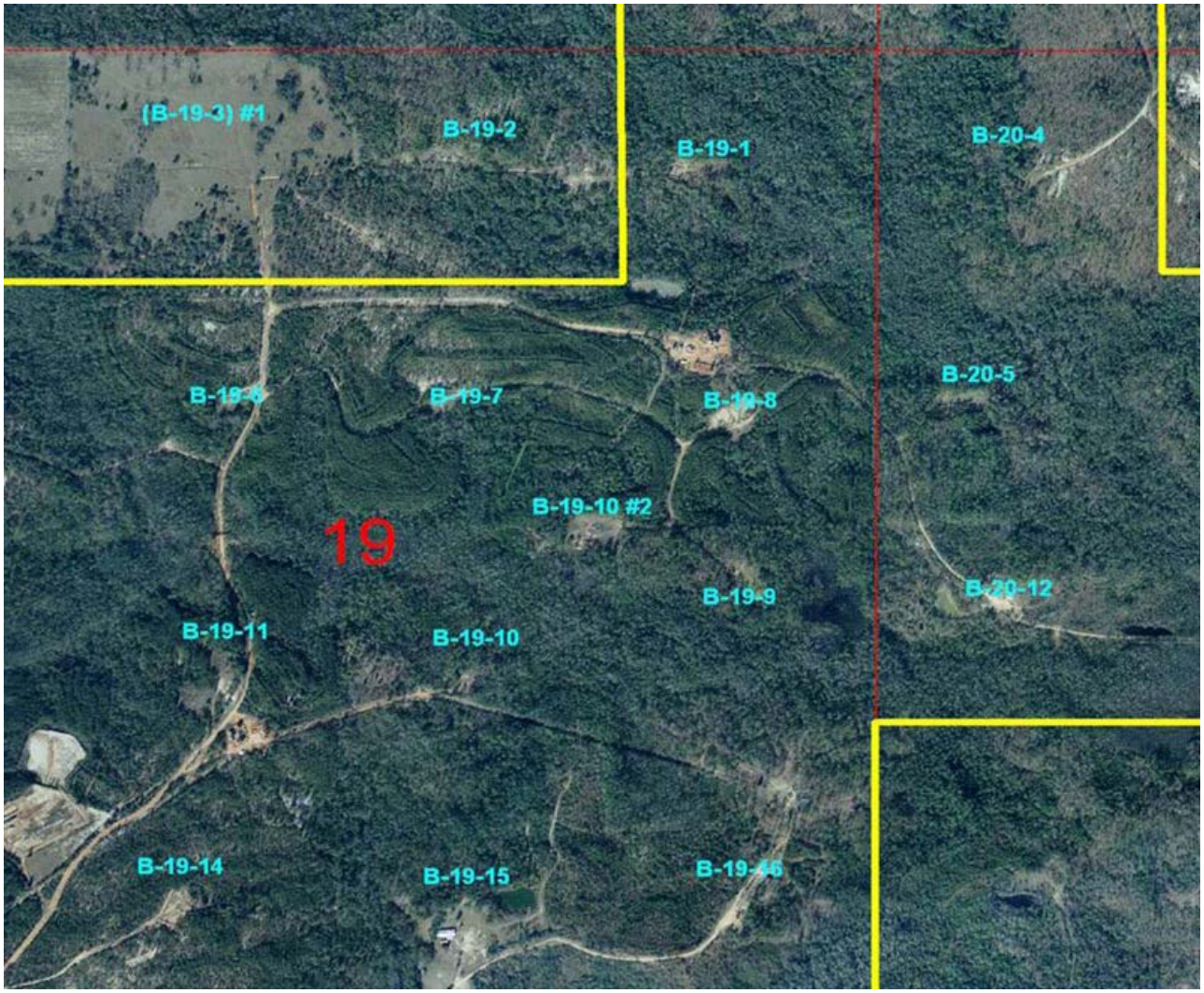


Figure 6.1. Aerial photograph of the study site showing the sampling locations, B-19-7, B-19-8, B-19-9, B-19-10 (also known as B-19-10 #1), and B-19-10 #2 in Citronelle Field, Southwest Alabama (Denbury Onshore).

The soil at Citronelle Field is classified by USDA as a Troup-Benndale. Troup (loamy, kaolinitic, thermic, Grossarenic, Kandiduduts) soil series are formed in unconsolidated sandy and loamy marine sediments on Coastal plain uplands. They have a thick sandy surface and subsurface layers, with loamy subsoil. This series is well drained and moderately permeable.

### *6.2.2. Soil Sampling*

Soil samples were collected at incremental depths of 0-5, 5-15, 15-30, 30-45, and 45-60 cm using a hand-operated soil auger, once in the summer, fall, winter, and spring during the study period. The samples were composited by depth and location at each well, put in sealable plastic bags, and transported to the laboratory at Alabama A & M University in cooler boxes. The samples were air dried on benches in the soil drying room and then ground using a Wiley mill (Wiley, Philadelphia, PA) to pass through a 2 mm mesh sieve, before performing chemical analyses. The

soils were analyzed for pH (Acumet LX pH meter) in deionized water in a 1:1 soil/water solution; total soil C and N (LECO TruSpec CN Analyzer, LECO Corp., St. Joseph, MI); extractable ammonium N ($NH_4^+$-N), nitrate N ($NO_3^-$-N), and P (EasyChem, Systea Scientific, Chicago, IL); and soluble salts electrical conductivity (EC) (Acumet LX conductance/resistance meter) (Bower and Wilcox, 1965). Samples for measurement of $NH_4^+$-N and $NO_3^-$-N were extracted using 2 g soil samples in 20 mL of 2 M KCl(aq), while those for measurement of P were extracted using 2 g soil samples in 20 mL of Mehlich III extractant. The soil and extractant solution were shaken for 5 to 10 minutes and filtered through Whatman #42 filter paper. The extracted solutions were analyzed for $NH_4^+$, $NO_3^-$, and P by a colorimetric method (Keeney and Nelson, 1982; Sims et al., 1995) using the Systea Scientific EasyChem analyzer.

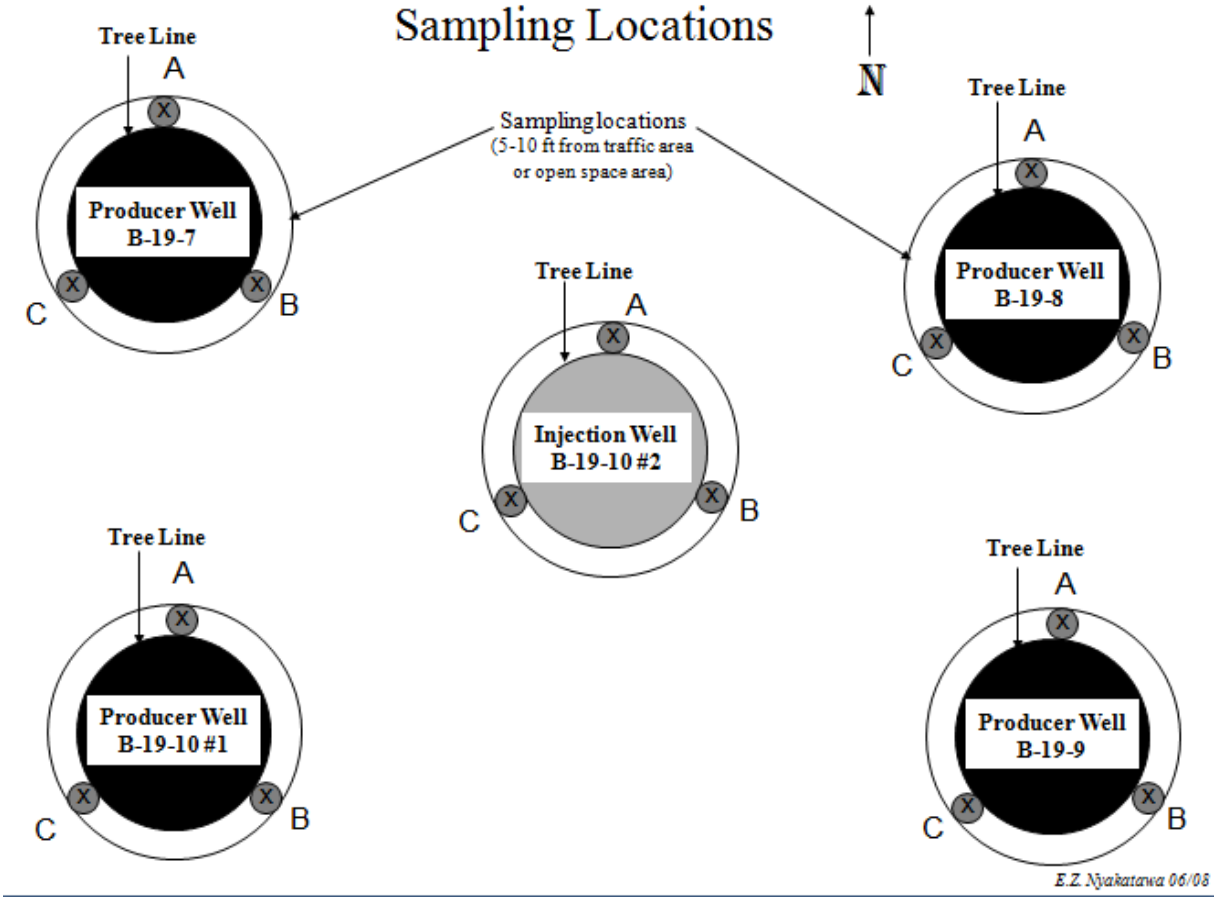


Figure 6.2. Sampling locations at Citronelle Field in Southwest Alabama (Nyakatawa, 2008). Well B-19-10 #1, at bottom left, had been temporarily abandoned when the present study began and could not be returned to production, so was plugged and abandoned.

### *6.2.3. Soil Gas Flux Sampling*

Carbon dioxide samples were collected using custom-built static flux chambers designed according to the USDA-ARS GRACEnet Chamber-based Trace Gas Flux Measurement Protocol (Figure 6.3). Each flux chamber consists of a fixed base and a removable cap.

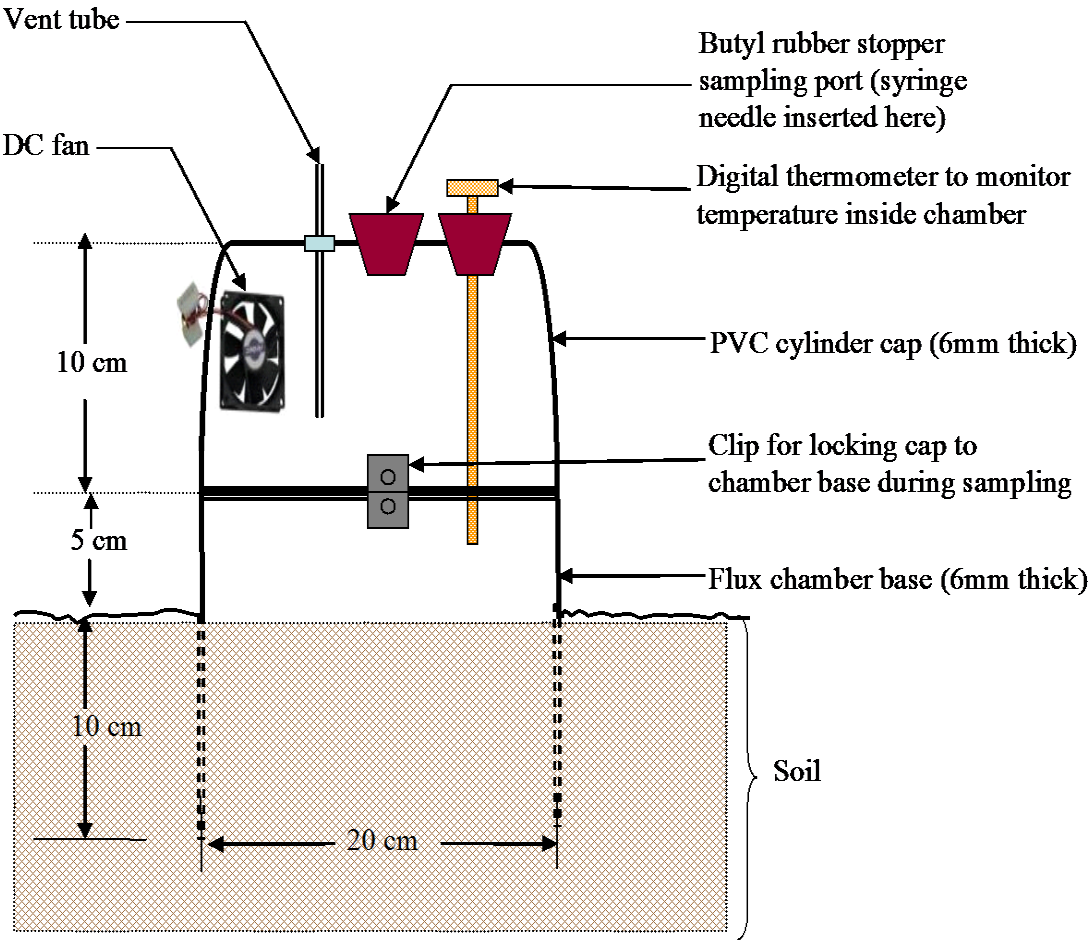


Figure 6.3. Schematic diagram of the flux chamber (Nyakatawa, 2005).

The base of the chamber was made from a 20 cm diameter, 6 mm thick, 15 cm long white PVC pipe, to enable the base of the chamber to cover approximately 314 $cm^2$ of the soil surface, about double the minimum soil surface area of 175 $cm^2$ required by the United States Department of Agriculture GRACEnet Sampling Protocol. The caps of the chambers were made from 10 cm long socket end-caps of the same white PVC pipe material used to make the base (Figure 6.3). The socket end-caps are designed to fit over the PVC pipe base. A plastic vent tube 10 cm long and 4.8 mm in diameter was inserted on one side of the flux chamber cap to equalize the pressures inside and outside the chamber. A sampling port consisting of a tight-fitting butyl rubber stopper into which a syringe needle was inserted during sampling was mounted on the cap. A second butyl rubber stopper holding a thermometer, to measure the temperature inside the chamber, was also mounted on the cap. A small fan, driven by a 12 V DC motor, was attached to the inside of the cap to mix the air inside the chamber during sampling.

The soil gas sampling system, consisting of the following equipment, was installed at each sampling site (Figure 6.4):

1. Surface gas sampling chamber
2. Soil thermometer (18 inches long)
3. Soil moisture tube
4. Soil gas sampling probes at depths of 0-20, 20-40, 40-60, 60-80, and 80-100 cm

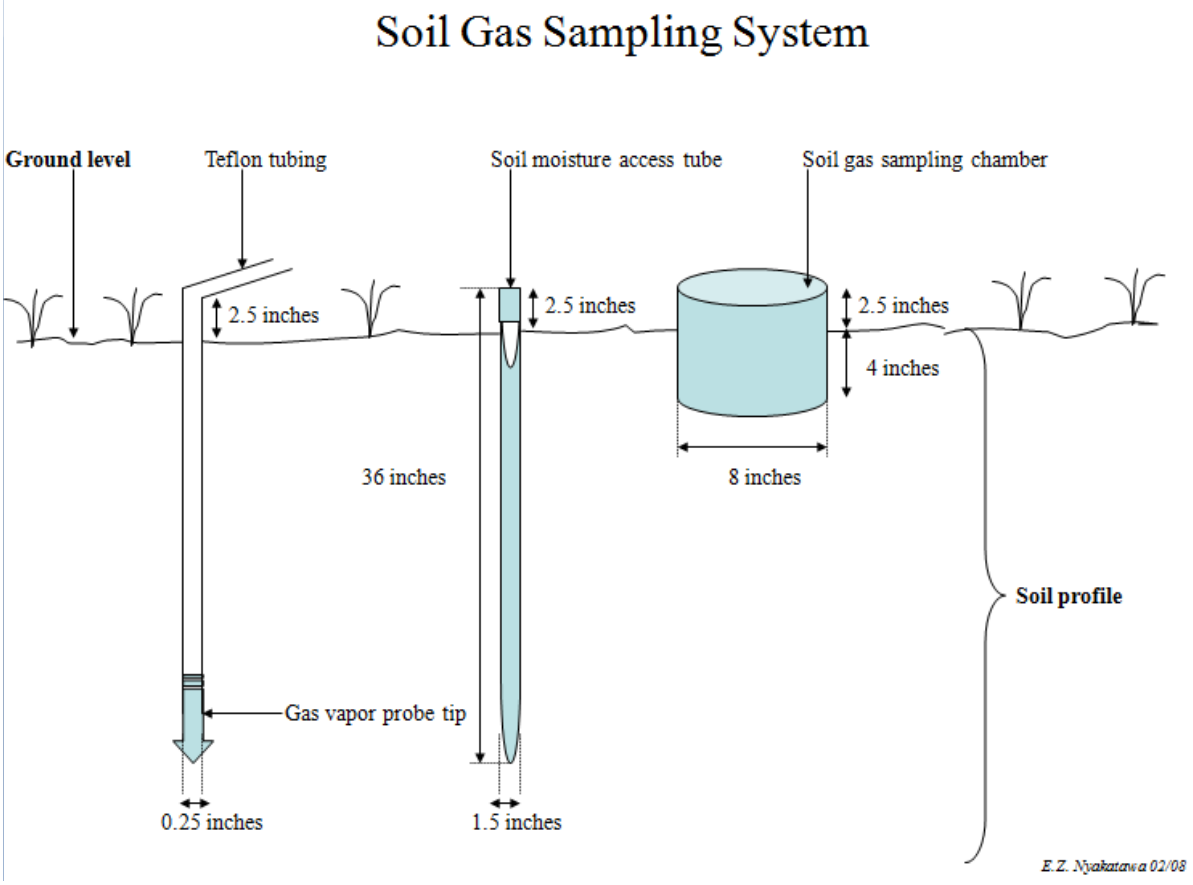


Figure 6.4. Soil gas sampling system at Citronelle Oil Field (Nyakatawa, 2008).

The chamber anchor bases were driven 10 cm into the ground, leaving about 5 cm above ground. Three chamber anchor bases were installed around each well at the locations labeled A, B, and C in Figure 6.2. The flux chambers were left open at all times, except during sampling (Figure 6.5, on the right). During sampling, the flux chamber cap was placed on the base of the chamber and soil gas samples were withdrawn into 30 mL polypropylene leak-proof disposable syringes, using a 22 gauge flat-end needle, at equally-spaced times of 0, 5, and 10 minutes, to enable the flux calculation. Sampling was conducted at regular intervals during the spring, summer, fall, and winter seasons.

Figure 6.5. Left: The $CO_2$ injection well. Right: Instruments at a sampling site, including the soil gas sampling chamber.

### *6.2.4. Soil Gas Flux Measurements*

The gas samples were analyzed using a CP-3800 GC gas chromatograph (Varian Inc., Palo Alto, CA) equipped with an electron capture detector (ECD), a flame ionization detector (FID) and a methanizer for $CO_2$ detection (Figure 6.6).

Carbon dioxide fluxes were calculated using the following equation (Hutchinson and Livingston, 1993):

$$f_o = \frac{\Delta C}{\Delta T} \times \frac{V}{A} \times \frac{M}{V_{mol}} \tag{6.1}$$

where $f_o$ is the flux of $CO_2$ to or from the soil (μg $m^{-2}$ $min^{-1}$), $\Delta C/\Delta T$ is the rate of change of $CO_2$ concentration inside the measuring chamber, $V$ (L) is the head-space volume in the measuring chamber, $A$ ($m^2$) is the area of soil covered by the measuring chamber, $M$ is the molecular weight of $CO_2$, and $V_{mol}$ is the molar volume of $CO_2$. During gas flux sampling, soil temperature in the top 45 cm (18 inches) of soil (using Mannix digital soil thermometers), chamber temperature, and soil moisture content at depths of 0-10, 20-30, 30-60, and 60-100 cm (using Theta Probe by Delta-T Devices, Cambridge, England) were recorded.

### *6.2.5. Statistical Analysis*

The data collected in this study were statistically analyzed using the General Linear Models (GLM) procedures of SAS software version 9.1.3 (SAS, 2007). Spearman's rank correlation coefficients were used to determine the relationships between $CO_2$ gas fluxes and soil properties. Regression analysis was used to develop regression models relating $CO_2$ fluxes to the environmental soil variables of temperature and moisture during sampling. The means were statistically analyzed and compared by depth at each well location.

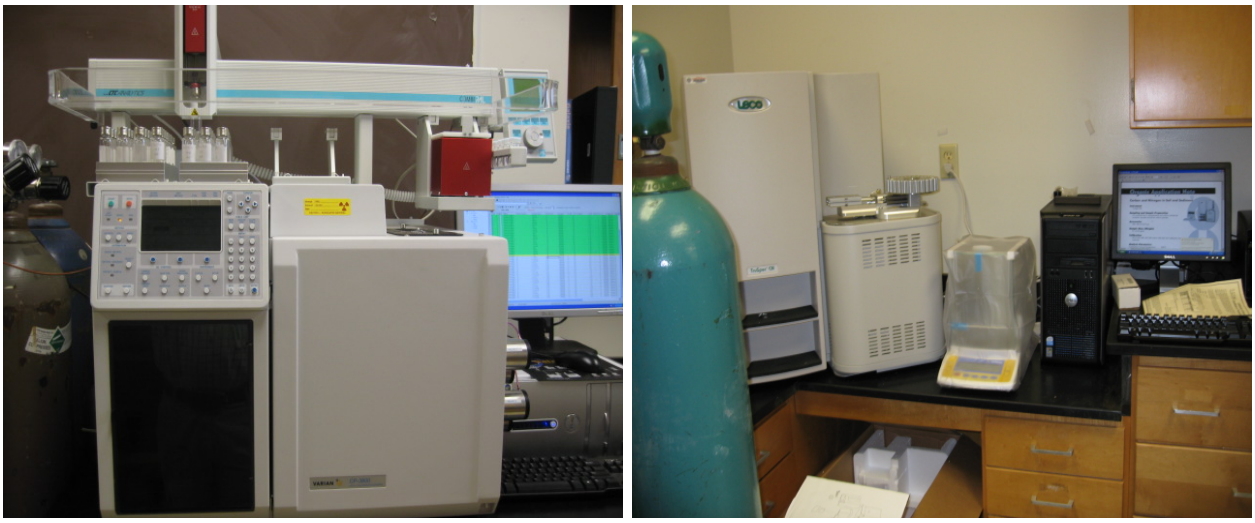

Figure 6.6. Left: Set up of the Varian CP-3800 GC for $CO_2$ analysis. Right: LECO TruSpec for soil C and N analysis.

## 6.3. Soil Characterization Measurements

The collection of soil characterization data, which was done by measuring chemical, physical, and biological properties of the soil around the oil wells was an important step in accomplishing the larger objective of monitoring soil surface $CO_2$ fluxes. This is based on the fact that soil $CO_2$ fluxes, which represent $CO_2$ exchanges between the soil and the atmosphere at their interface, occur naturally due to physical, chemical, and biological processes occurring in the soil in terrestrial ecosystems at any given time.

Depending on the prevailing conditions, the soil can be a net source, emitting $CO_2$ to the atmosphere, or a net sink, absorbing atmospheric $CO_2$. The major sources of soil $CO_2$ fluxes are the decomposition of organic matter and respiration by plant roots and soil fauna. Therefore, natural soil $CO_2$ fluxes are indicators of microbiological activity in the soil, responsible for mineralization of organic matter. Microbial activity occurs in soil surface layers where organic material, such as leaf litter, accumulates and provides a source of energy for soil microbes. The temperature and moisture content of soil are the most important physical factors affecting decomposition, and can have direct impact on soil $CO_2$ fluxes.

### *6.3.1. Soil pH*

Soil pH is one of the most important soil chemical properties, having a direct effect on soil biological, chemical, and physical process. Due to its influence on abiotic factors, which include carbon availability, nutrient availability, and solubility of metals, soil pH affects the soil microbial community. Fungi and bacteria are the principal microbial decomposers which aid in decomposing organic matter (Rousk et al., 2009). Decomposition of soil organic matter is slow in acidic soils (Jandl et al., 2007). Rousk et al. (2009) found that pH may also influence biotic factors in the case of fungi and bacteria in forest and agricultural soils.

The average pH measured in soils around the wells was 4.9 (Figure 6.7), which is acidic. The lowest pH value measured was 3.6, while the highest was 5.4. Our measurements are typical of this type of ecosystem, since acidic pH is common for soils under pine forest (Condo and Carter, 2002; Kamprath, 2011) which are low in organic C and lacking water-soluble basic cations such as $Ca^{2+}$, $Mg^{2+}$, and $K^{+}$. Nitrification can promote acidification.

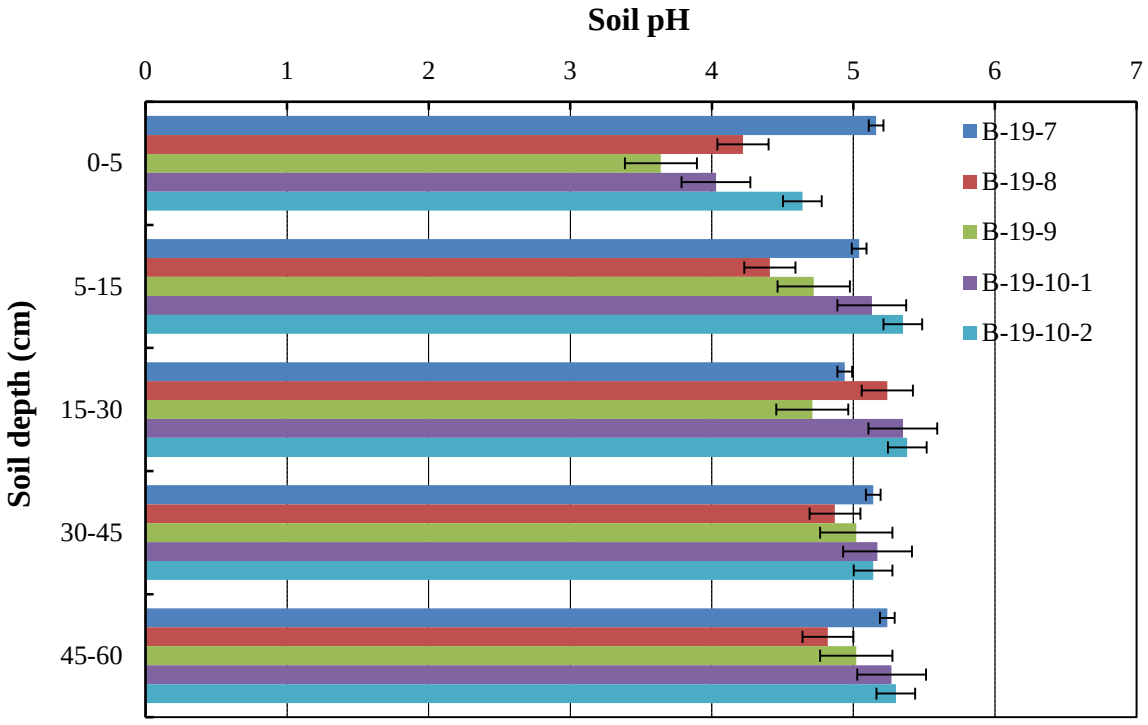


Figure 6.7. The pH of forest soils around the wells in the study area (the line bars represent standard errors).

Changes in soil pH only happen over a period of time, either naturally or if there is management of the soil. Over time, the pH of forest soils under pine trees stabilizes due to lack of soil management activities, in contrast to what happens in soil used for agricultural production. Therefore, as expected, we did not observe any significant changes in soil pH during the study period.

### *6.3.2. Soil Electrical Conductivity (EC)*

Soil electrical conductivity (EC) is an indicator of total dissolved solids (TDS). It gives an indirect measurement of salt content in the soil solution. Just as with soil pH, soil EC is an important soil chemical property having a direct effect on soil biological, chemical, and physical processes which affect soil microbial activities and, hence, soil $CO_2$ fluxes. Soil pH usually shows a strong relationship with EC (Johnson et al., 2001). In this study, we found positive correlations between soil pH and EC on all but one well, where soil pH was negatively correlated to EC. The measurement of EC is important in integrating physical, chemical, and biological factors which regulate functions in soil (Johnson et al., 2001).

In this study, we found that the surface soils were generally sandy with very low organic matter, most of it located in the 0-5 cm layer, and were characterized by high electrical conductivity of up to 5 $S \cdot m^{-1}$ (Figure 6.8). The highest EC values were observed at Well B-19-10 #1. These EC values are not typical of terrestrial forest soils. Since the study area is located near the Gulf of Mexico, the high EC values may indicate that the area could have been flooded by sea water some time ago. This theory was also supported by the fact that at most of the wells, the surface soils lacked a proper stratification order typically found in soil horizons of naturally settled soils. We sometimes found a band of sandy soil underneath a well-formed soil profile, which made it impossible to characterize the soil strength or compaction, close to the soil surface, using the intact core bulk density measuring system.

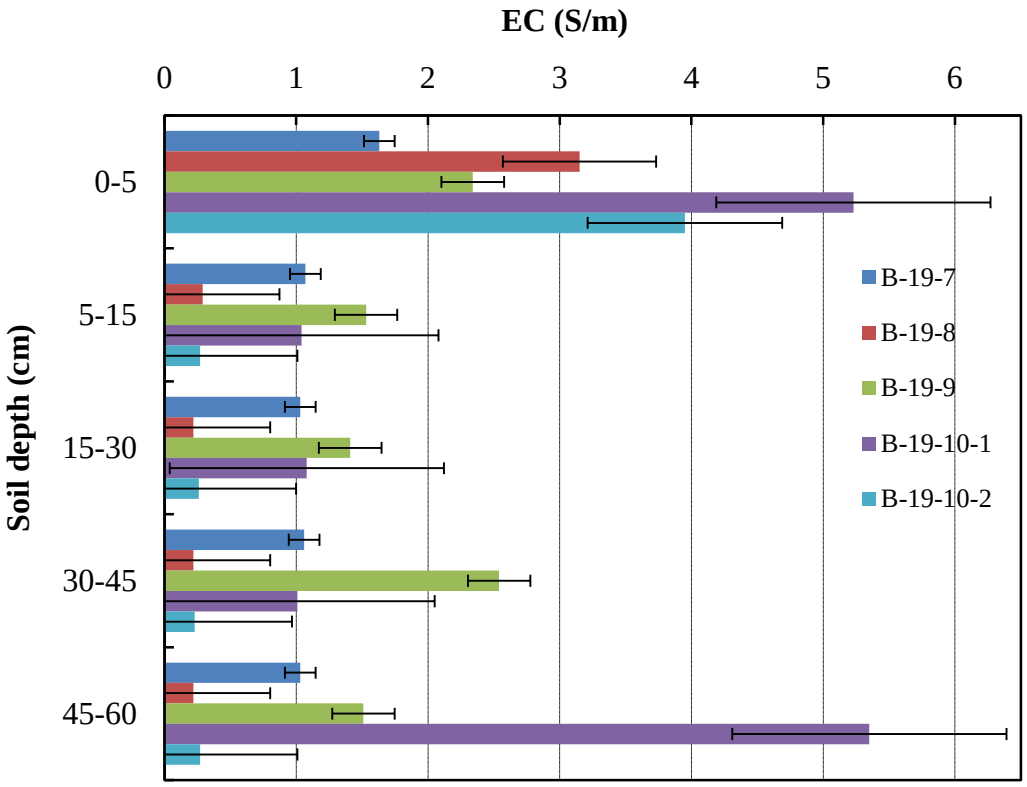


Figure 6.8. Electrical conductivity of forest soils around the wells in the study area (the line bars represent standard errors).

The significance of the low soil pH, coupled with high EC values of the surface soils around the oil wells in the study area, was that the surface soils were expected to have low microbial activity, low nutrient content, and low C and N content, due to the "harsh" environment. The expected implications of these characteristics would be low surface $CO_2$ emissions from the soil.

### *6.3.3. Soil Temperature*

Soil temperature provides the energy which drives the rate and extent of physical, biological, and chemical reactions occurring in the soil. It is one of the most important physical factors affecting microbial activity (Panosso et al., 2011), which affects, in turn, the decomposition of organic soil components. Therefore, soil temperature has both a direct and an indirect impact on surface $CO_2$ fluxes. In this study, soil temperature measurements showed a seasonal variation in which the temperatures were highest in the summer months, typically around August, with a mean for the month of 24.9 ºC across the sampling sites (Figure 6.9). The lowest temperatures were observed in winter with a mean of 15.5 ºC in March.

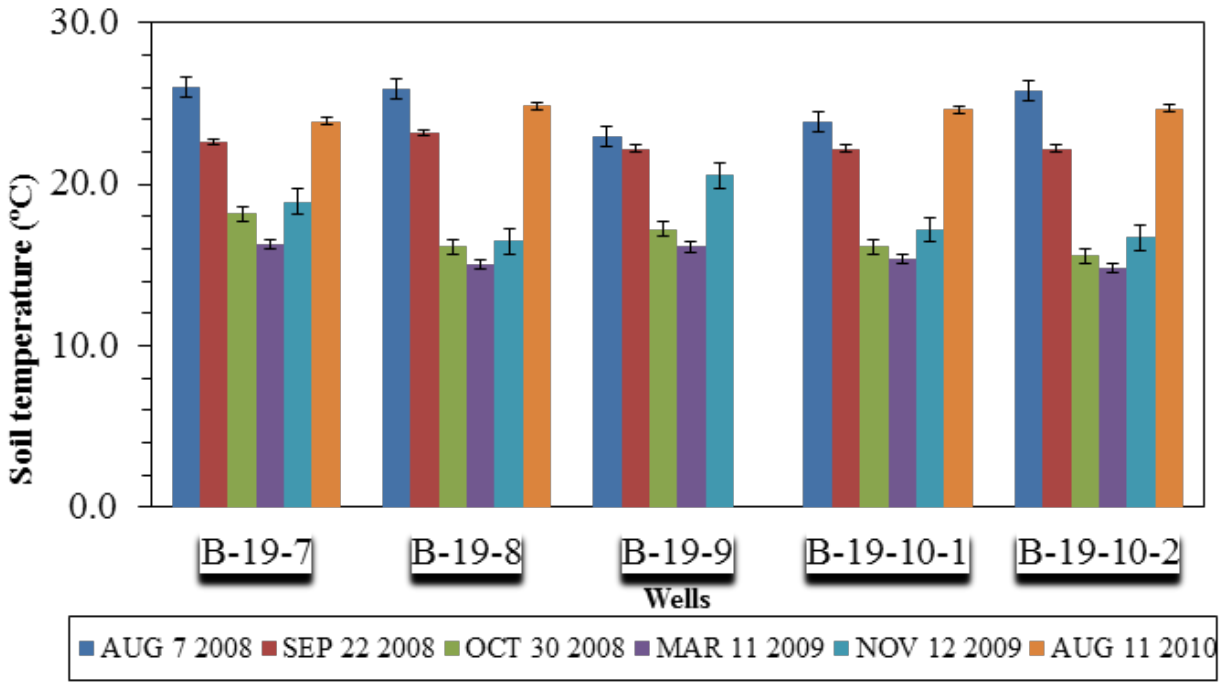


Figure 6.9. Seasonal soil temperatures around the wells in the study area from 2008 to 2010 (the line bars represent standard errors).

Soil microorganisms are particular about the temperatures at which they can exist and survive. Microbial activity and mineralization generally increase with temperature, with a doubling of activity accompanying each 10 $^{o}$C increase in temperature over the range from 5 to 35 $^{o}$C. The warmer soil temperatures in August may explain why the soil was a source of $CO_2$ at all wells in August 2008, except at Well B-19-8. Even though the temperature at Well B-19-8 in August was at the same level as the other wells, the differences in the observed $CO_2$ fluxes were possibly due to other factors in the soil.

### *6.3.4. Soil Moisture*

Soil moisture is another important physical factor which affects microorganisms, the decomposition of organic matter, and $CO_2$ fluxes (Brady and Weil, 2002; Li et al., 2008; Daly et al., 2009). Moisture regulates aerobic and anaerobic microbial activity (Havlin et al., 2005). Respiration decreases as microbial activity becomes inhibited due to the drying of the soil (Smith et al., 2003; Richardson et al., 2007). Decomposition rates usually increase with water potential from about -5 to about -0.05 MPa. However, the effect of moisture on gas fluxes is confounded with that of temperature and other soil biological and physical properties. For instance, soil $CO_2$ can be low due to reduced oxygen diffusion into the soil under high moisture conditions. Soil moisture measurements in the surface 10 cm of the soil (Figure 6.10), and in the 100 cm soil profile at each well during gas measurements, showed a similar pattern from well to well. The soil moisture levels were highest in the month of November 2009. The lowest soil moisture values were observed in March 2009 at Wells B-19-9 and B-19-10 #1 and in August 2010 at Wells B-19-7, B-19-8, and B-19-10 #2.

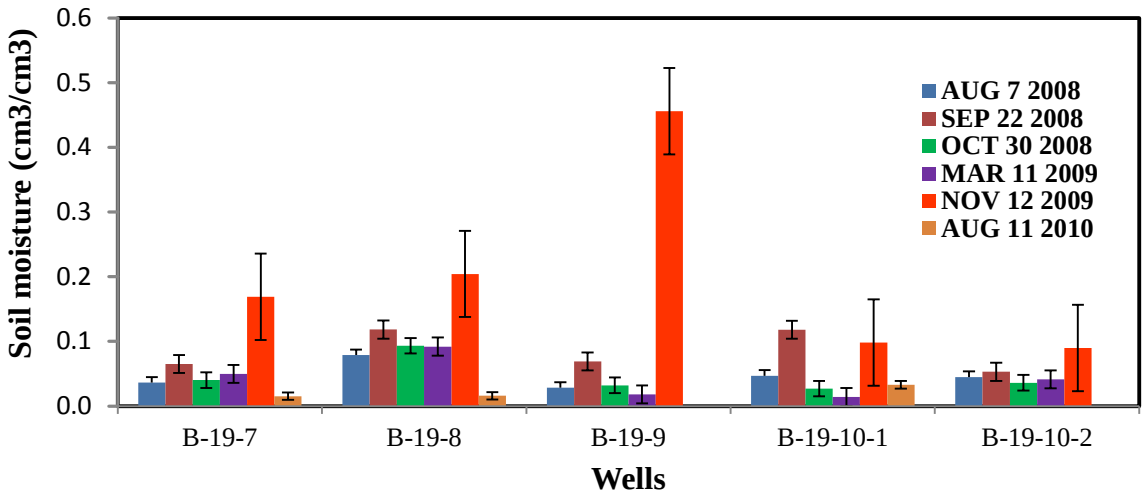


Figure 6.10. Soil moisture content at 10 cm depth around the wells in the study area from 2008 to 2010 (the line bars represent standard errors).

### *6.3.5. Soil Ammonium Nitrogen ($NH_4^+$-N) and Nitrate Nitrogen ($NO_3^-$-N)*

As soil microorganisms decompose the nitrogen tied up in organic compounds such as proteins, the nitrogen is released as ammonium ($NH_4^+$). The ammonium N is further converted to nitrate ($NO_3^-$), depending on soil environmental and chemical conditions such as soil moisture, temperature, and pH. Acidic pH and water availability inhibit N mineralization. A study by Reich et al. (1997) reported that mineralization was significantly related to temperature. In natural soils, the level of nitrogen in the inorganic forms, ammonium and nitrate, gives an indication of the level of microbial decomposition processes which also manifest themselves in surface $CO_2$ fluxes.

In the present study, we measured soil ammonium N and nitrate N so as to assess the mineralization potential of the soils in relation to surface $CO_2$ fluxes. Figure 6.11 shows the typical trend of measured soil ammonium N at each well, in which the amount of $NH_4^+$ decreased with increasing soil depth. The surface of the soil, from 0-5 cm depth, had the highest values of ammonium N, since mineralization is higher close to the surface due to the abundance of organic material as plant residues, mainly dead leaves and other decomposing plant litter, at the soil surface. Below this surface soil there was very little $NH_4^+$-N, which is to be expected. The $NH_4^+$-N content in the soil layer from 0-5 cm ranged from a low of 4.80 mg/kg (ppm) at Well B-19-8 to a high of 30 mg/kg at Well B-19-9.

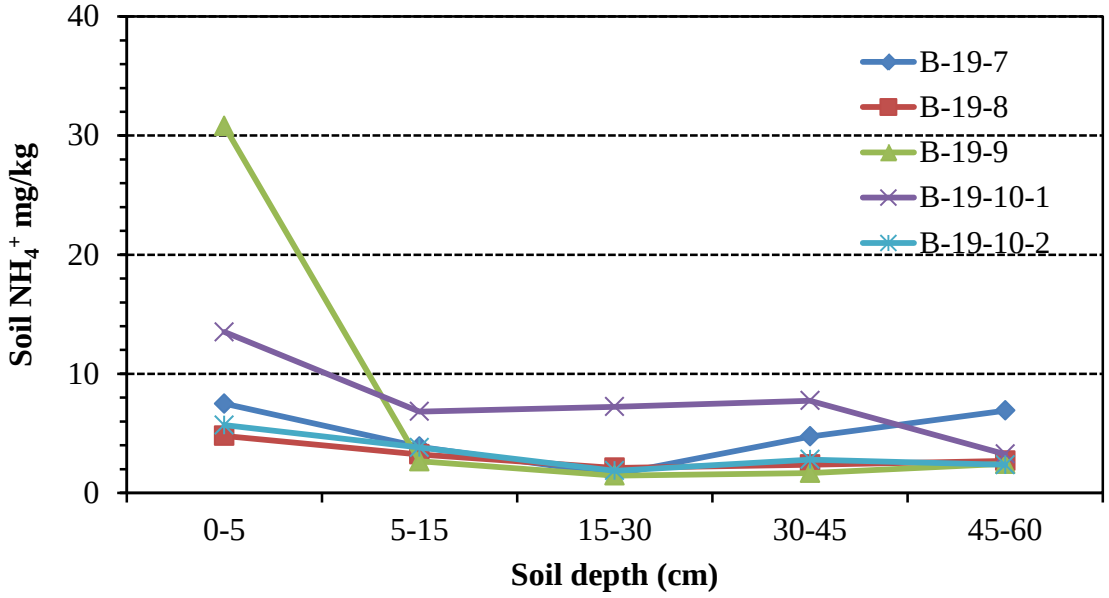


Figure 6.11. Soil $NH_4^+$-N in the 0-60 cm soil profiles around the wells in the study area on March 11, 2009.

A typical trend of soil nitrate N with depth at each well is shown in Figure 6.12. Unlike $NH_4^+$-N, the $NO_3^-$-N was more evenly distributed in the soil profile. Movement of nitrate ion in the soil is mainly via leaching, which can deposit it at lower soil depths or even transport it out of the soil profile to other ecosystems, such as surface and subsurface bodies of water.

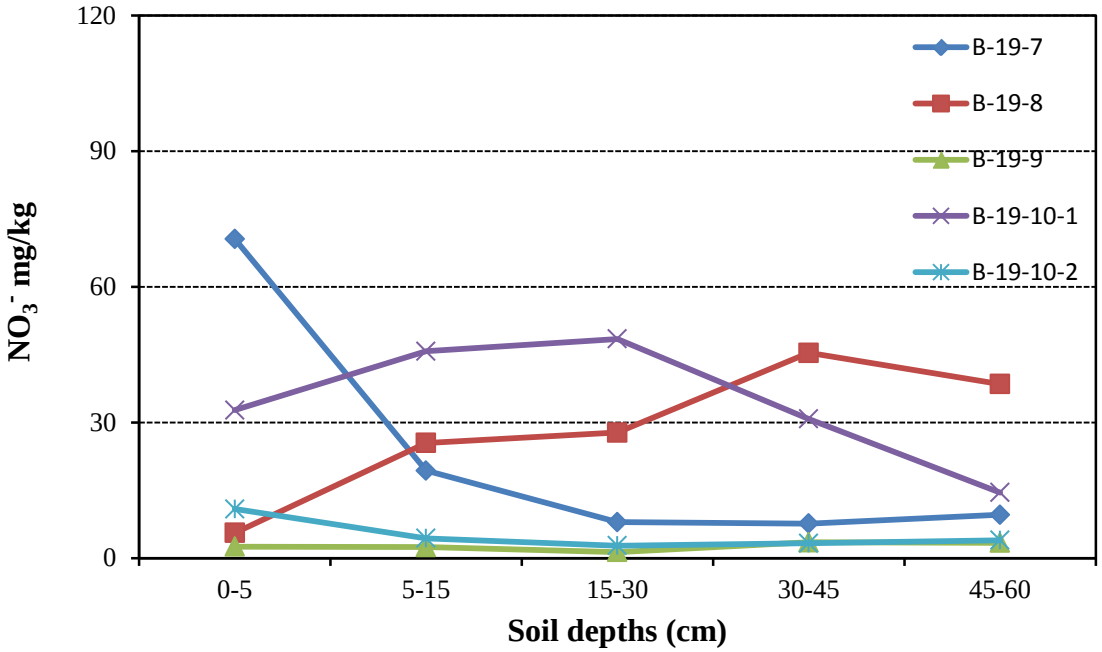


Figure 6.12. Soil $NO_3^-$-N in the 0-60 cm soil profiles around the wells in the study area in Spring 2008.

### *6.3.6. Soil Phosphorus*

Soil phosphorus is related to understory biomass productivity, which influences biological activity and decomposition processes driving soil $CO_2$ fluxes in forest ecosystems. In addition, the availability of P in forest soils has been reported to affect the allocation of C into above- and below-ground components in forest stands. Soil phosphorus is available in the form of $H_2PO_4^-$ ions between soil pH levels of 5.5 and 7.0. Generally, plant available or "extractable soil phosphorus" levels are very low in acidic soils due to the fixation of phosphate ions by Fe, Al, and Mn. Temperature also plays a role in the adsorption of P in soils; the higher the temperature the more P is adsorbed. Mineralization of phosphorous from organic matter is temperature dependent, due to microbial activity, which is also dependent on temperature. As temperature increases mineralization accelerates (Havlin et al., 2005).

Data for available soil phosphate levels in samples taken at depths from 0-5, 5-15, 15-30, 30-45, and 45-60 cm at each well in March 2009 are presented in Figure 6.13. The measurements show that, at each well, available P was highest at depths from 0 to 5 cm and, as expected, the concentration of available P decreased with increasing depth. This pattern is similar to that which was observed for soil ammonium, total C, and total N, which indicates that most of the biological activity in the soils around the wells is in the very top surface layer of the soil. Among the wells, some differences in available soil phosphorus were found in the 0-5cm depth. Also, soils at Well B-19-10 #1 had the highest available P levels compared to the other wells at depths from 0-5 cm to 30-45 cm (range from 202 to 60 mg $kg^{-1}$).

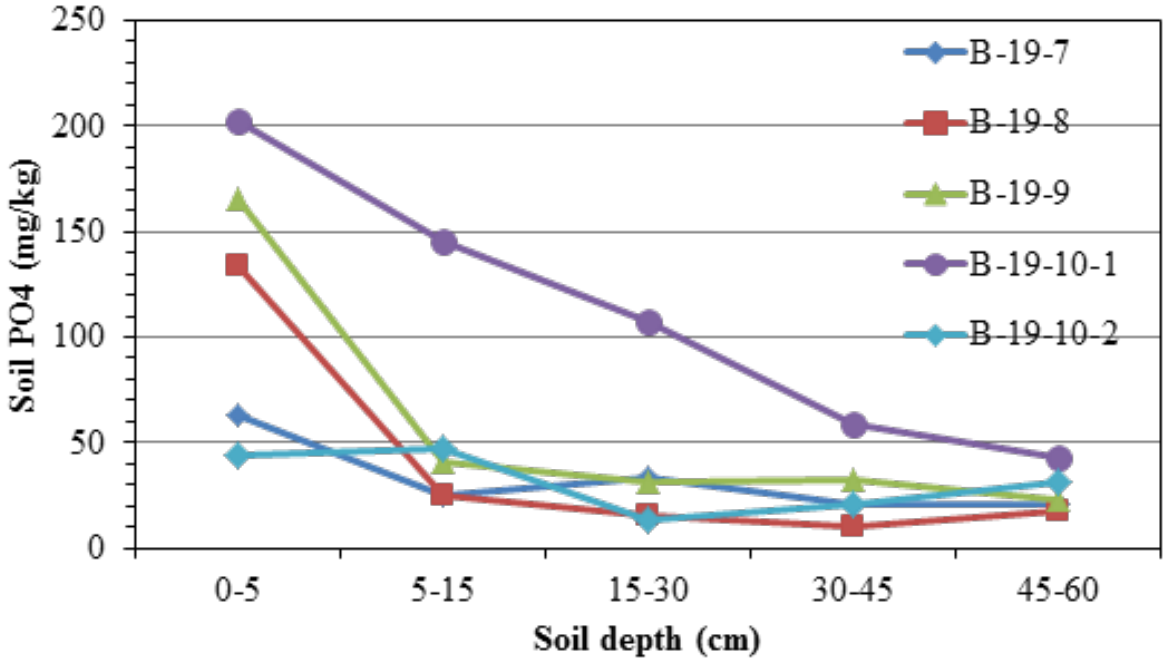


Figure 6.13. Soil inorganic phosphorus in the 0-60 cm soil profiles around the wells in the study area on March 11, 2009.

### *6.3.7. Soil Total Nitrogen (N) and Total Carbon (C)*

Surface soil $CO_2$ fluxes are the result of microbial decomposition of dead organic matter in the upper soil profile. This organic matter consists largely of C and N. Measurements of total soil N account for both organic and inorganic compounds. Approximately 95% of the total nitrogen in surface soils is organic N, in proteins, amino acids, and amino sugars. Soil carbon is important due to its effect on forest productivity, by being a principal source of energy for microorganisms (Panosso et al., 2011) and a principal component of soil organic matter (Nave et al., 2010). The measured total N and C in soil (Figures 6.14 and 6.15) show patterns similar to that of ammonium N, reflecting the accumulation of organic material close to the soil surface. Most of the measured C and N in the soils around the wells was found in the top 0-5 cm, which was largely composed of plant litter on the forest floor.

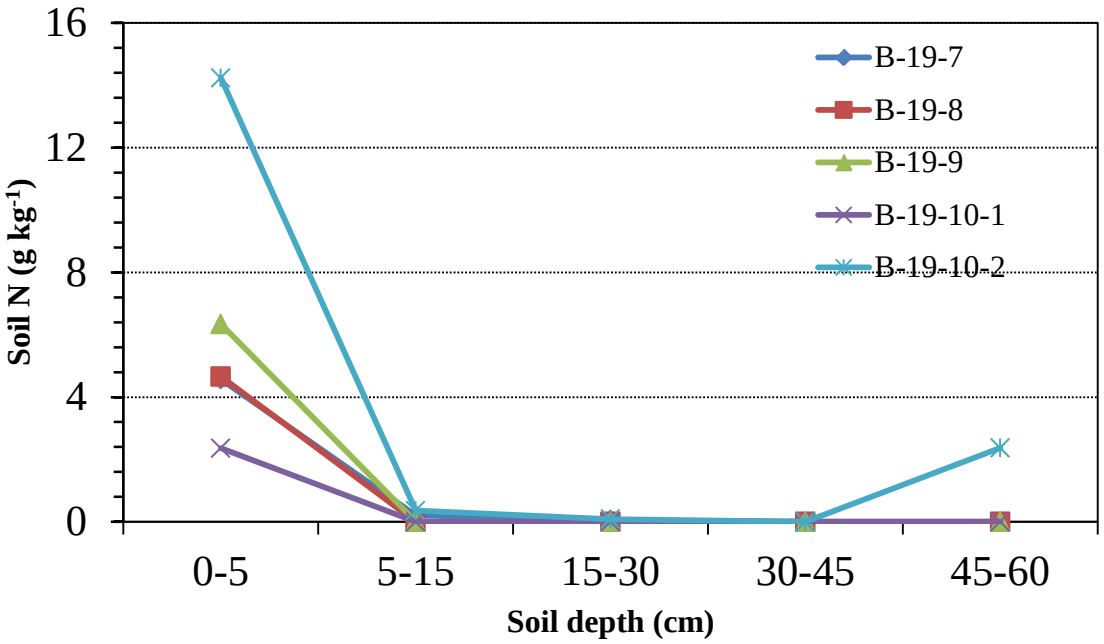


Figure 6.14. Total soil N in the 0-60 cm soil profiles around the wells in the study area on June 11, 2008.

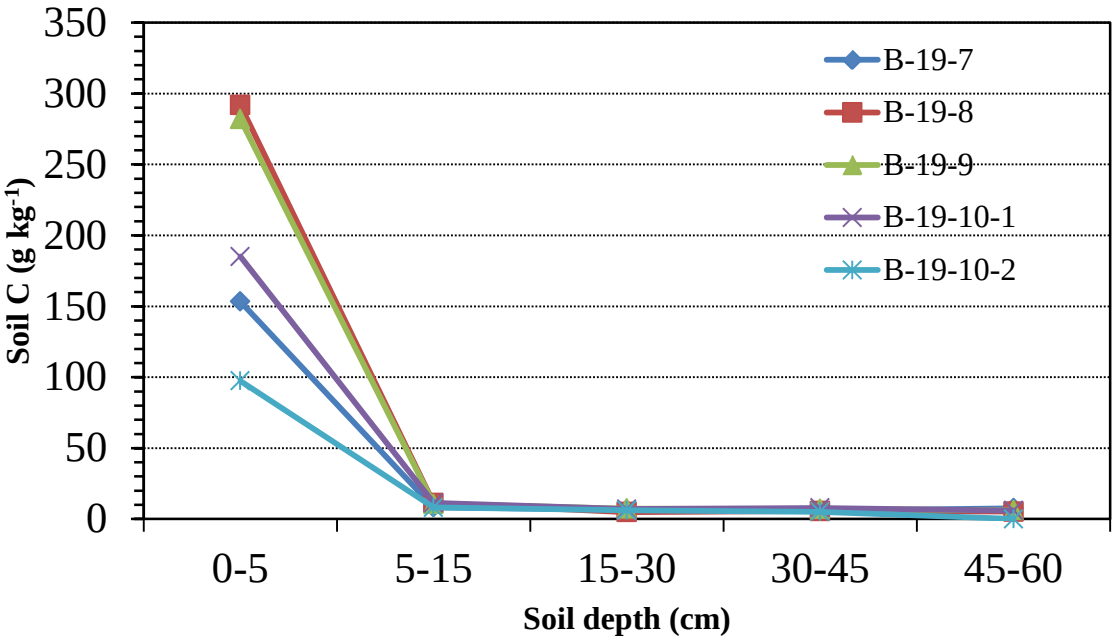


Figure 6.15. Total soil C in the 0-60 cm soil profiles around the wells in the study area on June 11, 2008.

## 6.4. Soil Surface $CO_2$ Fluxes

The process of documenting soil surface $CO_2$ fluxes was done in two steps. The first step involved measuring baseline or pre-injection $CO_2$ fluxes, i.e. the soil surface $CO_2$ fluxes before injection of $CO_2$ for enhanced oil recovery. The second step involved measuring soil $CO_2$ fluxes during and following the injection of $CO_2$. The baseline measurements were essential, because forest soils produce $CO_2$ from natural sources such as micro- and macro-organisms and root respiration. The wells at which soil $CO_2$ fluxes were measured were the three producers, Wells B-19-7, B-19-8, and B-19-9, plugged and abandoned Well B-19-10 #1, and the injector, Well B-19-10 #2. The pre-injection (baseline) $CO_2$ fluxes were measured on August 7, 2008, September 22, 2008, October 10, 2008, March 11, 2009, and November 12, 2009. During $CO_2$ injection and post-injection, the fluxes were measured during the period from August 11, 2010, to October 25, 2012. However, as of October 2011, Well B-19-9 was no longer monitored for soil surface $CO_2$ fluxes because the soil and gas sampling equipment at the measurement sites had been destroyed during timber harvesting operations by the land owner.

The measurements of soil $CO_2$ fluxes before, during, and after $CO_2$ injection are shown in Figure 6.16. The data are presented in a timeline format over the course of the study. Measurements were taken at times representative of the major seasons of the year: spring, summer, fall, and winter, in order to capture the seasonal variability associated with soil temperature and moisture content. Compared to the soil $CO_2$ fluxes observed in August 2008, before $CO_2$ injection, the fluxes in August 2010, during $CO_2$ injection, were lower than expected at Well B-19-7 (2.28 mg $CO_2$ $m^{-2}$ $min^{-1}$ vs. 0.12 mg $CO_2$ $m^{-2}$ $min^{-1}$), at Well B-19-10 #1 (1.29 mg $CO_2$ $m^{-2}$ $min^{-1}$ vs. -0.05 mg $CO_2$ $m^{-2}$ $min^{-1}$), and at Well B-19-10 #2 (0.53 mg $CO_2$ $m^{-2}$ $min^{-1}$ vs. -0.09 mg $CO_2$ $m^{-2}$ $min^{-1}$), as shown in Table 6.1. At Well B-19-8, the soil $CO_2$ fluxes during $CO_2$ injection, in August 2010, were slightly higher than those in August 2008, before $CO_2$ injection (0.40 mg $CO_2$ $m^{-2}$ $min^{-1}$ vs. -0.21 mg $CO_2$ $m^{-2}$ $min^{-1}$).

Table 6.1.
Measurements of Soil Surface $CO_2$ Fluxes near Five Wells in the $CO_2$-EOR Test Pattern in the Citronelle Oil Field, August 2008 and August 2010, before and during $CO_2$ injection, respectively.

| Well | B-19-7 | B-19-8 | B-19-9 | B-19-10 #1 | B-19-10 #2 |
|---|---|---|---|---|---|
| Sampling date | ----------Soil $CO_2$ flux (mg $CO_2$ $m^{-2}$ $min^{-1}$) ---------- | | | | |
| 08/07/2008 | 2.28 | -0.21 | 0.85 | 1.29 | 0.53 |
| 08/11/2010 | 0.12 | 0.40 | ----- | -0.05 | -0.09 |

The soil was a net sink for atmospheric $CO_2$ at Wells B-19-7 and B-19-8 in November of 2009. The soil at Well B-19-10 #1 was also a net sink for $CO_2$ in September and October of 2008, and in August 2010. The soil at Well B-19-10 #2 was a net sink for $CO_2$ in March 2009, August 2010, and May 2012. The highest net positive flux from the soil occurred at Well B-19-7 in August 2008, at a mean rate of 2.28 mg $m^{-2}$ $min^{-1}$. Other high net positive fluxes, between 1 and 2 mg $m^{-2}$ $min^{-1}$, were measured at Well B-19-10 #1 in August 2008, June 2012, and October 2012, and at Well B-19-10 #2 in October 2012. There was less $CO_2$ production and consumption at Wells B-19-8 and B-19-9, compared with the other locations. In August 2008, when the $CO_2$ flux from soil near

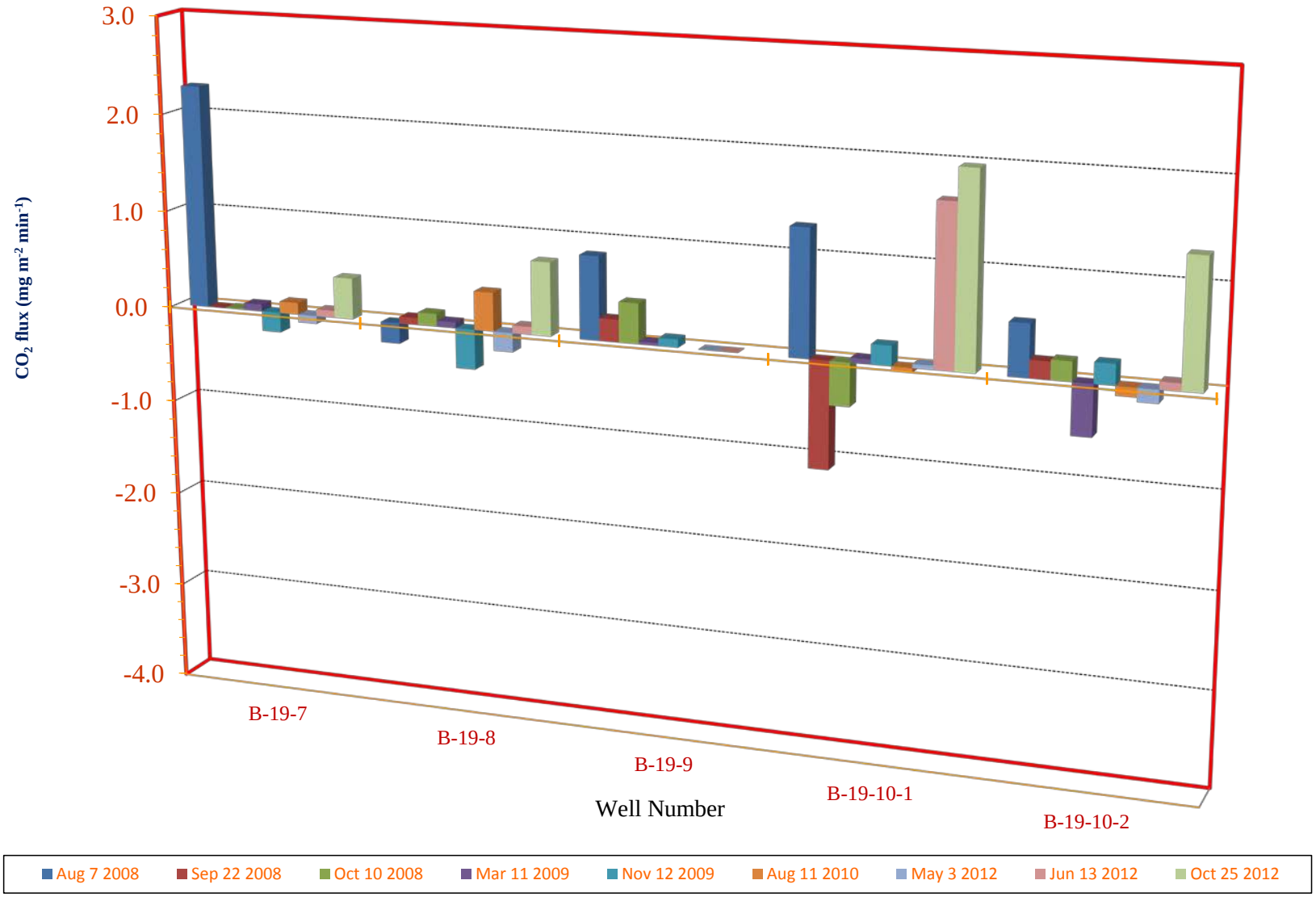


Figure 6.16. Measurements of soil surface $CO_2$ fluxes near five wells in the $CO_2$-EOR test pattern in the Citronelle Oil Field, August 2008 to October 2012, before, during, and after $CO_2$ injection.

Well B-19-7 was so high, the soil near Well B-19-8 was a sink for $CO_2$, at a mean rate of -0.21 mg $m^{-2}$ $min^{-1}$, even though the mean soil temperatures at the two wells were nearly identical (26.0 ºC at Well B-19-7 vs. 25.9 $^{o}$C at Well B-19-8).

## 6.5. Correlation Analysis

The results from an analysis of the correlations between $CO_2$ fluxes and chemical properties of the soil are presented in Table 6.2. The analysis showed that soil $CO_2$ fluxes were highly correlated with soil pH at Well B-19-8 (r = 0.995). At the other wells, $CO_2$ fluxes were negatively correlated with soil pH, but the correlations were not significant. The optimum pH for microbial activity is typically close to neutral pH, in the range 6.0-7.5. It is therefore expected that soil microbial activity and $CO_2$ emissions will increase with increasing soil pH from acidic to neutral, then decrease in the alkaline pH range.

Table 6.2.
Pearson Correlation Coefficients, r, between Soil $CO_2$ Fluxes and Soil Chemical Properties.
(probability values are given in parenthesis)

| | pH | EC ($S \cdot m^{-1}$) | Total N (g/kg) | $NH_4^+$-N (g/kg) | $NO_3^-$-N (g/kg) | $PO_4^{3-}$-P (g/kg) | Total C (g/kg) |
|---|---|---|---|---|---|---|---|
| **Well B-19-7** | | | | | | | |
| $CO_2$ flux (mg $CO_2$ $m^{-2}$ $min^{-1}$) | -0.0354 (0.98) | -0.7459 (0.46) | -0.2265 (0.46) | -0.0969 (0.77) | -0.1285 (0.74) | -0.3248 (0.39) | -0.8884 (<.0001) |
| **Well B-19-8** | | | | | | | |
| $CO_2$ flux (mg $CO_2$ $m^{-2}$ $min^{-1}$) | 0.9952 (0.06) | -0.8798 (0.34) | -0.4370 (0.16) | 0.2018 (0.53) | -0.6471 (0.06) | 0.0571 (0.88) | -0.4210 (0.12) |
| **Well B-19-9** | | | | | | | |
| $CO_2$ flux (mg $CO_2$ $m^{-2}$ $min^{-1}$) | -0.0492 (0.97) | -0.4680 (0.69) | -0.5516 (0.16) | 0.2112 (0.62) | -0.7015 (0.19) | -0.5429 (0.16) | 0.5969 (0.05) |
| **Well B-19-10 #1** | | | | | | | |
| $CO_2$ flux (mg $CO_2$ $m^{-2}$ $min^{-1}$) | -0.2664 (0.82) | 0.7784 (0.43) | -0.0555 (0.84) | 0.0058 (0.99) | 0.4951 (0.32) | -0.1441 (0.71) | -0.0707 (0.80) |
| **Well B-19-10 #2** | | | | | | | |
| $CO_2$ flux (mg $CO_2$ $m^{-2}$ $min^{-1}$) | -0.9400 (0.21) | 0.9990 (0.03) | 0.0389 (0.90) | 0.1199 (0.68) | -0.6269 (0.26) | -0.3215 (0.40) | 0.1707 (0.56) |

The correlation analysis showed that soil EC, which is related to soil microbiological properties, was negatively correlated with soil $CO_2$ fluxes at Wells B-19-7 (r = -0.745), B-19-8 (r = -0.880), and B-19-9 (r = -0.468). Soil EC was strongly positively correlated with soil $CO_2$ fluxes at Well B-19-10 #1 (r = 0.778) and B-19-10 #2 (r = 0.999). As with soil pH, soil microbiological activity, which drives soil $CO_2$ fluxes, is expected to increase with increasing EC to approximately the EC of water, then decrease with further increase in EC at higher salt concentrations.

The correlation analysis also showed that the soil $CO_2$ fluxes at each well and the average for all the wells were positively correlated with the soil temperatures measured during gas sampling. $CO_2$ fluxes at all the wells, except Well B-19-10 #1, were negatively correlated with soil moisture

in the 0-30 cm soil profile, while the $CO_2$ fluxes at all the wells were negatively correlated with soil moisture in the 0-100 cm soil profile. Bowden et al. (2004) also reported a positive correlation of $CO_2$ fluxes with temperature and a negative correlation with soil moisture in the organic horizon, which would be within the 0-30 cm soil profile in our data set. The correlation coefficients correspond to the expectation that soil temperature drives biological and chemical processes that promote $CO_2$ production, while high soil moisture can be associated with low $CO_2$ production, due to the fact that saturation of soil macropores with water displaces air needed by aerobic microbes.

There were weak correlations between soil $CO_2$ fluxes and soil total N and soil $NH_4^+$. This can be attributed to the fact that the majority of N found in the soil was in the surface soil/litter fraction, as the forest soils were very deficient in N. It was, however, interesting to note that $CO_2$ fluxes from soil near four out of the five wells (B-19-8, B-19-9, B-19-10 #1, and B-19-10 #2) were strongly negatively correlated with soil $NO_3^-$-N. As shown in Figure 6.12, $NO_3^-$-N was fairly uniformly distributed throughout the 0-60 cm soil profile. The presence of $NO_3^-$-N in the soil is indicative of adequate mineralization of organic material. Therefore, as mineralization of organic matter by microbial activity decreases and ends with the release of $NO_3^-$-N, $CO_2$ fluxes also decrease, due to slowing down of microbial activity, providing an explanation for the negative correlations between $CO_2$ flux and soil $NO_3^-$-N. The $CO_2$ fluxes were strongly correlated with total C at Wells B-19-7 (r = 0.888) and B-19-9 (r = 0.597). However, since the soils were very deficient in C, with most of it being in the surface litter, it is not possible to draw a reliable conclusion regarding the relationship between soil $CO_2$ fluxes and total soil C content.

Extractable P was negatively correlated with $CO_2$ fluxes at Wells B-19-7 (r = -0.325), B-19-9 (r = -0.543), B-19-10 #1 (r = -0.144), and B-19-10 #2 (r = -0.322). Well B-19-8 (r = 0.057) was the only well showing a positive correlation between P and $CO_2$ flux. Phosphorous is most readily available in soils having pH of 5.5-7.0 and is usually found in small amounts near the surface of the soil. Since the soils under consideration here are acidic (Figure 6.7), high positive correlations between P and $CO_2$ flux were not expected, since most of the P could be fixed in insoluble compounds with Fe and Al.

## 6.6. Regression Analysis

The Statistical Analysis System (SAS) Version 9.1.3 software (SAS Institute Inc., Cary, NC) was used to determine the best-fit regression models relating soil $CO_2$ fluxes to the environmental variables, soil temperature and soil moisture, measured during gas sampling. The statistical criteria used to establish the best model were the Adjusted Coefficient of Determination (adjusted $R^2$), Mallow's Cp Statistic, and the Mean Square Error. Since the objective was to find the best model and not necessarily to include all the variables in the model, any variable (at linear, quadratic, or higher order) that did not explain significant variation (based on adjusted $R^2$) was dropped from the model. The best regression models relating soil $CO_2$ fluxes to soil temperature ($T$) and soil moisture ($M$) during gas sampling at each well are given in Table 6.3.

Table 6.3.
Regression Models Relating Soil $CO_2$ Fluxes to Soil Temperature ($T$) And Soil Moisture ($M$).

| Well | Regression Model | |
|---|---|---|
| Well B-19-7 | $CO_2 = 4.3 + 9.0T - 0.1T^2 + 53.8M - 345M^2 + 565.3M^3$ | ($R^2 = 0.71$) |
| Well B-19-8 | $CO_2 = 15.8 - 2.6T + 0.1T^2 + 23.0M - 143.9M^2 + 218.5M^3$ | ($R^2 = 0.11$) |
| Well B-19-9 | $CO_2 = 0.9 + 0.01T - 10.4M + 20.1M^2$ | ($R^2 = 0.35$) |
| Well B-19-10 #1 | $CO_2 = 52.6 - 6.4T + 0.3T^2 - 222.2M + 2039.0M^2 - 5488.9M^3$ | ($R^2 = 0.37$) |
| Well B-19-10 #2 | $CO_2 = 78.2 + 12.0T - 0.6T^2 - 16.7M + 43.0M^2 - 25.5M^3$ | ($R^2 = 0.70$) |

The regression models having the highest adjusted $R^2$ were obtained at Wells B-19-7 ($R^2$ = 0.71) and B-19-10 #2 ($R^2$ = 0.70). This indicates that the environmental variables of soil temperature and moisture measured during gas sampling, as they appear in the model, accounted for at least 70% of the variation in observed soil $CO_2$ fluxes at these two wells. The regression model with the lowest adjusted $R^2$ was the one fit to the measurements at Well B-19-8, where soil temperature and soil moisture accounted for only 11% of the variation in observed soil $CO_2$ fluxes. However, attempts to include properties such as soil chemical composition in the model were complicated by the fact that chemical properties were determined from soil samples, which are collected less frequently than the gas samples, moisture measurements, and temperature measurements. The approach was therefore to find possible associations between these variables and soil $CO_2$ fluxes using correlation analyses (Section 6.5), as opposed to establishing their possible roles as predictor variables. Chemical properties such as C and N in the soil profile may play a significant role in explaining some of the remaining variation. Despite the typical seasonal and spatial variability associated with sampling for gas measurements, the measured data show a similar trend from well to well whereby the soil $CO_2$ fluxes were generally higher in the warmer months and lower in the cooler months at each of the well locations.

## 6.7. Recent Measurements of Soil $CO_2$ Flux

The most recent measurements of soil $CO_2$ fluxes, on May 3, June 13, and October 25, 2012, are included in Figure 6.16, for comparison with the earlier measurements before, during, and after $CO_2$ injection and at different times of the year. Baseline soil surface $CO_2$ fluxes around the wells were higher in June 2012, with values of 1.64 mg $CO_2$ $m^{-2}$ $min^{-1}$ at Well B-19-10 #1, 0.08 mg $CO_2$ $m^{-2}$ $min^{-1}$at Wells B-19-8 and B-19-10 #2, and 0.07 mg $CO_2$ $m^{-2}$ $min^{-1}$at Well B-19-7. In May 2012, the fluxes were 0.042 mg $CO_2$ $m^{-2}$ $min^{-1}$ at Well B-19-10 #1, -0.196 mg $CO_2$ $m^{-2}$ $min^{-1}$ at Well B-19-8, -0.136 mg $CO_2$ $m^{-2}$ $min^{-1}$at Well B-19-10 #2, and -0.081 mg $CO_2$ $m^{-2}$ $min^{-1}$at Well B-19-7. In October 2012, the highest soil surface $CO_2$ flux, 1.97 mg $CO_2$ $m^{-2}$ $min^{-1}$ was observed at Well B-19-10 #1 while the lowest surface $CO_2$ flux, 0.42 mg $CO_2$ $m^{-2}$ $min^{-1}$ was observed at Well B-19-7.

As highlighted in the summary of previous work, above, soil surface $CO_2$ fluxes around the wells have typically been significantly lower in the months from September through May. We also see that the soil $CO_2$ fluxes in May 2012, which averaged -0.09 mg $CO_2$ $m^{-2}$ $min^{-1}$ were significantly lower than those in June 2012, which averaged 0.47 mg $CO_2$ $m^{-2}$ $min^{-1}$. These observations are consistent with those reported earlier, that there are no indications that post-injection soil $CO_2$ fluxes

around the wells follow a different pattern compared to pre-injection (baseline) soil $CO_2$ fluxes. We therefore conclude that the fluctuations or differences in the observed soil $CO_2$ fluxes are simply due to the natural variability associated with soil gas fluxes, which can be attributed to natural processes such as soil biochemical activity and to variation in soil physical properties such as temperature and moisture content.

## 6.8. Summary and Conclusions

The surface soils around the wells in the study area of Citronelle Oil Field in Southwest Alabama are characterized by acidic soil pH, ranging from 3.60 to 5.40, with a mean pH for all sites of 4.90. Acidic pH is typical in soils under pine forests. The soils in the study area are sandy with very low organic matter in the upper layer at depths from 0-5 cm and are characterized by high EC of up to 5 $S \cdot m^{-1}$. The study area is located near the Gulf of Mexico and there are indications that at some point the area was flooded by sea water, which could explain the high EC.

Soil temperatures during gas sampling were highest in the month of August, with a mean for the summer season of 24.9 ºC. The lowest soil temperatures were recorded in March, with a mean of 15.5 ºC. Soil moisture content, which is dependent on the season and rainfall, fluctuated over time. Measurements of soil $NH_4^+$-N, P, total N, and total C in the forest soils around the wells showed a similar pattern whereby most of the soil nutrients were found in the top 0-5 cm of the soil and decreased rapidly with depth. This was attributed to contributions of N, P, and C from surface litter on the forest floor, since the forest soils themselves were deficient in soil nutrients.

There was a seasonal variation in $CO_2$ emission rates. Carbon dioxide fluxes were higher in the warmer months and lower in the cooler months at each of the well locations. The month having the highest $CO_2$ fluxes was August and the lowest rates occurred at the beginning of winter. The mean $CO_2$ flux during the summer, over all of the sampling locations, was 0.95 mg $CO_2$ $m^{-2}$ $min^{-1}$, compared with a mean over all of the sampling locations in the winter of -0.06 mg $CO_2$ $m^{-2}$ $min^{-1}$. The mean in March was -0.06 mg $CO_2$ $m^{-2}$ $min^{-1}$ and in November, -0.02 mg $CO_2$ $m^{-2}$ $min^{-1}$. The highest $CO_2$ flux was 2.28 mg $CO_2$ $m^{-2}$ $min^{-1}$, around Well B-19-7 in August 2008, but $CO_2$ fluxes from soil near that well decreased markedly when temperatures decreased, during the period from September 2008 to November 2009.

Regression and correlation analyses showed that soil $CO_2$ fluxes were generally correlated with the soil temperature and moisture content recorded at the time the soil gas sample was collected. However, the results for regression models and correlation coefficients were different from well to well, which can be attributed to other factors such as variation in underlying soil properties. The observation that soil $CO_2$ flux is temperature and moisture dependent agrees with results from other studies. The warmer the temperature, the more $CO_2$ is released through soil respiration. During cooler months $CO_2$ production rates decrease with the slowing down of microbial activity. Soil moisture content can increase or decrease soil $CO_2$ fluxes, depending on factors such as time of year, soil temperature, and other soil properties.

There are no indications that post-injection soil $CO_2$ fluxes around the wells follow a different pattern compared to pre-injection (baseline) soil $CO_2$ fluxes. We therefore conclude that the fluctuations or differences in observed soil $CO_2$ fluxes are simply due to the natural variability associated with soil gas fluxes, which can be attributed to natural processes such as soil biochemical activity and to soil physical properties such as temperature and moisture content.

**Acronyms, Abbreviations, and Symbols in Section 6**

| | |
|---|---|
| $A$ | area of soil covered by the soil gas sampling chamber, $m^2$ |
| ARS | Agricultural Research Service, U.S. Department of Agriculture |
| EC | electrical conductivity, S/m |
| ECD | electron capture detector |
| EOR | enhanced oil recovery |
| $f_o$ | flux of $CO_2$ to or from the soil surface, µg/($m^2$ min) |
| FID | flame ionization detector |
| GLM | General Linear Models |
| GRACEnet | Greenhouse gas Reduction through Agricultural Carbon Enhancement network, U.S. Department of Agriculture, Agricultural Research Service |
| $M$ | molecular weight of $CO_2$, g/mol; soil moisture, $cm^3/cm^3$ |
| $NH_4^+$-N | nitrogen in ammonium ion, mg/kg |
| $NO_3^-$-N | nitrogen in nitrate ion, mg/kg |
| P | available phosphorus in phosphates, $PO_4^{3-}$ |
| PVC | polyvinyl chloride |
| r | Pearson product-moment correlation coefficient, dimensionless |
| $R^2$ | adjusted coefficient of determination, dimensionless |
| SAS | Statistical Analysis System (SAS Institute Inc., Cary, NC) |
| $T$ | soil temperature, $^oC$ |
| TDS | total dissolved solids, mg/L or wt ppm |
| USDA | U.S. Department of Agriculture |
| $V$ | volume of head space in the soil gas sampling chamber, L |
| $V_{mol}$ | molar volume of $CO_2$ at the temperature and pressure in the soil gas sampling chamber, L/mol |
| $\Delta C/\Delta T$ | rate of change in $CO_2$ volume fraction in the soil gas sampling chamber, ppmv/min |

**References in Section 6**


Bower, C. A., and L. V. Wilcox, 1965. Soluble Salts. In C. A. Black (Ed.). Methods of Soil Analysis. Soil Sci. Soc. Amer. pp 933-951.

Bowden, R. D., E. Davidson, K. Savage, C. Arabiaa, and P. Steudler, 2004. Chronic nitrogen additions reduce total soil respiration and microbial respiration in temperate forest soils at the Harvard Forest. Forest Ecology and Management 196:43–56.

Brady, N. C., and R. R. Weil, 2002. The nature and properties of soils. 13th ed.

Condo, A. J., and R. C. Carter, 2002. Soil pH and tree species suitability in Mississippi. http://msucares.com/pubs/publications/p2311.pdf.

Daly, E., S. Palmroth, P. Stoy, M. Siqueira, A. C. Oishi, J. Y. Juang, R. Oren, A. Porporato, and G. G. Katul, 2009. The effects of elevated atmospheric $CO_2$ and subsurface $CO_2$ production and concentration dynamics in a maturing pine forest. Biogeochemistry 94:271-287.

Havlin, J. L., J. D. Beaton, S. L. Tisdale, and W. L. Nelson, 2005. Soil Fertility and Fertilizers. An Introduction to Nutrient Management.pp.45-47.

Hutchinson, G. L., and G. P. Livingston, 1993. Use of chamber systems to measure trace gas fluxes.

Jandl, R., L. Vesterdal, M. Olsson, O. Bens, F. Badeck, and J. Rock, 2007. Carbon sequestration and forest management. CAB Reviews: Perspectives in Agriculture, Veterinary Science, Nutrition and Natural Resources. 2,No. 017. http://academic.research.microsoft.com/Paper/6732232

Johnson, C. K., J. W. Doran, H. R. Duke, B. J. Wienhold, K. M. Eskridge, and J. F. Shanahan. 2001. Field-scale electrical conductivity mapping for delineating soil condition. Soil Sci. Soc. Am. J. 65:1829-1837.

Kamprath, E. J., 2011. Soil acidity and liming. Agronomy.agr.state.nc.us. Accessed February 17, 2011.

Keeney, D. R., and D. W. Nelson, 1982. Nitrogen-Inorganic. In: Page, A. L. Miller, R. H. Keeney, D. R. (Eds.), Methods of Soil Analysis. Part 2. Chemical and Microbial Properties, 2nd ed., American Society of Agronomy, Madison, WI, pp. 643-659.

Li, H. J., J. X. Yan, X. F. Yue, and M. B. Wang, 2008. Significance of soil temperature and moisture for soil respiration in a Chinese mountain area. Agricultural and Forest Meteorology 148:490-503.

National Energy Technology Laboratory, 2012. "2012 United States Carbon Utilization and Storage Atlas," Fourth Edition (Atlas IV). http://www.netl.doe.gov/research/coal/carbon-storage/atlasiv

Nave, L. E., E. D. Vance, C. W. Swanston, and P. S. Curtis, 2010. Harvest impacts on soil carbon storage in temperate forests. Forest Ecology and Management. http://www.nrs.fs.fed.us/pubs/jrnl/2010/nrs_2010_nave_001.pdf.

Panosso, A. R., J. Marques, Jr., D. M. B. P. Milori, A. S. Ferraudo, D. M. Barbieri, G. T. Pereira, and N. La Scala, Jr., 2011. Soil $CO_2$ emission and its relation to soil properties in sugarcane areas under Slash-and-burn and Green harvest. Soil & Tillage Research 111:190-196.

Reich, P. B, D. F. Grigal, J. D. Aber, and S. T. Gower, 1997. Nitrogen mineralization and productivity in 50 hardwood and conifer stands on diverse soils. Ecology 78(2):335-347.

Richardson, A. D., D. Y. Hollinger, J. D. Aber, S. V. Ollinger, and B. H. Braswell, 2007. Environmental variation is directly responsible for short-but long-term variation in forest-atmosphere. Global Change Biology 13:788–803,

Rousk., J., P. C Brookes, and E. Bååth, 2009. Contrasting soil pH effects on fungal and bacterial growth suggest functional redundancy in carbon mineralization. Applied and Environmental Microbiology 75(6): 1589–1596.

Sims, G. K., T. R. Ellsworth, and R. L. Mulvaney, 1995. Microscale determination of inorganic nitrogen in water and soil extracts. *Comm. Soil Sci. Plant Anal. 26: 303-326.*

Smith, K. A., T. Ball, F. Conen, K. E. Dobbie, J. Massheder, and A. Rey, 2003. Exchange of greenhouse gases between soil and atmosphere: interactions of soil physical factors and biological processes. European Journal of Soil Science. 54:779-791.

# 7. Monitoring of $CO_2$ in Ambient Air and Growth of Vegetation

Xiongwen Chen and Kathleen A. Roberts
Department of Biological and Environmental Sciences
Alabama A&M University, Normal, Alabama

## 7.1. Measurements of $CO_2$ in Ambient Air

The volume fractions of $CO_2$ in ambient air were measured at least once every quarter from September 2007 to June 2012 at 104 locations in the Citronelle Oil Field and City of Citronelle. The sampling points are shown on a map of the City of Citronelle and surrounding area in Figure 7.1. The measurements for a given month or quarter were made over two consecutive days; one day in the City and the second day in the oil field.

The averages and standard deviations of the $CO_2$ measurements are shown as a function of time in Figure 7.2. The average values lie between approximately 340 and 390 ppmv, with the exception of a single outlier, measured in June 2009. The measurements exhibit the gradual upward trend of the worldwide average $CO_2$ in the atmosphere, superimposed on seasonal variation. The globally averaged marine surface monthly mean mole fraction of $CO_2$ in dry air, in September 2007, was 380.50 ± 0.13 ppm, and in June 2012 it was 392.68 ± 0.13 ppm (Dlugokencky and Tans, 2014).

Local concentrations of $CO_2$, shown in Figure 7.3, characteristic of the atmosphere over a small region of Earth's surface including the City of Citronelle and the oil field, were obtained from the NASA satellite-based Atmospheric Infrared Sounder (AIRS) database (NASA, 2012). The data shown in Figure 7.3 are the area-averaged time series for the $CO_2$ volume fraction in the region 88 to 89$^o$ West and 31 to 32$^o$ North, an area in which the City of Citronelle and the oil field are located in the southeast corner. The measurements are integrated over the column of atmosphere from Earth's surface to the NASA satellite in low Earth orbit. Similarities in the seasonal changes in $CO_2$ are visible in the AIRS measurements and the measurements at ground level, in Figure 7.2, but, on average, the AIRS measurements are slightly higher. Leakage or release of $CO_2$ from the test site would have negligible influence on the AIRS measurements, because the mass of air in the atmosphere over an area 1$^o$ x 1$^o$ at 31.5$^o$ North is approximately 118 billion tons, or 14.7 million times the total mass of $CO_2$ delivered to the site for the test.

The large number of sampling points enabled the investigators to construct contour plots showing the distribution of $CO_2$ volume fractions across the region. An example, in Figure 7.4, shows the spatial distribution of $CO_2$ across the region in August 2009, before $CO_2$ injection began, in August 2010, near the end of the $CO_2$ injection, and in August 2011, almost a year after the $CO_2$ injection was complete. Similar figures, for seven other months of the year, are included in Appendix C. Also in Appendix C, Figure C.1, is a map of the Citronelle, AL, area including latitude and longitude, that can be used to determine the approximate locations of high or low $CO_2$ volume fractions, or other features, in the contour plots. No correlation of the distribution of $CO_2$ with the location or timing of the $CO_2$ injection can be discerned by inspection of the $CO_2$ contour

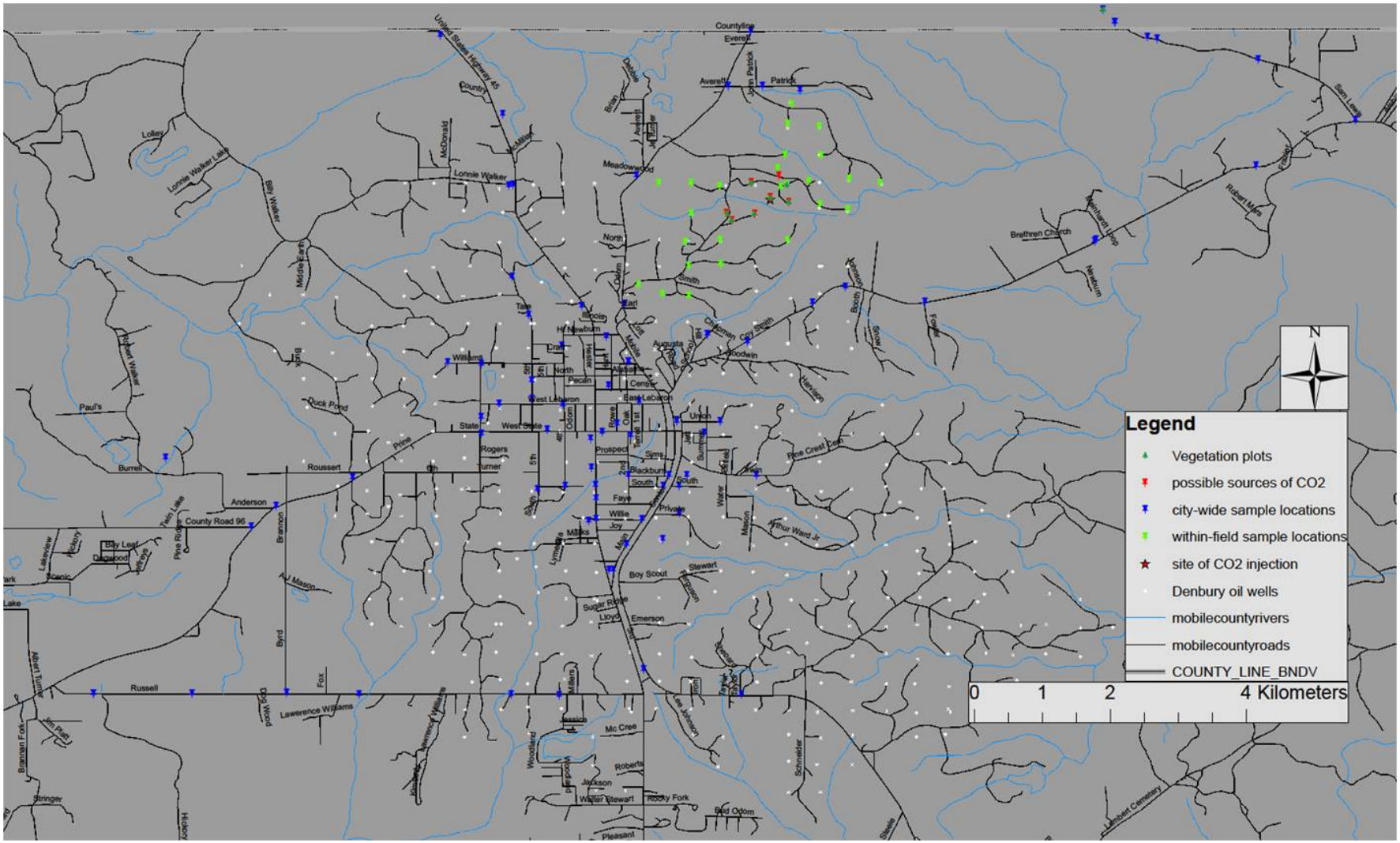


Figure 7.1. Map of the City of Citronelle and the Citronelle Oil Field showing the locations of wells (white dots), the wells and tank batteries in the study area (red pins), air sampling points surrounding the study area (green pins), and air sampling points within the densely populated area of the city (blue pins). The locations of the vegetation plots (dark green pine trees) can be identified more clearly in Figure 7.5.

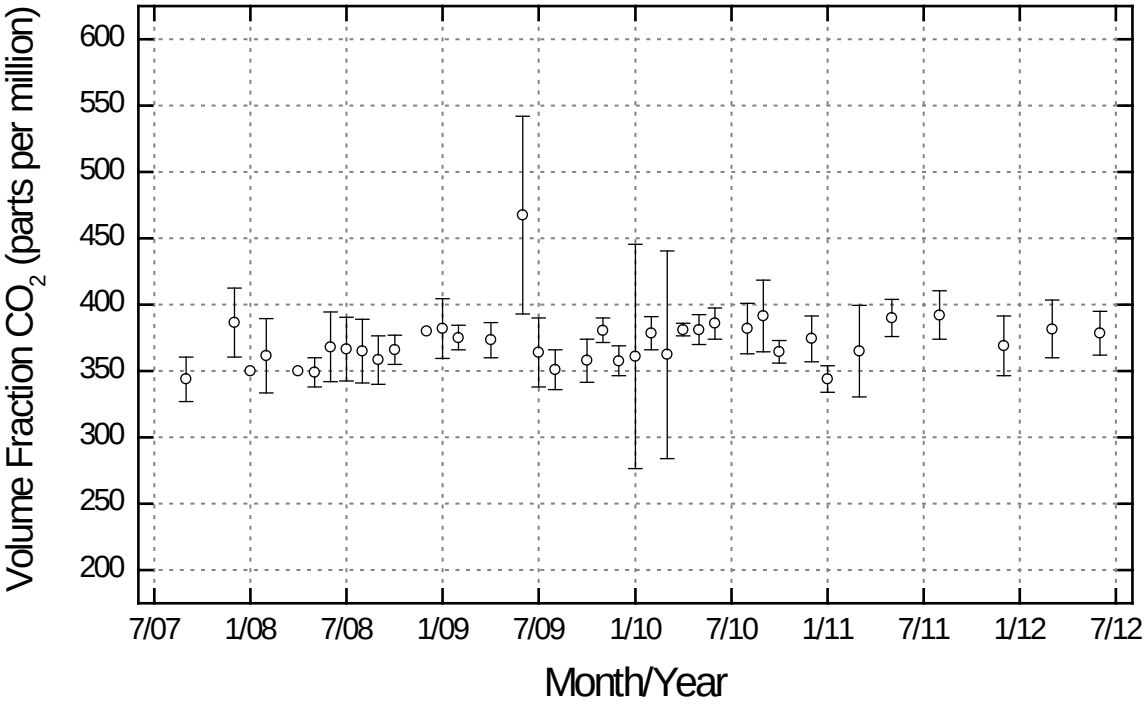


Figure 7.2. Average atmospheric $CO_2$ volume fraction (parts per million) at ground elevation across the City of Citronelle and Citronelle Oil Field from September 2007 to June 2012.

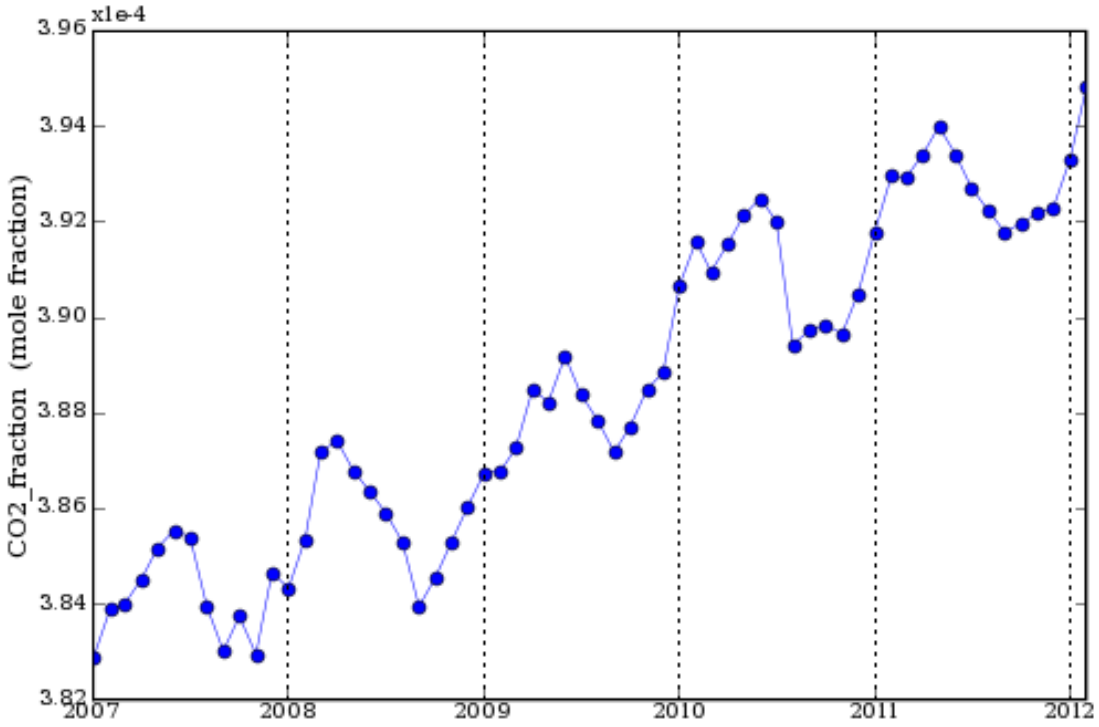


Figure 7.3. Area-averaged time series (AIRX3C2M.005) in the region 88-89° West and 31-32° North, including the City of Citronelle and the Citronelle Oil Field. Data from the NASA Atmospheric Infrared Sounder <http://airs.jpl.nasa.gov/>. Multiply the mole fraction values on the y-axis by 100 to convert to mole or volume parts per million.

a. August 2009

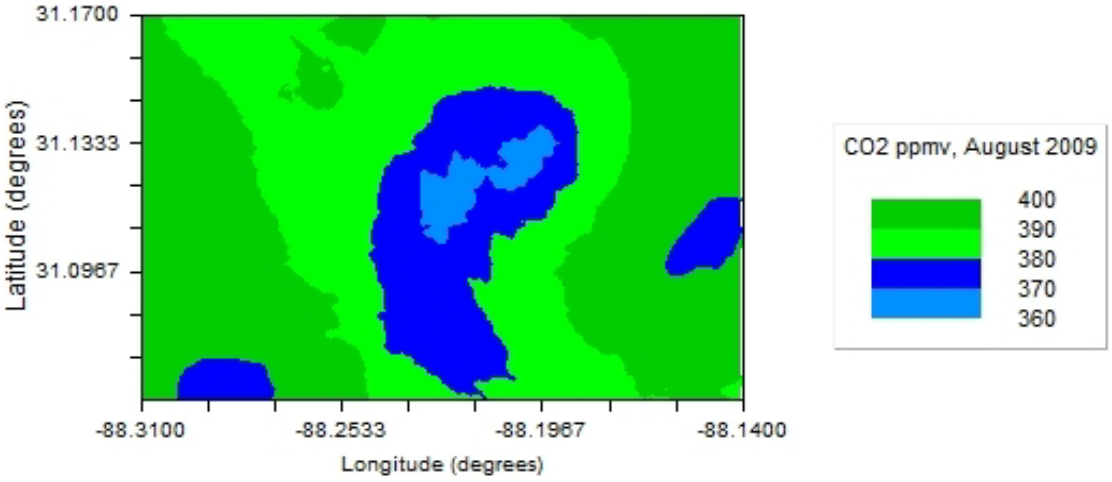


b. August 2010

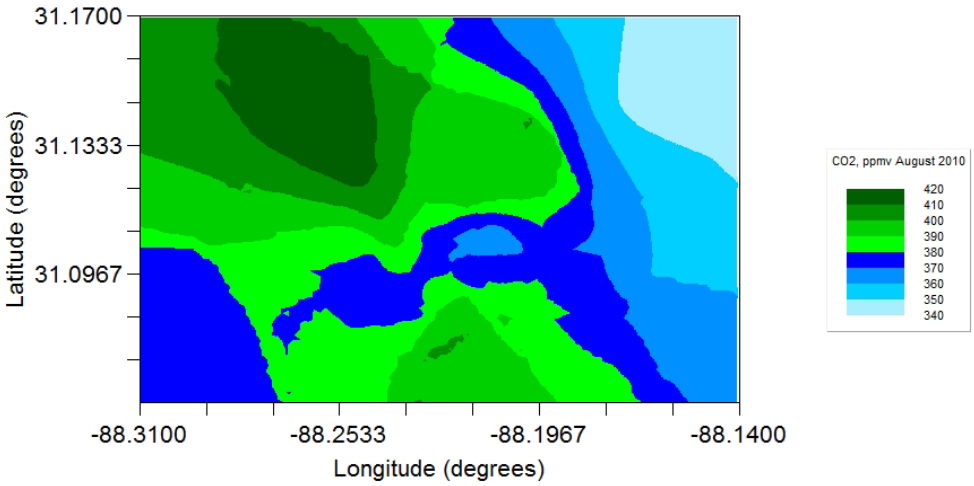


c. August 2011

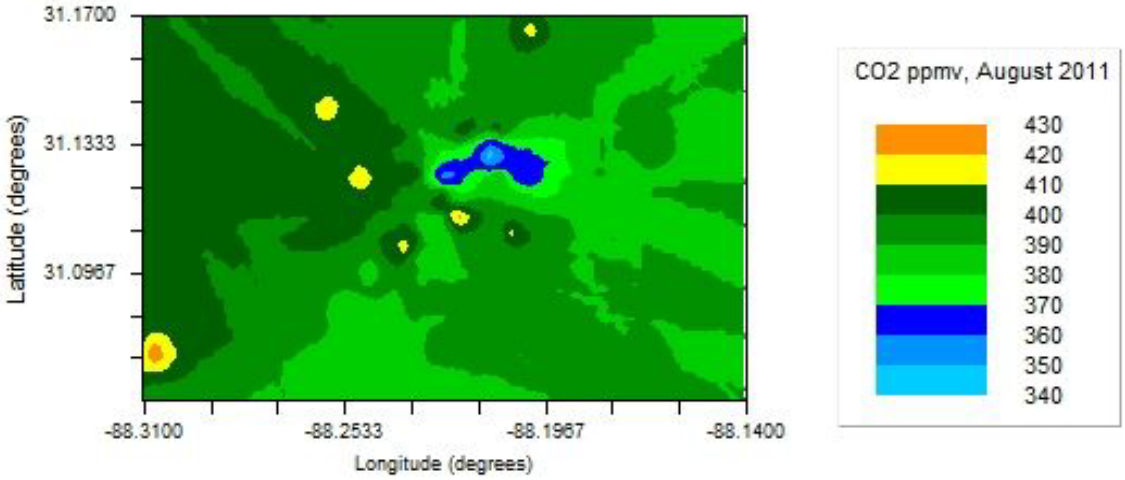


Figure 7.4. Contour plots showing the spatial distribution of the $CO_2$ volume fraction across the City of Citronelle and Citronelle Oil Field in August 2009, August 2010, and August 2011.

plots. Roberts (2013) conducted a thorough statistical analysis of the measurements and found that the variables most closely correlated with the $CO_2$ volume fraction were ambient temperature and pressure, season of the year, and wind speed and direction. She also found that the grand average, over all of the sampling points and over all sets of measurements taken after $CO_2$ breakthrough was detected at Well B-19-11 in May 2010, was 2.3 ppmv higher than the grand average over all the sets of measurements taken before breakthrough occurred, not including the global increase in atmospheric $CO_2$ during the same period, of approximately 2 ppmv/year, from $CO_2$ sources worldwide (Dlugokencky and Tans, 2014).

## 7.2. Growth of Vegetation

To determine whether emissions of $CO_2$ vented from the tank batteries, or upward migration of $CO_2$ from the EOR targets to the ground surface, had any effect on vegetation at the study site, 10 m x 10 m test plots were established near the injector, producers, and tank batteries, in which to monitor plant species distribution and growth. Eight test plots and two reference plots were first established in 2008. Harvesting of timber by the land owner destroyed one of the test plots during the first year, so that plot was replaced with another one at a similar, nearby location. The two reference plots were also lost due to a change in land use in the wildlife management area where they were located. Four new reference plots were established in 2009, adjacent to a municipal golf course west of the oil field. The locations of the plots, in their final configuration, are shown in Figure 7.5. A key to the locations and functions of the plots is provided in Table 7.1. Field inventories of the plots were conducted in 2008, 2009, 2010, and 2011. The growth of woody plants in the plots during the three time intervals, 2008-2009, 2009-2010, and 2010-2011 is shown in Figure 7.6.

Comparison of the 2008-2009 growth rates with those in 2009-2010 shows that the plant growth rate increased from the first period to the second in two plots and decreased in five of them. Comparison of the 2009-2010 growth rates with those in 2010-2011 shows that the plant growth rate increased from the second period to the third in three plots and decreased in five of them. The overall trend is one of decreasing growth rates, rather than the increase in rates that might be expected under the influence of elevated levels of $CO_2$.

One plot, VP1, on the far left in Figure 7.6, exhibited a consistent increase in the rate of growth of vegetation during the four-year period. As shown in Table 7.1, Plot VP1 is located near the injector, Well B-19-10 #2. This is an interesting observation, in view of the fact that elevated levels of $CO_2$ in ambient air were not consistently detected there, nor were elevated $CO_2$ fluxes from soil near that well reported by Ermson Nyakatawa and his coworkers (Section 6). With the possible exception of vegetation near Well B-19-10 #2, the differences in growth rate from place-to-place and year-to-year are most likely explained by patterns of rainfall, temperature, and solar insolation than by $CO_2$ plumes associated with the $CO_2$ storage tank, injection equipment, wells, or tank batteries. Roberts (2013), in her conclusion from this component of her study, made the following observation: "Overall this suggests that the oilfield area may have been exposed to increased levels of $CO_2$ when compared to the reference area and that within the oilfield the increase in growth rate counter to that of the oilfield in general suggests an area exposed to a greater concentration of $CO_2$, perhaps due to topographical or meteorological influence." Some additional comments on the results from the direct measurements of vegetation may be found in the abstract of a presentation by Roberts and Chen (2012), reproduced below.

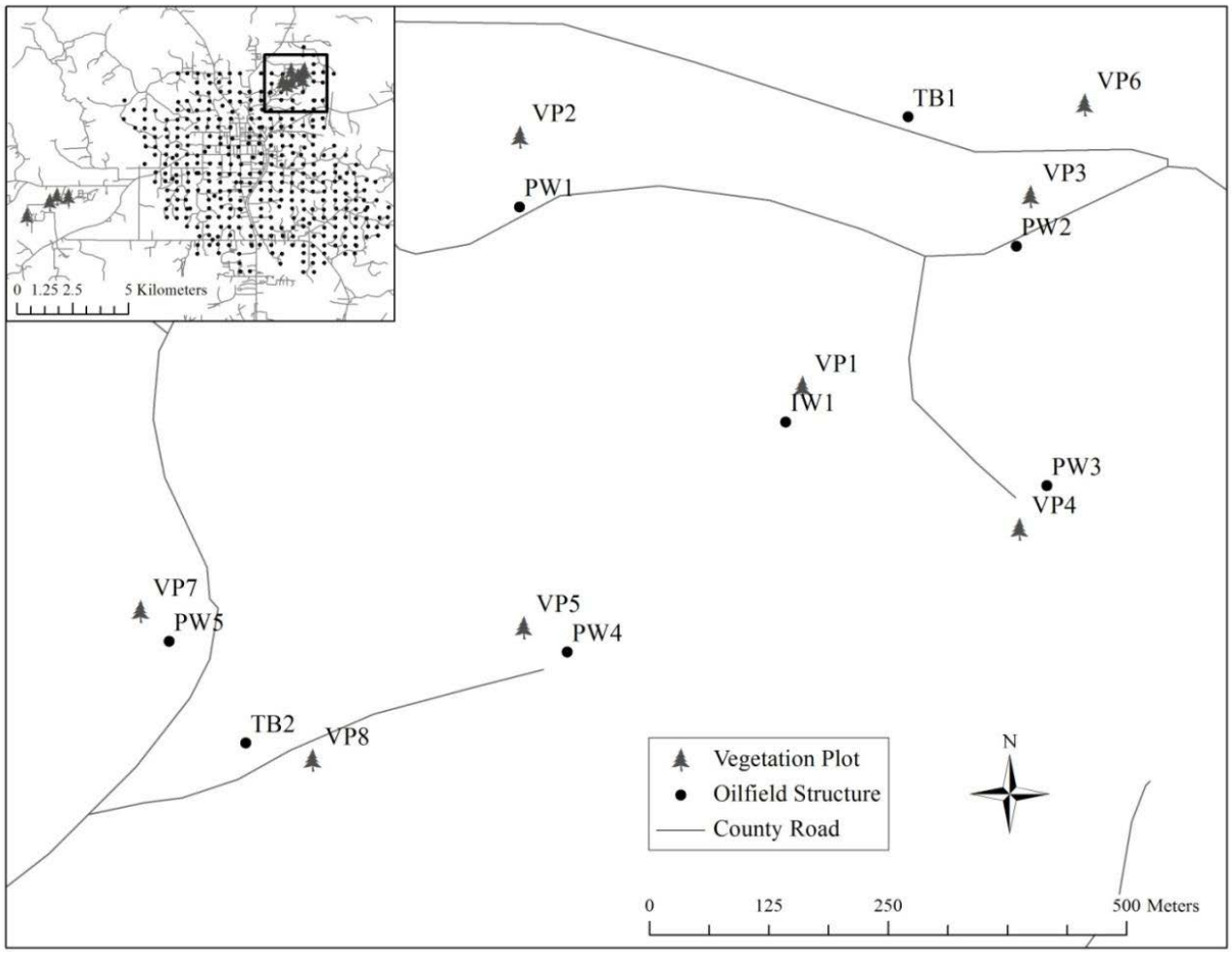


Figure 7.5. Locations of the vegetation test plots (VP) relative to the $CO_2$ injection well (IW), oil production wells (PW), and tank batteries, (TB). The inset shows the location of the study area in the Citronelle Oil Field and the locations of the four reference plots (pine tree symbols at far left). Figure from Roberts (2013).

Table 7.1. Locations and Descriptions of the 10 m x 10 m Vegetation Plots.

| Vegetation Plot | Location | Description |
|---|---|---|
| VP1 | Well B-19-10 #2 | Injection well |
| VP2 | Well B-19-7 | Production well |
| VP3 | Well B-19-8 | Production well |
| VP4 | Well B-19-9 | Production well |
| VP5 | Well B-19-10 #1 | Plugged and abandoned well |
| VP6 | Tank Battery B-19-8 | Tank battery |
| VP7 | Well B-19-11 | Production well |
| VP8 | Tank Battery B-19-11 | Tank battery |
| GC1 | Citronelle Golf Course | Control |
| GC2 | Citronelle Golf Course | Control |
| GC3 | Citronelle Golf Course | Control |
| GC4 | Citronelle Golf Course | Control |

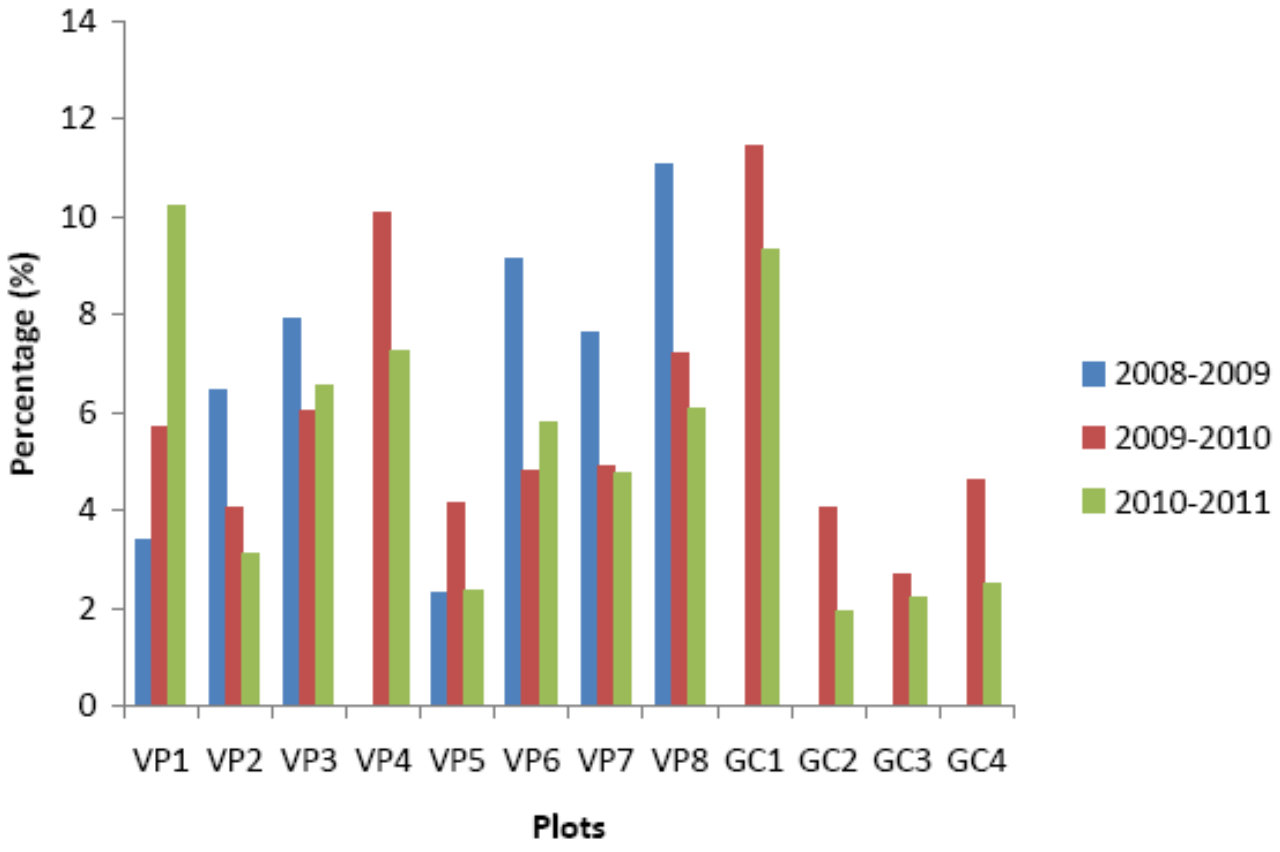


Figure 7.6. Comparison of growth, as the fractional (%) increase in basal area, in vegetation test plots in the study area and reference plots adjacent to the Citronelle Golf Course during the three periods, 2008-2009, 2009-2010, and 2010-2011. The locations of the plots are shown in Figure 7.5 and their functions are described in Table 7.1.

An alternative method was also examined for assessment of the condition of vegetation, from changes in the normalized difference vegetation index (NDVI) for each land use category (e.g. deciduous forest, evergreen forest, mixed forest, grassland, pasture, woody wetlands, and emergent herbaceous vegetation). The NDVI were extracted from satellite images of the injection area, oil field, and surrounding area, available from USGS (2012). A paper describing this work was presented at the 97th Annual Meeting of the Ecological Society of America, entitled, "Direct and indirect assessment of vegetation located near $CO_2$-mediated enhanced oil recovery ($CO_2$-EOR) activities" (Roberts and Chen, 2012). The paper includes analysis of data from two sources: (1) direct measurements, described above, of the growth rates of woody plants in test plots established near the inverted five-spot well pattern and in control plots adjacent to a golf course to the west of the oilfield and City of Citronelle, and (2) indirect measurements, from changes in the NDVI for each land use category, extracted from the satellite images available from USGS. The abstract of the paper follows (Roberts and Chen, Ecological Society of America, 97th Annual Meeting, Portland, OR, August 5-10, 2012, http://eco.confex.com/eco/2012/webprogram/Paper38361.html):

> This study examined the potential of vegetation monitoring to determine if there are local ecological effects of $CO_2$ mediated Enhanced Oil Recovery ($CO_2$-EOR). Injection of $CO_2$ into geological reservoirs containing crude reduces the viscosity and allows for the movement and recovery of crude that was previously cost prohibitive using other methods. $CO_2$ injection into geological reservoirs may also serve as a means to reduce atmospheric $CO_2$ through geological sequestration. However, monitoring and verification is essential to ensure that geological sequestration is effective and without negative effects to the surrounding environment. Monitoring of vegetation was accomplished using small scale, direct measurement, as well larger scale indirect measurements to determine whether $CO_2$-EOR activities impact surrounding vegetation. The direct, small scale component was accomplished by examining the basal area increase in plots located adjacent to oil field structures as well as control plots outside of the oilfield, before and after $CO_2$ breakthrough. Indirect larger scale measurements were used to look for stress in vegetation adjacent to the injection area as well as the larger oilfield area and areas just beyond. Normalized Difference Vegetation Index (NDVI) values for hardwoods, evergreen and mixed forest were determined by Land Use Land Cover (LULC) 2006 classification.
>
> Results of a before after control impact paired (BACIP) analysis of the basal area of plots indicate that there is no statistical significance between control and impact areas between all basal area, hardwoods, conifers and size for all plots after reported breakthrough. Some plots experienced high increase in percent growth. Two plots with a greater increase were subjected in part to logging activity and the growth may be attributed to an increase in available sunlight. This does not suggest influence of $CO_2$ on growth; however, it does suggest that additional observation and study are needed to separate influences of logging activity and potential $CO_2$ influence. Small differences in NDVI values are observed in both deciduous and mixed forest but these differences appear to be similar with respect to season. There were no differences observed in NDVI of evergreen forests. Overall, detrimental impacts on vegetation surrounding an EOR-$CO_2$ project were not observed at the scales of observation used in this study.

**Acronyms in Section 7**

| | |
|---|---|
| AIRS | Atmospheric Infrared Sounder |
| BACIP | before-after control-impact paired |
| EOR | enhanced oil recovery |
| LULC | Land Use Land Cover |
| NASA | National Aeronautics and Space Administration |
| NDVI | normalized difference vegetation index |
| USGS | U.S. Geological Survey |

**References in Section 7**


Dlugokencky, E., and P. Tans, "Trends in Atmospheric Carbon Dioxide," National Oceanic & Atmospheric Administration, Earth System Research Laboratory, Global Monitoring Division, http://www.esrl.noaa.gov/gmd/ccgg/trends/global.html (accessed May 7, 2014).

National Aeronautics and Space Administration, Jet Propulsion Laboratory, California Institute of Technology, AIRS Atmospheric Infrared Sounder, AIRS Carbon Dioxide Data, http://airs.jpl.nasa.gov/ (accessed April 2012).

Roberts, K. A., "Ecological Monitoring and Assessment of Enhanced Oil Recovery ($CO_2$-EOR) for Carbon Storage," Ph.D. Dissertation, Department of Biological and Environmental Sciences, Alabama A&M University, Normal, AL, December 2013.

Roberts, K. A., and X. Chen, "Direct and indirect assessment of vegetation located near $CO_2$-mediated enhanced oil recovery ($CO_2$-EOR) activities," Ecological Society of America, 97th Annual Meeting, Portland, OR, August 5-10, 2012, http://eco.confex.com/eco/2012/webprogram/Paper38361.html

U.S. Geological Survey, Earth Resources Observation and Science Center, USGS Global Visualization Viewer, http://glovis.usgs.gov/ (accessed 2012).

# 8. Geophysical Testing and Simulation

Shen-En Chen, Yangguang Liu, Peng Wang, and Benjamin Smith
University of North Carolina at Charlotte

## 8.1. Geophysical Testing at Citronelle

The purpose of geophysical monitoring of the $CO_2$ injection into an existing test well in the Citronelle Oil Field, Alabama, was to determine the stressing effects resulting from the $CO_2$-oil replacement in the Donovan Sand. Geophysical testing, using the passive Refraction Microtremor (ReMi) technique, was conducted to compare the seismic properties of the oil field before, during, and after $CO_2$ injection. The measurements were made at well sites along lines running from North to South and from Northeast to Southwest, to the South and Southwest of the injection well, as shown in Figure 8.1. The sensors were placed at 24 locations on each line, at the sites of the wells listed in Table 8.1. Line 1 covers a 30,100-ft span with 1,309 ft typical sensor spacing, while Line 2 covers a 25,600-ft span with 1,113 ft typical sensor spacing. The injection well is located near the intersection of the two lines, in the northeast corner of the Field.

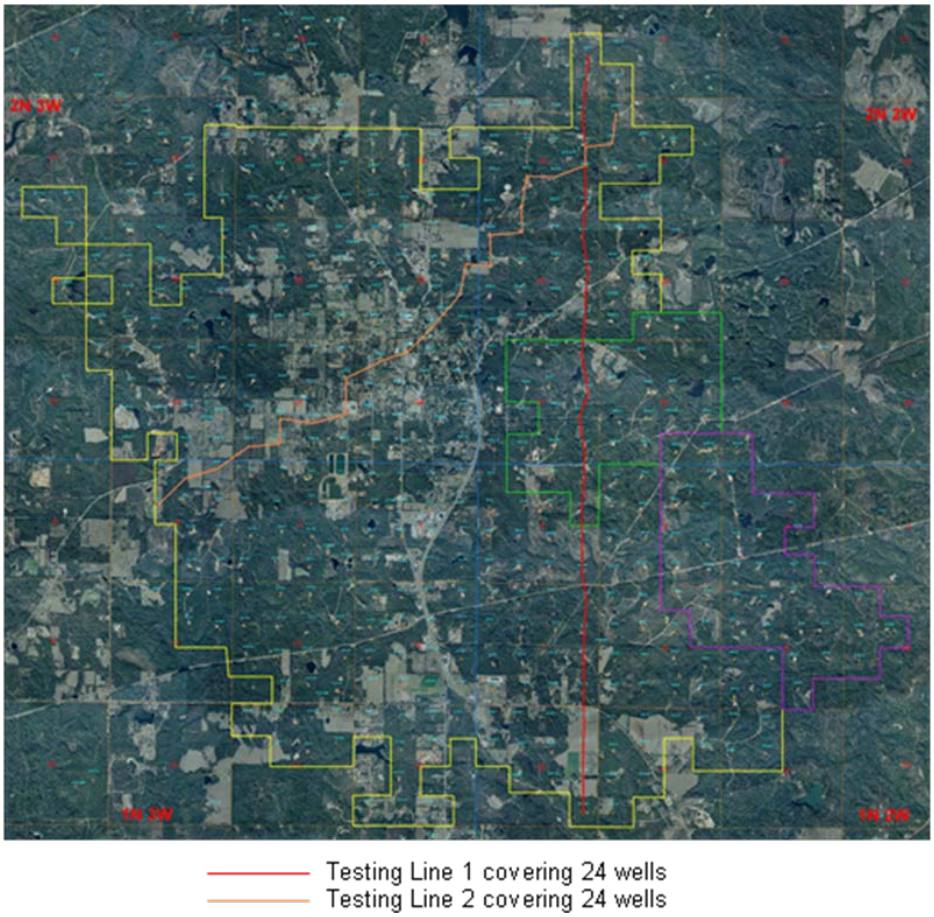


Figure 8.1. The seismic testing lines, shown in orange (northeast to southwest) and red (north to south), superimposed on the aerial photo of Citronelle Field from Denbury Onshore.

Baseline data, prior to $CO_2$ injection, were collected during visits to the test site in October 2008, January 2009, and May 2009. An analysis of those data was presented in a Quarterly Progress Report (October 30, 2009). Measurements coinciding with the start of significant $CO_2$ injection were made on December 9-10, 2009, then during steady $CO_2$ injection on March 11-12, 2010, and September 8-9, 2010. Measurements after returning to water injection were made on November 17-18, 2010, March 16-17, 2011, and May 17-18, 2011.

Table 8.1. Wireless Sensor Testing Locations.

| Line 1 | Well # | Line 2 | Well # |
|---|---|---|---|
| 1 | B-18-9 | 1 | B-20-4 |
| 2 | B-18-16 | 2 | B-20-5 |
| 3 | B-19-1 | 3 | B-19-8 |
| 4 | B-19-8 | 4 | B-19-9 |
| 5 | B-19-9 | 5 | B-19-10 #1 |
| 6 | B-19-16 | 6 | B-19-11 |
| 7 | B-29-4 | 7 | B-19-14 |
| 8 | B-30-8 | 8 | B-30-3 |
| 9 | B-30-9 | 9 | B-30-4 |
| 10 | B-30-16 | 10 | B-30-5 |
| 11 | B-31-1 | 11 | A-25-8 |
| 12 | B-31-8 #1 | 12 | A-25-9 |
| 13 | B-31-9 | 13 | A-25-15 #1 |
| 14 | B-31-16 | 14 | A-36-3 |
| 15 | D-6-1 #1 | 15 | A-36-4 |
| 16 | D-6-8 | 16 | A-35-8 |
| 17 | D-6-9 | 17 | A-35-9 |
| 18 | D-6-16 | 18 | A-35-10 #2 |
| 19 | D-7-1 | 19 | A-35-11 |
| 20 | D-7-8 | 20 | A-35-14 |
| 21 | D-7-9 | 21 | A-35-13 |
| 22 | D-7-16 | 22 | C-2-4 |
| 23 | D-18-1 | 23 | C-3-1 |
| 24 | D-18-8 | 24 | C-3-7 |

The micro-seismic data from the 24 measurement locations in each of the two sensor lines were placed in seven groups: Channel 1 to Channel 18 as Group 1, Channel 2 to Channel 19 as Group 2, Channel 3 to Channel 20 as Group 3, Channel 4 to Channel 21 as Group 4, Channel 5 to Channel 22 as Group 5, Channel 6 to Channel 23 as Group 6, and Channel 7 to Channel 24 as Group 7. A two-dimensional shear-wave velocity profile for each sensor line was then constructed by combining the profiles obtained from the seven groups of data. The shear-wave velocity versus

depth data from the seven groups for each line of sensors were then averaged to obtain the shear-wave velocity profile versus depth for that line. Analyses of the tests conducted on May 17-18, 2011, were presented in a Quarterly Progress Report (July 30, 2011, pp. 29-31).

The theory behind the passive geophysical monitoring technique and the analysis results are summarized in Chen et al. (2011) and Liu (2012). Extensive studies of the stress wave speed distributions have been conducted, notably the effects of $CO_2$ injection stages on the wave speeds. One of the key contributions of Liu's work (2012) is the use of a bi-linear model to describe the geo-static pressure distribution, before, during, and after injection of $CO_2$, summarized in Table 8.2.

Table 8.2. Summary of Linear Equations and R-Squared Values for the Ten Tests.

| Test No. | Injection | Line1-Top | Line1-Bottom | Line2-Top | Line2-Bottom |
|---|---|---|---|---|---|
| 1 | Water | $y = 0.8423x - 1321$<br>$R^2 = 0.9173$ | $y = 2.9947x - 17318$<br>$R^2 = 0.7101$ | $y = 0.9956x - 1393$<br>$R^2 = 0.9298$ | $y = 2.559x - 10718$<br>$R^2 = 0.8299$ |
| 2 | Water | $y = 0.8619x - 770$<br>$R^2 = 0.9271$ | $y = 3.3249x - 18337$<br>$R^2 = 0.774$ | $y = 1.0562x - 1765$<br>$R^2 = 0.8579$ | $y = 3.505x - 19217$<br>$R^2 = 0.7555$ |
| 3 | Water | $y = 0.919x - 1373.9$<br>$R^2 = 0.8942$ | $y = 2.1086x - 7979$<br>$R^2 = 0.7702$ | $y = 0.9327x - 1398$<br>$R^2 = 0.9066$ | $y = 3.426x - 18414$<br>$R^2 = 0.7028$ |
| 4 | $CO_2$ | $y = 0.6336x - 888.5$<br>$R^2 = 0.9183$ | $y = 2.8679x - 15287$<br>$R^2 = 0.8069$ | $y = 0.7069x - 1196$<br>$R^2 = 0.8829$ | $y = 1.8893x - 6689$<br>$R^2 = 0.8064$ |
| 5 | $CO_2$ | $y = 0.8235x - 1131$<br>$R^2 = 0.9452$ | $y = 2.3749x - 10666$<br>$R^2 = 0.8275$ | $y = 0.7606x - 833$<br>$R^2 = 0.8636$ | $y = 1.415x - 2426$<br>$R^2 = 0.8325$ |
| 6 | $CO_2$ | $y = 0.979x - 1515$<br>$R^2 = 0.9252$ | $y = 1.8158x - 7328$<br>$R^2 = 0.7833$ | $y = 1.0254x - 1705$<br>$R^2 = 0.91$ | $y = 1.7348x - 6294$<br>$R^2 = 0.8242$ |
| 7 | $CO_2$ | $y = 0.9384x - 1377$<br>$R^2 = 0.9326$ | $y = 1.9345x - 8701$<br>$R^2 = 0.8231$ | $y = 1.0957x - 1939$<br>$R^2 = 0.8367$ | $y = 1.1354x - 1171$<br>$R^2 = 0.8136$ |
| 8 | Water | $y = 0.9696x - 1492$<br>$R^2 = 0.9393$ | $y = 1.9233x - 8220$<br>$R^2 = 0.8239$ | $y = 0.9515x - 1369$<br>$R^2 = 0.9091$ | $y = 1.6881x - 6134$<br>$R^2 = 0.8259$ |
| 9 | Water | $y = 0.9755x - 1395$<br>$R^2 = 0.9339$ | $y = 1.5094x - 5065.2$<br>$R^2 = 0.7751$ | $y = 0.9975x - 1494$<br>$R^2 = 0.9052$ | $y = 1.4032x - 3910$<br>$R^2 = 0.7941$ |
| 10 | Water | $y = 0.9656x - 1348$<br>$R^2 = 0.9402$ | $y = 1.5672x - 5653$<br>$R^2 = 0.7913$ | $y = 0.9936x - 1468$<br>$R^2 = 0.9243$ | $y = 1.4889x - 4864$<br>$R^2 = 0.7837$ |

The composite bilinear curves constructed using the average values from each of the three stages of $CO_2$ injection (before, during, and after injection), and for each of the two sensor lines, indicated that two distinct behaviors can be observed, as shown in Figures 8.2 (Sensor Line 1) and 8.3 (Sensor Line 2). The gap between the two sets of lines is identified as the Wilcox Group (calcareous clay, > 4000 ft) and Selma Group (chalk, ~ 5000 ft). The upper layer stress changes due to $CO_2$ injection are varied and can either increase or decrease depending on the conditions existing in the strata.

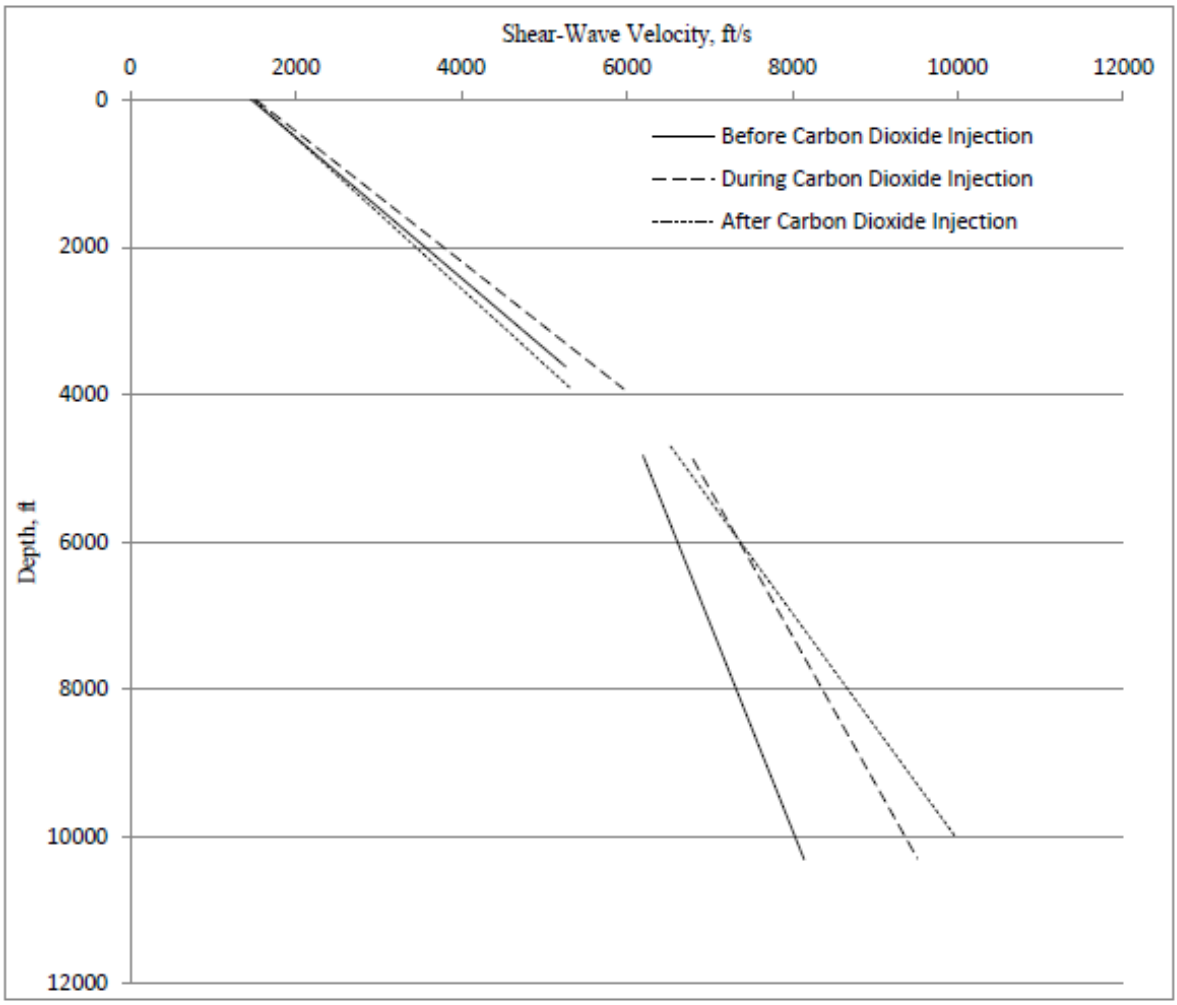


Figure 8.2. Bi-linear model of the shear wave velocity profile for Sensor Line 1, for the three stages of the injection process: before, during, and after $CO_2$ injection.

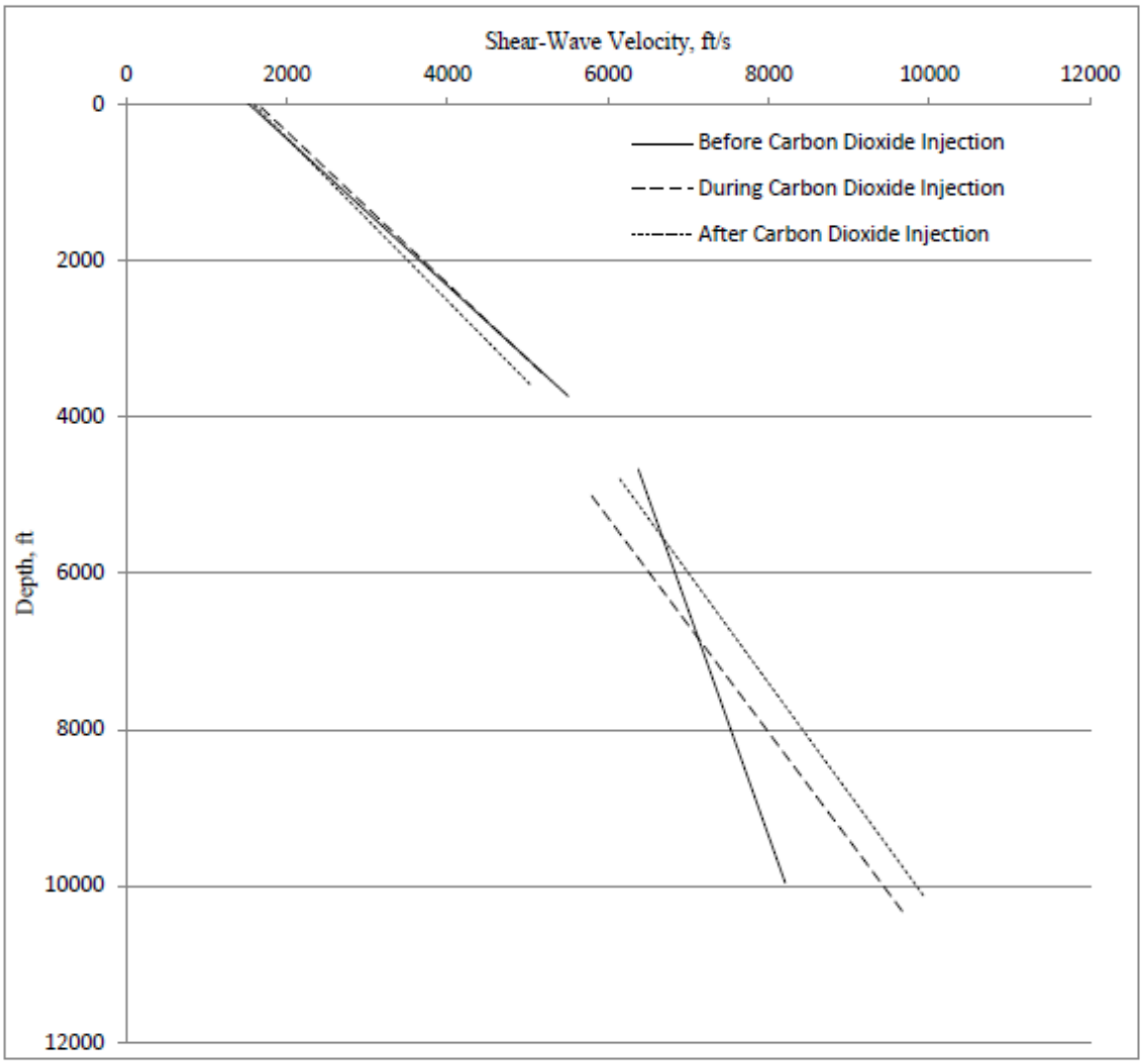


Figure 8.3. Bi-linear model of the shear wave velocity profile for Sensor Line 2, for the three stages of the injection process: before, during, and after $CO_2$ injection.

## 8.2. Simulation of $CO_2$ Flow through Porous Media

To understand the effects of porosity and saturation on stress waves, a laboratory experiment was designed to simulate high-porosity rocks saturated with mixed crude oil, water, and $CO_2$, to determine the effects of the fluid saturations on stiffness and shear-wave velocity. To accelerate the $CO_2$ flow, a simulated rock specimen was developed for that purpose. The highly porous specimen was designed to investigate the Biot correlation between wave speed and the change in stress state in the pore space, during $CO_2$ flow. Two experiments were conducted. The first experiment utilized a cylindrical structure of materials having different porosities and Fiber Bragg Grating (FBG) sensors to measure the external hoop strain during material expansion. The second experiment focused on $CO_2$ adsorption within the material.

***Experiment 1: Simulated Porous Cylinder.*** The "Physical Problem" is the monitoring of mechanical stressing of cylindrical specimens filled with variable mixtures and permeated with $CO_2$ that is encased within a relatively less permeable material. This experiment is to demonstrate the expansion effect due to $CO_2$ injection. The specimen was prepared through a simple cement casting process to form a cylinder having a hollow center. The casting process necessitates the use of simple materials: two polyvinyl chloride (PVC) tubes having different diameters, to create the inner and outer surfaces of the cylinder; a base plate, to prevent the cement from leaking out from the cylindrical boundaries and to form the base; and a release agent, to prevent the PVC mold from adhering to the final product. A photograph of a cylinder after its initial construction is shown in Figure 8.4. The average dimensions of the cylinder were: outer diameter, 15.5 cm; inner diameter, 9 cm; and height, 30 cm.


Figure 8.4. Experimental design for fiber optic monitoring of a SCARC specimen.

The FBG strain sensors were attached to the cylinders and the planar (hoop) strains were evaluated at three locations: the top, middle, and bottom of the specimen. Each location had a distributed sensing fiber with eight FBG regions, equally spaced around the circumference. Figure 8.5 shows the FBG sensor locations around a specimen. The fibers continuously monitor the wavelength of the distributed sensors, which is typically in the vicinity of 1,500 nm. The spacing of the sensors provides the wavelength differentials that are transformed into hoop strain values using the following equation,

$$Strain = 0.845 \cdot (f_1 - f_0) \cdot 1000 \quad (1)$$

where $f_0$ is the initial wavelength and $f_1$ is the measured wavelength. It is recognized that under perfect construction, testing, and instrumental conditions the sensors should register identical hoop strain values. It is expected that differences in the strain values, among distributed sensors on the same fiber, will provide evidence of local mechanical behavior caused by differences in geometry, load propagation, or material non-uniformity.

Following the formation of the hollow cylindrical specimens and the application of the FBG sensors, mixtures having variable composition were introduced into the mold. The components of the mixture were fly ash, cement, water, and aluminum powder. The aluminum reacts with water and slowly expands the mixture, creating voids in the dried specimen. The goal of using different blends of materials was to simulate different levels of stress on the hollow cylinder, which simulates surrounding impermeable materials. The results presented here were obtained with a mixture

having an ash-to-cement ratio of 50% by weight. The interaction of the mixture and its cylindrical containment was studied for 100 hours. The strain behaviors for the top, middle, and bottom rings of Cylinder #5 are shown in Figures 8.6, 8.7, and 8.8. Using the FBG sensor measurements, the stressing and cracking of the concrete cylinder can be traced and the straining of the cylinder in both tension (positive microstrain) and compression (negative microstrain) can be determined. The stress history is important because it indicates that within the oil layer, the stress distribution is not necessarily homogenous.

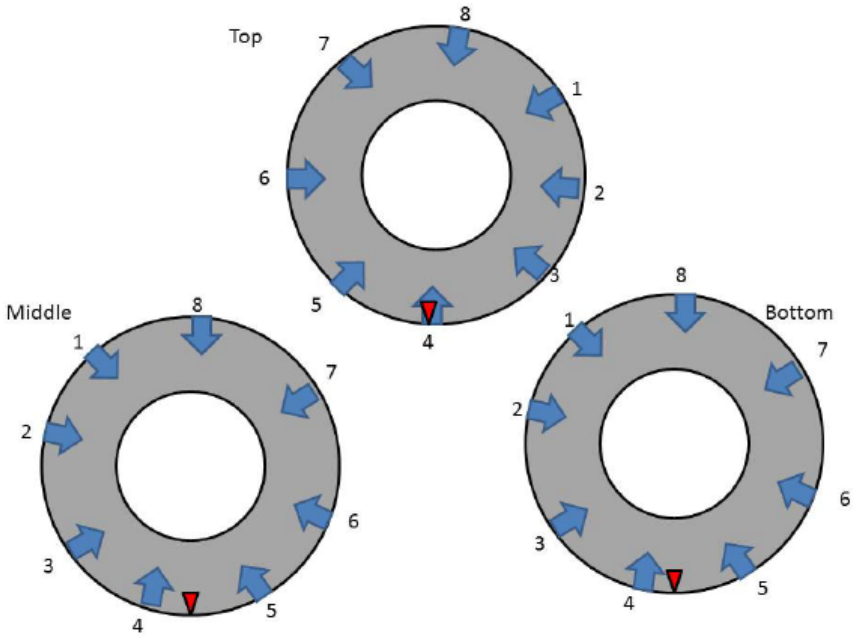


Figure 8.5. Cylinder #5 sensor locations.

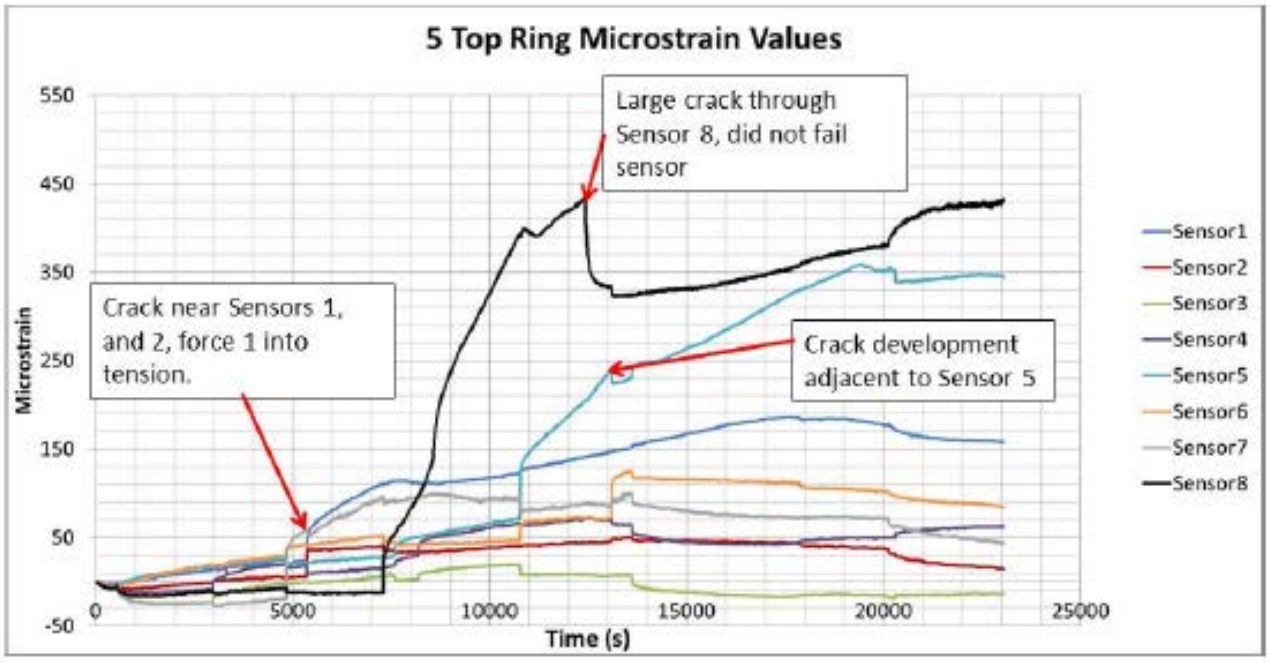


Figure 8.6. Cylinder #5 Top Ring FBG sensor responses in microstrain vs. time.

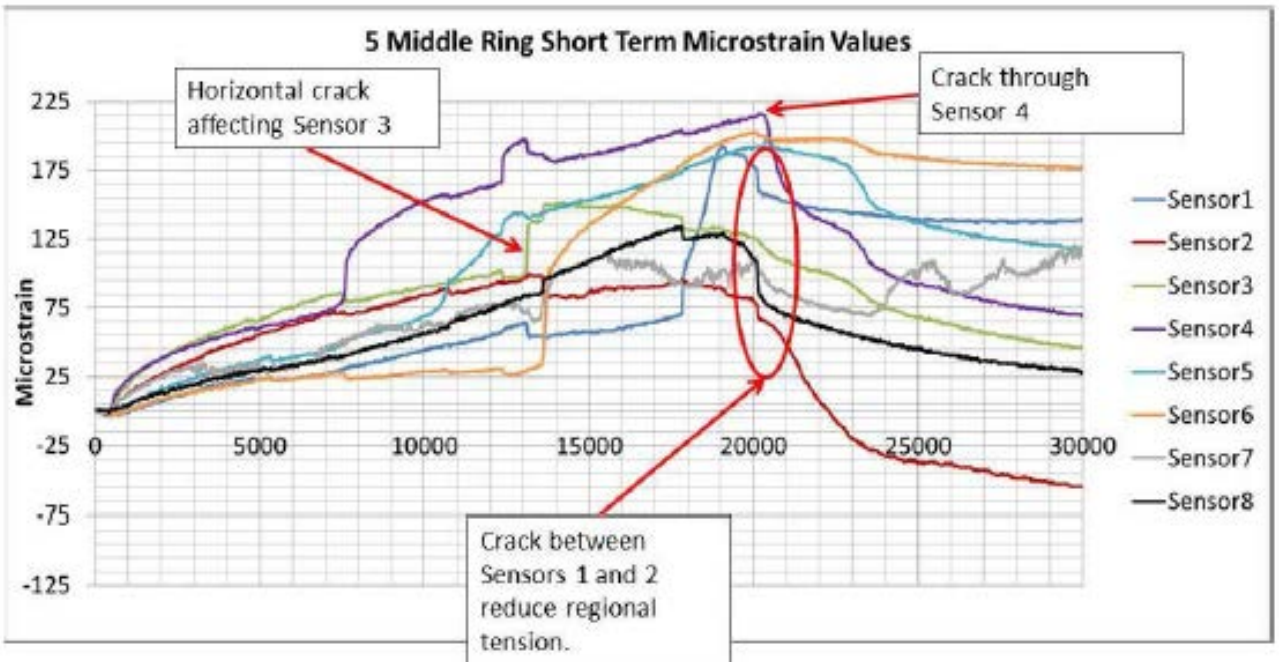


Figure 8.7. Cylinder #5 Middle Ring FBG sensor responses in microstrain vs. time.

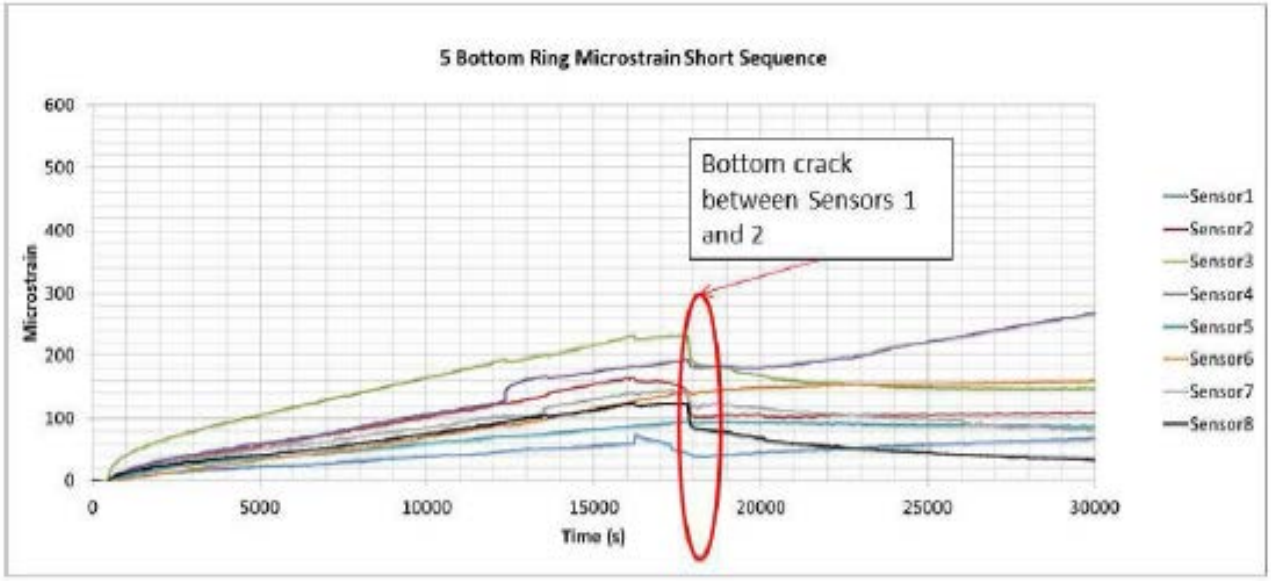


Figure 8.8. Cylinder #5 Bottom Ring FBG sensor responses in microstrain vs. time.

***Experiment 2: $CO_2$ Adsorption Experiments.*** The objectives of the adsorption experiments were to:

1. Study the $CO_2$ adsorption ratios in different types of mixture compositions.
2. Study the relationship between material porosity and degree of physical adsorption.

The experimental setup includes a reaction cell (Figure 8.9a), reference cell (Figure 8.9b), high precision pressure sensor (Figure 8.9c), and data logger (Figure 8.9d). A diagram of the

experimental setup is shown in Figure 8.10. This system was developed so that we can study the amount of $CO_2$ that can be stored in the source rocks and possibly determine the effect of sorption rate. Due to its late development during the course of the present project, only very limited experiments have been performed.


Figure 8.9. Instrumentation for the adsorption measurements.
a. Reaction cell.
b. Reference cell.
c. High-precision pressure sensor.
d. Data logger.

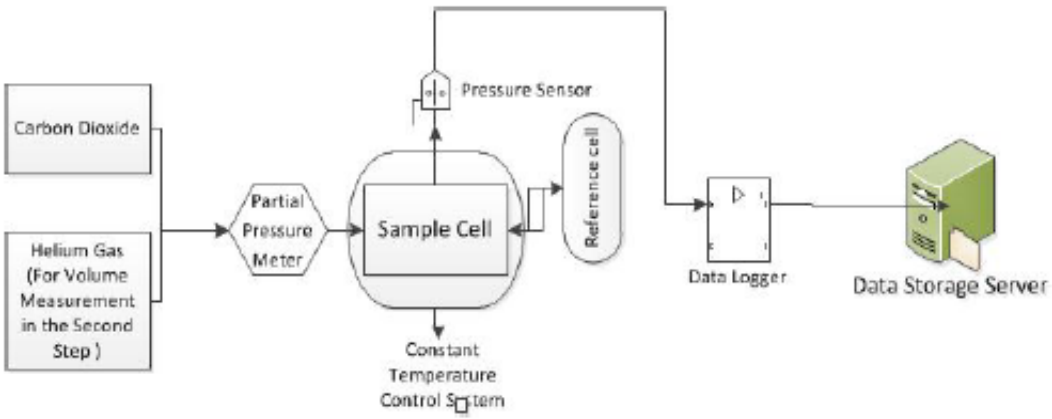


Figure 8.10. Diagram of the adsorption experiment.

## 8.3. Simulation of Oil and $CO_2$ Flow through Porous Media

The experimental setup shown in Figures 8.9 and 8.10 was used to study the sorption of a sample of oil from Citronelle into a simulated rock. The simulated rock is essentially a hardened cement cylinder, representing high density soft rock. Figure 8.11 shows the rock sample with a cored depression in the middle, serving as a reservoir for oil. Figure 8.12 shows the reservoir filled with oil. The sample was then placed under $CO_2$ pressure. Figure 8.13 shows that the oil was forced into the specimen. Figure 8.14 shows the $CO_2$ pressure (in microvolts) versus time, indicating that a significant amount of $CO_2$ was absorbed into the oil and simulated rock. This experiment helped us to visualize the interaction between $CO_2$ gas under pressure and the oil in reservoir rock. Figure 8.14 shows an interesting initial sorption reversal process that may be a function of the content and acidity of the oil. Our experience with pure and acidic water is that acidity can help reduce the sorption reversal process.

Figure 8.11. Specimen with cored reservoir.

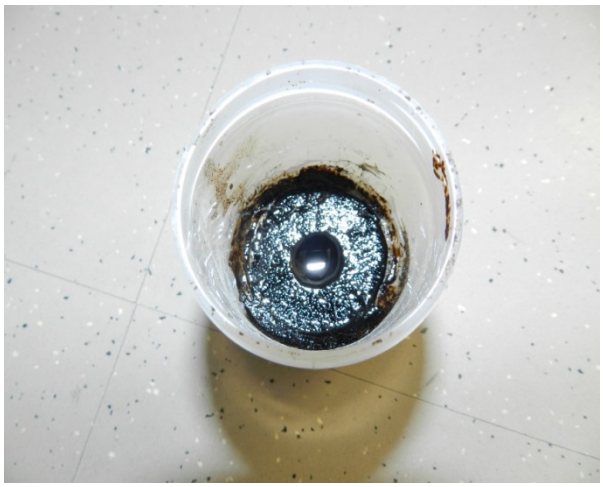

Figure 8.12. Reservoir filled with oil.

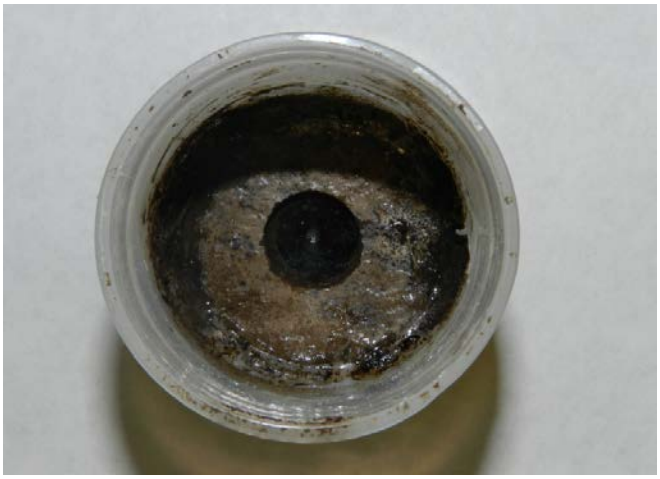

Figure 8.13. Oil forced into the rock by $CO_2$.

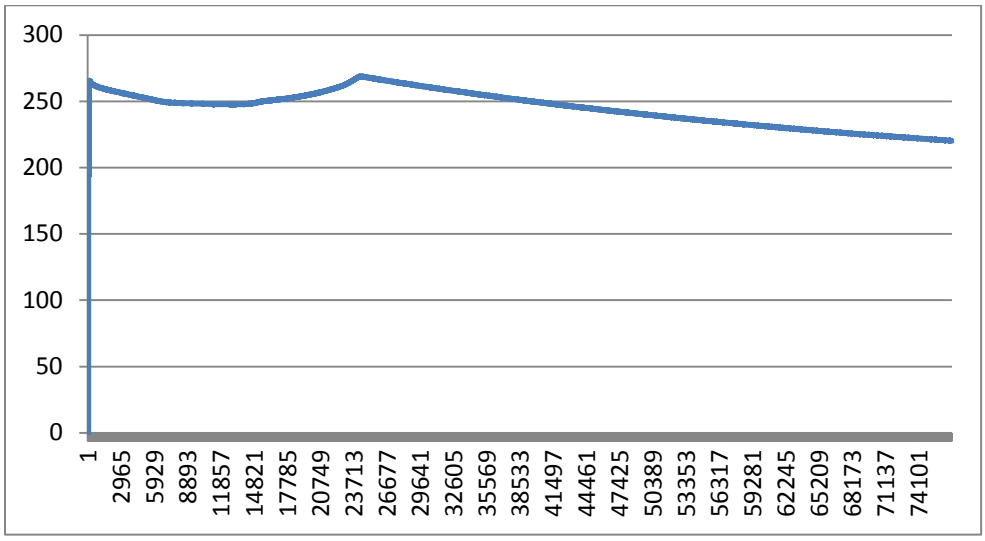


Figure 8.14. $CO_2$ pressure (in microvolts) versus time in seconds for the oil/rock sample.

## 8.4. Evidence for Carbonation

Carbonation of minerals has been identified in previous studies of $CO_2$ injection in oil fields. The effect is potential blockage of flow paths and reduced EOR. SEM (Scanning Electronic Microscope) and EDS (Energy Dispersive X-ray Spectroscopy) measurements were performed on the samples, providing evidence for carbonation, as shown in the figures below. The images were obtained using the simulated specimens (without oil), not from samples of reservoir rock from Citronelle. Figure 8.15 shows the difference between carbonated and non-carbonated specimens, where the cotton-like image on the right is carbonates. Figures 8.16 to 8.18 show EDS images and data containing evidence for the existence of carbonates.

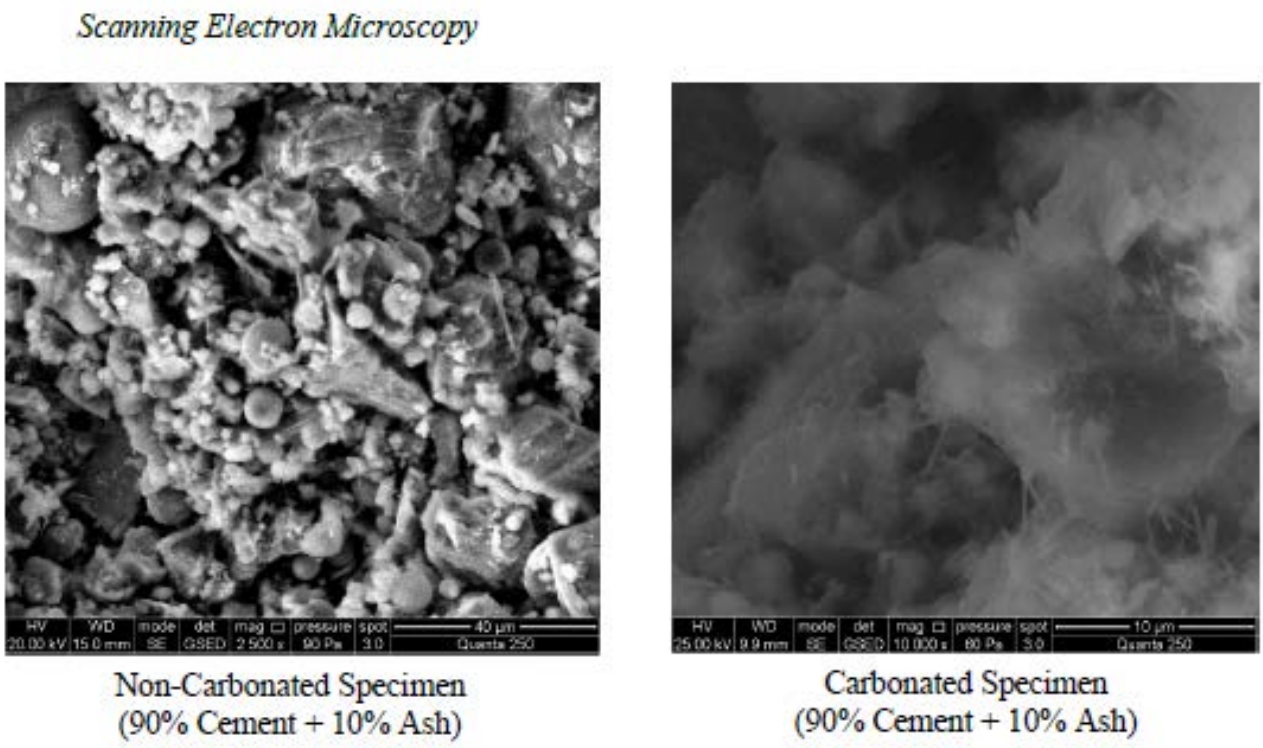


Figure 8.15. SEM images comparing the structures of carbonated and non-carbonated specimens.

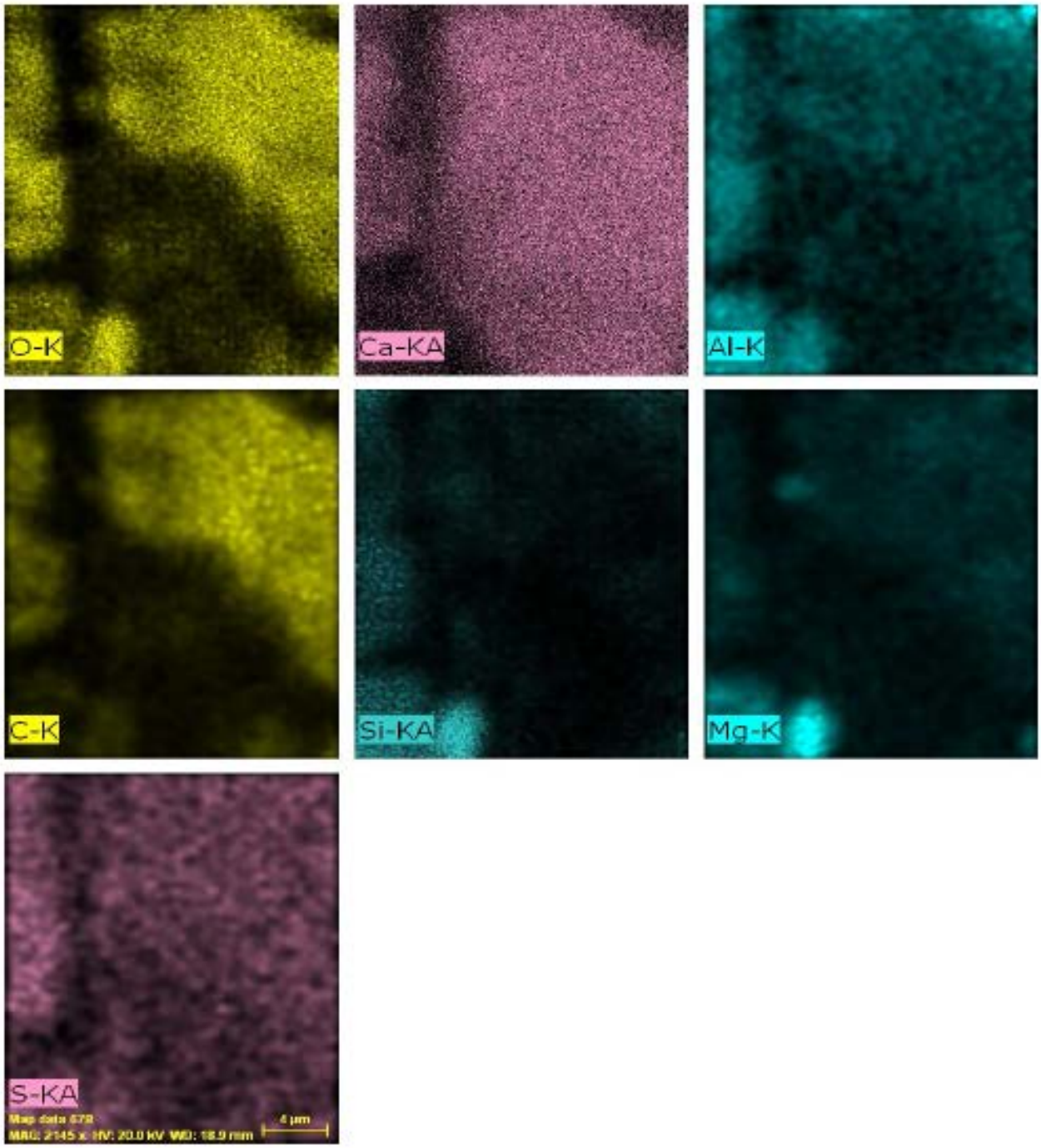


O-K, Ca-KA, Al-K, C-K, Si-KA, Mg-K, S-KA
Date: 12/19/2012 11:45:40 AM
Image size: 300 x 394
Mag: 2144.77211796247x

Figure 8.16. The similarity of the oxygen (top row, left) and carbon (middle row, left) element maps provides evidence for the presence of carbonates.

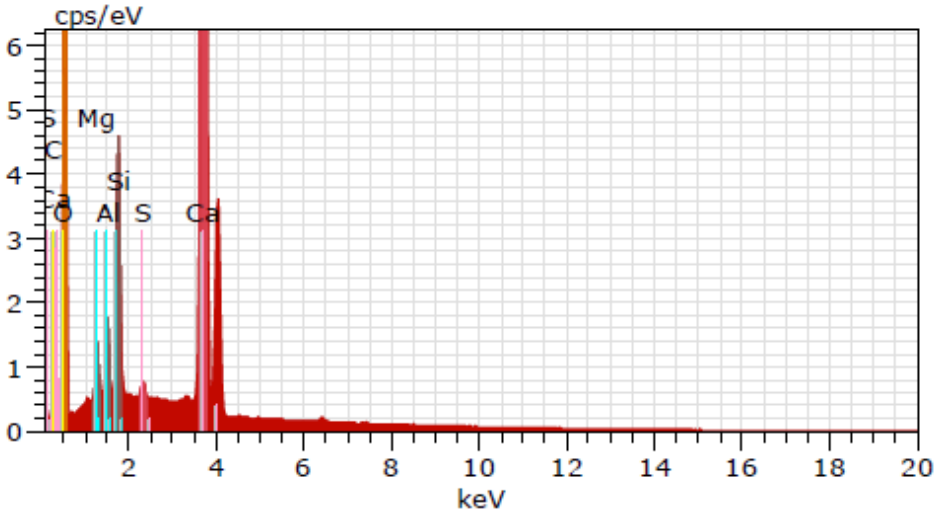


Figure 8.17. The energy spectrum showing strong carbon and oxygen peaks, again suggesting the presence of carbonates.

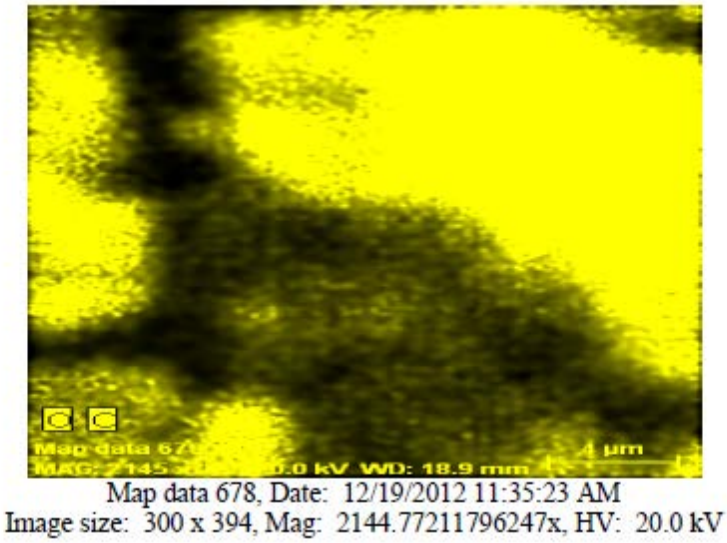


Figure 8.18. EDS image of the porous sample with yellow coloring indicating carbon content, interpreted as carbonated material.

## 8.5. Simulation of Wave Propagation

To verify the geophysical test results, simulation of wave propagation using Multiple-Degrees of Freedom (MDF) lumped mass models was performed (Liu, 2014). The modeling was done using Matlab. The oil-producing layer was divided into four elements and the entire oil field was modeled as 534 different layers. The vibration source was assumed to be random waves having multiple frequency components, with a forcing amplitude of 675 lb force. The results indicate that waves having frequencies up to 4 Hz can travel to ground surface. Figure 8.19 shows the shear wave speed distributions from an actual field test (Line 2 of Test 6, during $CO_2$ injection) and from

the numerical simulations (from displacement, velocity, and acceleration time histories). The results from the simulations are in reasonable agreement with the experimental observations.

Using the MDF model, stressing of the oil-producing layer and the strata above it can be studied separately. The results indicate that the geophysical testing method was able to distinguish stress changes in the oil-bearing layer from stress changes in the other strata.

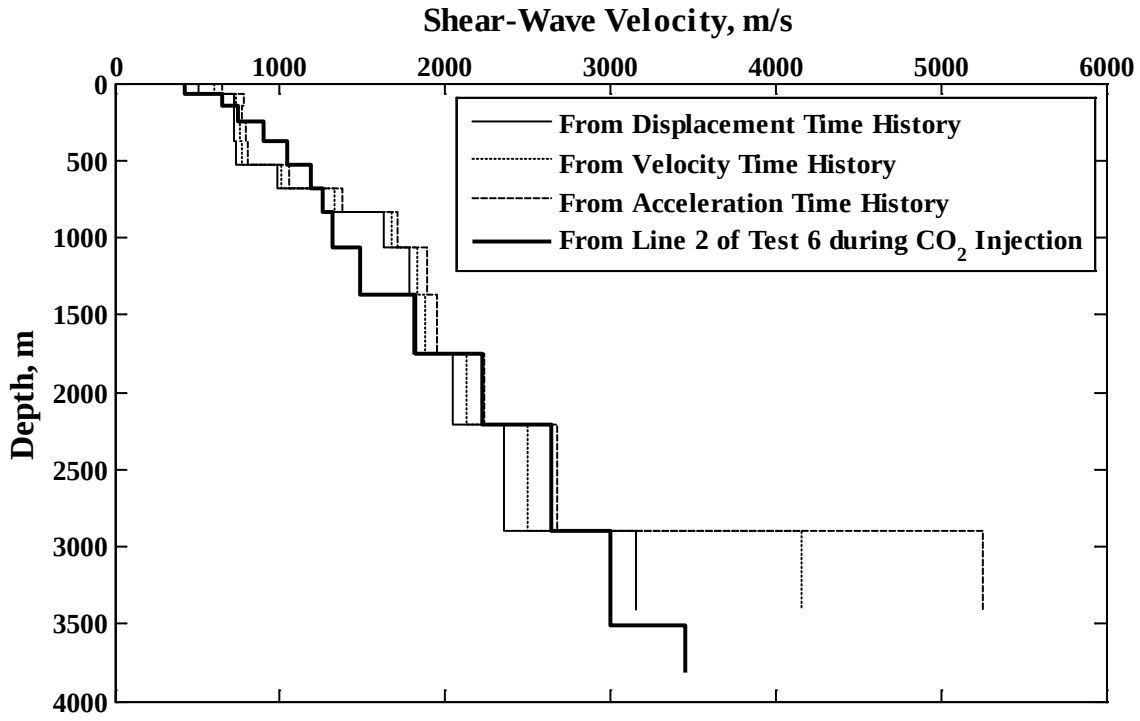


Figure 8.19. Comparison of shear wave velocities obtained from simulation results and experimental data (Line 2 of Test 6).

**Acronyms, Abbreviations, and Symbols in Section 8**

| | |
|---|---|
| DoReMi | derivative of refraction microtremor |
| EDS | energy dispersive X-ray spectroscopy |
| $f_0$ | initial wavelength, m |
| $f_1$ | measured wavelength, m |
| FBG | fiber Bragg grating |
| MDF | multiple degrees of freedom |
| PVC | polyvinyl chloride |
| ReMi | refraction microtremor |
| SCARC | simulated carbon ash retention cylinder |
| SEM | scanning electronic microscope |

**References in Section 8**

Chen, S.-E., Y. Liu and P. Wang, "DoReMi - A Passive Geophysical Monitoring Technique for $CO_2$ Injection," SPE-149265-PP, Society of Petroleum Engineers Eastern Regional Meeting, Columbus, OH, August 17-19, 2011.

Liu, Y., "DoReMi - A Passive Geophysical Technique and Development of Bilinear Model for $CO_2$ Injection," M.S. Thesis, Department of Civil and Environmental Engineering, University of North Carolina at Charlotte, Charlotte, NC, 2012.

Liu, Y., "Study of $CO_2$ Injection at Citronelle Oil Field using Lumped Mass Modeling and Field Data Validation," Ph.D. Dissertation, Infrastructure and Environmental Systems, Department of Civil and Environmental Engineering, University of North Carolina at Charlotte, Charlotte, NC, 2014.

# 9. Visualization of the Interaction between $CO_2$, Oil, and Water during Enhanced Oil Recovery*

Konstantinos Theodorou* and Corey Shum
University of Alabama at Birmingham

---

The complexity of the interaction between $CO_2$, oil, and water in a geologic formation makes animation of the evolution of fluid saturations during $CO_2$ and water flooding an especially useful tool for understanding enhanced oil recovery and its dependence on reservoir conditions and injection parameters.

## 9.1. Simulation of $CO_2$-Enhanced Oil Recovery using MASTER 3.0

The reservoir simulation results were obtained by Konstantinos Theodorou (2013) using MASTER 3.0 (Ammer and Brummert, 1991; Ammer, Brummert, and Sams, 1991; Zeng, Grigg, and Chang, 2005). The simulator was used with all its miscible gas injection features enabled, and $CO_2$ as the injected gas.

The simulations were based on a single layer, 40- by 32-block grid. Each block in the grid measured 53.65 m by 53.65 m (176 ft by 176 ft). The thickness of each block in the simulation grid varied according to the sand thickness contours. Figures 9.1 and 9.2 show the thickness contours of Sands 14-1 and 16-2, respectively, in the area of the simulation grid. The thicknesses were estimated from computer-generated net pay contours (Esposito et al., 2010).

The simulation grid was extended beyond the inverted five-spot well pattern, to include the influence of peripheral oil production and water injection wells on the behavior of the wells in the five-spot. Sixteen wells were considered in the simulation, and their arrangement within the simulation grid is shown in Figure 9.3. Table 9.1 lists the well number, permit number and type (producer or injector) for each well included in the simulation.

The primary reservoir parameters specified in the simulations of the $CO_2$-EOR pilot test are listed in Table 9.2. The average reservoir pressure in the simulation grid was estimated to be 31.0 MPa (4500 psi). The value is based on fluid head and bottom hole pressure (BHP), recorded in a reservoir pressure field log dated October 1992, that was retrieved (September 9, 2008) from the Citronelle Oil Field archives at the Alabama State Oil and Gas Board. Pressure in the simulation grid is considerably higher than the average reservoir pressure of the Citronelle Oil Field, estimated to be 20.7 MPa (3000 psi) (Esposito et al., 2010). Low permeabilities in the simulation grid have caused reservoir pressure to increase locally during the simulation of water flood, to establish the baseline for oil production prior to $CO_2$ injection.

---

*K. Theodorou, "Carbon Dioxide Enhanced Oil Recovery from the Citronelle Oil Field and Carbon Sequestration in the Donovan Sand, Southwest Alabama," Ph.D. Dissertation, Interdisciplinary Engineering, University of Alabama at Birmingham, Birmingham, AL, 2013. Dr. Theodorou is now an Instructor of Mathematics at the Jefferson State Community College in Birmingham, AL.

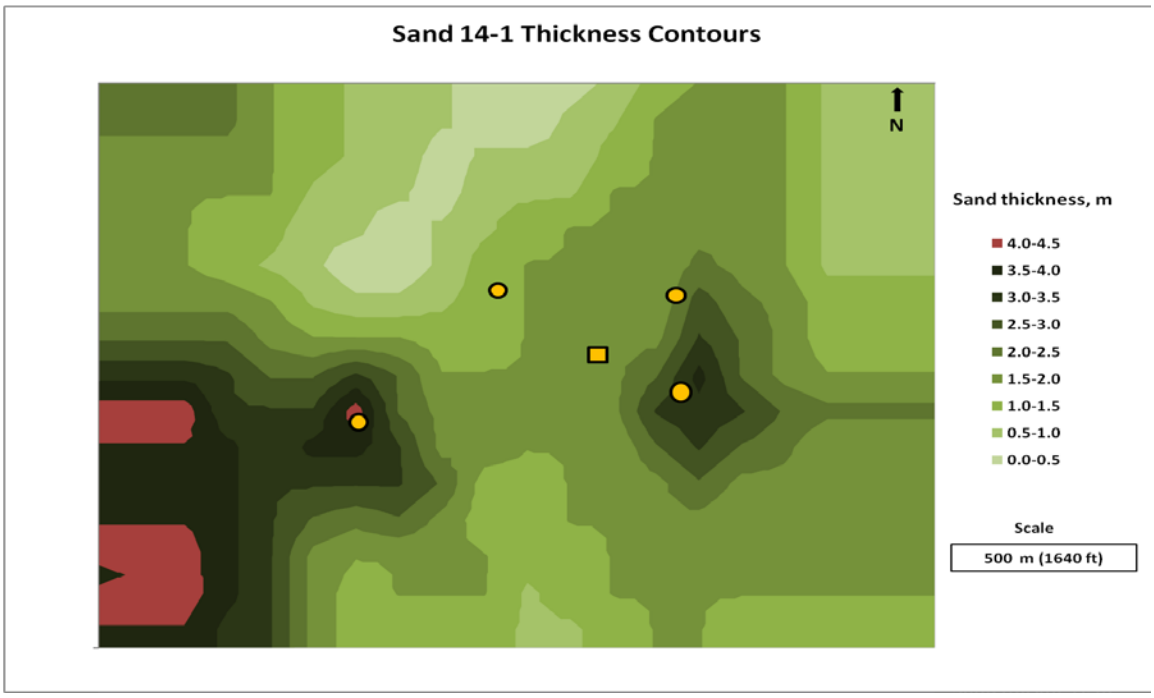


Figure 9.1. Sand 14-1 thickness contours within and surrounding the inverted five-spot well pattern. The contour interval is 0.5 m (1.64 ft). The injector, Well B-19-10 #2, is indicated by the rectangular marker.

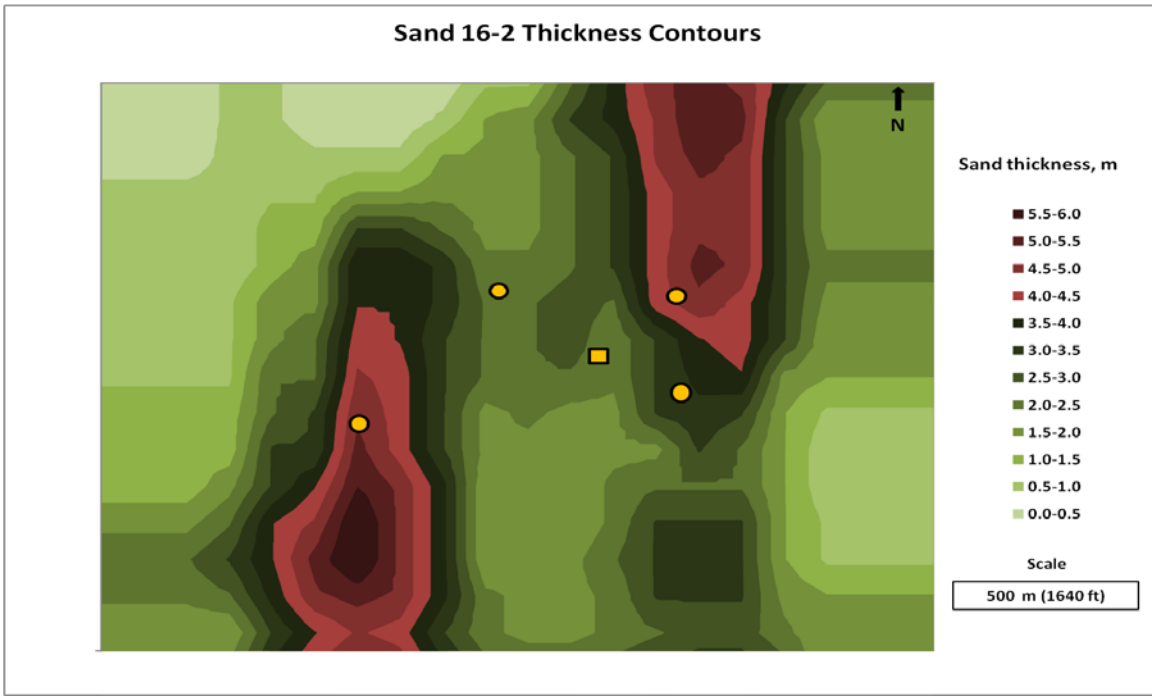


Figure 9.2. Sand 16-2 thickness contours within and surrounding the inverted five-spot well pattern. The contour interval is 0.5 m (1.64 ft). The injector, Well B-19-10 #2, is indicated by the rectangular marker.

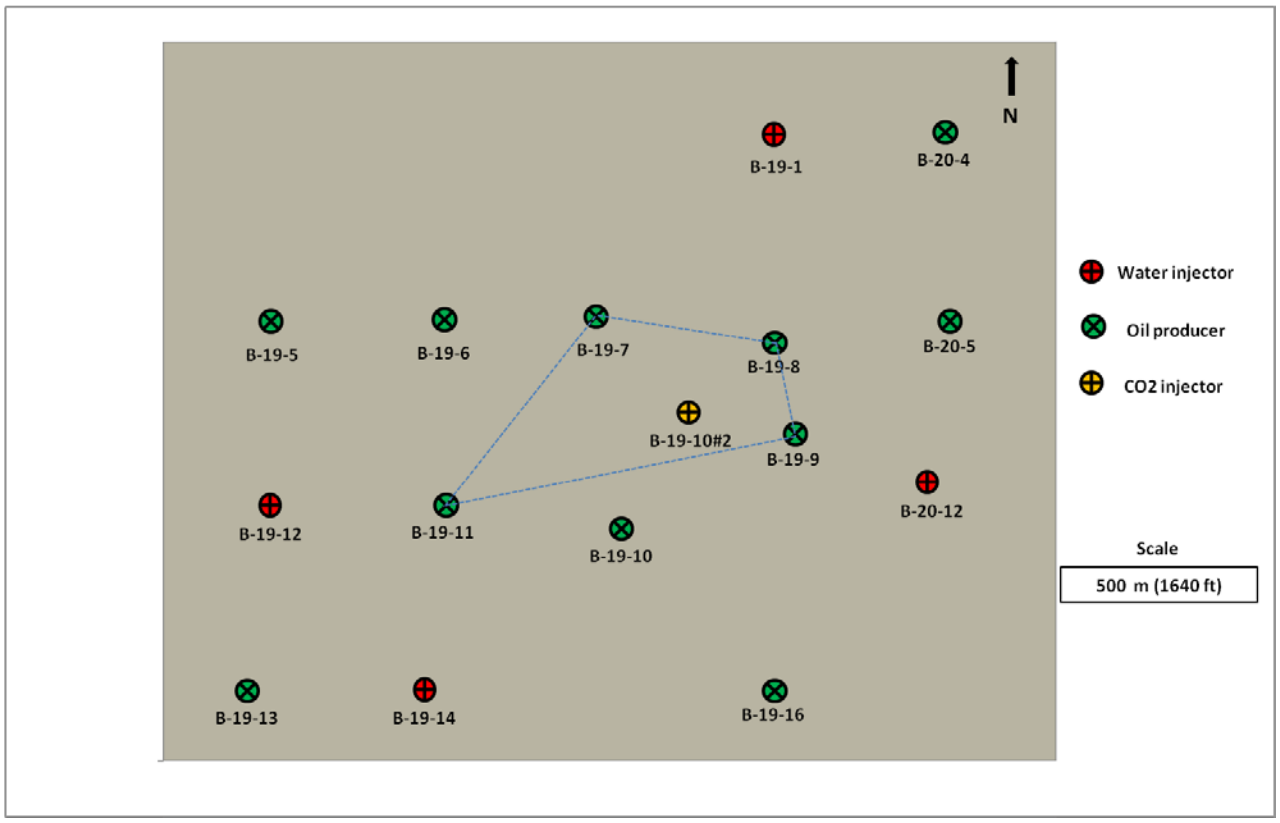


Figure 9.3. Wells included in the $CO_2$-enhanced oil recovery simulation grid. The dashed line indicates the inverted five-spot well pattern (after Merit Energy Company, Citronelle Field, Posted Well Data, 2004).

During the initial water injection, the distribution of water flow into Sands 14-1 and 16-2 was 82% and 18%, respectively. Tracer tests indicated that the distribution of injected $CO_2$ volumes into Sands 14-1 and 16-2 was 57% and 43%, respectively. Injection rates were divided according to these values in the simulations.

Table 9.1. Wells in the Simulation of the $CO_2$-EOR Pilot Test.

| Well Number | Permit Number | Type |
|---|---|---|
| B-19-5 | 1232 | Oil producer |
| B-19-6 | 1214 | Oil producer |
| B-19-7 | 1215 | Oil producer |
| B-19-8 | 1235 | Oil producer |
| B-19-9 | 1205 | Oil producer |
| B-19-10 | 1206 | Oil producer |
| B-19-10 #2 | 3232 | Water/$CO_2$ injector |
| B-19-11 | 1209 | Oil producer |
| B-19-13 | 787 | Oil producer |
| B-19-16 | 1208 | Oil producer |
| B-20-4 | 1256 | Oil producer |
| B-20-5 | 1230 | Oil producer |
| B-19-1 | 1254 | Water injector |
| B-19-12 | 1197 | Water injector |
| B-19-14 | 898 | Water injector |
| B-20-12 | 1225 | Water injector |

Table 9.2. Model Parameters used in the $CO_2$-EOR Pilot Test and WAG Recovery Simulations.

| Parameter | Value | Source |
|---|---|---|
| Average oil reservoir pressure | 31.0 MPa (4500 psi) | Field pressure log, 1992 |
| Reservoir oil saturation | 0.55 dimensionless | Unit Manager's Report, 1999 |
| Reservoir water saturation | 0.45 dimensionless | Unit Manager's Report, 1999 |
| $CO_2$-oil miscibility pressure | 19.3 MPa (2800 psi) | Gilchrist, 1981 |
| Average porosity | 0.1361 dimensionless | Fowler et al., 1998 |
| Average permeability | 10 mdarcy | Fowler et al., 1998 |

## 9.2. Visualization of the Migration of $CO_2$, Oil, and Water

Corey Shum, in the UAB Enabling Technology Laboratory, programmed animations showing the evolution of fluid saturations in Sands 14-1 and 16-2 of the Citronelle Oil Field during two $CO_2$ injections of 7500 tons each, separated by a period of water injection. The raw output from the reservoir simulation was parsed with a custom application to extract the oil, water, and $CO_2$ saturation results for each point in space and time. This data was then exported to a standard 3-D data visualization format, VTK <http://www.vtk.org/>. ParaView <http://www.paraview.org/> and custom tools were then used to create animations of the time-dependent data.

The animations may be downloaded and run from the following URL's:

Simulation of $CO_2$-EOR in Sand 14-1: https://dl.dropbox.com/s/9br413mpbsyd8ek/oil14.mp4?dl=1

Simulation of $CO_2$-EOR in Sand 16-2: https://dl.dropbox.com/s/77oprxjx9gxafxa/oil16.mp4?dl=1

Screen shots from the animations are shown in Figures 9.4 to 9.7. As shown in Figure 9.4, the inverted five-spot test pattern in the Citronelle Oil Field is represented at the top with a cutout of satellite photographic imagery. Lines from the well locations are extruded down the image, to identify corresponding locations in the $CO_2$, oil, and water saturation graphs. The levels of saturation are represented both by height at each location on the graph for each fluid component and also by color, according to the color legend at the upper left in the image. As the simulation progresses, the day and the injection activity are displayed in the lower-right corner of the image. The days are counted from the beginning, in 1982, of the Alabama State Oil and Gas Board record of production from the Citronelle Field (Alabama State Oil and Gas Board, 2012).

$CO_2$, oil, and water saturations in Sands 14-1 and 16-2 are shown before any $CO_2$ was injected in Figure 9.4, at the end of the first $CO_2$ injection in Figure 9.5, at the end of the water injection in Figure 9.6, and at the end of the second $CO_2$ injection in Figure 9.7. The progress of $CO_2$ sweep, the development and migration of the oil bank, and the residual oil and water saturations left behind are all clearly visible. Watching the animation provides a new perspective and appreciation of the complex interactions among the fluids and phases.

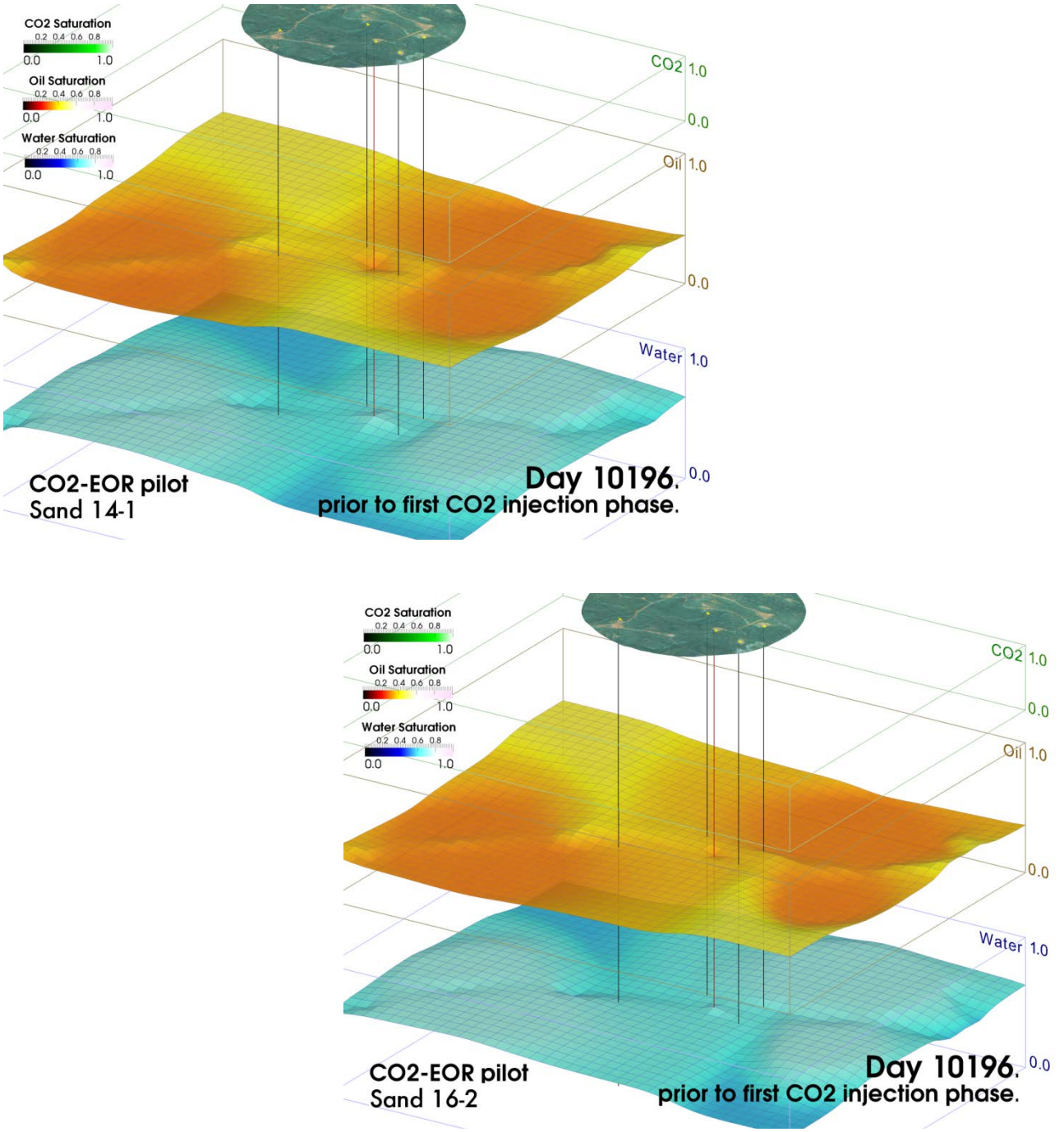


Figure 9.4. Screen shots of the animations of oil and water flows in Sands 14-1 (top) and 16-2 (bottom), before $CO_2$ injection. The animation was programmed by Corey Shum, based on simulations by Konstantinos Theodorou (2013) using MASTER 3.0 (Ammer and Brummert, 1991; Ammer, Brummert, and Sams, 1991; Zeng, Grigg, and Chang, 2005). An aereal view of the test well pattern is shown at the top of each figure, with the oil (yellow/orange), and water (blue) saturations on scales from 0 to 1, below. The vertical lines represent the injector (red) and producers (black). The saturations are also indicated by variations in intensity of the color. Low saturations are shown by more intense color, and vice versa, so that regions of high saturation do not obscure regions of lower saturation behind them, when peaks appear in the graphs due to $CO_2$ and water injection.

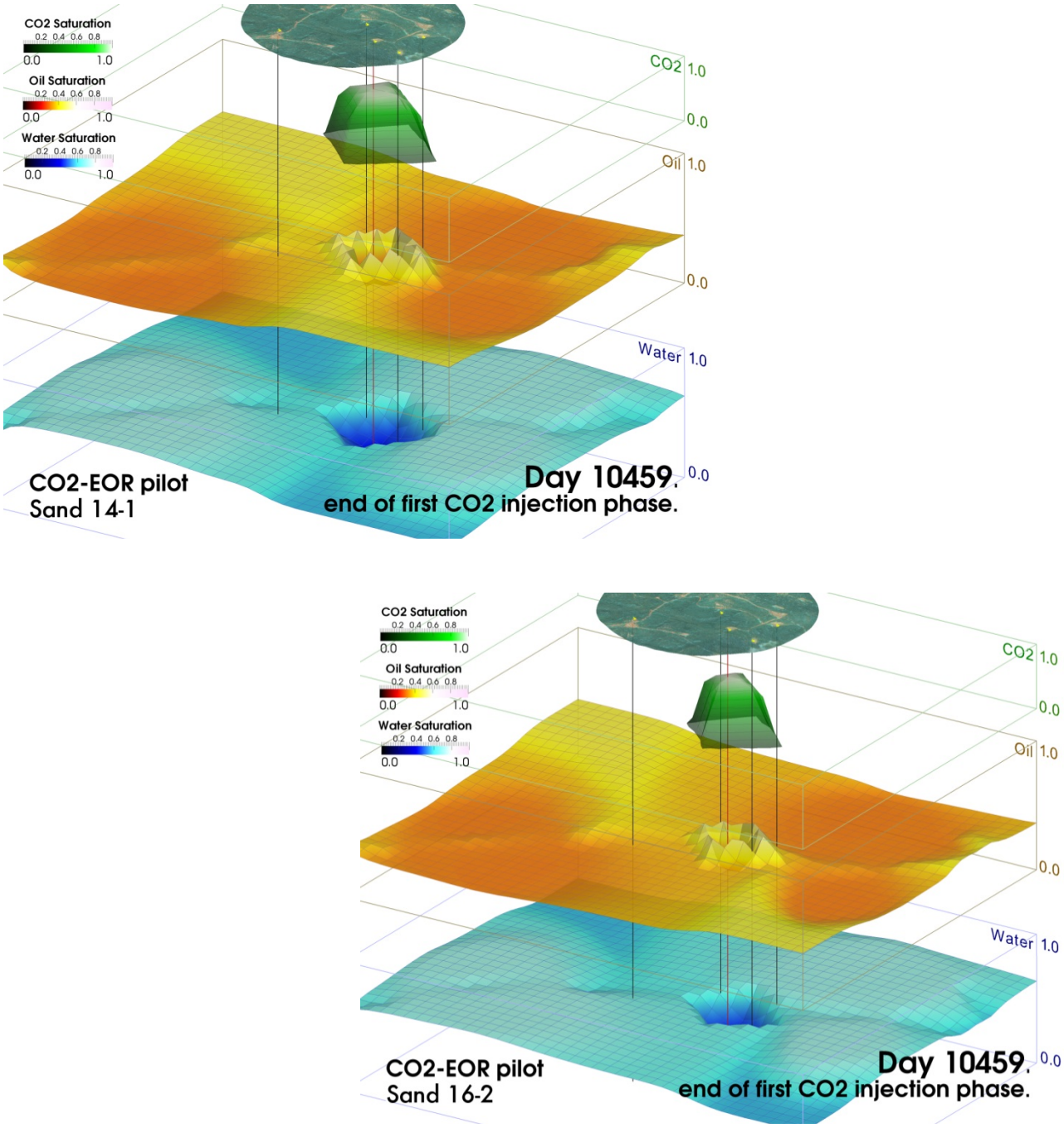


Figure 9.5. Screen shots of the animations of $CO_2$ (shown in green), oil, and water flows in Sands 14-1 (top) and 16-2 (bottom), at the end of the first injection of 7500 tons of $CO_2$, after 263 days of $CO_2$ injection. Elevated oil saturations associated with the oil banks are clearly visible, but the banks have not yet reached all three of the producers closest to the injector. The $CO_2$ flow into Sand 14-1 is greater than into Sand 16-2, resulting in further progress of the oil bank away from the injector in Sand 14-1.

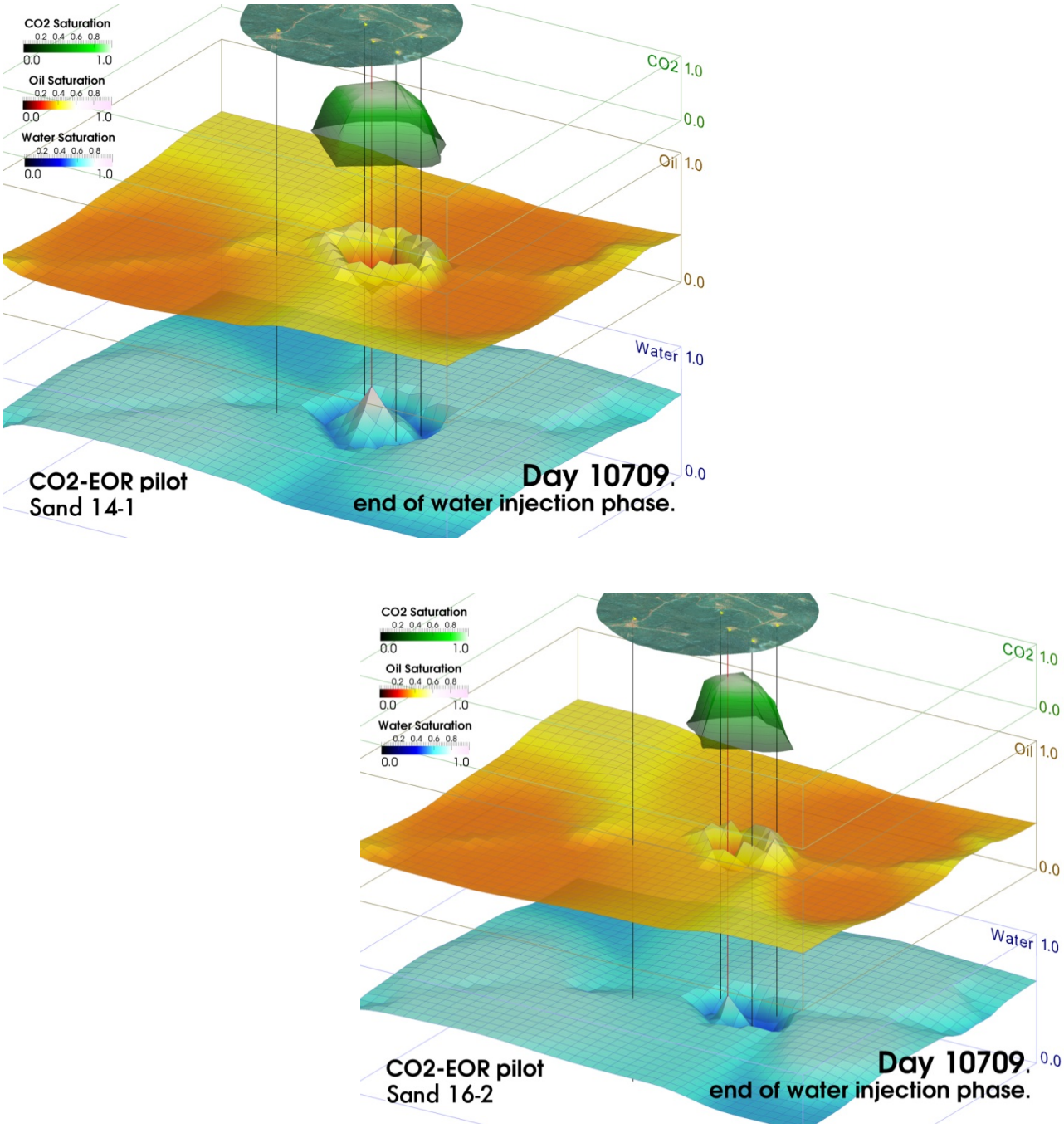


Figure 9.6. Screen shots of the animations of $CO_2$, water, and oil flows in Sands 14-1 (top) and 16-2 (bottom), at the end of the water injection period following the first injection of 7500 tons of $CO_2$, 513 days after the beginning of the first $CO_2$ injection. Water injection produces a peak in water saturation at the injector, but $CO_2$ saturation remains at a high level near the injector, even at the end of the water injection phase. The distance of the oil bank from the injector is greater in Sand 14-1 than in Sand 16-2, continuing the trend established during $CO_2$ injection, because the water flow, like the $CO_2$ flow, is greater into Sand 14-1 than into Sand 16-2.

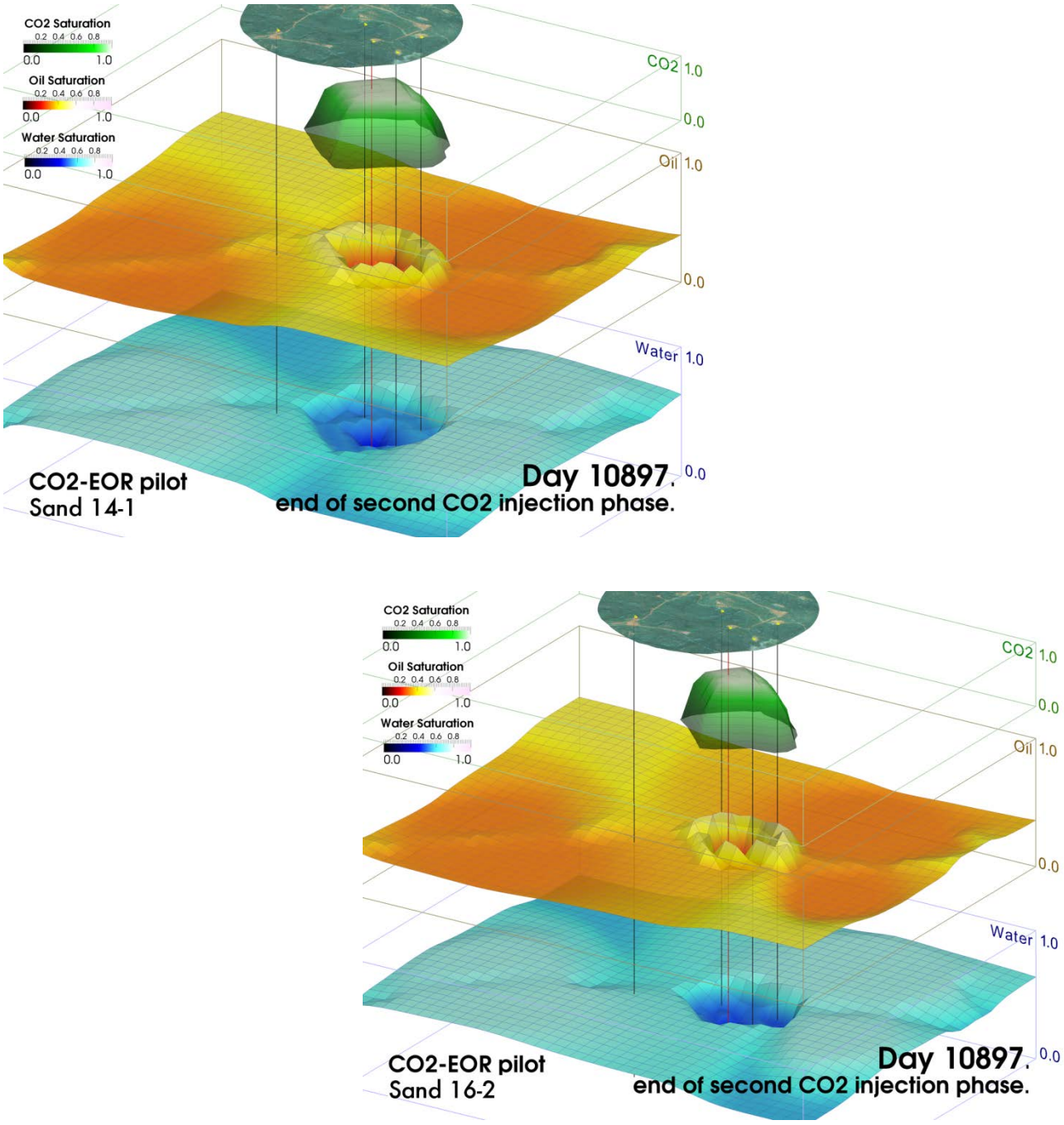


Figure 9.7. Screen shots of the animations of $CO_2$, water, and oil flows in Sands 14-1 (top) and 16-2 (bottom), at the end of the second injection of 7500 tons of $CO_2$, 701 days after the beginning of the first $CO_2$ injection. The oil bank has now reached three of the four production wells in both sands.

**Acronyms in Section 9**

| | |
|---|---|
| BHP | bottom hole pressure |
| MASTER | Miscible Applied Simulation Techniques for Energy Recovery (Ammer and Brummert, 1991; Ammer, Brummert, and Sams, 1991; Zeng, Grigg, and Chang, 2005) |
| VTK | Visualization Toolkit <http://www.vtk.org/> |

**References in Section 9**


Alabama State Oil and Gas Board, 2012. http://www.gsa.state.al.us/

Ammer, J. R., and A. C. Brummert, "Miscible Applied Simulation Techniques for Energy Recovery Version 2.0, User's Guide," U.S. Department of Energy, DOE/BC--91/2/SP, February 1991.

Ammer, J. R., A. C. Brummert, and W. N. Sams, "Miscible Applied Simulation Techniques for Energy Recovery Version 2.0, Technical Manual," U.S. Department of Energy, DOE/BC--91/2/SP, February 1991.

Esposito, R. A., J. C. Pashin, D. J. Hills, and P. M. Walsh, "Geologic Assessment and Injection Design for a Pilot $CO_2$-Enhanced Oil Recovery and Sequestration Demonstration in a Heterogeneous Oil Reservoir: Citronelle Field, Alabama, USA," *Environmental Earth Sciences*, **2010**, *60*, 431-444.

Fowler, M. L., L. E. Safley, M. A. Young, R. H. Stechmann, E. S. Blair, and R. E. Crumb, "Reservoir Management Strategy for Citronelle Field, Mobile County, Alabama," Report No. NIPER/BDM-0353, Prepared for the National Petroleum Technology Office, U.S. Department of Energy, Tulsa, OK, by BDM Petroleum Technologies, Bartlesville, OK, 1998.

Gilchrist, R. E., "Miscibility Study (Repeat 50% P.V. Slug) in Cores, Citronelle Unit, Mobile County, Alabama," Ralph E. Gilchrist, Inc., Houston, TX, November 3, 1981.

Theodorou, K., "Carbon Dioxide Enhanced Oil Recovery from the Citronelle Oil Field and Carbon Sequestration in the Donovan Sand, Southwest Alabama," Ph.D. Dissertation, Interdisciplinary Engineering, University of Alabama at Birmingham, Birmingham, AL, 2013.

Unit Manager's Report, "Reservoir Analyses of Oil Migration: Citronelle Oil Field, Mobile County, Alabama," Technical Report for the Unit Manager, Citronelle Unit, July 29, 1999.

Zeng, Z., R. B. Grigg, and S. H. Chang, "Miscible Applied Simulation Techniques for Energy Recovery Version 3.0," Modifications of Version 2.0 User's Guide (Ammer and Brummert, 1991) and Technical Manual (Ammer, Brummert, and Sams, 1991), under DOE Contract No. DE-FG26-01BC15364, U.S. Department of Energy, July 26, 2005. http://www.netl.doe.gov/technologies/oil-gas/Software/Software_main.html

# 10. Reservoir Management*

Konstantinos Theodorou*
University of Alabama at Birmingham

---

A series of simulations was conducted using MASTER 3.0 (Ammer and Brummert, 1991; Ammer, Brummert, and Sams, 1991; Zeng, Grigg, and Chang, 2005) to examine the post-pilot-test performance of the oil field when $CO_2$ is injected under various WAG schemes for enhanced oil recovery (Theodorou, 2013). The simulations utilized the 40 by 32-block grid with the same wells in the extended pattern as in the simulations described in Section 9.1. As before, the fraction of $CO_2$ into Sand 14-1 was 57% while the fraction into Sand 16-2 was 43%. The injected water was divided into 82% into Sand 14-1 and 18% into Sand 16-2. The porosity and permeability of the sands were 13.61% and 10 mdarcy, respectively.

The $CO_2$-EOR pilot test was simulated according to the actual $CO_2$ injection rates recorded during the $CO_2$ injection. All the WAG schemes examined followed immediately after the pilot test injection period. The 10-year WAG was simulated assuming a $CO_2$ injection rate of 28.1 t/day (31 short tons/day) into Well B-19-10 #2. The input parameters were as given in Table 9.2. Simulations for Sand 14-1 were performed separately from Sand 16-2 and the results were combined to determine the total daily oil production.

Results for the oil production rates are shown in Figure 10.1 for symmetric WAG schemes, in which the water injection interval has the same duration as the $CO_2$ injection interval. Figure 10.2 shows the results for asymmetric WAG schemes, in which the water injection interval was held constant at 6 months while the $CO_2$ injection interval was varied from a short period of 2 months to a long period of 24 months. Incremental oil recoveries for the various WAG schemes and the total and net amounts of $CO_2$ injected are summarized in Table 10.1.

Figure 10.1 indicates that symmetric WAG schemes perform better than continuous $CO_2$ injection, particularly after 5 to 6 years of oil recovery. Figure 10.2 indicates that, for asymmetric WAG schemes, oil recovery increases as the length of the $CO_2$ injection interval increases. However, this pattern reaches a point of maximum return and begins to decline when the $CO_2$ injection interval reaches 24 months.

Table 10.1 indicates that the optimal symmetric WAG schedule is 3 months $CO_2$ followed by 3 months of water. Compared with the symmetric WAG schedules, continuous $CO_2$ injection yields the best production rates in the short term, but it declines more rapidly and lags all the WAG schemes after about 5 to 6 years.

---

*K. Theodorou, "Carbon Dioxide Enhanced Oil Recovery from the Citronelle Oil Field and Carbon Sequestration in the Donovan Sand, Southwest Alabama," Ph.D. Dissertation, Interdisciplinary Engineering, University of Alabama at Birmingham, Birmingham, AL, 2013. Dr. Theodorou is now an Instructor of Mathematics at the Jefferson State Community College in Birmingham, AL.

Continuous $CO_2$ injection underperforms all the asymmetric WAG schedules except 2 months of $CO_2$ followed by 6 months of water. The best performing WAG cycle, 12 months of $CO_2$ injection followed by 6 months of water injection, results in incremental oil recovery of 128,735 STB over 10 years, a 10% increase in recovery compared with continuous $CO_2$ injection.

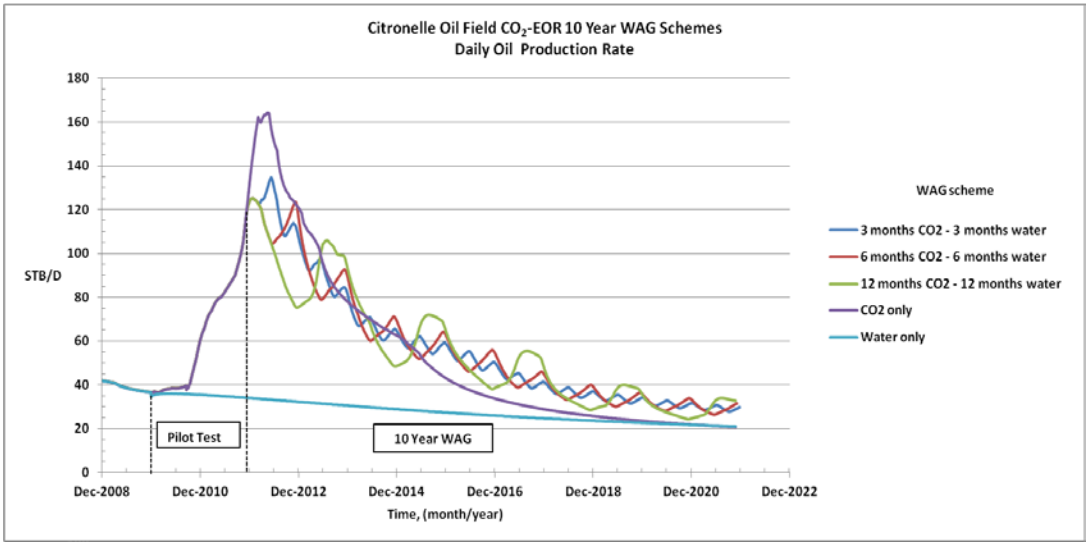


Figure 10.1. Simulated oil production rates for symmetric WAG schemes. Water-only and $CO_2$-only schemes are also included.

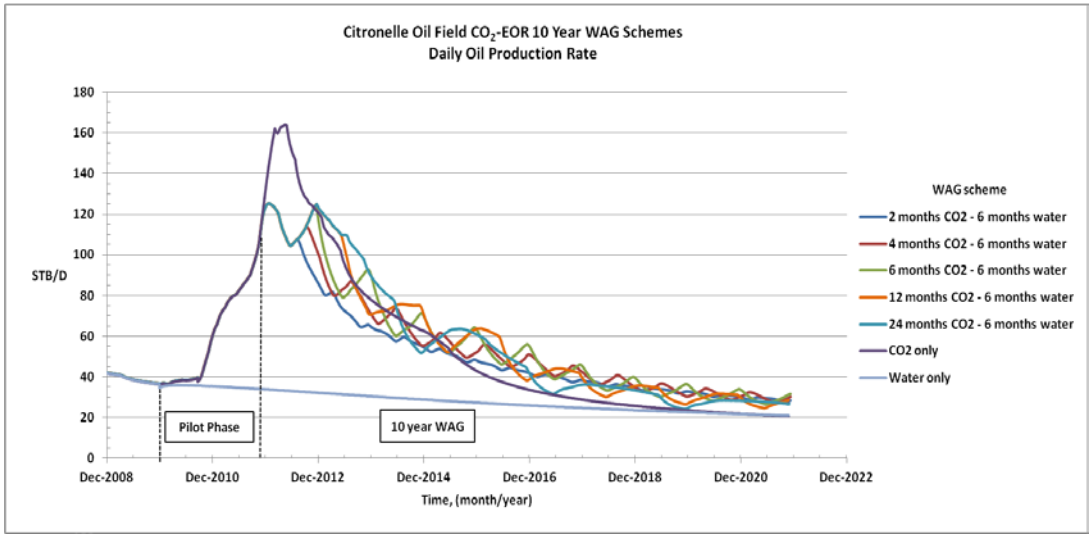


Figure 10.2. Simulated oil production rates for asymmetric WAG schemes. The water injection interval is held constant at 6 months while the $CO_2$ injection interval is progressively increased. Water-only and $CO_2$-only schemes are also included.

Table 10.1.
Oil Production and $CO_2$ Utilization for WAG Scenarios Using
Symmetric Schemes (GROUP 1) and Asymmetric Schemes (GROUP 2).

| - - - - WAG Schedule - - - - | - - - - - - - - - - - - - - - - - - - - - - - - - Results - - - - - - - - - - - - - - - - - - - - - - - - - | | | | |
|---|---|---|---|---|---|
| | | **GROUP 1** | **Symmetric (water interval = $CO_2$ interval)** | | |
| **WAG injection schedule (total time is 10 years)** | **EOR oil, STB** | **EOR incremental oil, STB** | **$CO_2$ injected, 1000 scf** | **$CO_2$ recovered, 1000 scf** | **Net $CO_2$ in place, 1000 scf** |
| 3 months $CO_2$ - 3 months water | 249,806 | 127,675 | 1,466,125 | 909,727 | 556,398 |
| 6 months $CO_2$ - 6 months water | 248,394 | 126,263 | 1,466,125 | 900,141 | 565,984 |
| 12 months $CO_2$ - 12 months water | 244,668 | 122,537 | 1,466,125 | 887,508 | 578,617 |
| | | **GROUP 2** | **Asymmetric (water interval ≠ $CO_2$ interval)** | | |
| **WAG injection schedule (total time is 10 years)** | **EOR oil, STB** | **EOR incremental oil, STB** | **$CO_2$ injected, 1000 scf** | **$CO_2$ recovered, 1000 scf** | **Net $CO_2$ in place, 1000 scf** |
| 2 months $CO_2$ - 6 months water | 228,837 | 106,706 | 858,250 | 426,804 | 431,446 |
| 4 months $CO_2$ - 6 months water | 243,275 | 121,144 | 1,223,015 | 701,774 | 521,241 |
| 6 months $CO_2$ - 6 months water | 248,394 | 126,263 | 1,466,125 | 900,141 | 565,984 |
| 12 months $CO_2$ – 6 months water | 250,866 | 128,735 | 1,830,826 | 1,253,621 | 577,205 |
| 24 months $CO_2$ – 6 months water | 249,133 | 127,002 | 2,195,565 | 1,578,381 | 815,506 |
| Only $CO_2$ | 238,607 | 116,476 | 2,681,905 | 2,114,059 | 567,846 |
| Only water | 122,131 | 0 | 0 | 0 | 0 |

**Acronyms and Abbreviations in Section 10**

| | |
|---|---|
| EOR | enhanced oil recovery |
| MASTER | Miscible Applied Simulation Techniques for Energy Recovery (Ammer and Brummert, 1991; Ammer, Brummert, and Sams, 1991; Zeng, Grigg, and Chang, 2005) |
| scf | standard cubic feet |
| STB | stock tank barrel |
| WAG | water alternating gas recovery |

**References in Section 10**


Ammer, J. R., and A. C. Brummert, "Miscible Applied Simulation Techniques for Energy Recovery Version 2.0, User's Guide," U.S. Department of Energy, DOE/BC--91/2/SP, February 1991.

Ammer, J. R., A. C. Brummert, and W. N. Sams, "Miscible Applied Simulation Techniques for Energy Recovery Version 2.0, Technical Manual," U.S. Department of Energy, DOE/BC--91/2/SP, February 1991.

Theodorou, K., "Carbon Dioxide Enhanced Oil Recovery from the Citronelle Oil Field and Carbon Sequestration in the Donovan Sand, Southwest Alabama," Ph.D. Dissertation, Interdisciplinary Engineering, University of Alabama at Birmingham, Birmingham, AL, 2013.

Zeng, Z., R. B. Grigg, and S. H. Chang, "Miscible Applied Simulation Techniques for Energy Recovery Version 3.0," Modifications of Version 2.0 User's Guide (Ammer and Brummert, 1991) and Technical Manual (Ammer, Brummert, and Sams, 1991), under DOE Contract No. DE-FG26-01BC15364, U.S. Department of Energy, July 26, 2005. http://www.netl.doe.gov/technologies/oil-gas/Software/Software_main.html

# 11. Technology Transfer

A bibliography of the presentations, workshops, publications, dissertations, and theses describing work supported by, or connected with, the present project may be found in Appendix A. Results of work under the project have been presented by members of the project team at seventeen national and international conferences and at twelve regional and local meetings. Fourteen peer-reviewed papers describing work related to the project have been published, including comprehensive reviews of the geology of Citronelle Dome and its prospects for $CO_2$-enhanced oil recovery and capacity for $CO_2$ storage (Esposito et al., 2008, 2010). Graduate students supported by the project have produced four theses and four dissertations describing their work. The intent, throughout the project, was to keep the reservoir engineering and carbon storage communities well informed about the progress of the work, its implications for successful $CO_2$-EOR and storage in geologic formations of the type found in Citronelle Dome, and the benefits to be gained from thorough analysis and pilot testing in the design of a commercial $CO_2$ flood. The project was the subject of the lead article in the Fall 2009 issue of *E&P Focus*.

Staff members at the Geological Survey of Alabama developed a core workshop focused on the sedimentology, diagenesis, and reservoir characteristics of the Donovan Sand in the Citronelle Field. The Donovan Sand was laid down in a complex mosaic of depositional environments and was subsequently affected by several dramatically different episodes of diagenesis, beginning with repeated development of oxidized soils, formed when parts of the Donovan landscape were exposed while the unit was still being deposited. The core workshop focuses on the geologic history of the Donovan and its depositional, diagenetic, and reservoir complexity, as an illustration of how sedimentology can control critical characteristics of this type of hydrocarbon reservoir. The workshop is conducted to educate interested groups about the Citronelle Field, an example of a sedimentologically and diagenetically complex but structurally simple siliciclastic reservoir. The workshop has been presented to participants in the Research Experience in Carbon Sequestration (RECS) Program (Tomski, 2014) in 2012, 2013, and 2014.

As a result of research performed at the Geological Survey of Alabama in connection with the present project, hundreds of thin sections from the Citronelle Field have been added to the Survey's thin section archive. The archive records are being modernized and standardized to make this resource more accessible to potential users.

Eric Carlson, at the University of Alabama, has developed, with support from the present project, an open-source framework named nSpyres, for simulation of large-scale porous media systems. The framework is based on the Python programming language, and makes substantial use of numerical and visualization packages that are freely available and are easy to install on multiple platforms (not Android, but almost any other major operating system). Algorithms are tested in vectorized Python and then performance profiled. Key bottlenecks are identified, and those portions are rewritten, usually in C, and hooked to the framework. The performance routines are most often written to take advantage of specific hardware, but they may improve performance substantially, even without specific hardware optimizations. The formulation used for the

framework (in particular, the operator splits) allows for substantial flexibility in the specific physical processes modeled, and promotes high levels of parallelism. The performance of nSpyres on a benchmark problem is documented in Section 4.4 of this report. Results from high resolution simulations of waterflooding in the pilot test region are presented in Section 4.5. In addition to nSpyres, Dr. Carlson has also developed a productivity environment to make it convenient to interact with source data and simulation results. The simulator will be providing its exceptional capabilities on large-scale, fine-grid porous media problems to the reservoir engineering community in the near future, as soon as a new server has been completed.

A bibliography of publications containing data and information on the Citronelle Oil Field and Southwestern Alabama geology is attached as Appendix B to this report.

**Acronym in Section 11**

RECS Research Experience in Carbon Sequestration, http://www.recsco2.org/

**References in Section 11**

Esposito, R. A., J. C. Pashin, and P. M. Walsh, "Citronelle Dome: A Giant Opportunity for Multi-Zone Carbon Storage and Enhanced Oil Recovery in the Mississippi Interior Salt Basin of Alabama," Environmental Geosciences, 2008, 15 (2), 53-62.

Esposito, R. A., J. C. Pashin, D. J. Hills, and P. M. Walsh, "Geologic Assessment and Injection Design for a Pilot CO2-Enhanced Oil Recovery and Sequestration Demonstration in a Heterogeneous Oil Reservoir: Citronelle Field, Alabama, USA," Environmental Earth Sciences, 2010, 60, 431-444.

Tomski, P., RECS, Research Experience in Carbon Sequestration, 2014, http://www.recsco2.org/

# 12. Milestones

## 12.1. Milestones Summary

The project was divided into three research phases, corresponding to the three budget periods. The emphasis in Phase I (Budget Period 1: January 1, 2007 to August 31, 2008) was on selection of a test site, detailed study of its geology, determination of oil-$CO_2$ minimum miscibility pressure, reservoir simulation of $CO_2$-EOR, and establishment of background conditions at the site. The focus in Phase II (Budget Period 2: September 1, 2008 to December 31, 2010) was on the first $CO_2$ injection, of 8036 tons, and the associated measurements and monitoring. A no-cost extension of Phase II from its original end date of April 30, 2010, to December 31, 2010, was approved, to complete the first $CO_2$ injection. Work in Phase III (Budget Period 3: January 1, 2011 to January 31, 2014) included documentation of the response to the first $CO_2$ injection and presence or absence of environmental effects, large-scale fine grid reservoir simulations and visualization, oil-water-$CO_2$ phase behavior, development of a reservoir management plan, seismic monitoring, and a comprehensive evaluation of the findings from all components of the project. A request for no-cost extension of the project to January 31, 2014, was approved by NETL, to provide time to perform the proposed tests and complete the analysis of the response to $CO_2$ injection.

The stratigraphy, sedimentology, and petrology of the Rodessa Formation in the vicinity of the test site were analyzed and documented at an unprecedented level of detail; realistic and informative reservoir simulations were performed; the environmental and ecological conditions surrounding the site were documented, before, during, and following $CO_2$ injection; seismic signals from the target formation were recorded under the baseline water flood condition, during $CO_2$ injection, and during $CO_2$ migration from the injection zone; the minimum miscibility pressure and absence of precipitation from oil in the presence of $CO_2$ were established; and a favorable economic analysis was conducted that identifies the optimum $CO_2$ slug size for water-alternating-gas oil recovery under specified $CO_2$ cost and oil price constraints.

The first injection, of 8036 tons of $CO_2$, began on a continuous basis in January 2010 and was completed in September 2010. Oil production at Tank Battery B-19-8 responded quickly to $CO_2$ injection, in January 2010, reversing the trend of declining production that occurred while troubleshooting the pumping of liquid $CO_2$. However, several problems associated with the $CO_2$ injection also appeared, including excessive gas production at Well B-19-11, to the southwest of the injector, a low water injection rate on returning to water injection at the conclusion of the $CO_2$ injection, and failure of the down-hole power oil pumps, due to erosion-corrosion by particles mobilized by the mixture of water and carbon dioxide.

Replacement of the power oil pumps with ones made of better materials and having longer stroke brought the frequency of pump pulls back to normal.

A pressure-transient test in November and December 2011 made the unexpected discovery of a hydraulic fracture intersecting the injector and having a total length of 600 to 1000 ft. The

fracture, most likely in the direction of maximum horizontal compressive stress in the Southeastern U.S., would explain the early breakthrough of $CO_2$ at wells to the east-northeast and west-southwest of the injector and would have provided a preferential pathway for $CO_2$, undermining the sweep efficiency of $CO_2$ in the pilot test.

An injection profile test was conducted in January 2012 to determine if either of the target sands was primarily responsible for the low water injection rate. The test established that 35% of the water flow was to Sand 14-1 and 65% was to Sand 16-2, so neither injection zone was completely blocked, but comparison with the results of an injection profile run before $CO_2$ injection showed that loss of flow into the upper, finer-grained, Sand 14-1 was primarily responsible for the low injectivity to water.

Injected water was treated with surfactant from July 25 to November 7, 2012, to determine whether capillary blocking was responsible for the loss in injectivity to water following the injection of $CO_2$. The water injection rate responded to the surfactant, recovering approximately one-third of the loss resulting from the $CO_2$ injection. Though significant, the improvement accompanying surfactant injection did not come close to restoring the injection rate to the average level before $CO_2$ injection, and the effect was transient, disappearing after about 6 months. The discovery of flakes of internal plastic coating and particles of scale in the injector during repair of a tubing leak suggested that plugging of the finer-grained sand by fine particles of scale was the likely cause of the low injectivity to water. The tubing was replaced with bare steel tubing and the well was flowed back in an attempt to flush out the particles. Treatment of the injector with hydrocarbon solvent and asphaltene dispersant was also done to remove any heavy components that may have precipitated when $CO_2$ mobilized lighter fractions. The combined effect of these measures was a slight increase in water injection rate, but the injectivity could not be restored to levels approaching those observed before the $CO_2$ injection.

Completion of the Milestones in Phases I, II, and III is described in the following Sections 3.2, 3.3, and 3.4, respectively.

## 12.2. Phase I Milestones

There were four Milestones scheduled during Research Phase I (Budget Period 1). They were completed as follows:

***Oil-$CO_2$ MMP determined:*** Measured as 2340 ± 160 psig using the rolling ball viscometer designed and built especially for this project.

***Permit to conduct Field Test No. 1:*** Infill well B-19-10 #2 was re-permitted as a gas injector.

***Economic and market analysis:*** Determined the optimum $CO_2$ slug size during WAG recovery as a function of oil price and discount factor.

***Justification for proceeding to Phase II:*** Submitted and approved.

## 12.3. Phase II Milestones

The critical path milestones scheduled during research Phase II are specified in Table 12.1. The conclusions, findings, and accomplishments from completion of the Milestones are described below.

***Geomechanical stability analysis (Phase II Milestone):*** Geomechanical stability analyses were performed using a 1-dimensional effective stress model, a 3-dimensional finite element model, and the geophysical testing results. Both models indicated only small deformations as a result of overburden pressure on the Donovan Sands (0.56 to 0.75 ft for the Upper Donovan and 0.28 to 0.39 ft for the Lower Donovan) and a strain rate of 0.14 to 0.19%, below the expected rupture limit of 0.3% for quasi-brittle materials.

Shear-wave velocities were measured using the Refraction Microtremor (ReMi) technique to depths of 12,500 ft using wireless geophones placed along two straight paths spanning 30,100 and 25,600 ft, to the south and southwest, respectively, of the injection well. Shear-wave velocities recorded before and during $CO_2$ injection suggested a 10% increase in stress associated with $CO_2$ injection, in layers above the injection zone. Detection of changes associated with $CO_2$ injection at the depth of the Donovan Sands by Refraction Microtremor measurements represents a significant advance in the application of the ReMi technique.

Table 12.1.
Critical Path Milestones, Research Phase II (Budget Period 2),
September 1, 2008 to December 31, 2010.

| Phase II Task | Critical Path Milestone Description | Completion Date |
|---|---|---|
| Task 23 | Geomechanical stability analysis completed. | July 1, 2009 |
| Task 30 | Documentation, through measurements of atmospheric $CO_2$, of the presence or absence of environmental effects of $CO_2$ injection. | Sept. 2, 2010 |
| Task 32 | Justification for proceeding to Phase III submitted. | Oct. 14, 2010 |
| Task 17 | Phase II $CO_2$ injection, 7500 tons, completed. | Sept. 15, 2010 |

***Documentation of environmental effects (Phase II Milestone):*** Measurements of soil gas composition versus depth, $CO_2$ flux from soil, soil temperature, soil moisture, and soil elements (carbon, nitrogen, and phosphorus) were made from August 2008 to August 2010, before and during $CO_2$ injection, at a total of 15 locations surrounding the injector, three producers, and a plugged and abandoned well within the test pattern. The growth of trees and plants and their species distribution were monitored in test plots near the injector, producers, and tank batteries. Measurements of $CO_2$ in ambient air were recorded at 104 points on a grid across Citronelle, from September 2007 to June 2012. No sustained elevated levels of $CO_2$ above the normal variation, no unusual $CO_2$ flux from soil, and no significant changes in the growth or distribution of vegetation

were associated with the injection of $CO_2$ during Phase II, but please see the discussions of $CO_2$ levels and the growth of vegetation under Phase III, below.

***Justification for proceeding to Phase III (Phase II Milestone):*** The justification and application for continuation of the project into Phase III and Budget Period 3 were submitted to the Project Manager on October 14, 2010.

***Phase II $CO_2$ injection complete (Phase II Milestone):*** Injection of 8036 tons of $CO_2$ was completed on September 25, 2010. After initial problems pumping liquid $CO_2$, all of which were resolved by the persistent efforts of Denbury's team of engineers and technicians, continuous carbon dioxide injection into the inverted five-spot chosen for testing began at the end of January 2010 and continued to the end, without any significant interruption, at an average rate of 31 tons/day, in good agreement with the rate of 35 tons/day anticipated by reservoir simulations using SENSOR (Coats Engineering, Inc.).

## 12.4. Phase III Milestones

The critical path Milestones during Phase III are specified in Table 12.2. The milestones included four key components of the project: (1) documentation and analysis of the response of the reservoir to $CO_2$ injection, (2) documentation of the presence or absence of environmental effects, (3) reservoir simulation and visualization, and (4) the capacity of the formation for $CO_2$ storage.

Table 12.2.
Critical Path Milestones, Research Phase III (Budget Period 3),
January 1, 2011, to January 31, 2014.

| Phase III Task | Critical Path Milestone Description | Completion Date |
|---|---|---|
| Task 44 | Evaluation of Rodessa Formation $CO_2$ storage capacity. | May 31, 2011 |
| Task 33 | Field Test No. 2 completed.[a] | Nov. 30, 2011 |
| Tasks 41 & 42 | Documentation, through measurements of atmospheric $CO_2$ and growth of vegetation, of the presence or absence of environmental effects of $CO_2$ injection. | Mar. 31, 2012 |
| Task 36 | Presentation of results as dynamic simulations. | Aug. 31, 2012 |
| New Task[b] | Surfactant injection to test for capillary blocking by gas. | Nov. 30, 2012 |

a. In the absence of a second $CO_2$ injection, the title of this task is understood to read: "Monitoring of response to the Phase II $CO_2$ injection," with a completion date of January 31, 2014.
b. The new task was dictated by the need to diagnose low water injectivity following $CO_2$ injection. The Milestone was added following approval of a no-cost extension from August 31, 2012 to February 28, 2013, to satisfy the requirement that there be at least two Milestones in each year of the project.

***Evaluation of Rodessa Formation $CO_2$ storage capacity (Phase III Milestone):*** The capacity of Citronelle dome for sequestration of $CO_2$ has been examined in detail. The total capacity of Citronelle Dome, including both saline formations and the oil reservoirs, according to the conservative estimation procedure of the DOE Carbon Sequestration Regional Partnerships (2006) is between 60 and 240 x $10^9$ kg (66 to 265 million short tons). A more detailed analysis by Esposito et al. (2008), including factors accounting for formation heterogeneity and residual oil and water saturations, estimated that the total $CO_2$ storage capacity is between 480 and 1900 x $10^9$ kg (530 to 2100 million short tons). A calculation based upon the work of Pruess et al. (2001) and Xu et al. (2001), suggests that up to 315 x $10^9$ kg (350 million short tons) of the stored $CO_2$ could be mineralized by conversion to solid carbonates over geologic time.

***Documentation, through measurements of atmospheric $CO_2$ and growth of vegetation, of the presence or absence of environmental effects of $CO_2$ injection (Phase III Milestone):*** Xiongwen Chen and Kathleen Roberts of Alabama A&M University measured $CO_2$ in ambient air at least once each quarter, from September 2007 to June 2012, at 104 sampling locations in the Citronelle Oil Field and City of Citronelle. The measurements were made at all of the sampling points over two consecutive days; one day in the City of Citronelle and the other in the Oil Field. The measurements are presented in Section 7.1 and Figure 7.2.

Only one anomalous reading appears in the entire set of $CO_2$ measurements, in June 2009, after the $CO_2$ storage tank was filled for the first time, in March 2009, and during unsuccessful attempts to inject $CO_2$, before continuous $CO_2$ injection began in December 2009. The rest of the $CO_2$ measurements are consistent with the seasonal variations and long-term trends of the local NASA satellite-based Atmospheric Infrared Sounder data (http://airs.jpl.nasa.gov/) and worldwide average atmospheric $CO_2$ levels, and with the worldwide rate of increase in atmospheric $CO_2$ of approximately 2 ppmv/year (Ed Dlugokencky and Pieter Tans, NOAA/ESRL, www.esrl.noaa.gov/gmd/ccgg/trends/). Roberts (2013) reported an increase of 2.3 ppmv $CO_2$ in the averages over all sets of data taken before and after breakthrough of $CO_2$ at Well B-19-11 in May 2010, after correcting for the worldwide increase in atmospheric $CO_2$ during the period, but the scatter of the $CO_2$ measurements used to construct the averages is almost an order of magnitude larger.

Xiongwen Chen and Kathleen Roberts of AAMU also established 10 m x 10 m square test plots near the injector, producers, and tank batteries, in which to monitor growth of vegetation. Inventories of the vegetation plots were conducted in 2008, 2009, 2010, and 2011. The growth rates of trees and shrubs during the three time intervals, 2008-2009, 2009-2010, and 2010-2011 are presented in Figure 7.6 and discussed in Section 7.2. Comparison of the growth rates during 2008-2009 with those during 2009-2010 shows that the plant growth rate increased from the first period to the second in two plots and decreased in five of them. Comparison of the growth rates during 2009-2010 with those during 2010-2011 shows that the plant growth rate increased from the second period to the third in three plots and decreased in five of them. The overall trend is one of decreasing growth rates, rather than the increase in rates that might be expected had there been elevated levels of $CO_2$.

One plot, located near the injector, Well B-19-10 #2, did exhibit an increase in the rate of growth of vegetation during the four-year period. This is an interesting and unexpected observation, in view of the fact that neither elevated levels of $CO_2$ in ambient air nor elevated $CO_2$ fluxes from soil were consistently observed near that well. Changes in growth rate from place-to-place and year-to-year are more likely explained by patterns of rainfall, temperature, and solar

insolation than by $CO_2$ plumes associated with the $CO_2$ storage tank, injection equipment, wells, or tank batteries. Roberts and Chen (2012) concluded that the increase in rate of growth of vegetation in the plot near the injector was not significant and most likely could be explained by other factors.

***Presentation of results as dynamic simulations (Phase III Milestone):*** The complexity of the interaction between $CO_2$, oil, and water in a geologic formation makes animation of the evolution of fluid saturations during $CO_2$ and water flooding an especially useful tool for understanding enhanced oil recovery and its dependence on reservoir conditions and injection parameters. Using reservoir simulation results obtained by Konstantinos Theodorou (2013) using MASTER 3.0 (Ammer and Brummert, 1991; Ammer, Brummert, and Sams, 1991; Zeng, Grigg, and Chang, 2005), Corey Shum, in the UAB Enabling Technology Laboratory, programmed animations showing the evolution of fluid saturations in Sands 14-1 and 16-2 of the Citronelle Oil Field during two $CO_2$ injections of 7500 tons each, separated by a period of water injection. The raw output from the reservoir simulation was parsed with a custom application to extract the oil, water, and $CO_2$ saturation results for each point in space and time. The data were then exported to a standard 3-D data visualization format, VTK. ParaView and custom tools were used to create animations of the time-dependent data.

The animations may be downloaded and run from the following URL's:

Simulation of $CO_2$-EOR in Sand 14-1: https://dl.dropbox.com/s/9br413mpbsyd8ek/oil14.mp4?dl=1

Simulation of $CO_2$-EOR in Sand 16-2: https://dl.dropbox.com/s/77oprxjx9gxafxa/oil16.mp4?dl=1

Should any difficulty in locating or running the videos be encountered, please send a message to Peter Walsh at <pwalsh@uab.edu>.

Screen shots from the animations are shown in Figures 9.4 to 9.7 in the present report. $CO_2$, oil, and water saturations in Sands 14-1 and 16-2 are shown before any $CO_2$ was injected in Figure 9.4, at the end of the first $CO_2$ injection in Figure 9.5, at the end of the water injection in Figure 9.6, and at the end of the second $CO_2$ injection in Figure 9.7. The progress of $CO_2$ sweep, the development and migration of the oil bank, and the residual oil and water saturations left behind are all clearly visible. Watching the animation provides a new perspective and appreciation of the complex interactions among the fluids and phases.

***Surfactant injection to test for capillary blocking by gas (Phase III Milestone):*** Injected water was treated with surfactant from July 25 to November 7, 2012. The water injection rate during surfactant injection, and during the period from July 30 to October 14, 2012, when the pressure was constant at 3900 psig, averaged 95 bbl water/day. During the period following $CO_2$ injection but before the surfactant treatment, from September 26, 2010, to July 24, 2012, on the days when the pressure was 3900 psig, the average water injection rate was 63 bbl water/day. The surfactant treatment was therefore associated with a 50% increase in injection rate. Though certainly significant, the increase accompanying surfactant injection did not come close to restoring the injection rate to the average level of 160 bbl water/day before $CO_2$ injection, when the average pressure was only 3600 psig. Also, when the surfactant treatment ended, the water injection rate returned to the level where it had been before the treatment began, so the positive effect of surfactant was only temporary. The conclusion from the surfactant treatment is that while capillary blocking of water injection was significant, it was not the primary effect responsible for the loss in injectivity experienced on returning to water injection following the $CO_2$ slug.

**Acronyms and Abbreviations in Section 12**

| | |
|---|---|
| EOR | enhanced oil recovery |
| MASTER | Miscible Applied Simulation Techniques for Energy Recovery (Ammer and Brummert, 1991; Ammer, Brummert, and Sams, 1991; Zeng, Grigg, and Chang, 2005) |
| ReMi | refraction microtremor |
| SENSOR | System for Efficient Numerical Simulation of Oil Recovery (Coats Engineering, Inc., http://www.coatsengineering.com/) |
| UAB | University of Alabama at Birmingham |
| VTK | Visualization Toolkit, http://www.vtk.org/ |

**References in Section 12**


Ammer, J. R., and A. C. Brummert, "Miscible Applied Simulation Techniques for Energy Recovery Version 2.0, User's Guide," U.S. Department of Energy, DOE/BC--91/2/SP, February 1991.

Ammer, J. R., A. C. Brummert, and W. N. Sams, "Miscible Applied Simulation Techniques for Energy Recovery Version 2.0, Technical Manual," U.S. Department of Energy, DOE/BC--91/2/SP, February 1991.

Dlugokencky, E., and P. Tans, "Trends in Atmospheric Carbon Dioxide," National Oceanic & Atmospheric Administration, Earth System Research Laboratory, Global Monitoring Division, http://www.esrl.noaa.gov/gmd/ccgg/trends/

DOE Carbon Sequestration Regional Partnerships, Capacity and Fairways Subgroup of the Geologic Working Group, "Proposed Methodology for Construction of a National Geological Carbon Sequestration Capacity Assessment," Final draft, Prepared for the U.S. Department of Energy, Regional Carbon Sequestration Partnership Program, October 1, 2006, 34 pp.

Esposito, R. A., J. C. Pashin, and P. M. Walsh, "Citronelle Dome: A Giant Opportunity for Multi-Zone Carbon Storage and Enhanced Oil Recovery in the Mississippi Interior Salt Basin of Alabama," *Environmental Geosciences*, **2008,** *15* (2), 53-62.

Pruess, K., T. Xu, J. Apps, and J. Garcia, "Numerical Modeling of Aquifer Disposal of $CO_2$," Paper No. SPE 66537, SPE/EPA/DOE Exploration and Production Environmental Conference, San Antonio, TX, February 26-28, Society of Petroleum Engineers, 2001, 16 pp.

Roberts, K. A., "Ecological Monitoring and Assessment of Enhanced Oil Recovery ($CO_2$-EOR) for Carbon Storage," Ph.D. Dissertation, Department of Biological and Environmental Sciences, Alabama A&M University, Normal, AL, December 2013.

Roberts, K. A., and X. Chen, "Direct and indirect assessment of vegetation located near $CO_2$-mediated enhanced oil recovery ($CO_2$-EOR) activities," Ecological Society of America, 97th Annual Meeting, Portland, OR, August 5-10, 2012, http://eco.confex.com/eco/2012/webprogram/Paper38361.html

Theodorou, K., "Carbon Dioxide Enhanced Oil Recovery from the Citronelle Oil Field and Carbon Sequestration in the Donovan Sand, Southwest Alabama," Ph.D. Dissertation, Interdisciplinary Engineering, University of Alabama at Birmingham, Birmingham, AL, 2013.

Xu, T., J. A. Apps, and K. Pruess, "Analysis of Mineral Trapping for $CO_2$ Disposal in Deep Aquifers," Paper LBNL-46992, Lawrence Berkeley National Laboratory, July 20, 2001, 62 pp. <http://repositories.cdlib.org/lbnl/LBNL-46992>

Zeng, Z., R. B. Grigg, and S. H. Chang, "Miscible Applied Simulation Techniques for Energy Recovery Version 3.0," Modifications of Version 2.0 User's Guide (Ammer and Brummert, 1991) and Technical Manual (Ammer, Brummert, and Sams, 1991), under DOE Contract No. DE-FG26-01BC15364, U.S. Department of Energy, July 26, 2005. http://www.netl.doe.gov/technologies/oil-gas/Software/Software_main.html

# 13. Summary, Conclusions, and Lessons Learned

## 13.1. Summary and Conclusions

The most significant conclusions and accomplishments from each of the principal research efforts in which the team has been engaged, over the life of the project, are summarized below.

***Communication and Technology Transfer.*** The wiki-based collaborative web site, maintained by Eric Carlson, proved to be an effective means for rapid dissemination of technical information through the research group. The site contained links to difficult-to-find reports of previous engineering work in the Citronelle Oil Field, reports generated under the present project, presentations at project review meetings, a wealth of data from the field, and results of the simulations of $CO_2$-EOR by Eric Carlson, using the SENSOR (Coats Engineering, Inc.) reservoir simulation software suite.

Fourteen peer-reviewed papers describing work directly related to the project were published, including comprehensive reviews of the geology of Citronelle Dome and its prospects for $CO_2$-enhanced oil recovery and capacity for $CO_2$ storage (Esposito et al., 2008, 2010). Results of work under the project have been presented by members of the project team at seventeen national and international conferences and at twelve regional and local meetings. A publicly accessible web site made the results available to specialists in the fields of enhanced resource recovery and carbon storage and to interested students, educators, and the general public. The project was the subject of the lead article in the Fall 2009 issue of *E&P Focus*.

***Reservoir Geology of the Donovan Sandstone in Citronelle Field.*** Citronelle Field is the product of a complex geologic history that is tied to the evolution of the Mississippi Interior Salt Basin. The field is trapped structurally in a simple domal structure that formed above a broad salt pillow. The Donovan sandstone is of Early Cretaceous age and constitutes a heterogeneous assemblage of sandstone reservoirs in which conglomerate and mudstone units form baffles and barriers to flow and is ultimately sealed by impermeable evaporites of the Ferry Lake Anhydrite. The burial history of the field is consistent with the decelerating extensional subsidence associated with the development of the Gulf of Mexico passive margin. Oil has been trapped within Donovan sandstone for more than 60 million years and now sits in a thermal window that is conducive to hydrocarbon cracking and accumulation of pyrobitumen.

Donovan sandstone bodies are organized into two retrogradational sequence sets. Individual depositional sequences are about 30 feet thick and have a frequency of about 100,000 years, suggesting climatic control of sedimentation by Milankovitch orbital processes. Analysis of the Donovan sandstone indicates that reservoir facies were deposited primarily in incised valleys containing dryland fluvial and associated estuarine deposits that accumulated along the landward fringe of an extensive platform lagoon. Widespread lagoonal and beach barrier deposits are preserved at the top of each sequence set and record two episodes of marine flooding in the Citronelle region.

Reservoir quality in Citronelle Field is influenced by a variety of depositional and diagenetic processes associated with soil formation and valley incision. Most sedimentation occurred as incised valleys were backfilled during rises of base level, and diagenesis was driven in large part by pedogenic processes. The Donovan sandstone was deposited primarily as a redbed succession, and intrusion of reducing fluids associated with oil emplacement resulted in the gray and yellowish-brown colors that are characteristic of the reservoir sandstone units.

Feldspar dissolution during pedogenesis was a fundamental control on reservoir quality in the Donovan sandstone and effectively differentiates pay zones from baffle and barrier strata. Accordingly, many pay zones are as much the product of diagenetic processes as they are of primary sedimentation. The interplay of depositional and diagenetic processes resulted in a multitude of reservoir sandstone bodies in which reservoir heterogeneity occurs at numerous scales. This heterogeneity is an important consideration for identifying and prioritizing $CO_2$ injection targets and understanding reservoir confinement and subsurface flow pathways.

***Reservoir Fluid Properties and Phase Behavior.*** A rolling ball viscometer with which to measure properties of oil-$CO_2$ mixtures at reservoir temperature and pressure was designed, assembled, tested, and calibrated. The instrument was used to establish that the minimum miscibility pressure for Citronelle oil is 2340 ± 160 psig, well below the upper limit of 2800 psi reported by Gilchrist (1981). A miscible $CO_2$ flood was therefore assured in the Upper Donovan Sands at Citronelle, at depths near 11,000 feet. The rolling ball viscometer is also an excellent tool with which to evaluate two important influences on miscibility: (1) the effects of impurities such as $N_2$ naturally present in a formation, or remaining in $CO_2$ after incomplete separation from gaseous combustion products, and (2) the extension of oil-$CO_2$ miscibility through addition of other gas constituents, such as light hydrocarbons, a component of the advanced $CO_2$-EOR technology proposed by Kuuskraa and Koperna (2006) and Kuuskraa et al. (2011).

***Reservoir Simulation.*** Eric Carlson succeeded in establishing a stable and accurate reservoir simulation algorithm for nSpyres, his open-source simulator for two-phase flow in porous media. Even using a highly non-optimized, strictly single-core solution, the simulator is competitive in solution speeds with the fastest simulators and simulation technologies in the world. The primary improvement in speed arises from a very stable method for solving the nonlinear implicit saturation equation system, which converges quickly and reliably, regardless of time step size. Selection of time step size depends entirely on the desired solution accuracy and resolution, with no need for consideration of stability. As long as there are only two mobile phases, it will be almost trivial to extend the framework to systems having multiple components or species. The superior performance of the simulator was demonstrated by comparison with published work on the benchmark Problem 2 of the SPE Tenth Comparative Solution (Christie and Blunt, 2001). High resolution simulations of waterflooding in the pilot test region produced useful and interesting comparisons of the performance of the flood under different assumptions regarding the relative permeability of water.

A methodology was developed with which to automatically estimate porosity and permeability at each cell of a simulation grid, if porosity is known as a function of depth at some locations in the formation of interest. Results from full-field, 50-year simulations of the Citronelle Field, using uniform permeabilities, were very promising. The open-source simulator will be made available to the reservoir engineering community in the near future, as soon as a new server has been completed.

***Water Flood, $CO_2$ Handling, and $CO_2$ Injection.*** Water flood, to establish baseline production, began in March 2008. Oil production from each of the four producers, under water flood, ranged from 4 to 9 bbl/day. An interference test established that there is communication between the injector and at least one nearby producer. No obvious short circuits or evidence for significant layering were detected. The low effective permeability of the sands suggested the presence of low permeability baffles and relative permeability effects on total mobility. An injection profile run in the injector showed that Sand 14-1 was taking water at a higher rate than Sand 16-2 (82 and 18% of the flow, respectively).

A 50-ton, refrigerated, liquid $CO_2$ storage tank was purchased from the TOM$CO_2$ Equipment Co. (Loganville, GA), moved to Citronelle, and installed on a pad at the test site in December 2008. Airgas Carbonic was chosen to provide liquefaction and transportation services. The first shipment of 40 tons of $CO_2$ was delivered by Airgas to Citronelle on March 2, 2009. The injector, four producers, $CO_2$ storage tank, charge pump, triplex pump, piping, flow meters, and gas/liquid separators were in place, connected, and prepared for $CO_2$ injection in July 2009. During the period from July to November 2009, the principal barrier to $CO_2$ injection was poor performance of the triplex positive displacement pump.

Modifications to the triplex pump enabled the Denbury Onshore group in Citronelle to begin continuous $CO_2$ injection, following a month-long interruption for tubing repair, on January 27, 2010, and maintain an average injection rate of 31 tons/day to the end of the injection on September 25, 2010. A tracer test during $CO_2$ injection showed that 60% of the $CO_2$ was flowing to Sand 14-1 and 40% to Sand 16-2. Scheduling of deliveries to maintain $CO_2$ supply was not a problem until the final months, when injection rates increased to $\geq$40 tons/day, sometimes requiring delivery of three tanker truckloads of liquid $CO_2$ per day.

***Response to $CO_2$ Injection.*** Oil production at Tank Battery B-19-8, where oil from three of the producers in the inverted five-spot was collected, responded quickly to $CO_2$ injection, in January 2010, reversing the period of declining production that occurred when there was no water or $CO_2$ injection while troubleshooting the triplex pump. The trend of increasing oil production continued to the end of the $CO_2$ injection, in September 2010. However, on returning to water injection when the $CO_2$ injection was complete, two problems surfaced. The first was a low water injection rate of only 67 ± 21 bbl/day, compared with the rate of 160 ± 18 bbl/day before the $CO_2$ injection. The second problem was excessive wear of the down-hole power oil pumps due to erosion-corrosion by particles mobilized by the carbon dioxide and water. As a result, oil production at Tank Battery B-19-8 suffered a marked decline from September 2010 to March 2011, from 59 to 21 bbl/day. Improvements to the power oil pumps restored the frequency of pump pulls to normal and oil production at Tank Battery B-19-8 recovered some of its loss over the next 12 months, reaching 44 bbl/day in March 2012. However, water injection rates never returned to the higher levels observed prior to $CO_2$ injection, and subsequent oil production (May 2012 to April 2014), in the range from 33 to 42 bbl/day, was lower than the rate of 45 bbl/day just before the start of $CO_2$ injection in December 2009.

Breakthrough of $CO_2$ was detected at Well B-19-11, the well in the test pattern farthest from the injector, in May 2010, and at two other wells in the inverted five-spot (B-19-8 and B-19-9) in August 2010. The carbon-13 to carbon-12 isotope ratio in $CO_2$ was used to positively establish the presence of injected $CO_2$ in the produced gas. A survey of the $CO_2$ content of produced gas from

wells within and outside the test pattern on April 12, 2011, detected $CO_2$ levels above that in native Citronelle gas (> 3 vol%) at Wells B-19-11 (57 vol%) and B-19-8 (25 vol%) in the inverted five-spot, at Well B-20-5 (10 vol%) to the northeast of the injector, and at Well A-25-10 (15 vol%) far to the southwest of the test pattern. Early breakthrough of $CO_2$ to Wells A-25-10, B-19-11, and B-20-5 indicated major extension of the injected $CO_2$ plume toward the east-northeast and west-southwest.

The response to $CO_2$ injection at Tank Battery B-19-11, where oil from Well B-19-11 is collected, was quite different from that observed at Tank Battery B-19-8. In contrast to the immediate increase in oil production observed at Tank Battery B-19-8, production at Tank Battery B-19-11 continued for four months on the trajectory that it had been following for the previous 10 months. Then, coinciding with the breakthrough of $CO_2$ at Well B-19-11, production at the battery abruptly declined, by approximately the typical production from Well B-19-11 (8 to 9 bbl/day), then continued a steady decline. Produced gas at Well B-19-11 was so excessive that the well was killed on September 2, 2010, three weeks before the end of $CO_2$ injection, and remained shut in until May 5, 2011. Because Well B-19-11 was shut in during the transition from $CO_2$ back to water injection, the wells on Tank Battery B-19-11 were not subject to the erosion-corrosion experienced in the wells on Tank Battery B-19-8.

A pressure-transient test in the injector, conducted in November and December 2011 provided strong evidence for the presence of a 600 to 1000-foot-long vertical fracture intersecting the injection well. The presence of a fracture was completely unexpected, because, though all of the production wells in the area had been hydraulically fractured, the injection well was not. Observations from cores indicate that natural fractures in the Donovan Sand are extremely rare, so induced fractures are expected to be the only fractures that could affect the $CO_2$ flood. Although the direction of such a fracture cannot be determined from the results of the pressure-transient test, a fracture in the direction of maximum horizontal compressive stress in the Southeastern U.S., typically between an azimuth of 70 and 80$^o$, is consistent with the locations, relative to the injector, of production wells where early breakthrough occurred. Whether a fracture was induced in the injection well during water or gas injection is unclear, although the lack of natural fractures in the reservoir may indicate that the reservoir is under significant stress and can be fractured easily when pore pressure is increased. Unexpected plume extension has strong implications for the applicability of $CO_2$-enhanced recovery in Citronelle Field and should be considered when selecting injection and production wells for enhanced recovery operations.

An injection profile test was conducted in January 2012 to determine if either of the target sands was primarily responsible for the loss in injectivity to water, following the $CO_2$ injection. The test established that 35% of the water flow was to Sand 14-1 and 65% was to Sand 16-2, so neither injection zone was completely blocked, but comparison with the results of an injection profile run before $CO_2$ injection showed that loss of flow into the finer-grained Sand 14-1 was primarily responsible for the low injectivity to water.

Injected water was treated with surfactant to reduce capillary pressure, if that were blocking the water flow. The surfactant treatment was conducted during the three months from July 25 to November 7, 2012. Though the surfactant was associated with a transient increase in injectivity, both during and following the treatment, after about 6 months water injection returned to the low rates typical of the period following $CO_2$ injection. The conclusion from the surfactant treatment is that while capillary blocking of water injection may have contributed to the loss in injectivity, it was

not the principal effect responsible for the large reduction in injectivity experienced on returning to water injection following the $CO_2$ slug.

Following the surfactant treatment, during repair of a tubing leak, flakes of the internal plastic coating (IPC) of the tubing and particles of iron oxide scale were found in the injector. Plugging of the finer-grained Sand 14-1 by fine particles of scale is considered the most likely explanation for the well's low injectivity to water following the $CO_2$ injection. Problems with IPC were experienced by Denbury Resources throughout its oilfield operations around that time.

Treatment of the injector with hydrocarbon solvent and asphaltene dispersant had only a transient effect on its injectivity to water. Paraffins or asphaltenes precipitated when supercritical $CO_2$ mobilized lighter components are not thought to have made a significant contribution to the loss in injectivity to water following the $CO_2$ injection.

A flow-back of the injector was conducted in an attempt to flush out particles, but the flow-back had no lasting effect. If particles were, in fact, responsible for the loss in injectivity, they were not easily dislodged.

Uncertainty introduced into the baseline oil production at both tank batteries, during the troubleshooting of $CO_2$ pumping and injection, undermined the ability to make a reliable estimate of the incremental gain or loss in oil production associated with the $CO_2$ injection.

***Surface Monitoring.*** A detailed study of soil conditions at the test site was conducted by members of the AAMU team, including measurements of soil moisture, temperature, pH, electrical conductivity, carbon, nitrogen, phosphorus, and $CO_2$ fluxes at three locations surrounding four of the five wells in the test pattern and around the plugged and abandoned well within the pattern. Four sets of soil samples and nine sets of soil gas samples were collected from August 2008 to October 2012. Carbon dioxide fluxes from soil ranged from approximately -1 to +2 mg/($m^2$·min), depending on location, and exhibited seasonal variation. The fluxes at all of the measurement sites were positively correlated with soil temperature and the measurements at most sites were negatively correlated with soil moisture, as expected. Soil gas samples collected in August 2010, toward the end of the $CO_2$ injection, showed no evidence of $CO_2$ seepage.

$CO_2$ in ambient air was measured at least once each quarter, from September 2007 to June 2012, at 104 sampling locations in the Citronelle Oil Field and City of Citronelle. Only one anomalous reading appears in the entire set of $CO_2$ measurements, in June 2009, after filling the $CO_2$ storage tank in March 2009 and during unsuccessful attempts to inject $CO_2$, but before continuous $CO_2$ injection began in December 2009. The rest of the $CO_2$ measurements are consistent with the seasonal variations and long-term trends of the local NASA satellite-based Atmospheric Infrared Sounder data and worldwide average atmospheric $CO_2$ levels. Roberts (2013) reported an increase of 2.3 ppmv $CO_2$ in the averages over all sets of data taken before and after breakthrough of $CO_2$ at Well B-19-11 in May 2010, after correcting for the worldwide increase in atmospheric $CO_2$ during the period, but the scatter of the $CO_2$ measurements used to determine the averages is almost an order of magnitude larger.

Ten meter by ten meter square test plots were established near the injector, producers, and tank batteries, in which to monitor growth of vegetation. Inventories of the vegetation plots were

conducted in 2008, 2009, 2010, and 2011. Comparison of the growth rates during 2008-2009 with those during 2009-2010 shows that the plant growth rate increased from the first period to the second in two plots and decreased in five of them. Comparison of the growth rates during 2009-2010 with those during 2010-2011 shows that the plant growth rate increased from the second period to the third in three plots and decreased in five of them. The overall trend is one of decreasing growth rates, rather than the increase in rates that might be expected had there been elevated levels of $CO_2$.

One plot, located near the injector, Well B-19-10 #2, did exhibit an increase in the rate of growth of vegetation during the four-year period. This is an interesting and unexpected observation, in view of the fact that neither elevated levels of $CO_2$ in ambient air nor elevated $CO_2$ fluxes from soil were consistently observed near that well. Changes in growth rate from place-to-place and year-to-year are more likely explained by patterns of rainfall, temperature, and solar insolation than by $CO_2$ plumes associated with the $CO_2$ storage tank, injection equipment, wells, or tank batteries. Roberts and Chen (2012) concluded that the increase in rate of growth of vegetation in the plot near the injector was not significant and most likely could be explained by other factors.

***Seismic Imaging and Geostability Analysis.*** Constraints imposed by the nature of land ownership and use at the test site required examination of alternatives to traditional seismic imaging techniques, but the great depth and small thickness of the target sands made this task especially challenging. A passive sensing technique using wireless sensors and Refraction Microtremor (ReMi) technology was developed that was able to construct subsurface seismic profiles at the test site using only ambient noise. Shear-wave velocity profiles were constructed from data recorded during nine field measurement campaigns, before, during, and following $CO_2$ injection.

Geomechanical stability analyses were performed using a 1-dimensional effective stress model, a 3-dimensional finite element model, and the geophysical testing results. Both models indicate only small deformations as a result of overburden pressure on the Donovan Sands (0.56 to 0.75 ft for the Upper Donovan and 0.28 to 0.39 ft for the Lower Donovan) and a strain rate of 0.14 to 0.19%, below the expected rupture limit of 0.3% for quasi-brittle materials.

An interesting trend appeared in the time dependence of the slope of shear-wave velocity versus depth in the region below about 5000 ft. While the slope in the upper region, above ~4000 ft, remained within relatively narrow limits during $CO_2$ and subsequent water injection, the slope in the lower region, below ~5000 ft, which was initially much steeper, declined and approached the slope in the upper region, evidently a result of pressurization by $CO_2$ and water. Interpretation of the shear-wave velocity versus depth profile using a multiple degrees of freedom lumped mass model indicated that the geophysical testing method was able to distinguish stress changes in the oil-bearing layer from stress changes in the strata above.

The record of normalized well-head pressure at the injector was consistent with the normalized equivalent stresses from the seismic sensor array at the depth of the target Donovan Sands during $CO_2$ injection. This encouraging result suggests that the geophysical testing technique may be useful for monitoring formation pressure.

A laboratory experiment was designed and set up at UNCC, with which to measure the effects of solid matrix composition, porosity, and fluid saturations (oil, water, and $CO_2$) on stiffness and shear-wave velocity. The results of these experiments are intended to assist in the interpretation of the observed variation of shear-wave velocity with depth and volumes of $CO_2$ and water injected.

***Reservoir Management.*** The low injectivity to water experienced following the $CO_2$ injection is disturbing. Not having the ability to inject water after $CO_2$ would limit the options available for reservoir management. Extension of Denbury's $CO_2$ pipeline from its easternmost point, at Eucutta, MS, to Citronelle, will be a large and costly undertaking. An attractive alternative is to use $CO_2$ captured from coal combustion products at Alabama Power Company's Plant Barry, only 12 miles from Citronelle. It is with this scenario in mind that a large-scale demonstration of $CO_2$ capture, pipeline transport, and underground injection for storage in the Southeast Citronelle Unit is underway at Plant Barry, led by the Southeast Regional Carbon Sequestration Partnership (SECARB) and primary sponsors, U.S. DOE, National Energy Technology Laboratory, and Southern States Energy Board, with industrial partners, Advanced Resources International, Alabama Power Co., Denbury Resources, Electric Power Research Institute, Geological Survey of Alabama, Southern Company, and Southern Natural Gas (Esposito et al., 2011; Koperna et al., 2012). WAG recovery would be an attractive option if $CO_2$ were supplied from Plant Barry, because it would provide a means to accommodate outages at the Plant, and because WAG can increase oil recovery, compared with continuous $CO_2$ injection.

An investigation of WAG performance was conducted using the MASTER 3.0 reservoir simulator, to compare incremental oil yield and $CO_2$ storage under different WAG schedules (Theodorou, 2013). According to the model examined, all except one of the WAG scenarios (2 months $CO_2$ - 6 months water) outperformed incremental oil production from $CO_2$-only injection, under conditions expected to be representative of the Citronelle Field. The best performing sequence, with respect to oil recovery over a 10-year project, was 12 months of $CO_2$ injection followed by 6 months of water injection. The net amount of $CO_2$ stored can be increased by 40%, by lengthening the period of $CO_2$ injection from 12 months to 24 months, with only a 1.4% penalty in incremental oil production.

Using the MASTER 3.0 simulation results, three-dimensional animated visualizations were programmed showing the evolution of fluid saturations in Donovan Sands 14-1 and 16-2 during two $CO_2$ injections of 7500 tons each, separated by water injection. The animations nicely capture the mobilization of oil by $CO_2$, development of the oil bank, the role of water in driving the bank, and the residual oil left unrecovered. A study of the sensitivity of oil recovery to reservoir permeability showed that oil recovery increased with decreasing permeability, due to the associated decrease in mobility and increase in $CO_2$-oil contact time.

Reservoir simulations using SENSOR (Coats Engineering, Inc.) showed that cumulative oil production increases with increasing amount of $CO_2$ injected, regardless of the assumed permeability distribution. However, in all cases considered, there was an optimum $CO_2$ slug size, from the point of view of the profitability of a $CO_2$-EOR project. The optimum size of $CO_2$ slug increases with increasing oil price. The discount factor has little impact on the optimum size of $CO_2$ slug at high oil prices, but does have some impact at low oil prices.

Kuuskraa et al. (2004) estimated the oil recoverable from Citronelle Field using $CO_2$-EOR to be 64 million bbl, or 17% of the original oil in place. Denbury Resources' estimate of the Field's EOR potential is 26 million bbl. Assuming 10% of OOIP to be economically recoverable (38 million bbl) using $CO_2$-EOR and a production rate increased to 1.1 million bbl/year (twice present production), the life of the field would be extended by 35 years.

The capacity of Citronelle Dome for $CO_2$ storage was estimated to be 530 to 2100 million short tons (Esposito et al., 2008), sufficient to store the $CO_2$ produced from coal-fired generation at nearby Alabama Power Plant Barry for at least 40 years.

## 13.2. Lessons Learned

In spite of the many years of combined experience that the members of the research team brought to the project, the special conditions and objectives of the work taught the group valuable lessons that will be useful, should members of the team find themselves engaged in testing under similar circumstances, or in the design of a large-scale $CO_2$ flood in a field similar to Citronelle.

The carbon-13 to carbon-12 isotope ratio in $CO_2$ was shown to be a robust method for distinguishing sources of $CO_2$, without added tracer.

The interplay of depositional and diagenetic processes during the evolution of Citronelle Field resulted in reservoir sandstone bodies in which heterogeneity occurs at disparate scales, an important consideration for prioritizing $CO_2$ injection targets and understanding flow pathways.

Pumping liquid $CO_2$ can be challenging, though this is expected to be a possible problem only for small-scale pilot projects, not commercial projects utilizing pipeline $CO_2$.

The refraction microtremor seismic technique, utilizing only existing ambient excitation sources, provided useful information on the stress state of the reservoir and formations above it.

A maximum injection pressure should be established by testing and calculation, to minimize the probability that pressure in the injection zone may initiate unwanted fractures or propagate existing fractures.

A test is needed to assess the integrity of internal plastic coating in new tubing.

If WAG recovery were implemented, power oil pumps that are not resistant to erosion-corrosion should be replaced to avoid loss of production during down time resulting from premature failure of the pumps.

Lack of response of water injection to treatment of the injector with surfactant showed that capillary blocking, following $CO_2$ injection, was not the principal reason for the low injectivity to water.

Lack of response of water injection to treatment of the injector with hydrocarbon solvent and asphaltene dispersant indicates that precipitation of paraffins or asphaltenes had little effect on injectivity to water, following $CO_2$ injection.

Unequivocal determination of the effect of a change in solvent conditions or effect of well treatment can take many months.

The loss in injectivity to water, following $CO_2$ injection, is thought to have been caused by plugging of the finer-grained target sand by fine particles of scale mobilized by the mixture of $CO_2$ and water. The particles could not be dislodged and removed by flow back.

The difficulties experienced on switching from $CO_2$ to water injection suggest that continuous $CO_2$ injection would be preferable to WAG.

Uncertainty introduced into the baseline oil production, during the troubleshooting of $CO_2$ pumping and injection, undermined our ability to make a reliable estimate of the incremental gain or loss in oil production associated with the $CO_2$ injection.

**Acronyms and Abbreviations in Section 13**

| | |
|---|---|
| DOE | U.S. Department of Energy |
| EOR | enhanced oil recovery |
| IPC | internal plastic coating |
| MASTER | Miscible Applied Simulation Techniques for Energy Recovery (Ammer and Brummert, 1991; Ammer, Brummert, and Sams, 1991; Zeng, Grigg, and Chang, 2005) |
| OOIP | original oil in place |
| ReMi | refraction microtremor |
| SECARB | Southeast Regional Carbon Sequestration Partnership |
| SENSOR | System for Efficient Numerical Simulation of Oil Recovery (Coats Engineering, Inc., http://www.coatsengineering.com/) |
| SPE | Society of Petroleum Engineers, Richardson, TX |
| UNCC | University of North Carolina at Charlotte, Charlotte, NC |
| WAG | water-alternating-gas recovery |

**References in Section 13**


Ammer, J. R., and A. C. Brummert, "Miscible Applied Simulation Techniques for Energy Recovery Version 2.0, User's Guide," U.S. Department of Energy, DOE/BC--91/2/SP, February 1991.

Ammer, J. R., A. C. Brummert, and W. N. Sams, "Miscible Applied Simulation Techniques for Energy Recovery Version 2.0, Technical Manual," U.S. Department of Energy, DOE/BC--91/2/SP, February 1991.

Christie, M. A., and M. J. Blunt, "Tenth SPE Comparative Solution Project: A Comparison of Upscaling Techniques," *SPE Reservoir Evaluation & Engineering*, **2001**, *4*, 308-317.

Esposito, R. A., J. C. Pashin, and P. M. Walsh, "Citronelle Dome: A Giant Opportunity for Multi-Zone Carbon Storage and Enhanced Oil Recovery in the Mississippi Interior Salt Basin of Alabama," *Environmental Geosciences,* **2008,** *15* (2), 53-62.

Esposito, R. A., J. C. Pashin, D. J. Hills, and P. M. Walsh, "Geologic Assessment and Injection Design for a Pilot $CO_2$-Enhanced Oil Recovery and Sequestration Demonstration in a Heterogeneous Oil Reservoir: Citronelle Field, Alabama, USA," *Environmental Earth Sciences,* **2010**, *60*, 431-444.

Esposito, R., R. Rhudy, R. Trautz, G. Koperna, and G. Hill, "Integrating Carbon Capture with Transportation and Storage," *Energy Procedia*, **2011**, *4*, 5512-5519.

Gilchrist, R. E., "Miscibility Study (Repeat 50% P.V. Slug) in Cores, Citronelle Unit, Mobile County, Alabama," Ralph E. Gilchrist, Inc., Houston, TX, November 3, 1981.

Koperna, G., D. Riestenberg, V. Kuuskraa, R. Rhudy, R. Trautz, G. R. Hill, and R. Esposito, "The SECARB Anthropogenic Test: A US Integrated $CO_2$ Capture, Transportation and Storage Test," *International Journal of Clean Coal and Energy 1*, **2012**, 13-26.

Kuuskraa, V. A., R. Lynch, and M. Fokin, "Site Selection and Process Identification for $CO_2$ Capture and Storage Test Centers," Summary Report: Geologic Assessment of $CO_2$ Storage Options, Four Proposed Southern Company Power Plants, Prepared under Agreement No. E2-P79/C5887 for the Electric Power Research Institute by Advanced Resources International, Arlington, VA, March 26, 2004.

Kuuskraa, V. A., and G. J. Koperna, "Evaluating the Potential for 'Game Changer' Improvements in Oil Recovery Efficiency from $CO_2$ Enhanced Oil Recovery," Report prepared for the U.S. Department of Energy, Office of Fossil Energy, Office of Oil and Natural Gas, by Advanced Resources International, Arlington, VA, February 2006.

Kuuskraa, V. A., T. Van Leeuwen, and M. Wallace, "Improving Domestic Energy Security and Lowering $CO_2$ Emissions with 'Next Generation' $CO_2$-Enhanced Oil Recovery ($CO_2$-EOR)," Report Prepared by Energy Sector Planning and Analysis, Advanced Resources International, for the National Energy Technology Laboratory, U.S. Department of Energy, under Contract No. DE-FE0004001, DOE/NETL-2011/1504, Activity 04001.420.02.03, June 20, 2011.

Roberts, K. A., "Ecological Monitoring and Assessment of Enhanced Oil Recovery ($CO_2$-EOR) for Carbon Storage," Ph.D. Dissertation, Department of Biological and Environmental Sciences, Alabama A&M University, Normal, AL, December 2013.

Roberts, K. A., and X. Chen, "Direct and indirect assessment of vegetation located near $CO_2$-mediated enhanced oil recovery ($CO_2$-EOR) activities," Ecological Society of America, 97th Annual Meeting, Portland, OR, August 5-10, 2012, http://eco.confex.com/eco/2012/webprogram/Paper38361.html

Theodorou, K., "Carbon Dioxide Enhanced Oil Recovery from the Citronelle Oil Field and Carbon Sequestration in the Donovan Sand, Southwest Alabama," Ph.D. Dissertation, Interdisciplinary Engineering, University of Alabama at Birmingham, Birmingham, AL, 2013.

Zeng, Z., R. B. Grigg, and S. H. Chang, "Miscible Applied Simulation Techniques for Energy Recovery Version 3.0," Modifications of Version 2.0 User's Guide (Ammer and Brummert, 1991) and Technical Manual (Ammer, Brummert, and Sams, 1991), under DOE Contract No. DE-FG26-01BC15364, U.S. Department of Energy, July 26, 2005. http://www.netl.doe.gov/technologies/oil-gas/Software/Software_main.html

# Appendix A: Communication of the Work

---

A bibliography of the presentations, workshops, refereed publications, Ph.D. dissertations, and Master's theses describing work connected with the project is given below. The works are listed chronologically in each section.

## A.1. Presentations and Workshops

J. C. Pashin and R. A. Esposito, "Citronelle Dome: A Giant Opportunity for Multi-Zone Carbon Storage and Enhanced Oil Recovery in the Mississippi Interior Salt Basin of Alabama," Presented at the Annual Convention and Exhibition of the American Association of Petroleum Geologists, Long Beach, CA, April 1-4, 2007.

J. C. Pashin, R. A. Esposito, and P. M. Walsh, "Citronelle Dome: A Giant Opportunity for Multi-Zone Carbon Storage and Enhanced Oil Recovery in the Mississippi Interior Salt Basin of Alabama," Poster presentation at the DOE/NETL Sixth Annual Conference on Carbon Capture and Sequestration, Pittsburgh, PA, May 7-10, 2007.

E. S. Carlson, Workshop on visualization for reservoir simulation, Rocky Mountain Mathematics Consortium Summer School, "Flow in Porous Media with Emphasis on Modeling Oil Reservoirs," University of Wyoming, Laramie, WY, June 18-29, 2007.

Wen-Ya Qi, Shen-En Chen, P. M. Walsh, R. A. Esposito, and J. C. Pashin, "Geosensing for $CO_2$ Sequestration Monitoring in an Oil Field: Possible Global Warming Solution," Presented at the 3rd National Conference on Environmental Science and Technology, North Carolina A&T State University, Greensboro, NC, September 12-14, 2007.

J. C. Pashin and R. A. Esposito, "Citronelle Dome: A Giant Opportunity for Multi-Zone Carbon Storage and Enhanced Oil Recovery in the Mississippi Interior Salt Basin of Alabama," Presented at the 2007 Annual Convention of the Gulf Coast Association of Geological Societies and the Gulf Coast Section of the Society for Sedimentary Geology, Corpus Christi, TX, October 21-23, 2007.

R. A. Esposito, J. C. Pashin, and P. M. Walsh, "Citronelle Dome: A Giant Opportunity for Multi-Zone Carbon Storage and Enhanced Oil Recovery in the Mississippi Interior Salt Basin of Alabama," *Gulf Coast Association of Geological Societies Transactions*, **2007**, *57*, 213-224.

J. C. Pashin, "$CO_2$-EOR Pilot in Tidal Deposits of the Cretaceous Donovan Sand, Citronelle Field, SW Alabama," Presented at the Annual Convention and Exhibition of the American Association of Petroleum Geologists, San Antonio, TX, April 20-23, 2008.

J. C. Pashin, R. A. Esposito, and P. M. Walsh, "Pilot Design for $CO_2$-EOR and Sequestration Potential in the Citronelle Oil Field in the Mississippi Interior Salt Basin of Alabama," Presented at the Seventh Annual Conference on Carbon Capture and Sequestration, Pittsburgh, PA, May 5-8, 2008.

J. C. Pashin, "$CO_2$-Enhanced Oil Recovery Program in Citronelle Field, Southwest Alabama," Presented at the annual State of Alabama - U.S. EPA Region IV Underground Injection Control Meeting, hosted by the Alabama State Oil and Gas Board, Mobile, AL, October 29, 2008.

J. C. Pashin, D. J. Hills, D. C. Kopaska-Merkel, R. A. Esposito, and P. M. Walsh, "$CO_2$-Enhanced Oil Recovery Program in Citronelle Field, Southwest Alabama," Presentation at the monthly luncheon meeting of the New Orleans Geological Society, New Orleans, LA, November 3, 2008.

D. J. Hills, J. C. Pashin, D. C. Kopaska-Merkel, and R. A. Esposito, "Stratigraphy of the Citronelle Oil Field, AL: Perspectives from Enhanced Oil Recovery and Potential $CO_2$ Sequestration," Presented at the Fall Meeting of the American Geophysical Union, San Francisco, CA, December 15-19, 2008. Citation for the abstract: *Eos Trans. AGU, 89*(53), Fall Meet. Suppl., Abstract U41C-0020.

D. J. Hills, D. C. Kopaska-Merkel, J. C. Pashin, P. M. Walsh, and R. A. Esposito, "Geologic Characterization Supporting Enhanced Oil Recovery Pilot, Citronelle Oil Field, Southwest Alabama," Paper No. 22-5, Poster presentation by D. J. Hills at the 58th Annual Meeting of Southeastern Section of the Geological Society of America, St. Petersburg, FL, March 12-13, 2009. Geological Society of America, *Abstracts with Programs*, **2009**, *41* (1), 55. http://gsa.confex.com/gsa/2009SE/finalprogram/abstract_154650.htm

J. C. Pashin, D. J. Hills, D. C. Kopaska-Merkel, R. A. Esposito, and P. M. Walsh, "Multizone $CO_2$-EOR Pilot in Heterogeneous Sandstone, Citronelle Field, Southwest Alabama," Presented at the Eighth Annual Conference on Carbon Capture and Sequestration, Pittsburgh, PA, May 4-7, 2009.

Wenya Qi and Shen-En Chen, "Geophysical Sensing for $CO_2$-EOR and Sequestration," Paper No. 0920, International Coalbed and Shale Gas Symposium, University of Alabama, Tuscaloosa, AL, May 18-22, 2009.

J. C. Pashin, "Revitalizing Alabama's Largest Oil Field: Paleoenvironments of the Early Cretaceous Donovan Sand, Citronelle Field, Southwest Alabama," Presentation to the Alabama Paleontological Society, Birmingham, AL, July 6, 2009.

L. J. Lyte and E. Z. Nyakatawa, "Carbon Dioxide Fluxes in a Forest Soil in the Citronelle Oil Field of South Alabama," poster presentation at the 2009 Annual Meeting of the American Society of Agronomy, Crop Science Society of America, and Soil Science Society of America, Pittsburgh, PA, November 1-5, 2009.

J. C. Pashin, "Enhanced Oil Recovery and Carbon Sequestration Potential of Estuarine Sandstone Deposits, Donovan Sand (Lower Cretaceous), Citronelle Field, Southwest Alabama," Colloquium in the Department of Geology and Geography, Auburn University, Auburn, AL, November 12, 2009.

J. C. Pashin, "Carbon Sequestration Activities in Alabama," U.S. EPA Region IV State Water Directors Meeting, Lake Guntersville State Park, Guntersville, AL, November 18, 2009.

K. A. Roberts and X. Chen, "Ecological Monitoring and Assessment of EOR at Citronelle, Alabama," Poster presented at the joint Alabama Academy of Science and Alabama A&M University Science, Technology, Engineering, and Mathematics Day, Huntsville, AL, March 31, 2010.

D. J. Hills, D. C. Kopaska-Merkel, and J. C. Pashin, "Depositional and Diagenetic Factors Influencing $CO_2$-Enhanced Oil Recovery in Estuarine Sandstone Facies of the Donovan Sand (Lower Cretaceous), Citronelle Field, Southwest Alabama," Poster presented at the American Association of Petroleum Geologists, AAPG Annual Convention and Exhibition, New Orleans, LA, April 11-14, 2010.

Shen-En Chen, Y. Liu, and P. Walsh, "DoREMI for $CO_2$-EOR and Sequestration," Presented at the 2010 Sino-US Environmental Protection and Energy Summit & Expo, Atlanta, GA, April 24-25, 2010.

P. M. Walsh, K. Theodorou, A. M. Shih, P. C. Shum, G. N. Dittmar, T. Boelens, S. Walker, T. Miller, M. Sullivan, J. C. Pashin, D. J. Hills, D. C. Kopaska-Merkel, R. A. Esposito, E. Z. Nyakatawa, L. J. Lyte, K. A. Roberts, X. Chen, E. S. Carlson, F. Dumkwu, C. A. Turmero, P. E. Clark, S.-E. Chen, Y. Liu, and W. Qi, "Carbon-Dioxide-Enhanced Oil Recovery and Sequestration in Citronelle Dome, Southwest Alabama," Proceedings of the Ninth Annual Conference on Carbon Capture and Sequestration, Pittsburgh, PA, May 10-13, 2010.

L. Lyte and E. Nyakatawa, "Carbon Dioxide Fluxes and their Relationship to Forest Soil Properties," Poster presented at the joint American Society of Agronomy, Crop Science Society of America, and Soil Science Society of America 2010 International Annual Meetings, Long Beach, CA, October 31 to November 4, 2010.

Shen-En Chen, Yangguang Liu, and Peng Wang, "DoReMi - A Passive Geophysical Monitoring Technique for $CO_2$ Injection," SPE-149265-PP, Society of Petroleum Engineers Eastern Regional Meeting, Columbus, OH, August 17-19, 2011.

Shen-En Chen and Peng Wang, "$CO_2$ Injection Monitoring Using an Innovative Surface Monitoring Technique," 3rd Annual World Congress of Well Stimulation and EOR, Xi'an, China, April 25-28, 2012.

E. S. Carlson, A. Islam, F. Dumkwu, and T. Bertalan, "nSpyres, An Open-Source, Python-based Framework for Simulation of Flow though Porous Media," Session on Open Source Software for Porous Media, 4th International Conference on Porous Media and Annual Meeting of the International Society for Porous Media, Purdue University, West Lafayette, IN, May 14-16, 2012.

P. M. Walsh, K. Theodorou, P. C. Shum, E. Z. Nyakatawa, X. Chen, K. A. Roberts, L. J. Lyte, G. N. Dittmar, K. Murphy, S. Walker, T. Boelens, P. Guerra, T. Miller, T. Henderson, M. Sullivan, D. Beasley, S. Brewer, F. Everett, J. C. Pashin, D. J. Hills, D. C. Kopaska-Merkel, R. A. Esposito, K. M. Ellison, E. S. Carlson, P. E. Clark, A. W. Islam, C. A. Turmero, F. Dumkwu, S.-E. Chen, W. Qi, Y. Liu, and P. Wang, "Citronelle Dome, Southwest Alabama: $CO_2$-Enhanced Oil Recovery Pilot Test and Opportunities for $CO_2$ Storage," Research Experience in Carbon Sequestration 2012, Birmingham, AL, June 7, 2012.

J. C. Pashin and Staff of the Geological Survey of Alabama, Well Log and Core Matching Workshop, Research Experience in Carbon Sequestration 2012, Tuscaloosa, AL, June 7, 2012.

K. A. Roberts and X. Chen, "Direct and indirect assessment of vegetation located near $CO_2$-mediated enhanced oil recovery ($CO_2$-EOR) activities," Ecological Society of America, 97th Annual Meeting, Portland, OR, August 5-10, 2012.

L. T. Staley, E. Z. Nyakatawa, and L. J. Lyte, "Potential for Carbon Storage in the Citronelle Oil Field: A Geological Sink in South Alabama," Poster presentation at the 4th North American Carbon Program All-Investigators Meeting, Albuquerque, NM, February 4-7, 2013. Poster No. 176. <http://www.nacarbon.org/cgi-bin/meeting_2013/mtg2013_ab_search.pl?action=3&ab_id=73>

J. C. Pashin, M. R. McIntyre, S. D. Mann, and D. J. Hills, Well Log and Core Matching Workshop at the Geological Survey of Alabama, Research Experience in Carbon Sequestration 2013, Tuscaloosa, AL, June 20, 2013.

J. C. Pashin and M. R. McIntyre, Well Log and Core Matching Workshop at the Geological Survey of Alabama, Research Experience in Carbon Sequestration 2014, Tuscaloosa, AL, June 5, 2014.

## A.2. Refereed Publications

X. Chen and Y. Wang, "Emergent Spatial Pattern of Herpetofauna in Alabama, USA," *Acta Herpetologica*, **2007**, *2* (2), 71-89.

X. Chen and K. A. Roberts, "Roadless Areas and Biodiversity: A Case Study in Alabama, USA," *Biodiversity and Conservation*, **2008**, *17*, 2013-2022.

R. A. Esposito, J. C. Pashin, and P. M. Walsh, "Citronelle Dome: A Giant Opportunity for Multi-Zone Carbon Storage and Enhanced Oil Recovery in the Mississippi Interior Salt Basin of Alabama," *Environmental Geosciences*, **2008,** *15* (2), 53-62.

X. Chen, "Topological Properties in the Spatial Distribution of Amphibians in Alabama USA for the use of Large Scale Conservation," *Animal Biodiversity and Conservation*, **2008**, *31.1*, 1-13.

X. Chen and R. Fraser, "Quantifying Impacts of Land Ownership on Regional Forest NDVI Dynamics: A Case Study at Bankhead National Forest of Alabama, USA," *Photogrammetric Engineering & Remote Sensing*, **2009**, *75* (8), 997-1003.

Strategic Center for Natural Gas and Oil, National Energy Technology Laboratory, U.S. Department of Energy, "Southern Alabama $CO_2$ EOR Project to Begin Production Soon," *E&P Focus*, Fall 2009 Oil & Natural Gas Program Newsletter, pp. 1, 3-5. http://www.netl.doe.gov/technologies/oil-gas/publications/newsletters/epfocus/EPNewsFall09.pdf

R. A. Esposito, J. C. Pashin, D. J. Hills, and P. M. Walsh, "Geologic Assessment and Injection Design for a Pilot $CO_2$-Enhanced Oil Recovery and Sequestration Demonstration in a Heterogeneous Oil Reservoir: Citronelle Field, Alabama, USA," *Environmental Earth Sciences 60*, **2010**, 431-444.

X. Chen and S. Burton, "Power Law Relationships in the Branches of Loblolly Pine, Red Maple and Sugar Maple Trees," *Dendrobiology*, **2010**, *63*, 3-9.

X. Chen, W. M. Post, R. J. Norby, and A. T. Classen, "Modeling Soil Respiration and Variations in Source Components using a Multi-Factor Global Climate Change Experiment," *Climatic Change*, **2011**, *107*, 459-480.

X. Chen, "Spatial Geometry of Amphibian Distribution in Alabama, USA," *Wildlife Biology in Practice*, **2010**, *6* (2), 57-68.

X. Chen, "Trends of Forest Inventory Data in Alabama, USA, During the Last Seven Decades," *Forestry*, **2010**, *83* (5) 517-526. <http://forestry.oxfordjournals.org/content/early/2010/10/29/forestry.cpq034.full.pdf+html>

R. A. Esposito, L. S. Monroe, and J. S. Friedman, "Deployment Models for Commercialized Carbon Capture and Storage," *Environmental Science & Technology*, **2011**, *45*(1), 139-146.

R. Esposito, R. Rhudy, R. Trautz, G. Koperna, and G. Hill, "Integrating Carbon Capture with Transportation and Storage," *Energy Procedia*, **2011**, *4*, 5512-5519.

K. A. Roberts and X. Chen, "Considerations for Ecological Monitoring of $CO_2$-mediated Enhanced Oil Recovery," *International Journal of Ecological Economics and Statistics*, **2012**, *27*(4). <http://www.ceserp.com/cp-jour/index.php?journal=ijees&page=article&op=view&path%5B%5D=1374>

X. Chen, "Distribution patterns of invasive alien species in Alabama, USA," *Management of Biological Invasions*, **2012**, *3*(1), 25-36. <http://www.reabic.net/journals/mbi/2012/1/MBI_2012_1_Chen.pdf>

### A.3. Dissertations and Theses

Francis A. Dumkwu, "Reservoir Engineering Analysis: Citronelle Oil Field, Alabama," M.S. Thesis, Department of Chemical and Biological Engineering, University of Alabama, Tuscaloosa, AL, 2009.

Wenya Qi, "Preliminary Studies and Baseline Results for the Development of DoReMi for $CO_2$ Injection Monitoring at Citronelle, Alabama," M.S. Thesis, Department of Civil Engineering, University of North Carolina at Charlotte, Charlotte, NC, 2010.

Richard A. Esposito, "Business Models for Commercial-Scale Carbon Dioxide Sequestration; with Focus on Storage Capacity and Enhanced Oil Recovery in Citronelle Dome," Ph.D. Dissertation, Interdisciplinary Engineering, University of Alabama at Birmingham, Birmingham, AL, 2010.

Latasha J.-T. Lyte, "Carbon Dioxide Fluxes in a Forest Soil in the Citronelle Oil Field in South Alabama," M.S. Thesis, Department of Natural Resources and Environmental Sciences, Alabama A&M University, Normal, AL, 2011.

Yangguang Liu, "DoReMi - A Passive Geophysical Technique and Development of Bilinear Model for $CO_2$ Injection," M.S. Thesis, Department of Civil and Environmental Engineering, University of North Carolina at Charlotte, Charlotte, NC, 2012.

Konstantinos Theodorou, "Carbon Dioxide Enhanced Oil Recovery from the Citronelle Oil Field and Carbon Sequestration in the Donovan Sand, Southwest Alabama," Ph.D. Dissertation, Interdisciplinary Engineering, University of Alabama at Birmingham, Birmingham, AL, 2013.

Kathleen A. Roberts, "Ecological Monitoring and Assessment of Enhanced Oil Recovery ($CO_2$-EOR) for Carbon Storage, Ph.D. Dissertation, Department of Biological and Environmental Sciences, Alabama A&M University, Normal, AL, December 2013.

Yangguang Liu, "Study of $CO_2$ Injection at Citronelle Oil Field using Lumped Mass Modeling and Field Data Validation," Ph.D. Dissertation, Infrastructure and Environmental Systems, Department of Civil and Environmental Engineering, University of North Carolina at Charlotte, Charlotte, NC, 2014.

# Appendix B: Bibliography of Publications on the Citronelle Oil Field and Southwest Alabama Geology

---


Advanced Resources International, "Basin Oriented Strategies for $CO_2$ Enhanced Oil Recovery: Onshore Gulf Coast," Report to U.S. DOE, February 2006.

Alverson, R. M., "Deep Well Disposal Study for Baldwin, Escambia and Mobile Counties," Alabama, Alabama Geological Survey, Circular 58, 1970.

Anonymous, "Engineering Study and Appraisal Report," Vol. I, Tables and Figures. The report is not dated, but the latest data included in it are from 1987. Contains a profitability analysis, projected operating expenses, predicted water flood performance data, an index of cored wells, production data, fluid rates, porosity and permeability data, oil and water saturations, and pilot water flood performance results.

Bolin, D. E., S. D. Mann, D. Burroughs, H. E. Moore, Jr., and T. L., Powers, "Petroleum Atlas of Southwestern Alabama," Alabama Geological Survey, Atlas 23, 1989.

Chen, Shen-En, Yangguang Liu, and Peng Wang, "DoReMi - A Passive Geophysical Monitoring Technique for $CO_2$ Injection," SPE-149265-PP, Society of Petroleum Engineers Eastern Regional Meeting, Columbus, OH, August 17-19, 2011.

Claypool, G. E., and E. A. Mancini, "Geochemical Relationships of Petroleum in Mesozoic Reservoirs to Carbonate Source Rocks of Jurassic Smackover Formation, Southwestern Alabama," *AAPG Bulletin*, Vol. 73, 1989, pp. 904-924.

Donahoe, R. J., "An Experimental Study of a Waterflood Enhanced Oil Recovery Case History: The Citronelle Field, Mobile County, Alabama," Final Report for 1986/1987 SOMED Project, Department of Geology, University of Alabama, Tuscaloosa, March 1988.

Dumkwu, F. A., "Reservoir Engineering Analysis: Citronelle Oil Field, Alabama," M.S. Thesis, Department of Chemical and Biological Engineering, University of Alabama, Tuscaloosa, AL, 2009.

Eaves, E., "Citronelle Oil Field, Mobile County, Alabama," American Association of Petroleum Geologists Memoir 24, 1976, pp. 259-275.
http://egrpttc.geo.ua.edu/reports/citronelle/eaves.html

Esposito, R. A., "Business Models for Commercial-Scale Carbon Dioxide Sequestration; with Focus on Storage Capacity and Enhanced Oil Recovery in Citronelle Dome," Ph.D. Dissertation, Interdisciplinary Engineering, University of Alabama at Birmingham, Birmingham, AL, 2010.

Esposito, R. A., and J. C. Pashin, "Electrical Utility Perspective on Carbon Capture and Sequestration: R&D Pathways and Activities in Southeast USA Geology," Paper No. 0901, International Coalbed and Shale Gas Symposium, University of Alabama, Tuscaloosa, AL, May 18-22, 2009.

Esposito, R. A., J. C. Pashin, and P. M. Walsh, "Citronelle Dome: A Giant Opportunity for Multi-Zone Carbon Storage and Enhanced Oil Recovery in the Mississippi Interior Salt Basin of Alabama," *Gulf Coast Association of Geological Societies Transactions,* **2007**, *57*, 213-224.

Esposito, R. A., J. C. Pashin, and P. M. Walsh, "Citronelle Dome: A Giant Opportunity for Multi-Zone Carbon Storage and Enhanced Oil Recovery in the Mississippi Interior Salt Basin of Alabama," *Environmental Geosciences*, **2008,** *15* (2), 1-10.

Esposito, R. A., J. C. Pashin, D. J. Hills, and P. M. Walsh, "Geologic Assessment and Injection Design for a Pilot $CO_2$-Enhanced Oil Recovery and Sequestration Demonstration in a Heterogeneous Oil Reservoir: Citronelle Field, Alabama, USA," *Environmental Earth Sciences*, **2010**, *60,* 431-444.

Esposito, R., R. Rhudy, R. Trautz, G. Koperna, and G. Hill, "Integrating Carbon Capture with Transportation and Storage," *Energy Procedia*, **2011**, *4*, 5512-5519.

Fowler, M. L., L. E. Safley, M. A. Young, R. H. Stechmann, E. S. Blair, and R. E. Crumb, "Reservoir Management Strategy for Citronelle Field, Mobile County, Alabama," Report No. NIPER/BDM-0353, Prepared for the National Petroleum Technology Office, U.S. Department of Energy, Tulsa, OK, by BDM Petroleum Technologies, Bartlesville, OK, 1998.

Fretwell, J. A., and E. S. Blair, "Optimized Hydraulic Pumping System Keeps Deep Water Flood Economical," *World Oil*, November 1999.

Gilchrist, R. E., "Miscibility Study (Repeat 50% P.V. Slug) in Cores, Citronelle Unit, Mobile County, Alabama," Ralph E. Gilchrist, Inc., Houston, TX, November 3, 1981.

Gilchrist, R. E., "Evaluation of Produced Fluids from the Carbon Dioxide Pilot Area in the Citronelle Unit, Mobile County, Alabama," Ralph E. Gilchrist, Inc., Houston, TX, April 16, 1982.

Grubb, H. F., "Summary of Hydrology of the Regional Aquifer Systems, Gulf Coastal Plain, South-Central United States - Regional Aquifer System Analysis - Gulf Coastal Plain," U. S. Geological Survey, Professional Paper 1416-A, 1998.

Hall, D. R., and D. E. Bolin, with contributions by E. V. St. Clair and G. W. Crawford, "The Petroleum Industry in Alabama, 1999-2007," Oil and Gas Report 3U, State Oil and Gas Board of Alabama, Published by the Geological Survey of Alabama for the State Oil and Gas Board, Tuscaloosa, AL, 2009.

Holtz, M. H., V. Núñez López, and C. L. Breton, "Moving Permian Basin Technology to the Gulf Coast: the Geologic Distribution of $CO_2$ EOR Potential in Gulf Coast Reservoirs," in: *Unconventional Reservoirs*, P. H. Luftholm and D. Cox (Eds.), West Texas Geological Society Publication #05-115, Fall Symposium, October 26-27, 2005.

Huddleston, B. P., & Co., Inc., "Northwest Citronelle Unit, Mobile County, Alabama: Production, Maps, Well Data Sheets, Engineering Worksheets," Vol. III, Houston, TX, November 30, 1978.

Kennedy, J. R., T. G. Bett, and R. E. Gilchrist, "Reservoir Engineering Study of the $CO_2$ Project in the Citronelle Unit, Mobile County, Alabama," Ralph E. Gilchrist, Inc., Houston, TX, February 18, 1983.

Kopaska-Merkel, D. C., "Jurassic Cores from the Mississippi Interior Salt Basin, Alabama," Alabama Geological Survey, Circular 200, 2002.

Kopaska-Merkel, D. C., D. R. Hall, S. D. Mann, and B. H. Tew, "Reservoir Characterization of the Smackover Formation in Southwest Alabama," Report No. DOE/BC/14425-7, Final report of work performed under Contract No. FG22-89BC14425, Prepared for the U.S. Department of Energy by the Geological Survey of Alabama, Tuscaloosa, AL, February 1993.

Koperna, G., D. Riestenberg, V. Kuuskraa, R. Rhudy, R. Trautz, G. R. Hill, and R. Esposito, "The SECARB Anthropogenic Test: A US Integrated $CO_2$ Capture, Transportation and Storage Test," *International Journal of Clean Coal and Energy 1*, **2012**, 13-26.

Kuuskraa, V. A., R. Lynch, and M. Fokin, "Site Selection and Process Identification for $CO_2$ Capture and Storage Test Centers," Summary Report: Geologic Assessment of $CO_2$ Storage Options, Four Proposed Southern Company Power Plants, Prepared under Agreement No. E2-P79/C5887 for the Electric Power Research Institute by Advanced Resources International, Arlington, VA, March 26, 2004.

Liu, Yangguang, "DoReMi - A Passive Geophysical Technique and Development of Bilinear Model for $CO_2$ Injection," M.S. Thesis, Department of Civil and Environmental Engineering, University of North Carolina at Charlotte, Charlotte, NC, 2012.

Liu, Yangguang, "Study of $CO_2$ Injection at Citronelle Oil Field using Lumped Mass Modeling and Field Data Validation," Ph.D. Dissertation, Infrastructure and Environmental Systems, Department of Civil and Environmental Engineering, University of North Carolina at Charlotte, Charlotte, NC, 2014.

Lyte, L. J., "Carbon Dioxide Fluxes in a Forest Soil in the Citronelle Oil Field in South Alabama," M.S. Thesis, Department of Natural Resources and Environmental Sciences, Alabama A&M University, Normal, AL, 2011.

Mancini, E. A., and D. J. Benson, "Regional Stratigraphy of the Upper Jurassic Smackover Carbonates of Southwest Alabama," *GCAGS Transactions*, Vol. 30, 1980, pp. 151-165.

Mancini, E. A., R. M. Mink, B. L. Bearden, and R. P. Wilkerson, "Norphlet Formation (Upper Jurassic) of Southwestern and Offshore Alabama: Environments of Deposition and Petroleum Geology," *AAPG Bulletin*, Vol. 69, 1985, pp. 881-898.

Mancini, E. A., R. M. Mink, J. W. Payton, and B. L. Bearden, "Environments of Deposition and Petroleum Geology of Tuscaloosa Group (Upper Cretaceous), South Carlton and Pollard Fields, Southwestern Alabama," *AAPG Bulletin*, Vol. 71, 1987, pp. 1128-1142.

Miller, J. A., "Ground Water Atlas of the United States, Segment 6: Alabama, Florida, Georgia, and South Carolina," U. S. Geological Survey, Hydrologic Investigations Atlas No. HA-730-G, 1990.

Petrusak, R., D. Riestenberg, P. Goad, K. Schepers, J. Pashin, R. Esposito, and R. Trautz, "World Class $CO_2$ Sequestration Potential in Saline Formations, Oil and Gas Fields, Coal and Shale: The U.S. Southeast Regional Carbon Sequestration Partnership has it All," SPE 126619, Society of Petroleum Engineers, Richardson, TX, 2009.

Qi, Wenya, "Preliminary Studies and Baseline Results for the Development of DoReMi for $CO_2$ Injection Monitoring at Citronelle, Alabama," M.S. Thesis, Department of Civil Engineering, University of North Carolina at Charlotte, Charlotte, NC, 2010.

Raymond, D. E., "The Lower Cretaceous Ferry Lake Anhydrite in Alabama, Including Supplemental Information on the Overlying Mooringsport Formation and the Petroleum Potential of the Lower Cretaceous," Alabama Geological Survey, Circular 183, 1995.

Roberts, K. A., "Ecological Monitoring and Assessment of Enhanced Oil Recovery ($CO_2$-EOR) for Carbon Storage, Ph.D. Dissertation, Department of Biological and Environmental Sciences, Alabama A&M University, Normal, AL, December 2013.

Strategic Center for Natural Gas and Oil, National Energy Technology Laboratory, U.S. Department of Energy, "Southern Alabama $CO_2$ EOR Project to Begin Production Soon," *E&P Focus*, Fall 2009 Oil & Natural Gas Program Newsletter, pp. 1, 3-5. http://www.netl.doe.gov/technologies/oil-gas/publications/newsletters/epfocus/EPNewsFall09.pdf

Theodorou, K., "Carbon Dioxide Enhanced Oil Recovery from the Citronelle Oil Field and Carbon Sequestration in the Donovan Sand, Southwest Alabama," Ph.D. Dissertation, Interdisciplinary Engineering, University of Alabama at Birmingham, Birmingham, AL, 2013.

Tucker, W. E., and R. E. Kidd, "Deep-Well Disposal in Alabama," Alabama Geological Survey, Bulletin 104, 1973.

Unit Manager's Report, "341 Tract Citronelle Unit, Citronelle Field, Mobile County, Alabama," Engineering Subcommittee Meeting, Citronelle, AL, August 1, 1997.

Unit Manager's Report, "Reservoir Analyses of Oil Migration: Citronelle Oil Field, Mobile County, Alabama," July 29, 1999.

Wilson, M. D., and J. R. Warne, "Sand Continuity Study: Citronelle Field, Mobile County, Alabama," Report prepared for Unit Manager, Citronelle Unit, November 25, 1964.

# Appendix C: Contour Plots of $CO_2$ Volume Fraction across the City of Citronelle and Citronelle Oil Field

Kathleen A. Roberts and Xiongwen Chen
Department of Biological and Environmental Sciences
Alabama A&M University, Normal, Alabama

---



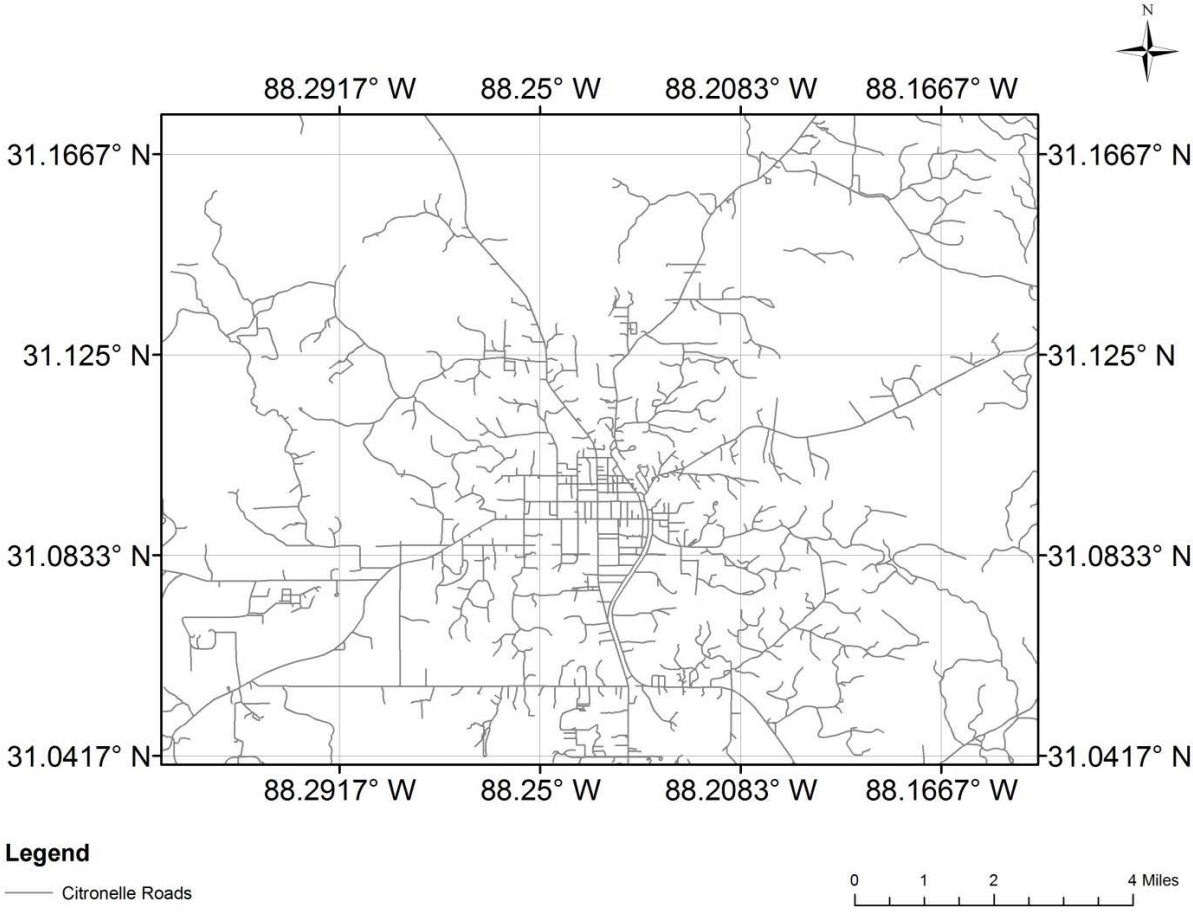


Figure C.1. Map of the Citronelle, AL, area, with coordinates that can be used to determine the approximate locations of high or low $CO_2$ volume fractions, or other features, in the contour plots, Figures 7.4 and C.2 to C.8.

a. January 2009

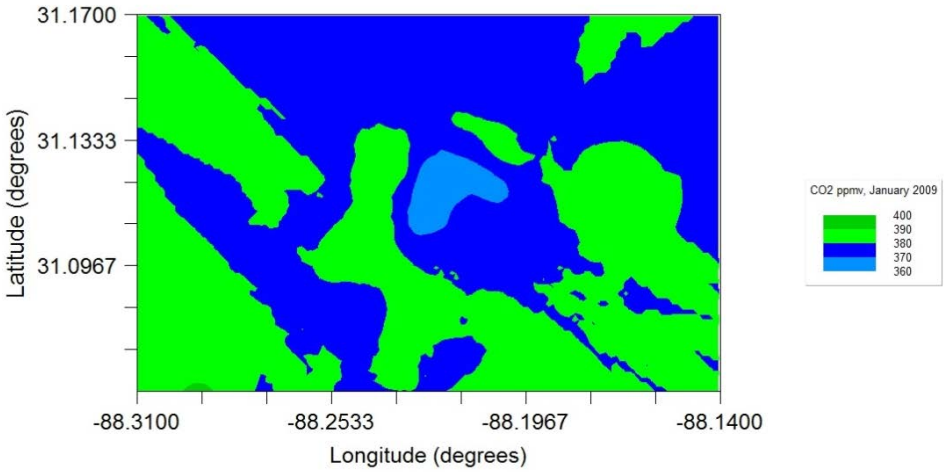


b. January 2010

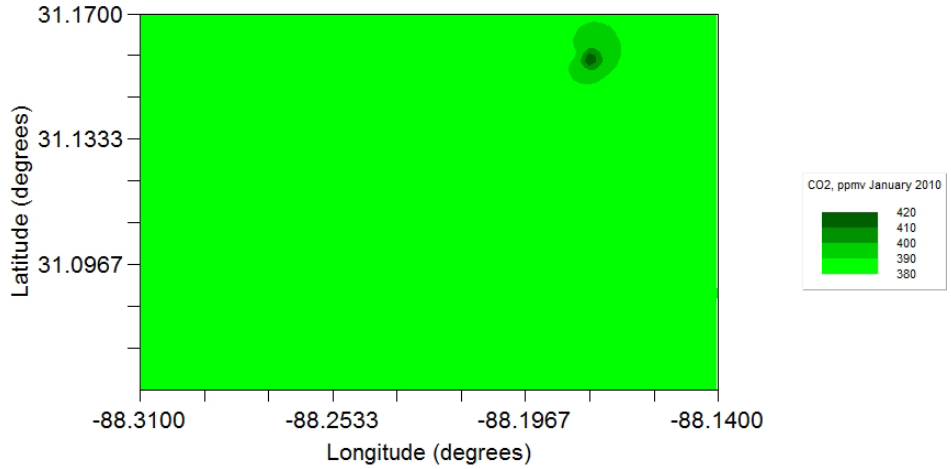


c. January 2011

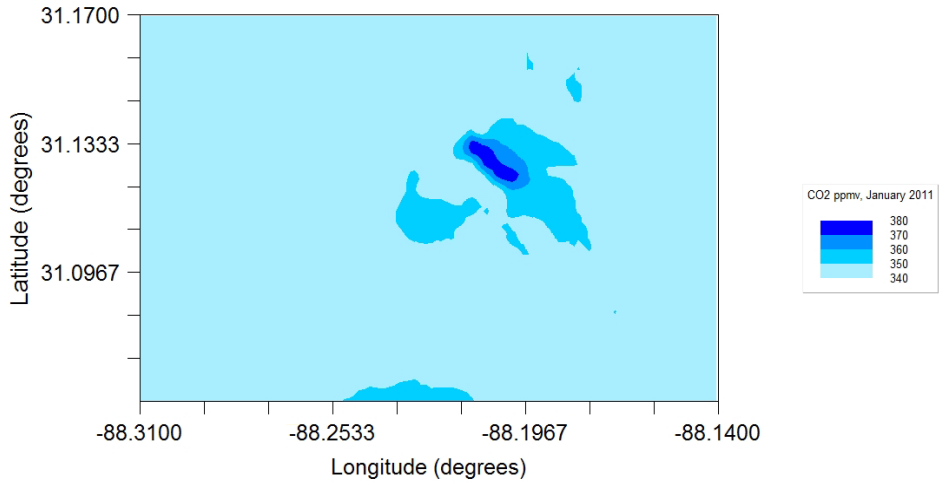


Figure C.2. Contour plots showing the spatial distribution of the $CO_2$ volume fraction across the City of Citronelle and Citronelle Oil Field in January 2009, January 2010, and January 2011.

a. March 2010

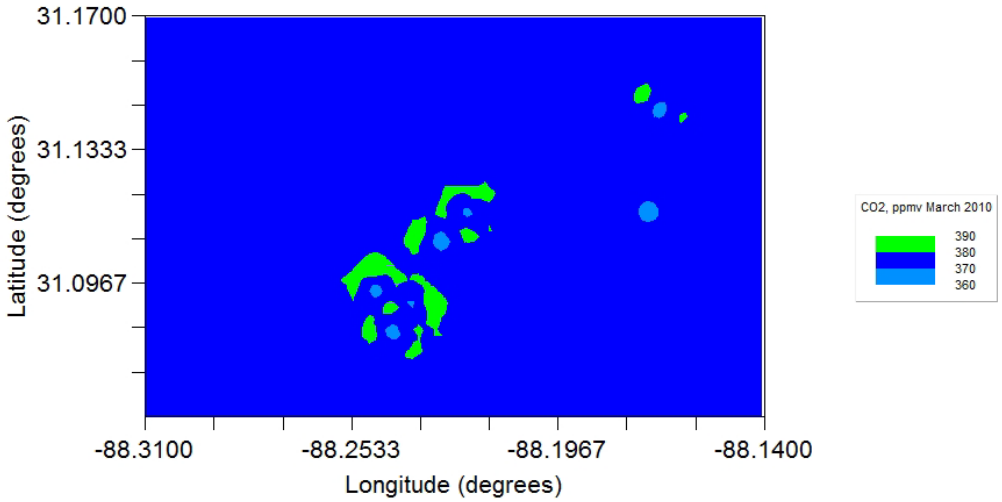


b. March 31 - April 1, 2011

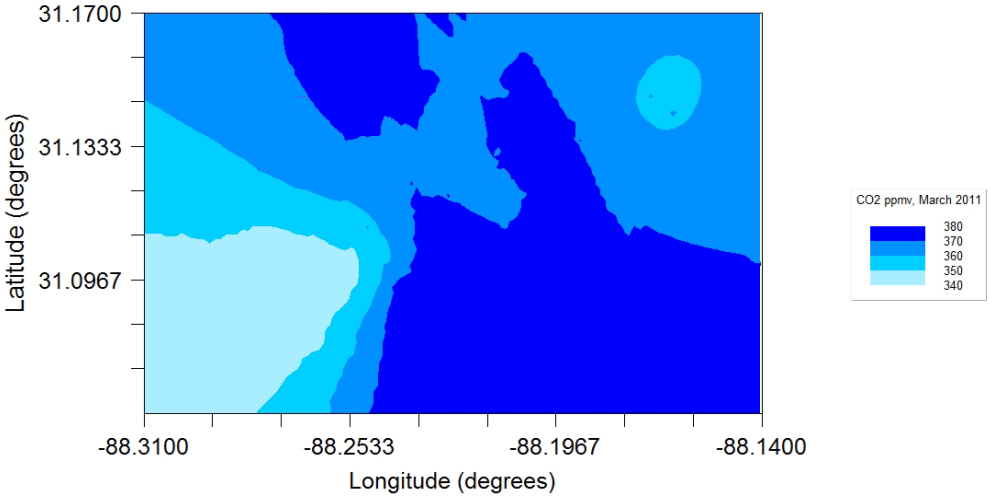


c. March 2012

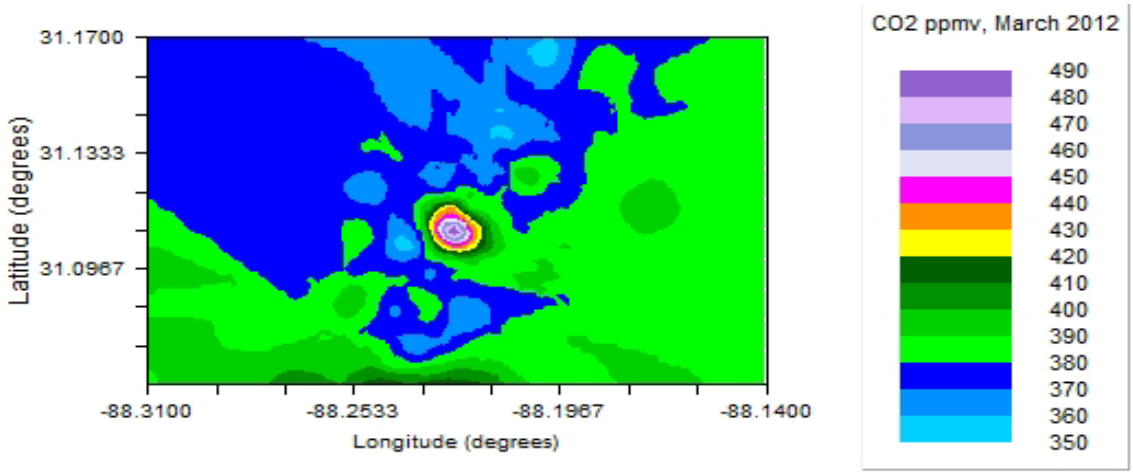


Figure C.3. Contour plots showing the spatial distribution of the $CO_2$ volume fraction across the City of Citronelle and Citronelle Oil Field in March 2010, March 2011, and March 2012.

a. April 2009

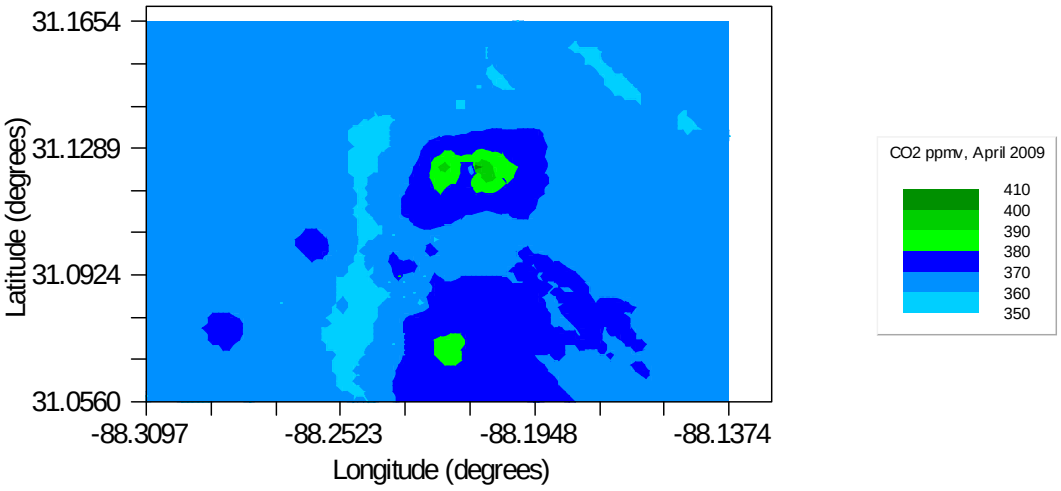


b. April 2010

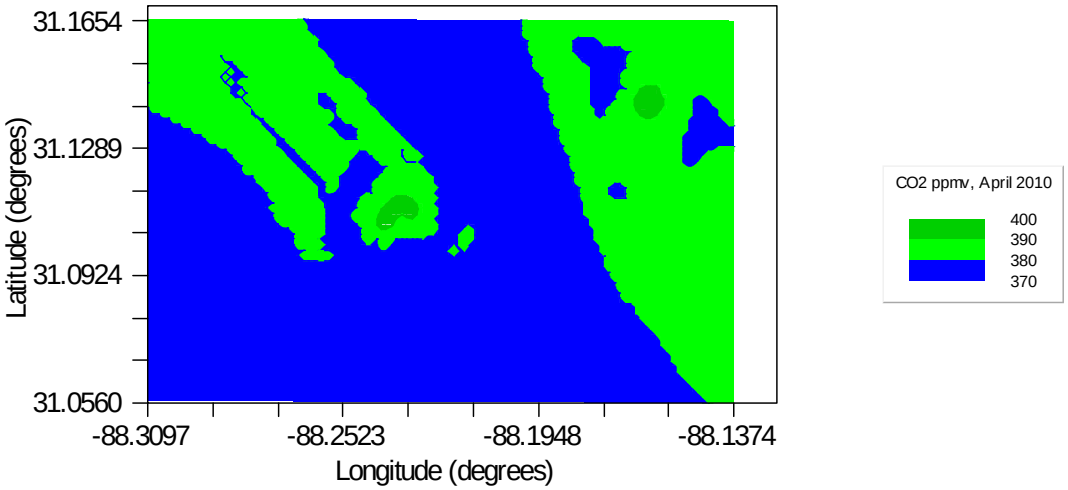


c. March 31 - April 1, 2011

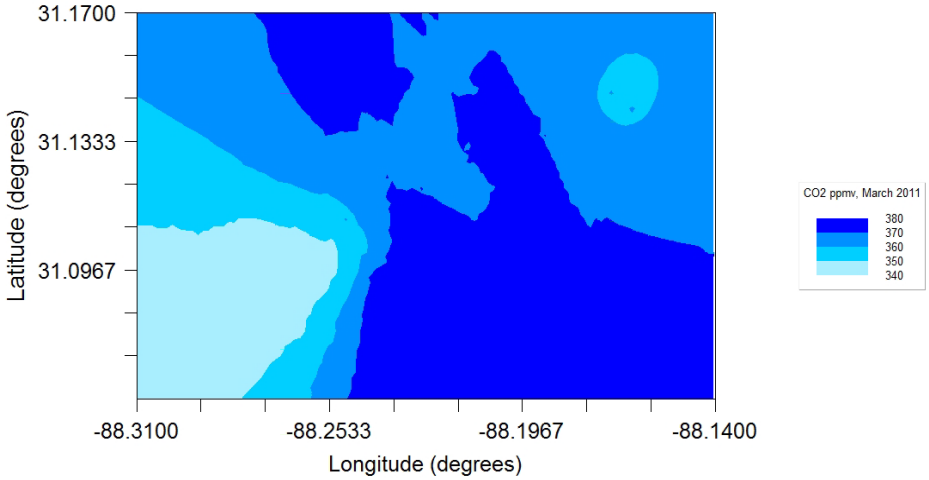


Figure C.4. Contour plots showing the spatial distribution of the $CO_2$ volume fraction across the City of Citronelle and Citronelle Oil Field in April 2009, April 2010, and March 31-April 1, 2011.

a. May 2008

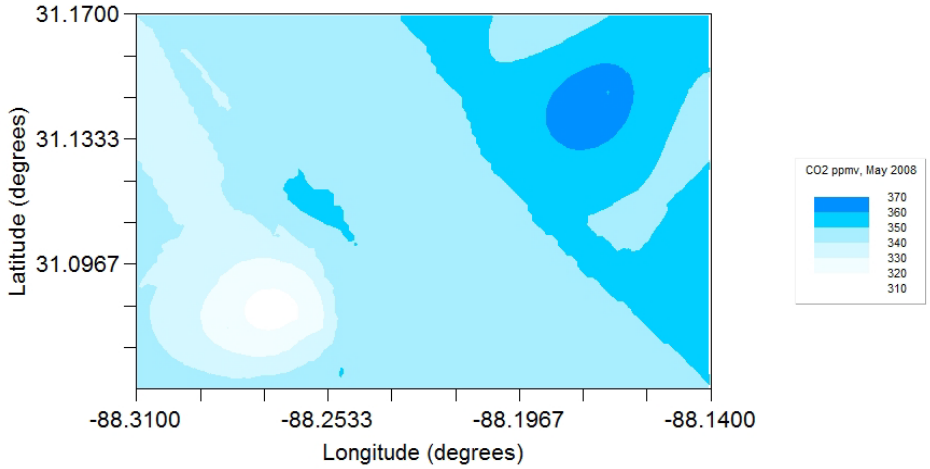


b. May 2010

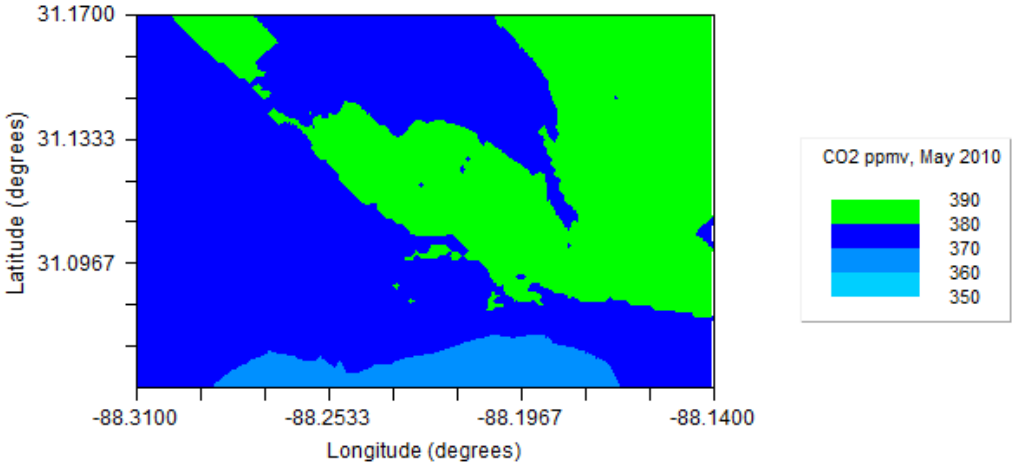


c. May 2011

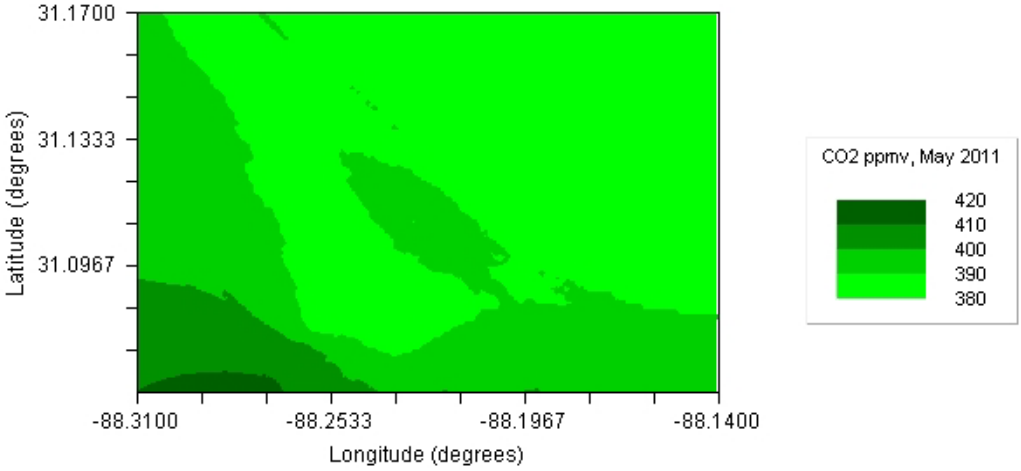


Figure C.5. Contour plots showing the spatial distribution of the $CO_2$ volume fraction across the City of Citronelle and Citronelle Oil Field in May 2008, May 2010, and May 2011.

a. June 2008

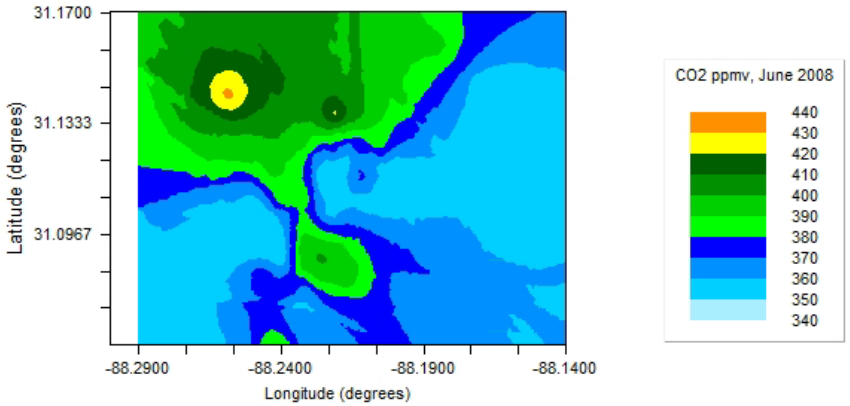


b. June 2009

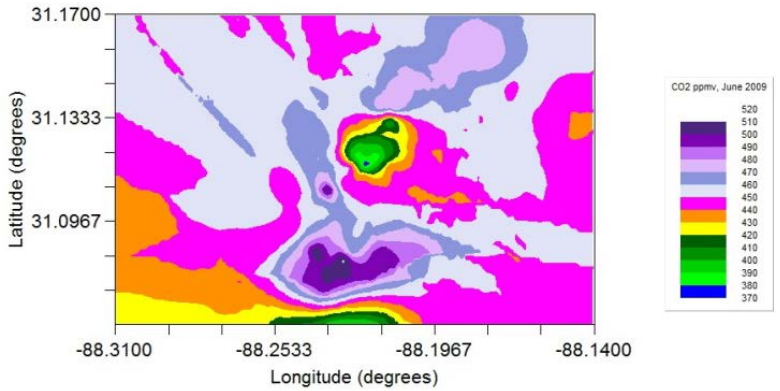


c. June 2010

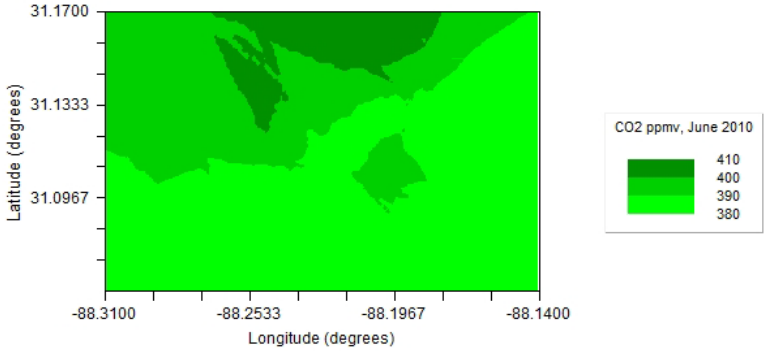


d. June 2012

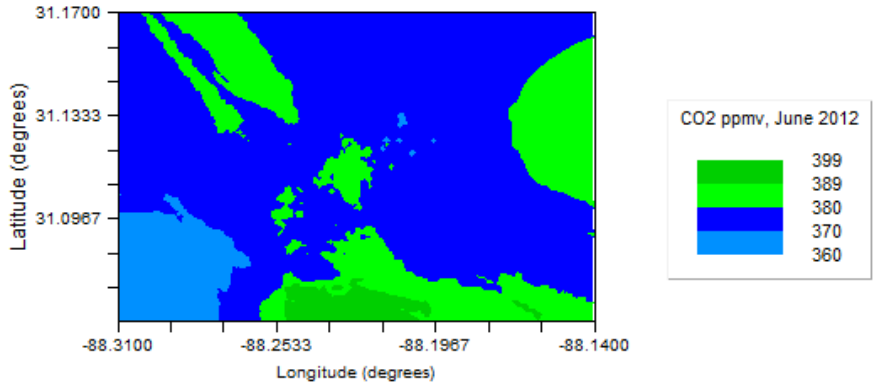


Figure C.6. Contour plots showing the spatial distribution of the $CO_2$ volume fraction across the City of Citronelle and Citronelle Oil Field in June 2008, June 2009, June 2010, and June 2012.

a. October 2008

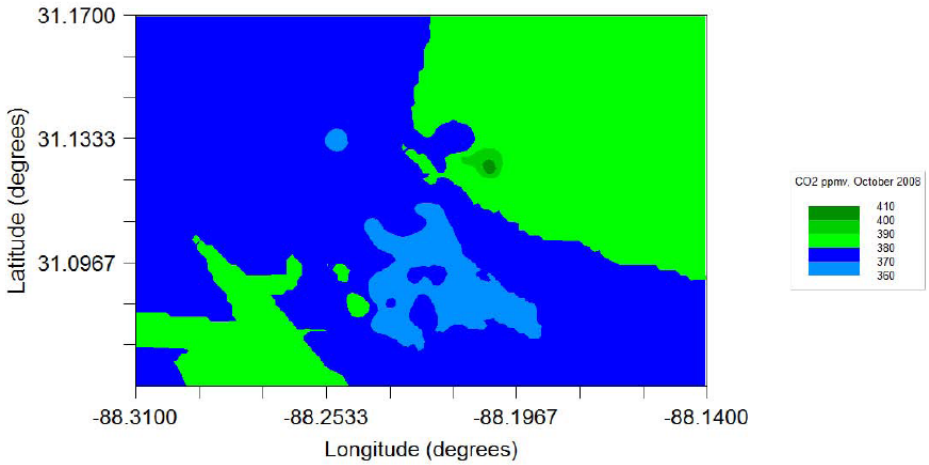


b. October 2009

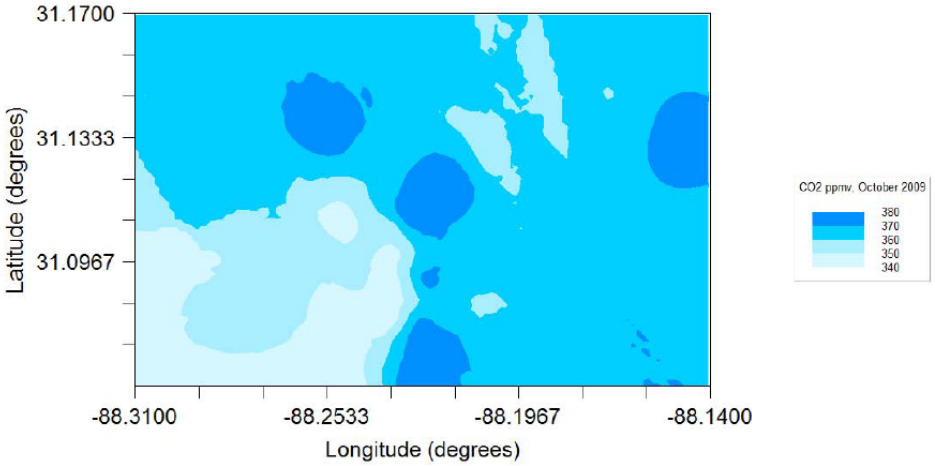


c. October 2010

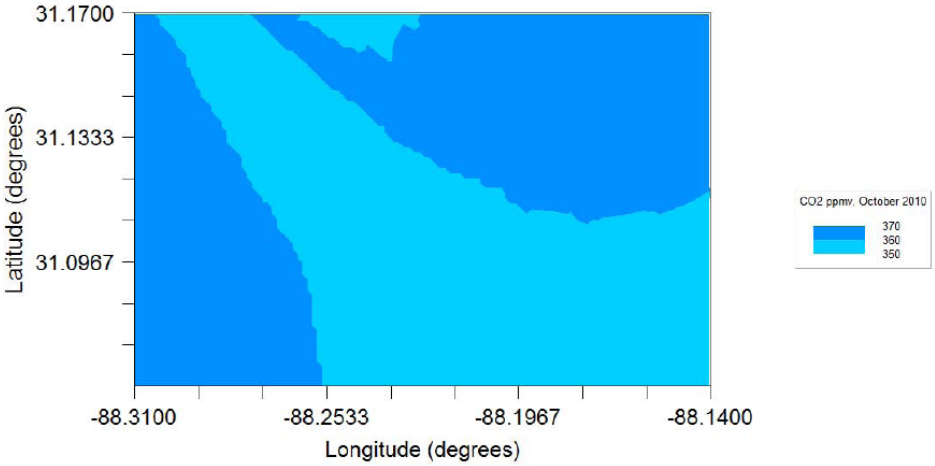


Figure C.7. Contour plots showing the spatial distribution of the $CO_2$ volume fraction across the City of Citronelle and Citronelle Oil Field in October 2008, October 2009, and October 2010.

a. December 2008

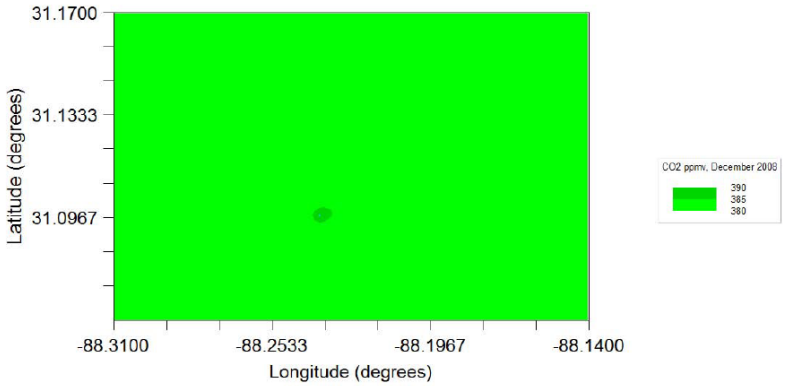


b. December 2009

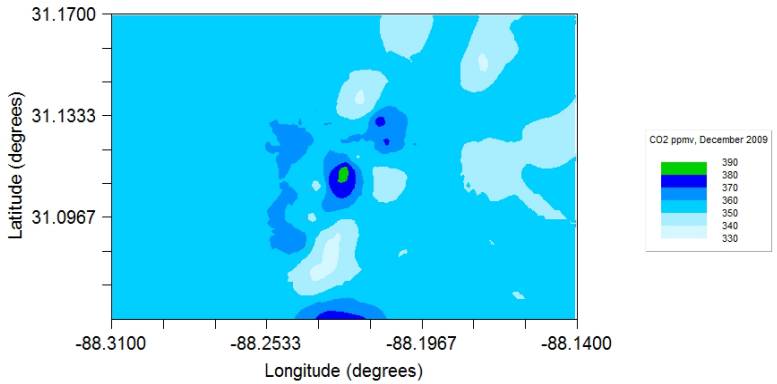


c. December 2010

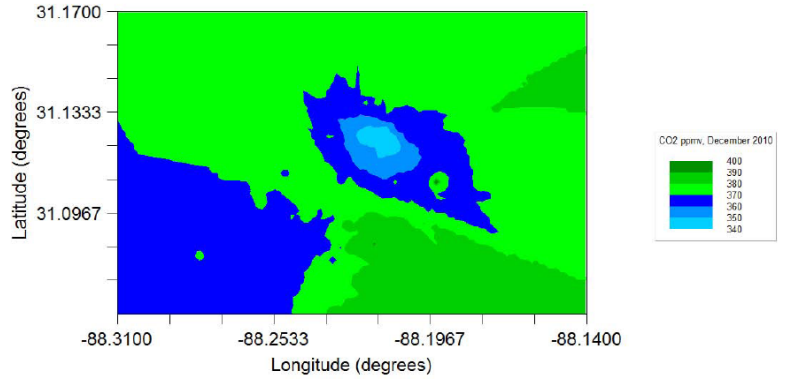


d. December 2011

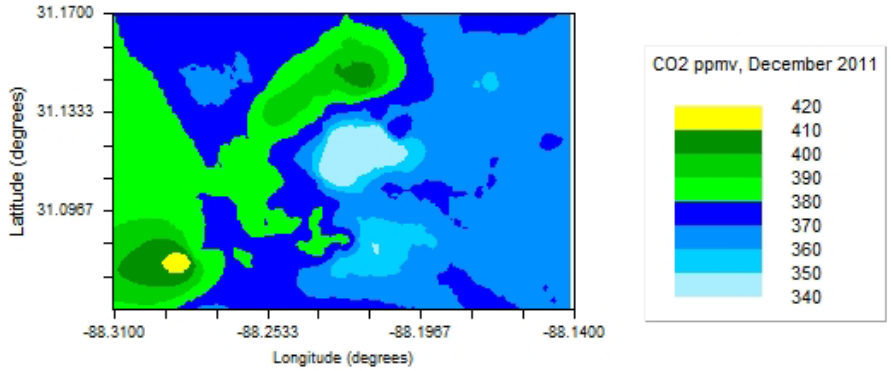


Figure C.8. Contour plots showing the spatial distribution of the $CO_2$ volume fraction across the City of Citronelle and Citronelle Oil Field in December 2008, December 2009, December 2010, and December 2011.